Dynamics of High Redshift Galaxies

Constraints of galaxy evolution 1–2 billion years after the Big Bang

Lilian Lai Yee Lee

SIGILL. UNIVERSITAT. LUDOVIC. MAXIM.

München 2025

Dynamics of High Redshift Galaxies

Constraints of galaxy evolution 1–2 billion years after the Big Bang

Lilian Lai Yee Lee

Dissertation
der Fakultät für Physik
der Ludwig-Maximilians-Universität
München

vorgelegt von
Lilian Lai Yee Lee
aus Hongkong

München, den 13 Oct 2025

Erstgutachter: Prof. Dr. Reinhard Genzel

Zweitgutachter: Prof. Dr. Volker Springel

Tag der mündlichen Prüfung: 24 Nov 2025

Zusammenfassung

Diese Arbeit präsentiert eine Studie über die Kinematik und die chemische Häufigkeitsverteilung massereicher sternbildender Galaxien (SFGs) während der ersten 1.5 Milliarden Jahre nach dem Urknall bei Rotverschiebungen von $4 < z < 6$. Sie nutzt eine leistungsstarke Sonde zur Untersuchung der Galaxienentstehung, nämlich deren Dynamik, die bislang in der entscheidenden Phase der kosmischen Geschichte — dem Zeitraum zwischen dem Ende der Reionisierung und dem Höhepunkt der kosmischen Sternentstehung — nur sehr unzureichend erforscht wurde.

Im Mittelpunkt der Analyse und Interpretation von Datensätzen steht die kinematische Modellierung, die bei hohen Rotverschiebungen, im Vergleich zu Daten lokaler Galaxies, aufgrund des Signal-Rausch-Verhältnisses (S/R) und der geringeren Auflösung Herausforderungen mit sich bringt. Die Arbeit beginnt mit einer umfassenden Untersuchung der aktuellen Methoden zur Modellierung von dreidimensionalen Datenätzen, die mit modernsten Instrumenten gewonnen wurden. Hierbei wird eine große Menge Modellgalaxien unter realistischen Beobachtungsbedingungen verwendet. Ein Vergleich verschiedener Modellierungscodes zeigt, dass bei typischen S/R-Werten die bestehenden Methoden zwar die Rotationsgeschwindigkeiten genau wiederherstellen können, es jedoch einen deutlichen Unterschied in der Geschwindigkeitsdispersion gibt, wobei die Auswirkungen der methodischen Unterschiede am deutlichsten zu erkennen sind. Parametrische Methoden zeichnen sich durch Stabilität und eine höhere Genauigkeit bei der Wiederherstellung wichtiger kinematischer Parameter aus.

Das dritte Kapitel präsentiert dann eine systematische Untersuchung von 32 massiven SFGs bei $4 < z < 6$ und liefert damit die größte systematische Charakterisierung der Kinematik typischer massiver SFGs in diesen Epochen auf Kiloparsec-Skala. Die Ergebnisse zeigen, dass etwa 50% der Galaxien scheibenartige Eigenschaften aufweisen. Die Scheiben zeichnen sich durch hohe Geschwindigkeitsdispersionen von etwa $70\,\mathrm{km\,s^{-1}}$ im Median aus, mit geringer Rotationsunterstützung. Diese Ergebnisse stützen die Annahme, dass gravitative Instabilitäten der Hauptgrund für Turbulenzen in diesen gasreichen Systemen sind, deren Eigenschaften hervorragend mit der auf der Toomre-Theorie basierenden vorhergesagten Entwicklung übereinstimmen, wonach die eigene Schwerkraft der Scheibe die stabilisierenden Effekte der Rotation und der internen Bewegungen überwiegt.

Die Verteilung von Metallen in Galaxien hängt eng mit ihrer Gasbewegung zusammen. Um dies zu untersuchen, analysiert die Arbeit die radialen Metallizitätsprofile der Gasphase

von SFGs bei $4 < z < 6$ mit JWST/NIRSpec. Diese Galaxien weisen flache bis leicht positive Metallizitätsgradienten auf, was auf eine effiziente Metallvermischung hindeutet. Ihr Gasreich-tum, ihre dispersionsdominierte Kinematik und ihre Übereinstimmung mit einer großen Menge an Literaturdaten, in der geschwindigkeitsdispersionsdominierte Systeme ebenfalls flache oder positive Gradienten aufweisen, deuten darauf hin, dass gravitative Instabilitäten durch großskalige Zuflüsse und Klumpenmigration eine schnelle radiale Vermischung bewirken könnten. Es gibt keinen deutlichen Unterschied in den Metallizitätsgradienten zwischen Scheiben und Nicht-Scheiben, eine Ähnlichkeit, die wahrscheinlich die für diese Epoche charakteristische starke kosmische Akkretion widerspiegelt.

Abstract

This thesis presents a study of the kinematics and chemical abundance distributions of massive star-forming galaxies (SFGs) during the 1.5 billion years after the Big Bang at redshifts $4 < z < 6$. It utilises a powerful probe of galaxy assembly, namely their dynamics, which have been very poorly explored at a critical time in cosmic history: the period between the End of Reionisation and peak cosmic star formation.

At the core of the analysis and interpretation of data sets is kinematic modelling, which poses challenges at high redshifts due to lower signal-to-noise ratio (S/N) and resolution compared to data from local galaxies. The thesis begins with an extensive investigation of current methodologies for modelling data cubes obtained from state-of-the-art facilities, using a large sample of mock galaxies with realistic observing conditions. A comparison of different modelling tools reveals that, for typical S/N values, while existing methodologies can accurately recover rotation velocities, there is a pronounced difference in velocity dispersion, with the impact of methodology differences being most apparent. Parametric methods excel in terms of stability and better fidelity in recovering key kinematic parameters of interest.

The third chapter presents a systematic study of a sample of 32 massive SFGs at $4 < z < 6$, providing the largest systematic, kiloparsec-scale characterisation of the kinematics of typical massive SFGs at these epochs. The results show that $\sim 50\%$ of the sample exhibits disk-like properties. The disks are characterised by high velocity dispersions of $\sim 70\,\mathrm{km\,s^{-1}}$ in median, with low rotational support. These findings support gravitational instabilities as the primary driver of turbulence in these gas-rich systems, with their properties being in excellent agreement with predicted evolution based on Toomre theory, in which the disk's own gravity outweighs the stabilising effects of rotation and internal motions.

The distribution of metals across galaxies is closely linked to their gas motion. To investigate this, the thesis examines the gas-phase radial metallicity profiles of SFGs at $4 < z < 6$ with JWST/NIRSpec. These galaxies show flat-to-slightly positive metallicity gradients, pointing to efficient metal mixing. Their gas richness, dispersion-dominated kinematics, and consistency with a large literature sample, where velocity-dispersion-dominated systems likewise display flat or positive gradients, indicate that gravitational instabilities could drive rapid radial mixing through large-scale inflows and clump migration. There is no marked difference in metallicity gradients between the disks and non-disks, a similarity that likely reflects the vigorous cosmic accretion characteristic of this epoch.

List of Figures

List of Tables

List of Abbreviations

AGN active galactic nuclei. 4, 11, 33, 44, 144, 183, 185, 187, 204, 205, 217
ALMA Atacama Large Millimeter/submillimeter Array. 5, 9, 20, 22, 29, 30, 83, 85, 102, 104, 105, 107, 108, 110, 117, 140–142, 148, 152, 177, 181, 184–186, 199, 225
ALPINE ALMA Large Program to Investigate C$^+$ at Early Times. xxiii, 103–105, 118, 167, 168, 177, 178, 180, 182, 184, 186, 188, 190, 192, 194, 196, 198, 200, 202, 204, 206, 208, 210, 212, 214, 216, 218, 220, 222, 224
AO Adaptive Optics. 20, 81, 85

CDM cold dark matter. 1, 2, 11, 104, 182
CMB cosmic microwave background. 1, 10, 228
CRISTAL [CII] Resolved ISM in STar-forming galaxies with ALMA. ix–xi, xiii, xxiii, 101, 103–105, 108, 110–112, 114–127, 129–141, 143–151, 154, 160, 163–169, 173–175, 177, 178, 180, 182–188, 190–192, 194–200, 202–206, 208, 210–212, 214, 216–218, 220, 222, 224

DM dark matter. vii, x, xxiii, 1, 2, 4, 11, 15–17, 26, 28, 29, 49, 51, 53, 59, 83, 102, 104, 120, 122, 123, 125, 126, 136–141, 173, 174, 226, 227

ELT Extremely Large Telescope. 214, 228
EoR Epoch of Reionisation. 9, 41
ERIS Enhanced Resolution Imager and Spectrograph. 20, 83, 85

HST *Hubble* Space Telescope. 2, 3, 5, 20, 24, 26, 108, 110, 116, 117, 140, 143, 144, 146–148, 151, 152, 201, 219, 229

IFU Integral Field Unit. 12, 20, 22, 33, 38, 40, 44, 46, 49, 50, 58, 60, 81, 84, 85, 102, 108, 113, 115, 122, 127, 141, 177, 179, 182, 184–186, 205, 211, 213–215, 219, 227, 228, 230
IGM intergalactic medium. 9–11, 201
ISM interstellar medium. 9, 11, 13, 19, 22, 29, 31, 33, 34, 37, 40, 45, 103, 104, 129, 132–134, 141, 179, 181, 229

JWST *James Webb* Space Telescope. x, xxiii, 2, 3, 9, 20, 26, 32, 37–39, 41, 44, 108, 110, 116–118, 121, 122, 127, 129, 140, 141, 143–150, 152, 163, 164, 167, 168, 177, 178, 180–182, 184, 186, 188, 190, 192, 194, 196, 198–200, 202, 204–

206, 208, 210, 212–214, 216, 218–220, 222–224, 230

LSF line spread function. 50, 53, 55, 57, 82, 88, 89, 187, 211

M/L mass-to-light ratio. 16, 49

MCMC Markov chain Monte Carlo. 47, 49, 50, 52–54

MS main sequence. vii, 5, 8, 11, 22, 26, 27, 29, 41, 42, 44, 45, 58, 80, 81, 83, 84, 101–105, 112, 113, 118, 119, 122, 123, 127–134, 136, 138–141, 163, 182, 185, 198, 213, 214

MW Milky Way. 8, 14, 15, 24, 37, 39, 40, 179, 196

NFW Navarro, Frenk & White. 16, 17, 28, 51, 122, 138, 140

NOEMA Northern Extended Millimeter Array. 5, 9, 20, 29, 83, 85, 102, 181

PDR photodissociation region. 31, 32, 103, 181

PSF point spread function. 28, 50, 53, 55, 57, 59, 88, 89, 163, 184, 186, 208, 211

R-J Rayleigh–Jeans. 8, 9, 166–168

RC rotation curve. ix, 15, 16, 18–20, 27, 28, 51–54, 77, 116–118, 120, 123, 124, 126, 129, 132, 133, 138, 148, 227

S/N signal-to-noise ratio. viii, ix, xxii, 17, 22, 28, 29, 43, 45, 46, 48, 50, 52, 54–56, 58, 60–70, 73–85, 90, 92–98, 100, 186, 187, 190, 203, 205, 208, 209, 211, 225, 226

SA spectro-astrometry. xiii, 106, 115, 116, 142–144, 146–150, 152, 170

SED spectral energy distribution. vii, 30, 129, 163, 166, 168, 183, 199, 201

SFG(s) star-forming galaxy/galaxies. vii, 5, 8, 9, 15, 22, 26, 27, 29–31, 34, 37, 41, 42, 44, 45, 58, 60, 80, 81, 83, 84, 101–105, 117, 118, 120, 122, 129, 130, 132, 134, 136, 138–140, 163, 181, 182, 185, 189, 198, 201, 206, 213, 214, 225, 226, 228, 229

SFR star formation rate. viii, 5, 6, 8, 9, 11, 31, 44, 57–60, 90, 91, 105, 113, 130, 133, 134, 136, 173, 176, 226

SINFONI Spectrograph for INtegral Field Observations in the Near Infrared. 20

SMG submillimetre-galaxy. 31, 107, 143, 144, 196, 228

sSFR specific star formation rate. xi, xxiii, 8, 11, 105, 179, 184, 206, 207, 214, 227

VLT Very Large Telescope. 5, 20

Publications

This cumulative dissertation is based on the following articles listed in chronological order:

1. **Disk Kinematics at High Redshift: DysmalPy's Extension to 3D Modeling and Comparison with Different Approaches**. 2025, ApJ, 978, 14, 10.3847/1538-4357/ad90b5.
   Lee L. Lilian, Förster Schreiber N. M., Price S. H., Liu D., Genzel R., Davies R., Tacconi L. J., Shimizu T. T., Shachar A. N., Espejo Salcedo J. M., Pastras S., Wuyts S., Lutz D., Renzini A., Übler H., Herrera-Camus R., Sternberg A. [Chap. 2]
2. **The ALMA-CRISTAL survey: Resolved kinematic studies of main sequence star-forming galaxies at $4 < z < 6$**. 2025, A&A, 701, A260, 10.1051/0004-6361/202555362.
   Lee L. Lilian, Förster Schreiber N. M., Herrera-Camus R., Liu D., Price S. H., Genzel R., Tacconi L. J., Lutz D., Davies R., Übler H., Naab T., Aravena M., Assef R. J., Barcos-Muñoz L., Bowler R. A. A., Burkert A., Chen J., Davies R. L., De Looze I., Díaz-Santos T., González-López J., Ikeda R., Mitsuhashi I., Posses A., Relaño Pastor M., Renzini A., Solimano M., Spilker J. S., Sternberg A., Tadaki K., Telikova K., Veilleux S., Villanueva V. [Chap. 3]
3. **The ALPINE-CRISTAL-JWST Survey: Gas-phase abundance gradients and kinematics of MS SFGs at $4 < z < 6$**. 2025, A&A, submitted.
   Lee L. Lilian, Förster Schreiber N. M., Fujimoto S., Faisst A. L., Herrera-Camus R., Genzel R., Tacconi L. J., Lutz D., Renzini A., Sanders R., Wisnioski E., Wuyts S., Parlanti E., Jones G., Übler H., Liu D., Chen J., Davies R. I., Tozzi G., Burkert A., Price S. H., Aravena M., Boquien M., Béthermin M., da Cunha E., Davies R. L., De Looze I., Dessauges-Zavadsky M., Ferrara A., Fisher D. B., Gillman S., Ginolfi M., Ibar E., Koekemoer A. M., Molina J., Naab T., Relaño M., Riechers D. A., Sanders D. B., Spilker J. S., Vallini L., Zamorani G., Ambra N., Dam P., Diaz-Santos T., Gómez-Espinoza D., Hadi A., Ikeda R., Posses A., Romano M., Sternberg A., Villanueva V., Wang W. [Chap. 4]

They are L. L. Lee's own work except where due acknowledgement is made, and that it has not been previously included in a thesis, dissertation or report submitted to this University or to any other institution for a degree, diploma or other qualifications.

The following list indicates other published work in reverse chronological order that are closely related to the work in this thesis. The author of this thesis has contributed as co-author to these papers throughout the duration of the PhD.

1. **The ALMA-CRISTAL Survey: Weak Evidence for Star-formation-driven Outflows in $z \sim 5$ Main-sequence Galaxies**. 2025, ApJ, 985, 243, doi: 10.3847/1538-4357/adced3

   Birkin J. E., Spilker J. S., Herrera-Camus R., Davies R. L., **Lee L. L.**, Aravena M., Assef R. J., Barcos-Muñoz L., Bolatto A., Díaz-Santos T., Faisst A. L., Ferrara A., Fisher D. B., González-López J., Ikeda R., Knudsen K., Li J., Li Y., de Looze I., Lutz D., Mitsuhashi I., Posses A., Relaño M., Solimano M., Tadaki K., Villanueva V.

   Lee L. L. contributed to the intepretion of the kinematic nature of the sample, in close relation to Paper II above.

2. **Galaxy morphologies at cosmic noon with JWST: A foundation for exploring gas transport with bars and spiral arms**. 2025, A&A, 700, A42, doi: 10.1051/0004-6361/202554725

   Espejo Salcedo J. M., Pastras S., Vácha J., Pulsoni C., Genzel R., Förster Schreiber N. M., Jolly J.-B., Barfety C., Chen J., Tozzi G., Liu D., **Lee L. L.**, Wuyts S., Tacconi L. J., Davies R., Übler H., Lutz D., Wisnioski E., Shangguan J., Lee M., Price S. H., Eisenhauer F., Renzini A., Shachar A. N., Herrera-Camus R.

   Lee L. L. contributed to the JWST data reduction and data post-processing, as well as manuscript editing.

3. **The ALMA-CRISTAL survey: Gas, dust, and stars in star-forming galaxies when the Universe was ~ 1 Gyr old: I. Survey overview and case studies**. 2025, A&A, 699, A80, doi: 10.1051/0004-6361/202553896

   Herrera-Camus R., González-López J., Förster Schreiber N., Aravena M., de Looze I., Spilker J., Tadaki K., Barcos-Muñoz L., Assef R. J., Birkin J. E., Bolatto A. D., Bouwens R., Bovino S., Bowler R. A. A., Calistro Rivera G., da Cunha E., Davies R. I., Davies R. L., Díaz-Santos T., Ferrara A., Fisher D., Genzel R., Hodge J., Ikeda R., Killi M., **Lee L. L.**, Li Y., Li J., Liu D., Lutz D., Mitsuhashi I., Narayanan D., Naab T., Palla M., Price S. H., Posses A., Relaño M., Smit R., Solimano M., Sternberg A., Tacconi L., Telikova K., Übler H., van der Giessen S. A., Veilleux S., Villanueva V., Baeza-Garay M.

   Lee L. L. contributed to the JWST data reduction and data post-processing.

4. **The ALMA-CRISTAL survey: Extended [C II] emission in an interacting galaxy system at $z \sim 5.5$**. 2025, A&A, 699, A256, doi: 10.1051/0004-6361/202449843

Posses A., Aravena M., González-ópez J., Förster Schreiber N. M., Liu D., **Lee L. L.**, Solimano M., Díaz-Santos T., Assef R. J., Barcos-Muñoz L., Bovino S., Bowler R. A. A., Calistro Rivera G., da Cunha E., Davies R. L., Killi M., de Looze I., Ferrara A., Fisher D. B., Herrera-Camus R., Ikeda R., Lambert T., Li J., Lutz D., Mitsuhashi I., Palla M., Relaño M., Spilker J., Naab T., Tadaki K., Telikova K., Übler H., van der Giessen S., Villanueva V.

Lee L. L. contributed to the kinematic modelling.

5. **The ALMA-CRISTAL survey: Complex kinematics of galaxies at the end of the reionization era**. 2025, A&A, 699, A5, doi: 10.1051/0004-6361/202452990

   Telikova K., González-López J., Aravena M., Posses A., Villanueva V., Baeza-Garay M., Jones G. C., Solimano M., **Lee L. L.**, De Looze I., Förster Schreiber N., Herrera-Camus R., Tadaki K., Assef R. J., Díaz Santos T., Ferrara A., Ikeda R., Lamperti I., Mitsuhashi I., Perna M., Relaño M., Übler H.

   Lee L. L. contributed to the kinematic modelling.

6. **Detailed study of a rare hyperluminous rotating disk in an Einstein ring 10 billion years ago**. 2024, Nature Astronomy, 8, 1181, doi: 10.1038/s41550-024-02296-7

   Liu D., Förster Schreiber N. M., Harrington K. C., **Lee L. L.**, Kamieneski P. S., Davies R. I., Lutz D., Renzini A., Wuyts S., Tacconi L. J., Genzel R., Burkert A., Herrera-Camus R., Alcalde Pampliega B., Vishwas A., Kaasinen M., Wang Q. D., Jiménez-Andrade E. F., Lowenthal J., Foo N., Frye B. L., Shangguan J., Cao Y., Agapito G., Agudo Berbel A., Barfety C., Baruffolo A., Berman D., Black M., Bonaglia M., Briguglio R., Carbonaro L., Chapman L., Chen J., Cikota A., Concas A., Cooper O., Cresci G., Dallilar Y., Deysenroth M., Di Antonio I., Di Cianno A., Di Rico G., Doelman D., Dolci M., Eisenhauer F., Espejo J., Esposito S., Fantinel D., Ferruzzi D., Feuchtgruber H., Gao X., Garcia Diaz C., Gillessen S., Grani P., Hartl M., Henry D., Huber H., Jolly J.-B., Keller C. U., Kenworthy M., Kravchenko K., Lee M. M., Lightfoot J., Lunney D., Macintosh M., Mannucci F., Ott T., Pascale M., Pastras S., Pearson D., Puglisi A., Pulsoni C., Rabien S., Rau C., Riccardi A., Salasnich B., Shimizu T., Snik F., Sturm E., Taylor W., Valentini A., Waring C., Wiezorrek E., Xompero M., Yun M. S.

   Lee L. L. contributed to the gravitational lens modelling.

7. **Evidence for Large-scale, Rapid Gas Inflows in $z \sim 2$ Star-forming Disks**. 2023, ApJ, 957, 48, doi: 10.3847/1538-4357/acef1a

   Genzel R., Jolly J.-B., Liu D., Price S. H., **Lee L. L.**, Förster Schreiber N. M., Tacconi L. J., Herrera-Camus R., Barfety C., Burkert A., Cao Y., Davies R. I., Dekel A., Lee M. M., Lutz D., Naab T., Neri R., Nestor Shachar A., Pastras S., Pulsoni C., Renzini A., Schuster K., Shimizu T. T., Stanley F., Sternberg A., Übler H.

Lee L. L. contributed to testings in support of the quantitative kinemaitcs modelling.

8. **An 600 pc View of the Strongly Lensed, Massive Main-sequence Galaxy J0901: A Baryon-dominated, Thick Turbulent Rotating Disk with a Clumpy Cold Gas Ring at $z = 2.259$**. 2023, ApJ, 942, 98, doi: 10.3847/1538-4357/aca46b

   Liu D., Förster Schreiber N. M., Genzel R., Lutz D., Price S. H., **Lee L. L.**, Baker A. J., Burkert A., Coogan R. T., Davies R. I., Davies R. L., Herrera-Camus R., Kodama T., Lee M. M., Nestor A., Pulsoni C., Renzini A., Sharon C. E., Shimizu T. T., Tacconi L. J., Tadaki K., Übler H.

   Lee L. L. contributed to the gravitational lens modelling.

Contents

致母親、外祖父

In memory of my mother and grandpa

Chapter 1

Introduction

1.1 Galaxy formation and evolution over cosmic time

Galaxies are the fundamental building blocks of the observable Universe, within which stars are organised, and make up $\sim 10\%$ of the cosmic baryon budget (e.g. M. Fukugita & P. J. E. Peebles, 2004; J. M. Shull et al., 2012). Over the past few decades, thanks to immense advancements in cosmological observations, the Λ cold dark matter (CDM) model, with cosmological constant Λ representing dark energy, has been established as the 'standard model' that provides the backbone for studies of galaxy formation and evolution.

The Universe originated in a much hotter, denser, and nearly homogeneous state and has been expanding for the past ≈ 13.8 billion years (H. Mo et al., 2010). Quantum fluctuations generated during the inflationary epoch were stretched to macroscopic scales; they later manifest as the temperature anisotropies observed in the cosmic microwave background (CMB, Fig. 1.1). The CMB is the relic radiation that last scattered at redshift $z \approx 1100$; it is observed today as a nearly perfect blackbody with a temperature $T_{\mathrm{CMB}}(z = 0) \approx 2.73\,\mathrm{K}$. At any z, its temperature scales as $T_{\mathrm{CMB}}(z) = 2.73(1 + z)\,\mathrm{K}$. Measurements of the CMB anisotropies from *Wilkinson Microwave Anisotropy Probe* (WMAP) to *Planck*, have been instrumental in consolidating a concordance cosmology within the ΛCDM model. ΛCDM describes remarkably well the present-day energy components and the form of the primordial fluctuation spectrum inferred from the temperature anisotropies.

Within the ΛCDM framework, the widely accepted picture of hierarchical structure formation attributes the growth of cosmic structures solely to gravity (V. Springel et al., 2006). Dark matter (DM) haloes and galaxies assemble hierarchically through halo mergers,

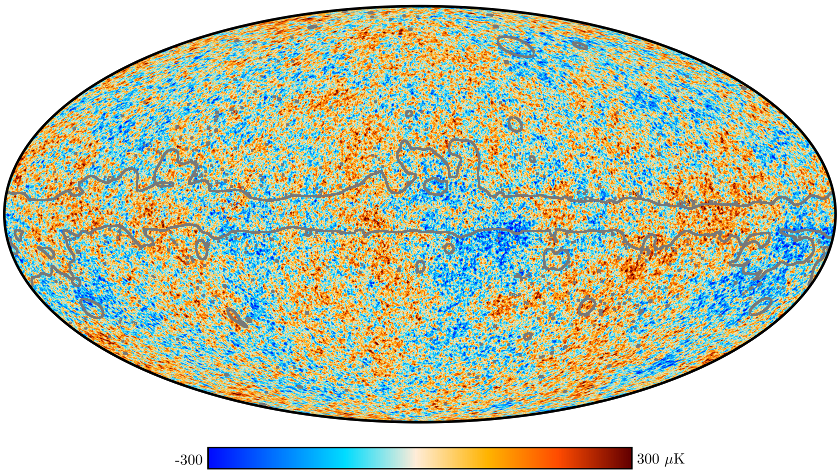

Figure 1.1 Temperature anisotropy map of the CMB observed with *Planck*. The colour scale represents the deviation from the characteristic temperature of the CMB $T_{\mathrm{CMB}} = 2.7255\,\mathrm{K}$, spanning a range of $\pm\,300\,\mu\,\mathrm{K}$. The grey contour outlines the Milky Way disk. [Figure courtesy: Planck Collaboration et al. 2020]

with minor mergers ($M_{\mathrm{satellite}}/M_{\mathrm{halo}} \lesssim 0.3$) occurring more frequently than major mergers — a direct consequence of the steeply decreasing power-law halo mass function (M. Boylan-Kolchin et al., 2008). Fig. 1.2 illustrates a sketch of the cosmic evolution of structure formation since the Big Bang. The figure also highlights the observational capabilities of the state-of-the-art James Webb Space Telescope (JWST), boasting a 6.5 m mirror and near-IR sensitivity that enables it to probe deep into the first few million years after the Big Bang, a significant leap forward in observational capabilities compared to the Hubble Space Telescope (HST).

Concurrently, advances in numerical methods and computing power have enabled high-resolution, gravity-only simulations of structure formation in the CDM model (V. Springel et al., 2005; A. A. Klypin et al., 2011). These simulations start from cosmological initial conditions and evolve the DM density field forward in time. They reproduce many observations from megaparsec scales down to a few kiloparsecs, including the halo mass function and large-scale clustering.

Our understanding of galaxy formation, however, still lags behind our grasp of the large-scale DM distribution. A large majority of bright galaxies in the local Universe are disk-shaped, with a small fraction being ellipsoidal (e.g. P. B. Nair & R. G. Abraham, 2010). Galactic disks form when gas cooling out of the halo largely retains its specific angular momentum (S. M. Fall & G. Efstathiou, 1980; H. J. Mo et al., 1998). The gas dissipates energy, settles in the minimum of the potential well, and gradually builds a rotating disk

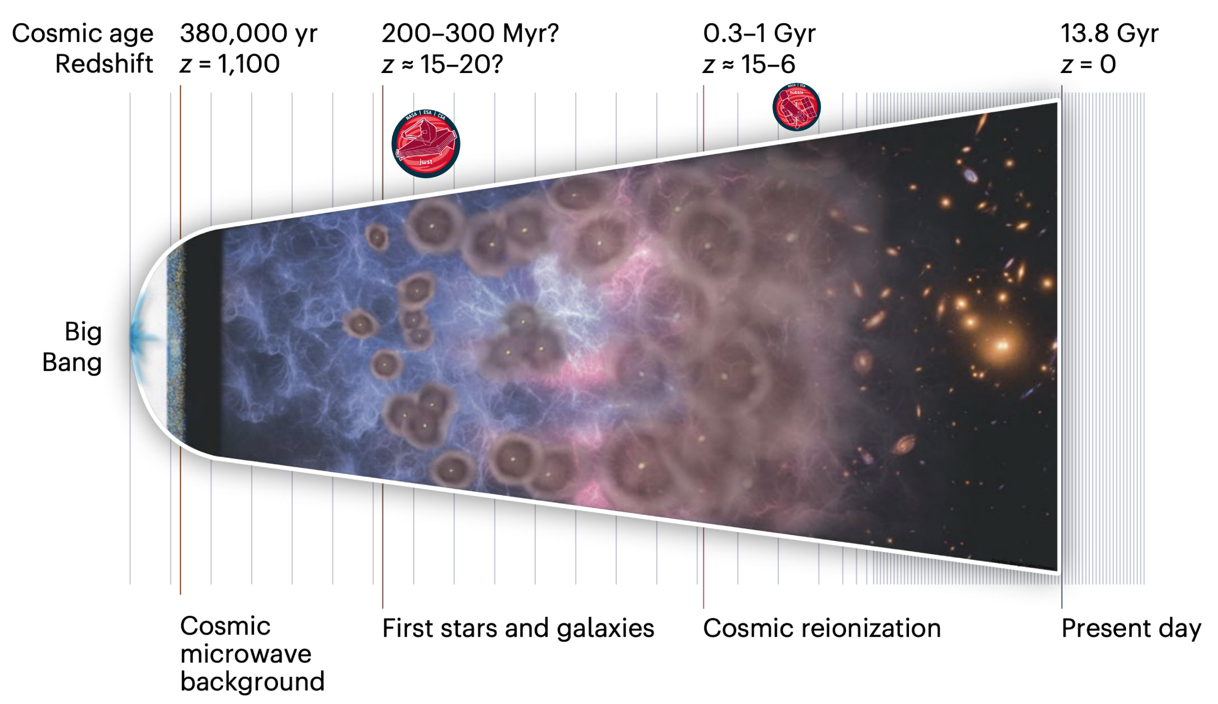

Figure 1.2 Artist illustration of the evolutionary stages of the Universe from the Big Bang to the present. James Webb Space Telescope (JWST) can probe deep into the first billion years of the Universe, thanks to its larger mirror compared to the Hubble Space Telescope (HST) and its spectral coverage of the near-IR regime. Note that the size and cosmic time depicted are not to scale. [Image adapted from A. Adamo et al. 2025.]

that subsequently grows through ongoing gas accretion and mergers.

The subsequent evolution of baryons does not mirror the hierarchical assembly of DM haloes in a straightforward way. It is a highly non-linear problem shaped by radiative cooling, angular-momentum transport, and feedback from both star formation and active galactic nuclei (AGN), tracing accreting massive black holes at the centre of galaxies, among other processes.

A major challenge in modelling galaxy formation is the enormous dynamical range involved—from sub-parsec molecular clouds to the megaparsec-scale cosmic web, spanning six orders of magnitude in length and over nine orders of magnitude in gas density ($n \approx 10^{-6}$–$10^{3}\,\mathrm{cm}^{-3}$).

The sub-parsec scales on which key processes, such as star formation and stellar or AGN feedback, operate remain inaccessible to current cosmological hydrodynamic simulations e.g. Illustris (M. Vogelsberger et al., 2014), IllustrisTNG (V. Springel et al., 2018) and EAGLE (J. Schaye et al., 2015), because of prohibitive computational cost. Consequently, these simulations rely on phenomenological prescriptions that attempt to capture unresolved (sub-grid) physics, in much the same spirit as semi-analytic models (SAMs). SAMs follow the bulk baryonic components of galaxies through a set of simplified flow equations, and achieve orders-of-magnitude savings in computation time (C. M. Baugh, 2006; A. J. Benson, 2010).

Both approaches parametrise unresolved processes and calibrate those parameters against a subset of observations. Encouragingly, state-of-the-art hydrodynamic simulations and modern SAMs now reach broadly consistent qualitative conclusions — for example, regarding stellar mass functions (SMFs), stellar-mass-to-halo mass (SMHM) relations and cosmic star-formation histories.

An intermediate strategy is the ‘zoom-in’ simulation (e.g. F. Marinacci et al., 2014; T. Naab et al., 2014; A. Wetzel et al., 2023): high-resolution ($< 500\,\mathrm{pc}$) re-simulations of individual haloes embedded in a lower-resolution cosmological volume. Zoom-ins can better resolve bars, spiral structure and feedback-driven outflows, making them ideal laboratories for targeted physical studies. However, they sample only a fraction of the full cosmological baryon cycle.

Although these approaches are compelling, they rely heavily on simple parametrisations of the physical mechanisms driving galaxy evolution. This field has evolved to the point where one cannot develop a complete theory from a simple set of assumptions and theories on a pencil and paper, because galactic evolution depends on many complicated, multi-component dynamical and baryonic processes that are poorly constrained from observations. Hence, attempts to understand galaxy formation and evolution inevitably involve multifaceted aspects of astronomical observations across all scales and the electromagnetic (EM) spectrum. They serve as an input to the models, which are instrumental in charting the history of when, where, and ultimately how galaxies formed and evolved. All models have to be continuously tested against observations, which drives our progress in understanding the formation and evolution of the Universe's fundamental building blocks.

In the following sections, I shall summarise the current observational progress and techniques that have been achieved in the past few decades, to see where we stand in our knowledge of the internal properties of galaxies at the kiloparsec level, their star formation history, kinematics, and chemical distributions from an observational perspective.

1.2 Cosmic star formation and the main sequence of star-forming galaxies

Over the past few decades, multi-wavelength surveys of galaxies at $z > 1$ (see Fig. 1.6) have greatly expanded our view of the high-redshift Universe. Observations from both space- and ground-based facilities, including HST, Herschel, Chandra, and XMM-Newton in space, and the Very Large Telescope (VLT), Subaru, the VLA/JVLA, NOEMA, and ALMA on the ground now span the broad EM spectrum from X-ray to radio (see review by N. M. Förster Schreiber & S. Wuyts, 2020). This increasingly complete census of the population has provided rich datasets to trace cosmic star formation history to less than 1 Gyr after the Big Bang. The star formation activity in galaxies culminated around 8–11 billion years ago, at redshifts $z \sim 1$–3 (Fig. 1.3), coincident with the peak of supermassive black hole (SMBH) growth. During this 'cosmic noon' period, as much as half the stars in today's galaxies were formed at 10–20× higher rates from 5–10× larger molecular gas reservoirs compared to the present (e.g. L. J. Tacconi et al., 2020).

Despite this very intense activity, most star-forming galaxies (SFG(s)) are observed to follow well-defined scaling relationships between fundamental global properties already at $z \sim 1-3$. One such relationship is the so-called 'main sequence' (MS) of SFG(s), a near-linear correlation between galaxy stellar mass ($M_\star$) and star formation rate (SFR) (Fig. 1.9), implying that galaxies formed new stars at a rate that is roughly proportional to their existing $M_\star$. Galaxies within ≈ 0.3 dex (in log(SFR)) of the MS account for $\approx 90\%$ of the cosmic star formation activity (G. Rodighiero et al., 2011; K. E. Whitaker et al., 2012; J. S. Speagle et al., 2014). On the other hand, there is a rare population of starburst outliers, comprising only 2% of the mass-selected SFGs at cosmic noon, with SFRs several times above the MS, most likely have elevated star formation activity induced

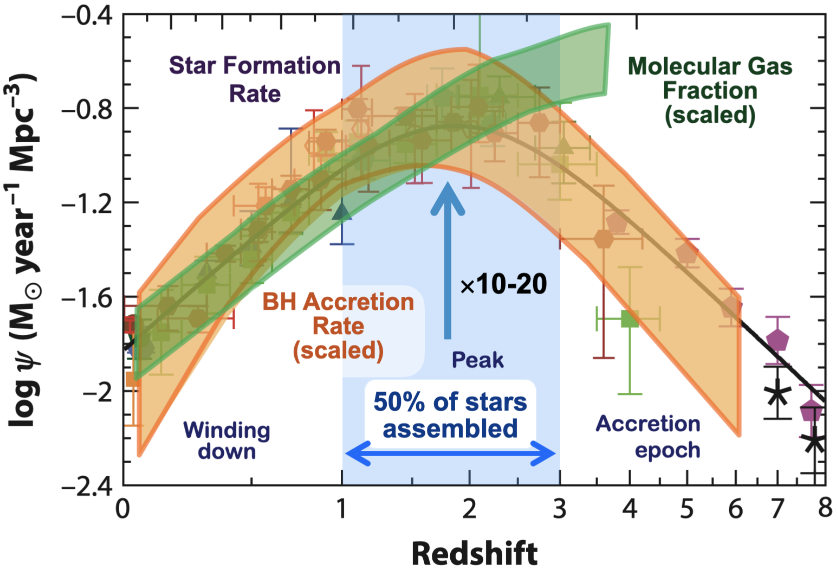

Figure 1.3 Redshift evolution of the cosmic star formation rate (SFR) volume density. The evolution of black hole accretion rate (orange) and molecular gas content (green) are scaled up to match the normalisation of the cosmic SFR density. Both the cosmic SFR and black hole accretion rate densities peaked at $z \approx 2$, an epoch known as the 'cosmic noon'. Note that the gas fraction here refers to the molecular-gas-to-stellar mass ratio. [Adapted from P. Madau & M. Dickinson 2014 and L. J. Tacconi et al. 2020 by Sedona Price]

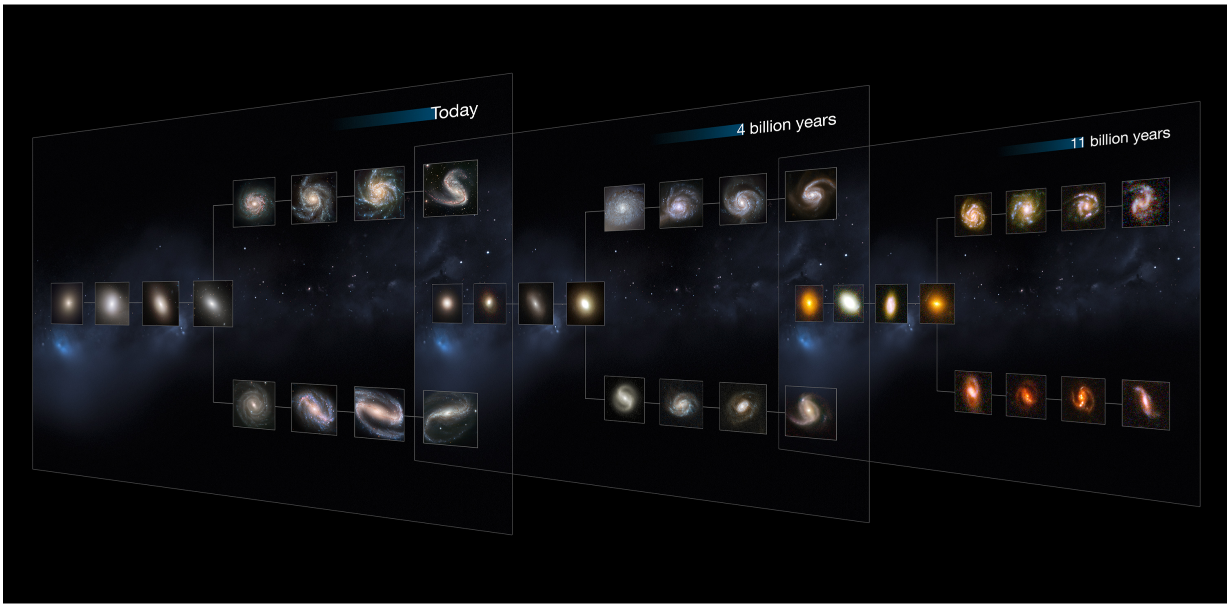

Figure 1.4 Hubble sequence of galaxies in the local Universe (*left*), 4 Gyr ($z \sim 0.5$, *middle*) and 11 Gyr ($z \sim 2.5$, *right*) ago. The Hubble sequence categorises and separates galaxies according to their morphology, from left to right: elliptical galaxies, lenticular galaxies in the middle, and spiral galaxies branching out on the right. The spiral galaxies on the lower branch are distinguished by their prominent bars that traverse the centre. [Image courtesy: NASA, ESA, and M. Kornmesser (ESO), based on B. Lee et al. 2013]

by galaxy interactions and collisions. The Hubble sequence (E. P. Hubble, 1926, Fig. 1.4) — a morphological classification that arranges galaxies from ellipticals and lenticulars to spirals and irregulars — was already in place 11 Gyr ago (R. Delgado-Serrano et al., 2010; S. Wuyts et al., 2011; B. Lee et al., 2013). Although not explicitly captured by the Hubble sequence, disk galaxies at higher redshifts are also observed to be geometrically thicker and morphologically clumpier, as we discuss further in Sect. 1.3.3. The existence of these scaling relations and the prevalence of disk structures that will be discussed in Sect. 1.3, imply that galaxy assembly and evolution are more orderly than chaotic, with internal secular processes playing a crucial role alongside external accretion and stochastic mergers in regulating galaxy life cycles.

But what drives the intense star formation at cosmic noon? From studies of the local galaxies, star formation is known to correlate strongly with cold ($T \approx 10$–$30\,\mathrm{K}$) molecular gas with densities $n(\mathrm{H_2}) \approx 10^2$–$10^5\,\mathrm{cm^{-3}}$, and only weakly with neutral atomic hydrogen H I (R. C. Kennicutt, 1989; F. Bigiel et al., 2011; A. Schruba et al., 2011). In other words, molecular gas is the fuel of star formation. In the local Universe, typical molecular depletion times $\tau_{\mathrm{depl.}}$ are $\sim$ 2–4 Gyr (e.g. F. Bigiel et al., 2011; R. C. Kennicutt & N. J. Evans, 2012; R. Genzel et al., 2015), whereas at $z \sim 2$ they drop to $< 1\,\mathrm{Gyr}$ (L. J. Tacconi et al., 2020). However, overall the depletion time only has a shallow dependence on redshifts with $\tau_{\mathrm{depl.}} \propto (1+z)^{-0.6}$ (compared to, for instance, the steep evolution of specific SFR, $\mathrm{sSFR} \propto (1+z)^3$ to $z \sim 2$), so the efficiency of burning the fuel has been almost unchanged, and similar physical processes may be operating in both local and cosmic noon galaxies.

On the other hand, because SFG(s) remain on the MS for more extended periods, sustained gas accretion is required to replenish the molecular gas reservoirs. Indeed, observations across redshifts reveal the cosmic rise in the SFR density is closely accompanied by increasing galactic molecular-gas-to-stellar mass ratio, as shown in Fig. 1.3. It reaches $\approx 50\%$ (in comparison, our MW has $f_{\mathrm{molgas}} \approx 10\%$) at $z \approx 2$. The trend implies that an increase in the gas fraction is likely responsible for the sustained high sSFRs at high redshift, which in turn implies that it is the higher baryonic accretion rates at early epochs that regulate the growth of galaxies, rather than large changes in the small-scale star-formation efficiency (R. Genzel et al., 2015; N. Scoville et al., 2016; D. Liu et al., 2019).

The molecular component referred to here is predominantly H_2.[1] However, it is observationally challenging to directly observe H_2, because it lacks a permanent dipole moment.[2] Consequently, an alternative tracer of the molecular gas is needed. Carbon monoxide (^{12}CO, hereafter CO), which has a small dipole moment and is relatively abundant ($\mathrm{CO}/\mathrm{H_2}$, $\approx 10^{-4}$ at near-solar metallicity), its rotational lines therefore serve as the primary tracer of cold molecular gas. Converting CO luminosities to H_2 masses is reasonably robust when an appropriate CO-to-H_2 conversion factor, α_{CO}, is adopted (R. Genzel et al., 2015; L. J. Tacconi et al., 2018) such that $M(\mathrm{H_2}) = \alpha_{\mathrm{CO}} \times L'_{\mathrm{CO(1-0)}}$ for $J = 1 \rightarrow 0$ transition, where α_{CO} depends on gas density, temperature and metallicity (A. K. Leroy et al., 2011; R. Genzel et al., 2012; A. D. Bolatto et al., 2013). For near-solar-metallicity MS disks at $z \sim 2$ a Milky Way (MW)–like value, $\alpha_{\mathrm{CO}} \approx 4.36\,[M_\odot(\mathrm{K}\cdot\mathrm{km}\cdot\mathrm{s}^{-1}\cdot\mathrm{pc}^2)]^{-1}$, which corresponds to typical conditions for giant molecular gas in our MW.

Nonetheless, CO line intensities can suffer from radiative-trapping effects and are observationally expensive: integrations often require many hours per source for integrated studies, and total gas masses depend on the α_{CO} values, which are increasingly uncertain at higher redshifts. A faster alternative, typically minutes per source, is to measure the Rayleigh–Jeans (R-J, $h\nu \ll kT$) dust continuum at $\gtrsim 300\,\mu\mathrm{m}$, which is almost always optically thin. The dust in question refers to solid particles with sizes ranging from nm to μm, primarily composed of heavy elements (e.g. O, C, Mg, Si and Fe), available in the

---

[1] Helium contributes to 36% of the mass fraction.

[2] Its lowest permitted transitions are the very weak quadrupole (E2) lines, with transition rate more than ten orders of magnitude slower than dipole (E1) transitions at the same wavelength.

interstellar medium (ISM, D. C. B. Whittet, 1992). These dust particles are well-mixed with the gas in the ISM. The initial 'seeds' of dust were formed in asymptotic giant branch (AGB) winds and supernova ejecta, but the majority of the dust mass observed today has been built up through subsequent accretion and coagulation processes (B. T. Draine, 2003). Despite accounting for only a small fraction ($\lesssim 1\%$) of the ISM mass, dust grains strongly shape observed spectra: they scatter and absorb most efficiently the stellar UV and optical photons (because most dust grains are of the size $\gtrsim 100\,\mathrm{nm}$) from massive stars and then re-radiate the absorbed energy (near-)thermally at far-IR/sub-millimetre (sub-mm) wavelengths, carrying $\sim 30\%$ of the bolometric luminosity of normal disk galaxies. Because the R-J dust emission scales linearly with total dust mass, it provides a useful indirect probe of the total molecular gas reservoir (N. Scoville et al., 2016, 2017; L. J. Tacconi et al., 2020), with an assumed dust-to-gas mass ratio. This is a technique we adopt in Chap. 3 (Eq. 3.8) to estimate the molecular gas mass of galaxies at $z > 4$.

All of the above illustrate our current understanding of typical SFG(s) at the cosmic noon epoch, but what about earlier cosmic times, particularly at $4 < z < 6$? This is not an arbitrary cosmic epoch to pose such a question. This epoch, occurring when the Universe was just 1 billion years old and lasting about six million years, precedes the peak of cosmic SFR at cosmic noon. It corresponds to the accretion epoch (accretion-dominated growth phase) shown in Fig. 1.3, which follows the end of the epoch of reionisation (EoR, Fig. 1.2). The EoR marks the last major phase transition in cosmic history, during which the IGM, comprising the bulk of cosmic baryons, change from neutral to almost fully ionised at $z \simeq 5.5$ (Fig. 1.5). Thus, one expects galaxy properties to change fundamentally as they emerge from reionisation. It is an epoch that was poorly explored prior to the advent of JWST, ALMA, and NOEMA, and was once thought to be characterised by much more chaotic galaxy assembly. However, as will be discussed throughout this thesis, our understanding of this period is now rapidly evolving thanks to the unprecedented capabilities of these facilities. The work presented in this thesis makes an important contribution to this emerging picture, shedding new light on the properties and evolution of galaxies during this era.

1.2.1 Gas regulator model

The picture outlined above can be understood in a simple framework based on mass balance in the ISM (alternatively called an equilibrium, bathtub or gas regulator model A. Dekel et al., 2009b; N. Bouché et al., 2010; S. J. Lilly et al., 2013):

$$\dot{M}_{\mathrm{inflow}} = \dot{M}_{\star} + \dot{M}_{\mathrm{outflow}} + \dot{M}_{\mathrm{gas}}, \tag{1.1}$$

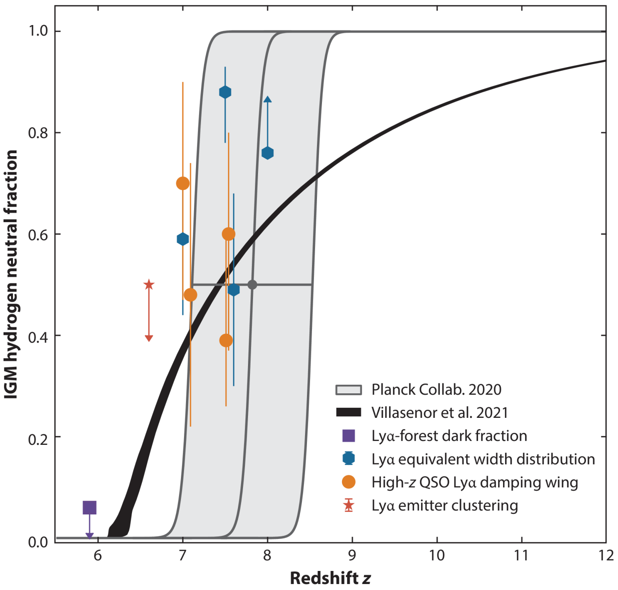

Figure 1.5 Neutral hydrogen fraction in the intergalactic medium (IGM) as a function of redshift. Results from low to high redshifts are traced by the dark fraction of the Lyα forests at $z < 6$, upper limits from the clustering of Lyα emitters at $z = 6.6$, and the equivalent width distribution of Lyα emitters at $z \sim 7$–8. Also shown is the modelled evolution of the neutral hydrogen fraction inferred from the Thomson scattering optical depth derived from Planck CMB polarisation (grey). In black is the predicted evolution of the neutral fraction from cosmological simulations constrained by the evolution of the Lyα forest transmitted flux power spectrum at $z < 6$. [Image courtesy: B. E. Robertson 2022 and references therein]

equating the baryonic mass accretion or inflow rate to SFR ($\dot{M}_\star$), mass outflow rate ($\dot{M}_{\rm outflow}$), and rate of change of the mass in the gas reservoir ($\dot{M}_{\rm gas}$). In a steady state, $\dot{M}_{\rm gas} = 0$, which is usually true when considering a time average over a Gyr. It is in essence a mass continuity rate equation. Inflow into halos is driven primarily by gravitational accretion from the intergalactic medium (IGM) and hence the cosmic growth of the halo determines the maximum rate of $\dot{M}_{\rm inflow}$. The rate at which DM halo grow, $\dot{M}_{\rm halo}$, is well characterised in ΛCDM and roughly given by $\dot{M}_{\rm halo} \propto M_{\rm halo}(1+z)^{2.25}$ (Eq. 1 in A. Dekel et al., 2009b).

We can rewrite Eq. (1.1) in terms of the specific star formation rate, sSFR, i.e. the slope of the MS (sSFR $= \dot{M}_\star/M_\star = {\rm SFR}/M_\star$):

$$\mathrm{sSFR} = \frac{\zeta(1+z)^{2.25}}{M_\star/M_{\rm DM} \times (1+\eta)}, \tag{1.2}$$

where ζ is the factor that describes the 'preventive-feedback' that prevents gas from reaching the ISM in galaxies. It is controlled by the cooling time in the hot virialised baryonic halo gas. For halos more massive than a threshold of $10^{12}\,M_\odot$, the infalling gas is shocked to the virial temperature $T_{\rm vir} \approx 10^6\,{\rm K}$ (M. J. Rees & J. P. Ostriker, 1977), a characteristic thermal temperature such that the gas's internal energy equals $-1/2$ of the total gravitational potential energy. Since the cooling (via Bremsstrahlung) is much longer than the Hubble time ($\approx 10^{10}$ yrs, and see Fig. 17 in M. Donahue & G. M. Voit, 2022), the accretion is extremely inefficient in such a hot halo, and $\zeta \ll 1$. The outflow mass loading factor, $\eta \equiv \dot{M}_{\rm outflow}/\dot{M}_\star$, has a power-law dependence on stellar mass and the circular rotation velocity V_{circ} (e.g. B. D. Oppenheimer & R. Davé, 2008). The dependence of sSFR on $M_\star$ and z therefore reflects the evolving interplay of gas accretion, star-formation and feedback across cosmic time.

To understand the inner workings of galaxies in the above framework and whether such a framework is valid at even higher redshifts, we must move beyond demographic averages and map the full baryon cycle, which calls for detailed, spatially resolved studies of individual systems across cosmic epochs to understand how galaxies assembled their mass and evolved into the present-day population as a function of lookback time (see Fig. 1.7 for an example at $z \approx 2$). In particular, hydrogen recombination lines and atomic forbidden emission lines from warm ionised gas, excited by star formation, AGN, and shocks, serve as powerful tracers of galaxy dynamics and as diagnostics of the physical conditions of the interstellar gas.

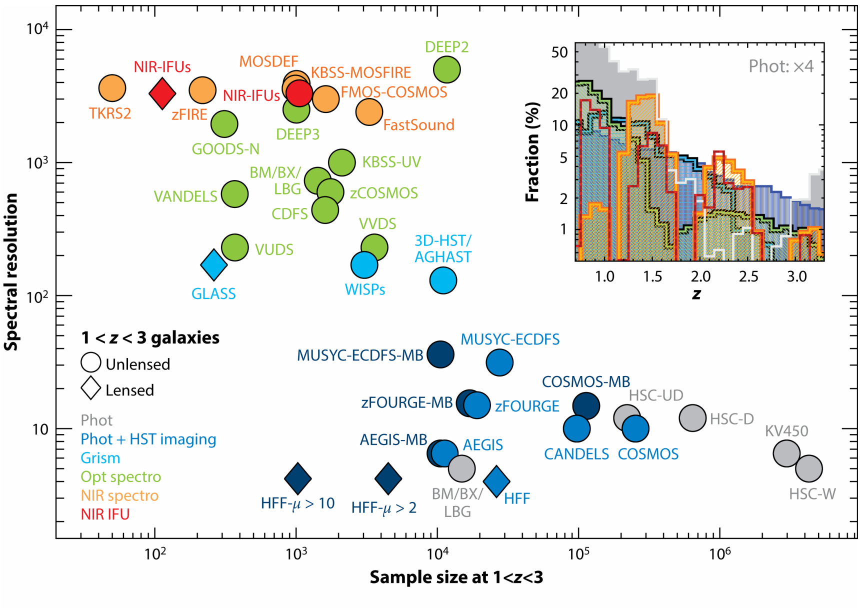

Figure 1.6 Recent observational landscape as of 2020 in terms of spectral resolution versus the number of galaxies at $z \sim 1$–3 collected in optical and near-IR surveys in the past two decades. The colour represents the type of the survey, from photometric imaging, spectroscopic to IFU. The symbols denote whether the samples are lensed. The insets show the combined redshift distributions (fraction in log), colour-coded by survey type, normalised by the total number of $z \sim 1$–3 galaxies. [Image courtesy: N. M. Förster Schreiber & S. Wuyts 2020]

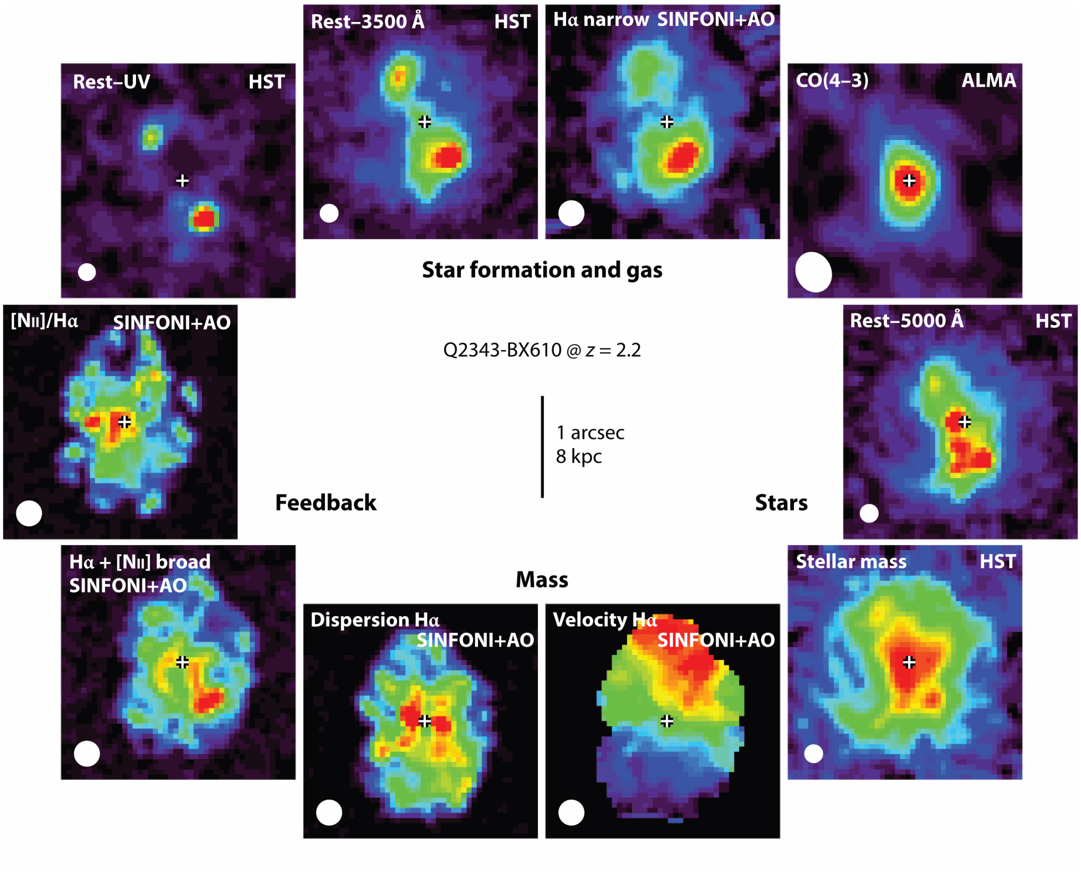

Figure 1.7 Multi-wavelength view of observed properties tracing physics probing the baryon cycle in a $z \approx 2$ galaxy, combining imaging and integral-field spectroscopy to trace stellar mass, star-formation activity, gas kinematics, and ISM conditions. [Image courtesy: N. M. Förster Schreiber & S. Wuyts 2020]

1.3 Kinematics of disk galaxies

Ever since V. M. Slipher (1914) first discovered rotational motions in the Sombrero Galaxy, galactic dynamics has been a principal tool for studying the structure and mass assembly of extragalactic systems. As will be discussed in the following, kinematics trace the full gravitational potential, not just the luminous parts consisting of stars and gas, but also the elusive dark-matter component, which in fact, dominates the overall mass budget. Kinematics also reveal a galaxy's dynamical state: ordered, rotation-dominated velocity fields are the hallmark of settled disks, whereas disturbed or irregular motions are induced by recent interactions and non-circular motions, such as outflows. Quantifying the balance between ordered rotation and random motions (dispersion) thus links directly to a galaxy's geometric structure. Hence, galactic dynamics provides a uniquely powerful record of mass assembly across cosmic time and reveals the dominant physical processes that have governed the growth of galaxies, e.g. smooth accretion versus mergers.

The enclosed dynamical mass can be inferred from the observed circular velocity, $V_{\rm circ}$, traced by for example the stars, related through the Poisson equation:

$$\frac{G\,M_{\rm enc}(R)}{R} = R\,\frac{{\rm d}\Phi(R)}{{\rm d}R} \;\equiv\; V_{\rm circ}^2, \tag{1.3}$$

where G is the gravitational constant, Φ is the gravitational potential and R is the galactocentric radius,

For galactic disks with surface brightness profiles well described by an exponential form $I(R) = I_0 \exp(-R/R_{\rm d})$, and similarly for the surface mass density $\Sigma(R) = \Sigma_0 \exp(-R/R_{\rm d})$, where R_d is the disk scale length and is related to the half-light radius $R_{\rm e} \approx 1.67 R_{\rm d}$. For our MW, $R_d = 2$–$3\,{\rm kpc}$. It is worth noting that the exponential form is a special case of the more general Sérsic profile (J. L. Sérsic, 1968), which describes the projected surface brightness distribution of galaxies. The Sérsic profile is given by the equation

$$I_n(R) \;=\; I(0)\,\exp\Big(-k\,R^{1/n}\Big) \;=\; I_e\,\exp\Big\{-\,b_n\Big[(R/R_e)^{1/n} - 1\Big]\Big\}, \tag{1.4}$$

where n is the Sérsic index. For $n = 1$, the profile reduces to the exponential form of disk galaxies. The value of b_n can be evaluated numerically using the relation $b_n = 2n - 0.324$ (L. Ciotti & G. Bertin, 1999). When $n = 4$, the profile becomes the de Vaucouleurs profile (G. de Vaucouleurs, 1948), which is commonly used to describe the galactic bulge and early-type, more spheroidal galaxies (see the left-hand side of the Hubble sequence in Fig. 1.4).

The potential of an axisymmetric disk of an exponential surface-density profile can be expressed as (P. Cuddeford, 1993; J. Binney & S. Tremaine, 2008):

$$\Phi(R,0) = -4G\Sigma_0 \int_0^R \frac{aK_1(a/R_\mathrm{d})}{\sqrt{R^2-a^2}} = -\pi G\Sigma_0 R[I_0(y)K_1(y) - I_1(y)K_0(y)], \tag{1.5}$$

where $y \equiv R/2R_d$, I_n and K_n are the (first- and second-kind) modified Bessel functions of the n-th order. Differentiating Eq. 1.5 with respect to R, we obtain the circular velocity of an infinitely thin exponential disk, i.e., the Freeman disk (K. C. Freeman, 1970):

$$V_\mathrm{circ}^2(R) \;=\; R\frac{d\Phi(R)}{dR} \;=\; 4\pi G\Sigma_0 R_\mathrm{d}\, y^2\,[\,I_0(y)K_0(y) \;-\; I_1(y)K_1(y)]\,, \tag{1.6}$$

with the enclosed mass within R:

$$M_\mathrm{enc}(R) = M_\mathrm{d}(R) \;=\; 2\pi\int_0^R \mathrm{d}R'\; R'\,\Sigma_0\, e^{-R'/R_\mathrm{d}} \;=\; 2\pi\Sigma_0 R_\mathrm{d}^2\left[1 - e^{-R/R_\mathrm{d}}\left(1+\frac{R}{R_\mathrm{d}}\right)\right]. \tag{1.7}$$

The Freeman disk is an approximation of a real galactic disk, because galaxy disks are not infinitesimally thin. In the direction perpendicular to the disk plane (along the z-axis), the three-dimensional density of the stars follows,

$$\rho(R,z) \;=\; \rho(R,0)\exp[-|h_z|/h_z(R)].^3 \tag{1.8}$$

For the thin disk of MW, $h_z/R_\mathrm{d} \approx 0.1$. Nearby SFG(s) often have thin disks, especially in the cold gas components (P. C. van der Kruit & K. C. Freeman, 2011).

Equations 1.6 and 1.7 are appropriate for describing the rotation curve (RC) and the enclosed mass of spiral galaxies, in the absence of a bulge or DM, with a V_circ that peaks at $\sim 2.2R_\mathrm{d}$, and then declines. Such a decline, however, was not observed in the data for NGC 300 and M33 in the same work by K. C. Freeman (1970). Although not fully recognised in the same work, this gave an early hint of the presence of some invisible matter, which we later discovered to be dark matter (DM). If DM is present and dominates over baryons at the outer disk, the RC would be flattened, deviating from the expected shape of the Freeman disk model.

In fact, the flattening of RCs is one of the early observational evidence that led to the discovery of DM,[4] an additional invisible and extended mass component required to maintain large rotational velocities well beyond the optical radius of disks seen in light.

---

[3] sech profile is a viable alternative.

[4] Together with the earlier, although not recognised at the time, the dynamical evidence from the Coma cluster by F. Zwicky (1933).

H. W. Babcock (1939) produced one of the first RCs of the Andromeda galaxy, and noted that the unexpectedly high outer-disk velocities (illustrated in Fig. 1.8) implied a rapidly increasing mass-to-light (M/L) ratio, hinting, though not yet conclusively, at the presence of substantial unseen matter. Later works, such as those by V. C. Rubin & W. K. Ford (1970) and M. S. Roberts & R. N. Whitehurst (1975), brought decisive evidence for the flat RCs of spiral galaxies. The latter study, in particular, observed the 21 cm emission of atomic hydrogen (H I) arising from its hyperfine transition, which traced a very large extent of the galaxy. This observation confirmed that the rotation of the Andromeda galaxy remains flat out to a radius of $\sim 30\,\mathrm{kpc}$ (Fig. 1.8). Flat rotation is now known to be a common feature among local spiral galaxies (Y. Sofue & V. Rubin, 2001).

In high-resolution N-body simulations of structure formation under the ΛCDM framework, the density profile of the simulated DM halo follows the form

$$\rho(R) = \frac{\rho_0}{(R/R_s)(1+R/R_s)^2}, \tag{1.9}$$

which is known as the Navarro-Frenk-White (NFW) profile (J. F. Navarro et al., 1996). Here, ρ_0 is the normalisation parameter, R_s is the scale radius, related to the halo radius, R_{vir}. The R_{vir} is the radius within which the mean mass density is approximately 200 times the critical density of the Universe, and c is the concentration parameter such that $R_s \equiv R_{\mathrm{vir}}/c$. The logarithmic slope of the NFW profile changes from -1 near the centre to -3 at large radii. The enclosed mass of the NFW profile is given by

$$M_{\mathrm{enc}}(R) = 4\pi\rho_0 R_s^3 \left\{ \log[1 + c(R/R_{\mathrm{h}})] - \frac{c(R/R_{\mathrm{h}})}{1 + c(R/R_{\mathrm{h}})} \right\}. \tag{1.10}$$

Although the NFW profile provides a reasonably successful description of observed dark matter profiles in galaxies on average, numerous studies have highlighted deviations from this simple functional form, particularly in the inner regions of galaxies. For instance, adiabatic contraction caused by the central condensation of cooled gas can result in cuspier inner profiles (e.g. A. Burkert et al., 2010), whereas dynamical friction can lead to flatter, cored DM profiles, as observed in local dwarf galaxies (G. Gilmore et al., 2007), massive galaxy clusters (S. F. Newman et al., 2013), and massive SFGs at cosmic noon (R. Genzel et al., 2020; S. H. Price et al., 2021, see discussion in Sect. 1.3.3). Alternative density profiles, such as the double-power-law two-power halo (2PH) model (J. Binney & S. Tremaine, 2008), also known as the Hernquist-Zhao profile (L. Hernquist, 1990; H. Zhao, 1996) are used at times to model the DM halo,

$$\rho(R) = \frac{\rho_0}{(R/R_s)^\alpha[1 + (R/R_s)^\gamma]^{(\beta-\alpha)/\gamma}}, \tag{1.11}$$

where α and β control the inner and outer slopes, respectively, with the extra γ that controls the breadth of the transition region. Note that NFW is a special case of Eq. 1.11 with $\alpha, \beta, \gamma = (1, 3, 1)$ and similarly for the generalised NFW (J. S. B. Wyithe et al., 2001) but with α being free.

At the core of dynamical studies lies the decomposition of the circular velocity profile, $V_{\rm circ}(R)$, into its constituent components, namely baryons (comprising gas and stars) and the DM halo. This decomposition enables the quantification of the relative contribution of dark matter and its distribution within the galaxy.

For an axisymmetric mass distribution, the circular velocity can be expressed as the quadrature sum of the individual components contributing to the full gravitational potential:

$$V^2_{\rm circ}(R) = V^2_{\rm baryons}(R) + V^2_{\rm DM}(R). \tag{1.12}$$

The baryonic component can be further decomposed into distinct sub-components, including the bulge and disk, as well as contributions from stars and gas in various phases (atomic, molecular, and ionised). Figure 1.8 presents an example of such a decomposition of circular velocity profile for a disk galaxy at $z = 1.4$. The simplified axisymmetric model is commonly used in kinematics studies at cosmic noon and beyond (e.g. A. Nestor Shachar et al., 2023; E. Parlanti et al., 2023), and will also be the framework of kinematics analysis in Chap. 3. However, observations of local disks often reveal deviations from this assumption, primarily due to interactions, warps, and other instabilities that introduce non-circular motions. These higher-order kinematics are challenging to constrain directly in most high-redshift data, owing to limitations in resolution and S/N, as will be discussed further in Sect. 1.3.3.

1.3.1 Tracing kinematics with gas

Observers rely on emission or absorption lines to study the kinematics of objects. The centroid velocity of these lines across a system provides information on the relative bulk motions, whereas the local line widths offer a measure of random motions, as well as any unresolved velocity gradients.

The framework outlined in the previous section is well-suited for kinematic studies that use stars as collisionless tracers with optical absorption lines e.g. Ca II and Mg b. However, these stellar absorption features are generally weak, and consequently challenging

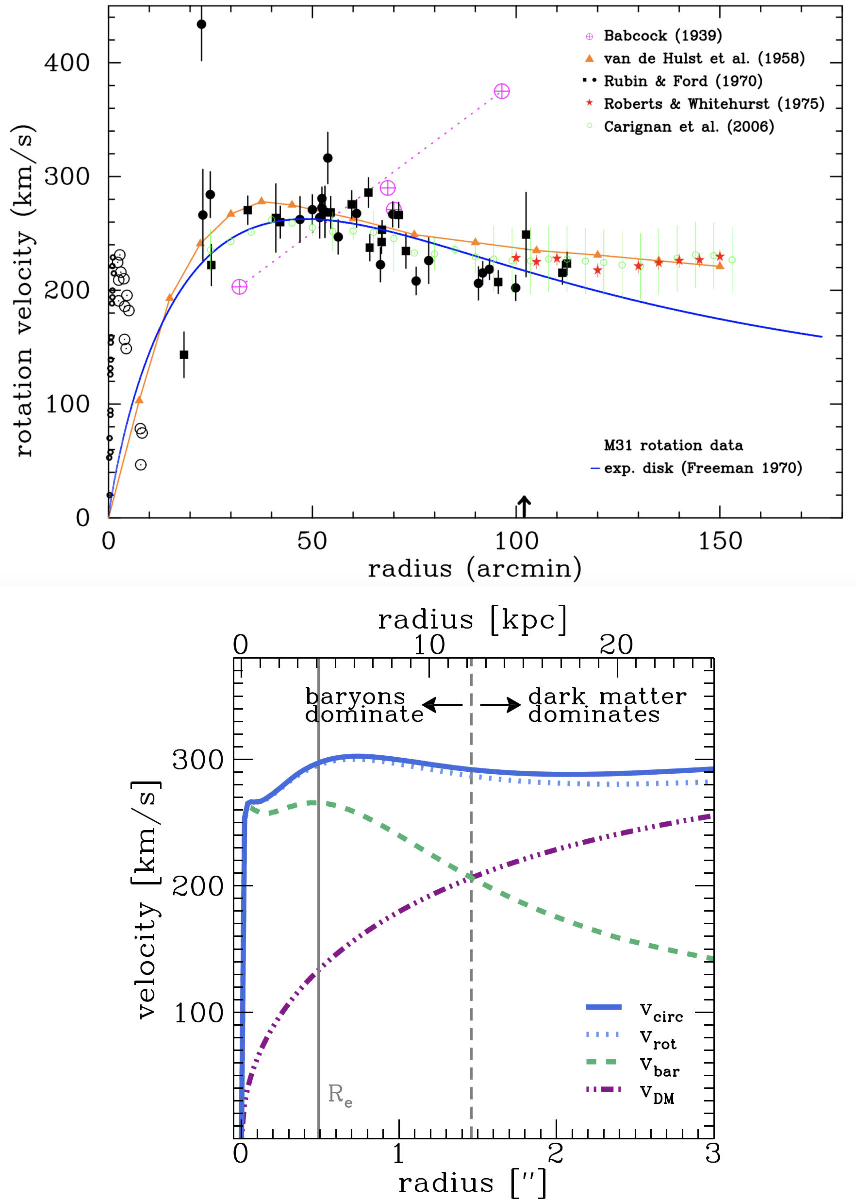

Figure 1.8 *Top:* RC of the Andromeda galaxy (M31). Individual data points are colour-symbol coded by source. Magenta circles: H. W. Babcock (1939); orange triangles: H. C. van de Hulst et al. (1957) black points: V. C. Rubin & W. K. Ford (1970); red stars: M. S. Roberts & R. N. Whitehurst (1975); green diamonds: C. Carignan et al. (2006). *Bottom:* Example of RC decomposition of a disk galaxy at $z = 1.4$ observed with Hα and CO. In solid blue is the intrinsic circular velocity $V_{\rm circ}$ of the galaxy, which here is further decomposed into the contributions from the baryons (gas and stars) component (dashed green) and dark matter (dot-dashed purple). Because of the collisional nature of gas, the pressure term would cause the observed RC ($V_{\rm rot}$ in dotted blue) to deviate from that of the intrinsic $V_{\rm circ}$ (Eq. 1.13). [Figure credits: A. Bosma 2023 (*top*) and H. Übler et al. 2018 (*bottom*)]

to measure accurately in spectra of faint distant galaxies at high redshift. It is further exacerbated at $z > 2$, where the rest–frame optical absorption features shift beyond $2.4\,\mu$m, well into the thermal IR, and the continuum surface brightness is low, so stellar velocity fields are largely inaccessible with ground-based facilities (see e.g. J. van Houdt et al., 2021; H. Übler et al., 2024a, for $z \sim 1$).

As a result, kinematic studies at high redshift have primarily relied on gas as a tracer, using its emission lines. The kinematics of warm, ionised gas ($T \sim 10^4\,$K) are routinely probed by bright nebular lines such as Hα, Hβ, [O III] λ5007 Å and [O II] λ3727 Å; these lines have been the workhorses for studying gas motions in cosmic noon galaxies. The CO rotational lines discussed in Sect. 1.2 trace the bulk of the ISM in the molecular phase and are observable at millimetre–centimetre wavelengths. They provide a valuable window into the kinematics of cold gas, although the integration times required for spatially resolved observations are typically longer. As will be discussed in more detail in Sect. 1.3.5, bright far-IR fine-structure lines from the cold, multiphase ISM shift into the sub-mm band for galaxies at $z \gtrsim 3$, and have become increasingly popular kinematic tracers of galaxies at $z \gtrsim 4$. Finally, H I traces the atomic gas reservoir, which often extends well beyond the optical radius of a galaxy, via its 21 cm hyperfine transition. Because this line is intrinsically faint, it is currently impractical to use it for studies far beyond the local Universe with existing instrumentation.

There are some complications associated with using gas as a kinematic tracer. Unlike stars, which can be treated as a collisionless fluid, with circular velocity in the form of Eq. 1.3, gas is a collisional fluid, which implies that kinetic energy can be exchanged through collisions. The ISM is multiphase, turbulent and continuously stirred by feedback and inflow, so it is rarely in strict local thermodynamic equilibrium (LTE). However, on small scales the velocity distribution of each phase can often be approximated as Maxwellian. As the microscopic velocity distribution is close to Maxwellian, we can lump all unresolved random motions into a single pressure term, $p = \rho\sigma^2$. As a result, for gas, Eq. 1.3 can be expressed as

$$V_\phi^2 = r\frac{d\Phi(r)}{dr} + \left(\frac{r}{\rho}\right)\frac{dp}{dr} = V_{\rm circ}^2 + \frac{r}{\rho}\frac{d(\rho\sigma_{\rm gas}^2)}{dr}, \tag{1.13}$$

where V_ϕ is the tangential velocity, and the equation holds true for any radial dependence of $\sigma_{\rm gas}$ and ρ. Hence, the pressure gradient ($dp/dr < 0$) would lower the observed rotation speed compared with the collisionless $V_{\rm circ}$. In regions with high velocity dispersion, just like the stellar velocity field, V_ϕ can deviate substantially from the $V_{\rm circ}$, which traces the true potential. Figure 1.8 shows an example of an application of Eq. 1.13 on an RC observed with Hα and CO.

1.3.2 Observational results of high redshift kinematics

Our access to a vast array of data has allowed us to study the Universe across an increasingly large portion of its history. The advent of 8–10 m class telescopes, advanced techniques such as adaptive optics (AO, R. Davies & M. Kasper, 2012), and millimetre to radio interferometry, and space-based observatories such as HST and JWST, to name a few, have collectively unlocked views of galaxies on scales as small as just 1 kpc in the rest-frame optical to near-IR part of the EM spectrum.

The field has particularly benefitted from the development of integral field units (IFUs) in the near-IR capable of sub-arcsecond angular resolution (typical size of a galaxy at $z \sim 2$ is $\sim 1''$), which represents a major leap forward compared to traditional long-slit spectroscopy. Notable IFU instruments include the SINFONI and ERIS instruments mounted on the Very Large Telescope (VLT), OSIRIS on Keck I, and the NIRSpec IFU module onboard the JWST, with typical spectral resolution of few tens of km s^{-1}, enabling access to lines from warm ionised gas phase, such as Hα, [O III] λ5007 Å, and [O II] λ3727 Å at $z \gtrsim 1$.

IFUs acquire simultaneously a spectrum at each spatial position across a two-dimensional field of view. When a galaxy is mapped in a specific spectral line, the images at different wavelengths provide relative velocity information from the Doppler shift of the spectral line in wavelength. The width of a spectral line at each spatial location can provide a measure of local random motions. Such observations produce a three-dimensional (3D) data cube (x, y, λ), which can be used to quantify the internal kinematics of the gas in the galaxy. From the cube, we can extract 1D, 2D, and full 3D information. The 1D radial profile directly gives the observed RC and the velocity-dispersion profile. In practice, the most robust approach is to fit the line-of-sight velocities and the line widths (dispersions) simultaneously.

In the analysis, observational effects such as projection and beam smearing, should be accounted for in order to recover the intrinsic RC. Various methods exist to extract RCs for high-redshift observations, and I will return to this in Sect. 1.3.4 and further address it in Chap. 2. Moreover, if a disk is not infinitely thin, some of the dynamical support that would otherwise come from rotation is supplied by random motions instead, with the consequence that the rotational velocity ($V_{\rm rot}$) is lower compared to the case of purely rotationally supported razor-thin disks. Sect. 1.3.3 will discuss this in more detail.

Another major observational breakthrough was the advent of interferometric arrays such as NOEMA and ALMA, which, through the basic principle of interferometry and image reconstruction via Fourier Transform techniques, map the line emission of distant sources at millimetre wavelengths, and essentially give the same 3D information as in IFU. Millimetre

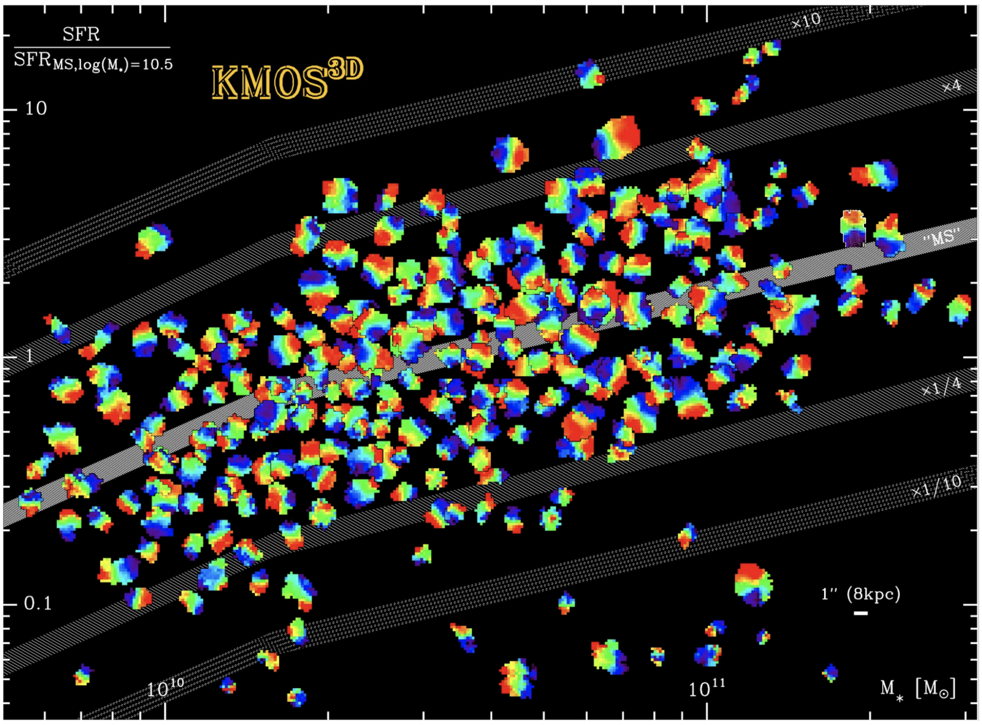

Figure 1.9 Hα velocity fields of galaxies in the KMOS^{3D} survey (E. Wisnioski et al., 2015) placed on main sequence at $z = 1$–2. The majority of galaxies exhibit a spider-like pattern from red to blue, indicating a prevalence of regular disk-like rotation in the sample. [Image modified from E. Wisnioski et al. 2015]

interferometry provides access to emission from the dominant cold gas in the ISM. Modern heterodyne receivers can easily achieve velocity resolutions of $\sim 0.1\,\mathrm{km\,s^{-1}}$, although in practice, particularly for high-redshift observations, spectral binning and smoothing are often necessary to achieve a reasonable S/N. Hence, the effective resolution is typically lower, but in many cases, it is better than most of the IFUs mentioned above. Chapter 3 will capitalise on ALMA to study the kinematic nature of galaxies a mere 1 billion years after the Big Bang.

Follow-up studies of targets selected from large surveys with high spectroscopic and angular resolution IFUs have brought decisive evidence of the prevalence of disks at cosmic noon and at least up to $z \sim 3$, with over 70% of galaxies on the MS showing regular rotation (Fig. 1.9), traced via rest-frame optical emission lines. However, unlike the local dynamically cold disks with $V_{\mathrm{circ}}/\sigma_0 \gtrsim 10$, these disks appear to be generally characterised by high intrinsic local gas velocity dispersions of $\sigma_0 \sim 30$–$90\,\mathrm{km\,s^{-1}}$ (Fig. 1.11) and weaker rotational support with low ratios of circular velocity to intrinsic velocity dispersion $V_{\mathrm{circ}}/\sigma_0 \sim 2$–6 (E. Wisnioski et al., 2015; H. Übler et al., 2019). The general finding of a majority of disks among massive ($M_\star \gtrsim 10^{10} M_\odot$) SFG(s), with increasing gas velocity dispersion σ_0 and decreasing rotational-to-dispersion support $v_{\mathrm{rot}}/\sigma_0$ out to $z \sim 3$ as the galactic gas mass fractions increase has played an important role in the emergence of the equilibrium growth model of galaxy evolution described in Sect. 1.2.1.

1.3.3 Physical driver of disk turbulence at high redshifts

The physical drivers of the (supersonic) turbulence (typically $\sim 50\,\mathrm{km\,s^{-1}}$ at $z \sim 2$) could be energetic input from star formation, accretion onto the galaxies, (local) gravitational instabilities and non-circular gas transport within galaxies, which become increasingly important at higher redshift because of gas richness (A. Dekel et al., 2009a; M. R. Krumholz et al., 2018).

Specifically, the instabilities referred to here are the Toomre instability, which can be understood by considering the following.

For linear tight-winding perturbation in a razor-thin fluid disk, the dispersion relation is given by:[5]

$$\left(\omega - m\Omega\right)^2 = \kappa^2 - 2\pi G\Sigma\,|k| + v_s^2 k^2, \tag{1.14}$$

where ω, k, and m are the angular frequency, radial wavenumber (> 0 for trailing arms) and the number of spiral arms, respectively. Ω, Σ, v_s, and κ are the angular frequency

---

[5] See J. Binney & S. Tremaine (2008) and F. H. Shu (1992) on the mathematical derivation of the dispersion relation for fluid disks.

(V_ϕ/R), surface density, sound speed, and epicyclic frequency

$$\kappa = \sqrt{4\Omega^2 + R\frac{d\Omega^2}{dR}} = \sqrt{2\left(\frac{V_\phi}{R}\right)^2 + 2\left(\frac{V_\phi}{R}\right)\frac{dV_\phi}{dR}} \tag{1.15}$$

of the fluid disk. For constant (flat) disk rotation $\frac{dV_\phi}{dR} = 0$, $\kappa = \sqrt{2}\Omega$, while for Keplerian rotation, $\frac{dV_\phi}{dR} = -\frac{1}{2}\frac{V_\phi}{R}$, $\kappa = \Omega$.

For axisymmetric short-wavelength disturbances such that $m = 0$ (and $|kR| \gg 1$), Eq. 1.14 is reduced to

$$\omega^2 = \kappa^2 - 2\pi G\Sigma\,|k| + v_s^2 k^2. \tag{1.16}$$

The disk is unstable if $\omega^2 < 0$, where a perturbation would grow exponentially of the form $e^{|\omega|t}$. Solving for k we have:

$$k = \frac{2\pi G\Sigma \,\pm\, \sqrt{(2\pi G\Sigma)^2 - 4v_s^2\kappa^2}}{2v_s^2}, \tag{1.17}$$

which has real root only if

$$Q \;\equiv\; \frac{v_s\,\kappa}{\pi G\Sigma} \;<\; 1, \tag{1.18}$$

where Q is a dimensionless quantity, first introduced by A. Toomre (1964) and commonly referred to as Toomre's Q. The Q is a function of radius, and $Q(R) < 1$ means local axisymmetric instability near R against short wavelength perturbation. In other words, it implies that if the surface density is high enough and the circular velocity and velocity dispersion are sufficiently low, the disk is gravitationally unstable against local collapse. Although Eq. 1.18 refers to fluid disk, it is a close enough analogy of a stellar disk, a collisionless fluid, with a modified dispersion relation in Eq. 1.14, and v_s is replaced by the velocity dispersion of the stars, $\sigma_\star$, and the constant π is replaced by 3.36, which in practice with real observations, is a negligible difference compared to other uncertainties. The Toomre Q is often used as a pseudo-temperature scale for galactic disks, with 'cold' disks meaning low σ and high Q.

For a real galactic disk composed of both stars and gas, one can also derive similar dispersion relations and stability criteria by treating the system as co-existing fluids with collisionless and collisional components with different surface densities and velocity (C. J. Jog & P. M. Solomon, 1984; A. B. Romeo, 1992; R. R. Rafikov, 2001). Using the simple approximation of B. Wang & J. Silk (1994) (see also A. B. Romeo & N. Falstad, 2013),

$$Q_{\rm total} = \left(Q_{\rm gas}^{-1} + \frac{2\sigma_{\rm gas}\sigma_\star}{\sigma_{\rm gas}^2 + \sigma_\star^2} Q_\star^{-1}\right)^{-1}, \tag{1.19}$$

where $Q_\star$ and $Q_{\rm gas}$ take a similar form of Eq. 1.18 with the surface densities corresponding to the respective components, and v_s replaced by the velocity dispersion of the stars $\sigma_\star$ and gas $\sigma_{\rm gas}$, respectively. Equation 1.19 is valid as long as $Q_{\rm gas} < Q_\star$, which is expected to hold for gas-rich systems such as star-forming galaxies at high redshift, or at low redshift, mergers and starbursts, since gas is dissipational and usually has a lower velocity dispersion than stars, so it tends to be the most unstable component in any gas-rich system.

Therefore, in high-redshift studies, the relation is often approximated in a simple form (e.g. A. Dekel et al., 2009a; R. Genzel et al., 2011):

$$Q \approx Q_{\rm gas} = \frac{\sigma_0\,\kappa}{\pi\,G\,\Sigma_{\rm gas}} = \left(\frac{\sigma_0}{v_c}\right)\left[\frac{a(v_c^2 R_{\rm disk}/G)}{\pi\,R_{\rm disk}^2\,\Sigma_{\rm gas}}\right] = \left(\frac{\sigma_0}{v_c}\right)\left(\frac{a\,M_{\rm tot}}{M_{\rm gas}}\right) = \left(\frac{\sigma_0}{v_c}\right)\left(\frac{a}{f_{\rm gas}}\right), \tag{1.20}$$

where $a = \sqrt{1...2}$ depends on the shape of the rotation curve: $a = 1$ for a dropping Keplerian curve, $a = 2$ for a flat DM-dominated curve.

Compared to local disks (Fig. 1.4), high redshift disks are geometrically thick with scale height $h_z \sim 0.2$–$0.3R_d$ (Eq. 1.8, cf. MW thin disk $h_z \sim 0.1R_d$), implied from their elevated gas velocity dispersion (Sect. 1.3.2), and inferred also from the morphologies of distant edge-on disk-like systems (e.g. D. M. Elmegreen et al., 2005; T. Tsukui et al., 2025). A disk with finite thickness reduces the gravitational force in the mid-plane, where star formation mostly takes place. Therefore, the disk could remain stable even below $Q = 1$ and a revised critical value lies around $Q \approx 0.68$ (P. Goldreich & D. Lynden-Bell, 1965; M. Behrendt et al., 2015).

Gravitational instability will lead to disk fragmentation. Indeed, high-redshift disks exhibit prominently clumpy and irregular morphologies (e.g. R. Genzel et al., 2011, 2014a; N. M. Förster Schreiber et al., 2011), yet with ordered rotation-dominated gas kinematics. Large kpc-sized clumps are observed in the ionised gas distribution tracing star formation, in the stellar populations, and in the molecular gas and dust content. These clumps are significantly larger than typical star-forming regions in the local Universe, as expected given the large disk turbulent velocities. In fact, in the early HST time, these UV-bright star-forming clumps were initially thought to trace the multiple components of galaxy mergers (L. L. Cowie et al., 1995; R. G. Abraham et al., 1996; S. van den Bergh et al., 1996). Mergers were once thought to dominate galaxy assembly out to $z \sim 1$ (e.g. T. J. Broadhurst et al., 1992; O. Le Fèvre et al., 2000), although arguments were also presented for clumps tracing instead giant star-forming complexes in individual host galaxies (W. N. Colley et al., 1996; M. Noguchi, 1998, 1999; D. M. Elmegreen et al., 2004). Ground-based kinematic measurements (R. Genzel et al., 2006) lent strong support to the rotating disk

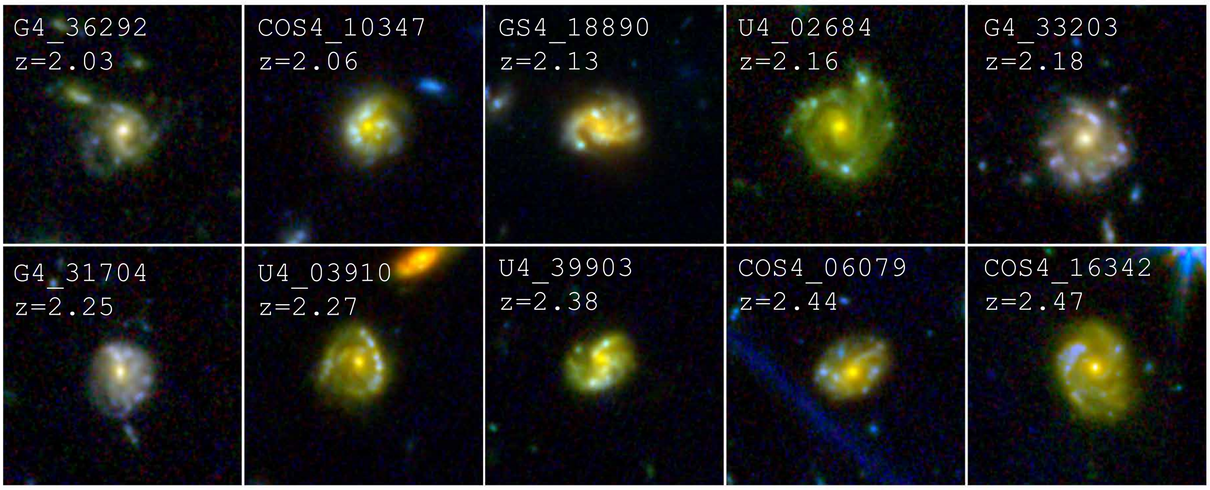

Figure 1.10 Colour images of ten example clumpy galaxies at $z > 2$ observed with JWST/NIRCam, identified in J. M. Espejo Salcedo et al. (2025). The field-of-view is $5.''\times5.''$, corresponding to $\sim 40\,\mathrm{kpc} \times 40\,\mathrm{kpc}$ at $z = 2$.

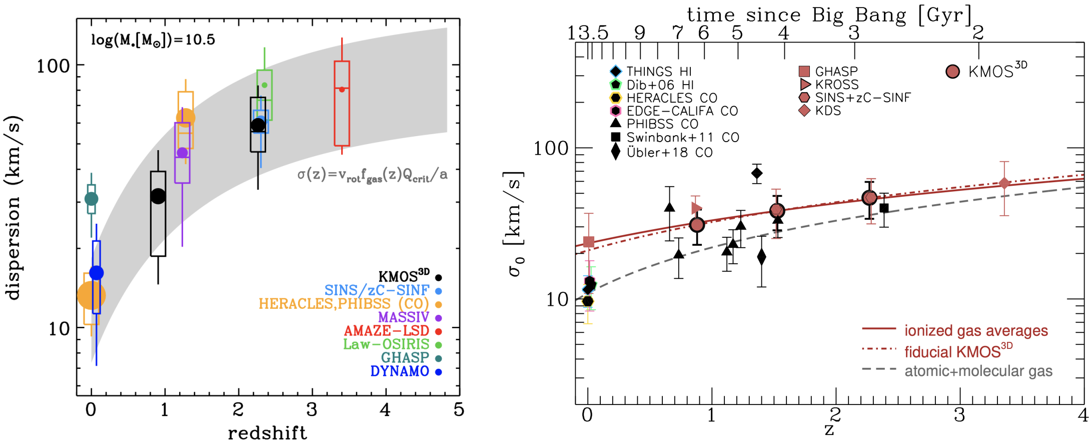

Figure 1.11 (*Left*) Velocity dispersion as a function of cosmic time up to $z = 4$. (*Right*) Same as *left*, but including also the linear-regression models for the ionised gas (red solid line) and colder gas phases (grey dashed line). [Figure adopted from E. Wisnioski et al. (2015) (*left*) and H. Übler et al. (2019) (*right*)]

nature for the majority of the systems (N. M. Förster Schreiber & S. Wuyts, 2020).

The prevalence of disk-like morphologies also became evident with near-IR imaging with HST, and now fully confirmed at higher-resolution rest-frame near-IR wavelengths with JWST (Fig. 1.10). Despite the clumps' brightness in the UV, they account for only typically $\lesssim 10\%$ of the host galaxy's stellar mass (S. Wuyts et al., 2012; Y. Guo et al., 2015, 2018; T. Shibuya et al., 2016; A. de la Vega et al., 2025). Over time, these clumps may then migrate and coalesce into a central classical bulge (e.g. M. Noguchi, 1999; A. Immeli et al., 2004a,b; F. Bournaud et al., 2007; B. G. Elmegreen et al., 2009; F. Bournaud, 2016; D. Ceverino et al., 2012; N. Mandelker et al., 2017) in several disk dynamical times. The migration of clumps, gravitational torques from clump–clump interactions, and in-plane radial gas flows now uncovered in the kinematics of $z > 1$ disks (S. H. Price et al., 2021; R. Genzel et al., 2023; T. Tsukui et al., 2024; H. Übler et al., 2024a; S. Pastras et al., 2025), may therefore provide an additional source of turbulence, in addition to those generated by feedback from stars and supernovae. At $z \lesssim 3$, the evolution of gas velocity dispersion with redshift correlates best with the increasing gas mass fractions and is consistent with the trend expected from marginally stable $Q \sim 1$ gas-rich disks (Fig. 1.11, see also N. M. Förster Schreiber et al., 2009; H. Übler et al., 2019). Chap. 3 will further explore this for galaxies at even earlier cosmic time at $z > 4$.

At $z \sim 1-3$, empirical results from deep observations of MS SFG(s) suggest that $\sigma_{\rm gas}$, is radially constant and isotropic, i.e. $\sigma(r) = \sigma_0$ (e.g. R. Genzel et al., 2011; H. Übler et al., 2019). Assuming the vertical density profile can be expressed by the hydrostatic Spitzer solution (L. Spitzer, 1942), a common parametrisation of $V_{\rm circ}$ for an exponential disk with a constant σ (e.g. A. Burkert et al., 2010, 2016) is given by:

$$V_{\rm circ}^2 = V_\phi^2(r) + 2\sigma_0^2\left(\frac{r}{R_d}\right) = V_{\rm rot}^2(r) + 3.36\sigma_0^2\left(\frac{r}{R_e}\right), \tag{1.21}$$

where R_d is the exponential disk scale length, which relates to the effective radius, R_e, by $1.678R_e$. This pressure-support correction is sometimes referred to as the 'asymmetric drift' correction, although it originates from a mechanism different from that of stellar dynamics.

The pressure-support correction becomes increasingly important at high redshift due to the elevated gas fraction, and neglecting it would lead to an underestimation of the enclosed mass. In particular, the DM fraction could be underestimated if this effect is not accounted for. However, even after accounting for this effect, observational findings of MS SFG(s) at $z \sim 1-3$ have generally found a relatively low central DM fraction (Fig. 1.12), or equivalently a high baryonic fraction, especially towards massive $\log(M_\star/M_\odot) \gtrsim 10$, centrally dense SFG(s). This implies that these galaxies have more cored DM profiles than

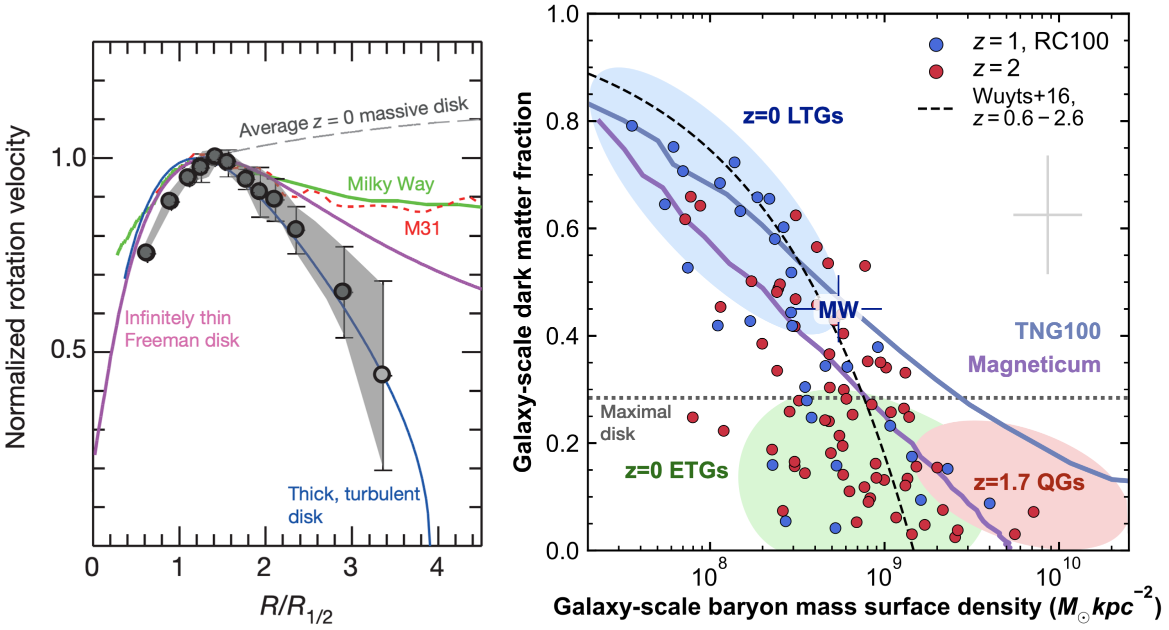

Figure 1.12 (*Left*) Binned-averaged RC of six typical SFG(s) at $0.9 < z < 2.4$ (grey circles and shading). The grey dashed line indicates the slope of a typical RC for $z = 0$ and $\log(M_\star/M_\odot) \approx 11$, disk galaxies. The solid green and dotted red curves are the RCs of the Milky Way (MW) and the Andromeda galaxy, respectively. The purple curve is the RC of an infinitely thin 'Freeman' disk. The blue curve represents a turbulent, thick exponential disk, including pressure-support corrections for an assumed $\sigma_0 = 50\,\mathrm{km\,s^{-1}}$ and $V_{\mathrm{rot}}/\sigma_0 \approx 5$ (Eq. 1.21). (*Right*) Galactic-scale dark matter fraction of 100 MS SFG(s) at $z \sim 1$–2.5 as a function of their baryonic mass surface density (R. Genzel et al., 2017, 2020; S. H. Price et al., 2021; A. Nestor Shachar et al., 2023, see also N. M. Förster Schreiber & S. Wuyts 2020). The blue and green ellipses indicate the corresponding parameter space for $z = 0$ late-type galaxies (LTGs) and early-type galaxies (ETGs), respectively (S. Courteau & A. A. Dutton, 2015). The red ellipse encapsulates the parameter range of $z \sim 2$ massive quiescent galaxies (QGs, J. T. Mendel et al., 2020). The dashed black line shows the best-fit relation from S. Wuyts et al. (2016) for 240 massive SFG(s). The light blue and purple lines denote the relations predicted by the cosmological simulations TNG100 (M. R. Lovell et al., 2018) and Magneticum (R.-S. Remus et al., 2017), respectively. The approximate value of the MW is annotated (J. Bovy & H.-W. Rix, 2013; J. Bland-Hawthorn & O. Gerhard, 2016). [*Left*: Image and values adopted from R. Genzel et al. (2017) and references therein. *Right*: Image adapted by Sedona Price]

the NFW profile in Eq. 1.9 (e.g. R. Genzel et al., 2020; A. Nestor Shachar et al., 2023). In particular, cored DM profiles at such mass scale have not been observed previously; they are more typically seen in dwarf galaxies (e.g. G. Gilmore et al., 2007) or in galaxy clusters (e.g. A. B. Newman et al., 2013). This finding suggests that the dynamical friction and effects of vigorous feedback, which are ubiquitous at high redshift, not only influence the processes within galaxies but also impact their surrounding halos by redistributing central DM towards the outer regions. Chap. 3 will further investigate this for galaxies beyond cosmic noon at $4 < z < 6$.

1.3.4 Challenges in observing and modelling high-redshift galaxies

More pragmatically, another layer of complexity in extracting kinematics from an observed data cube is the so-called beam-smearing effect. This effect arises when the convolution of the intrinsic line flux distribution with the point spread function (PSF) acts as a spatial blurring kernel that reduces local contrast. The velocity gradients are suppressed and appear shallower, and the unresolved velocity gradients contribute to the line broadening, thus inflating the observed velocity dispersion. The beam-smearing effect is most pronounced when (i) the intrinsic velocity gradient is steeper, (ii) the PSF is broader relative to the size of the galaxy, and (iii) the disks are more inclined.

Furthermore, high-redshift objects are increasingly fainter to detect due to cosmic surface brightness dimming, which goes with $(1+z)^{-4}$. Coupled with the beam-smearing effects, this makes modelling high-redshift disks more challenging than modelling local nearby galaxies. Chapter 2 will examine the various strategies developed for high-redshift studies over the past decade.

The strategies can be broadly categorised into two approaches. One approach involves highly flexible tilted-ring models, which fit each annulus independently. In this method, the galaxy is decomposed into annuli and populated with ‘clouds’ in each annulus. Each annulus is then fitted independently, allowing it to have its own inclination and position angle. This approach was initially motivated by observations of warps in local galaxies (e.g. D. H. Rogstad et al., 1974; K. G. Begeman, 1989). It offers maximal freedom to match more varied RC shapes. However, it requires high signal-to-noise ratios (S/N), and its physical interpretation in terms of bulge-disk-DM decomposition is less straightforward.

The other approach is based on axisymmetric analytic mass models with a small number of global parameters. Compared to the previous one, it is less versatile but describes the data well at high redshifts when the S/N is modest. There are different variations in the parametric approach, among which multi-component mass models have an advantage in better constraining the contributions of the bulge, disk, and DM to the mass budget separately. They also provide more flexibility in the modelling compared to those models that lump everything into a single mathematical representation such as the arctan function. As will be demonstrated in Chap. 2, failing to account for the sensitivity of S/N and model choices can introduce substantial scatter from one study to another.

Lastly, the ISM consists of gas in different phases, including atomic, molecular, and ionised gas. The different ISM phases not only have different thermo-dynamical properties, such as temperatures, densities, and pressures, but they also have different spatial distributions and dynamical properties. However, observational results at $z \sim 2$ and beyond so far do not indicate a significant difference in velocity dispersion, though the number of galaxies with disk velocity dispersion measurements in more than one gas phase is still limited (e.g. R. Genzel et al., 2013; H. Übler et al., 2018; J. Molina et al., 2019; D. Liu et al., 2023). A larger sample is needed to either confirm or rule out this finding. Chap. 3 will revisit this topic.

1.3.5 Beyond cosmic noon with far-infrared lines

Figure 1.11 illustrates that, until roughly a decade ago, spatially resolved kinematic studies of representative MS SFG(s) were effectively limited to $z \lesssim 4$. The limitation arose because the key rest-frame optical nebular lines (e.g. Hα and [O III] λ5007 Å) are redshifted beyond $\simeq 2.5\,\mu$m, where strong telluric water-vapour absorption and low instrument throughput make ground-based observations not feasible. The low-J rotational lines from CO are faint and also beyond reach. On the other hand, the bright far-infrared fine-structure lines, particularly the [C II] 158 μm line (rest wavelength 157.74 μm, rest frequency 1900.5369 GHz), offer a powerful alternative. The [C II] line was first detected in the Flame Nebula and Orion Nebula by R. W. Russell et al. (1980). The first extragalactic detection of [C II] in nearby galaxies was made using the NASA Kuiper Airborne Observatory (M. K. Crawford et al., 1985; G. J. Stacey et al., 1991). For $z \gtrsim 4$, [C II] becomes observable with ground-based (sub-)mm interferometers, such as NOEMA (for $z \gtrsim 6$) and ALMA. Figure 1.13 shows the observed frequency of the [C II] line as a function of redshift overlaid on top of the ALMA receiver bands. For a galaxy at $z = 5$, [C II] line is observed at ~ 0.95 mm, comfortably within ALMA Band 7 (1.09–0.80 mm 275–373 GHz). Both ALMA and NOEMA now enable $\sim$0\farcs1–0\farcs3 resolution studies of distant faint galaxies, corresponding to ~ 1 kpc at $z > 4$.

The [C II] line emission is a powerful line for tracing the star formation and kinematics of galaxies. Since the ionisation potential of carbon is lower than that of hydrogen (11.25 vs.

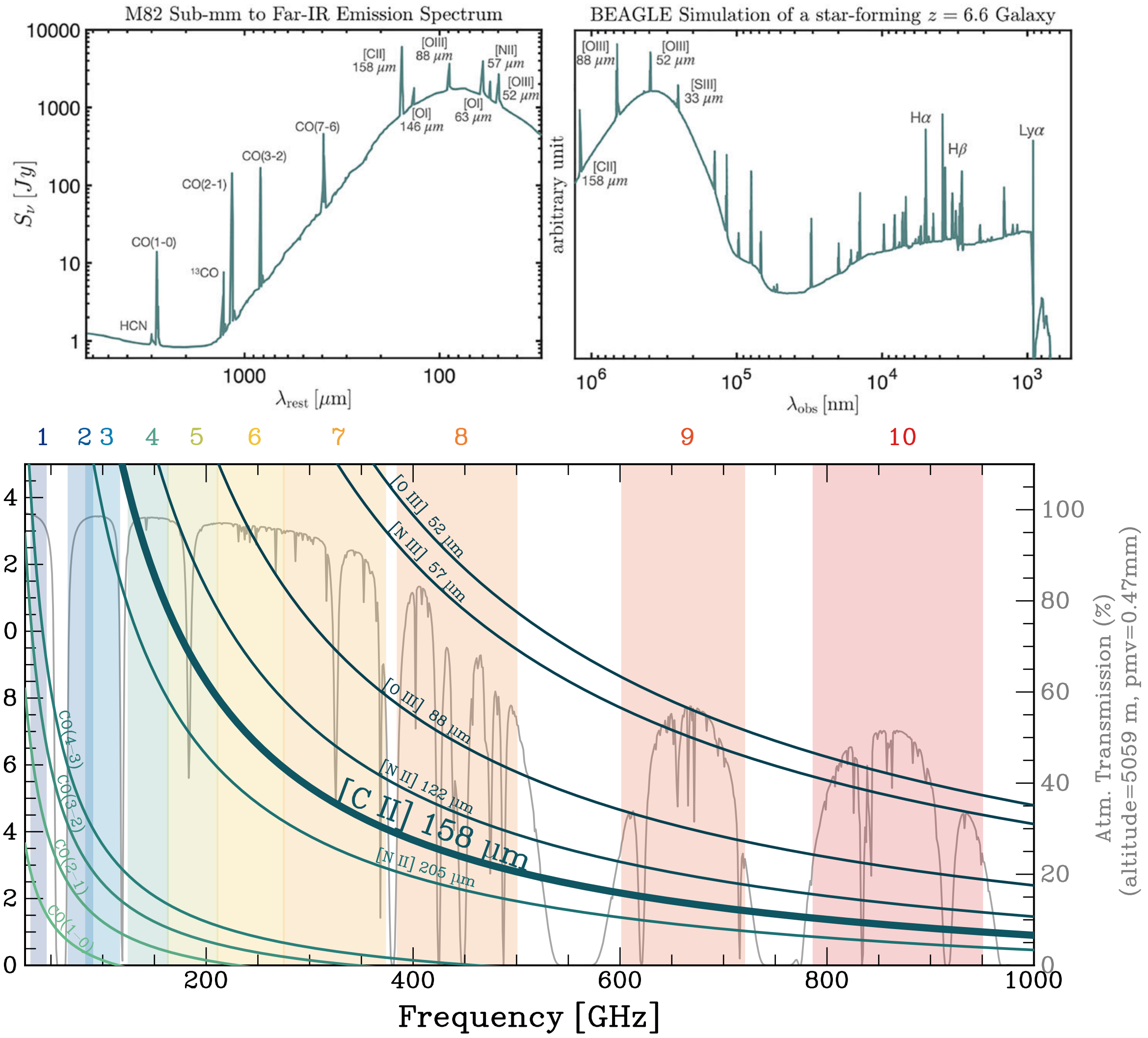

Figure 1.13 *Top*: Spectral energy distribution (SED) of M82 (*left*) and a simulated SFG(s) at $z = 6.6$ (*right*). [Image credit: Original spectra of M82 from R. Genzel 1991 and simulated galaxy from Y. Harikane et al. 2018. Figure adapted by J. L. Bernal & E. D. Kovetz 2022] *Bottom*: Observed frequencies of the commonly observed sub-mm and FIR emission lines (dark green curves). The grey spectrum in the background is the atmospheric transmission at the ALMA site, about 5100 metres in altitude. The coloured vertical bands from blue to red are the ALMA bands from Band 1 to Band 10. For $4 < z < 6$ galaxies, the [C II] 158μm line with its frequency redshifted into ∼ 350–400 GHz, could be easily detected with Band 7.

13.6 eV), photons with wavelengths between 1102 Å and the Lyman limit (912 Å), which are not absorbed by hydrogen, are available for the ionisation of carbon. The resulting C^+ ion is widely present in the ISM, and is particularly strong in photo-dissociation region (PDR, Fig. 1.14), but is also associated with the cold neutral medium (CNM), CO-dark molecular gas, and low-density ionised gas. The C^+ ion can be efficiently collisionally excited, leading to the magnetic dipole transition (M1) from $^2P_{3/2}$ to $^2P_{1/2}$, which results in the [C II] 158μm line. Generally, forbidden lines are usually optically thin $\tau \approx 10^{-2}$, which means that the [C II] line can efficiently carry energy away, and is a major coolant of the ISM (G. J. Stacey et al., 1991; D. J. Hollenbach & A. G. G. M. Tielens, 1999; J. Bernard-Salas et al., 2012; P. F. Goldsmith et al., 2012). Far-IR lines are also not affected by dust extinction, which can pass through ISM without much hindrance. The [C II] line is often the single brightest emission line in the spectrum of galaxies (Fig. 1.13 top). The luminosity of the line can be as high as 1% of the dust luminosity. Coupled with its easy excitation in a range of ISM conditions, it is an ideal tracer of the kinematics of galaxies to very extended regions for the study carried out in Chap. 3.

Notwithstanding the considerable efforts invested in studying [C II] at $z > 4$, the majority of galaxies studies so far comprises short-lived, maximum-starburst galaxies that have recently undergone or are undergoing dissipative major mergers (e.g. F. Lelli et al., 2021; F. Rizzo et al., 2021; F. Roman-Oliveira et al., 2023a). These galaxies belong to a class known as submillimetre galaxies (SMG, N. Bouché et al., 2007; L. J. Tacconi et al., 2008). The choices were understandably so, because the enhanced merger-boosted SFRs lead to higher [C II] luminosity, which is easier to observe for resolved studies. However, this limitation hinders our ability to understand the average evolution of the bulk of the population. Chapter 3 will address this shortfall by presenting the first systematic study of the largest high-resolution sample of typical SFG(s) at $4 < z < 6$.

1.4 Chemical abundance and its spatial distribution in high-redshift SFGs

The previous section has discussed the kinematics of disks and how observers study them with gas emission lines as a tracer. In addition to directly observing gas motion, studying the distribution of metals (elements heavier than helium) is also a powerful tracer of a galaxy's evolutionary history. When stars evolve and explode as supernovae, they inject newly synthesised metals into the ISM. These metals become mixed (on $\sim$ 10–100 Myr timescales) with the surrounding gas and are locked into subsequent generations of stars, so each region

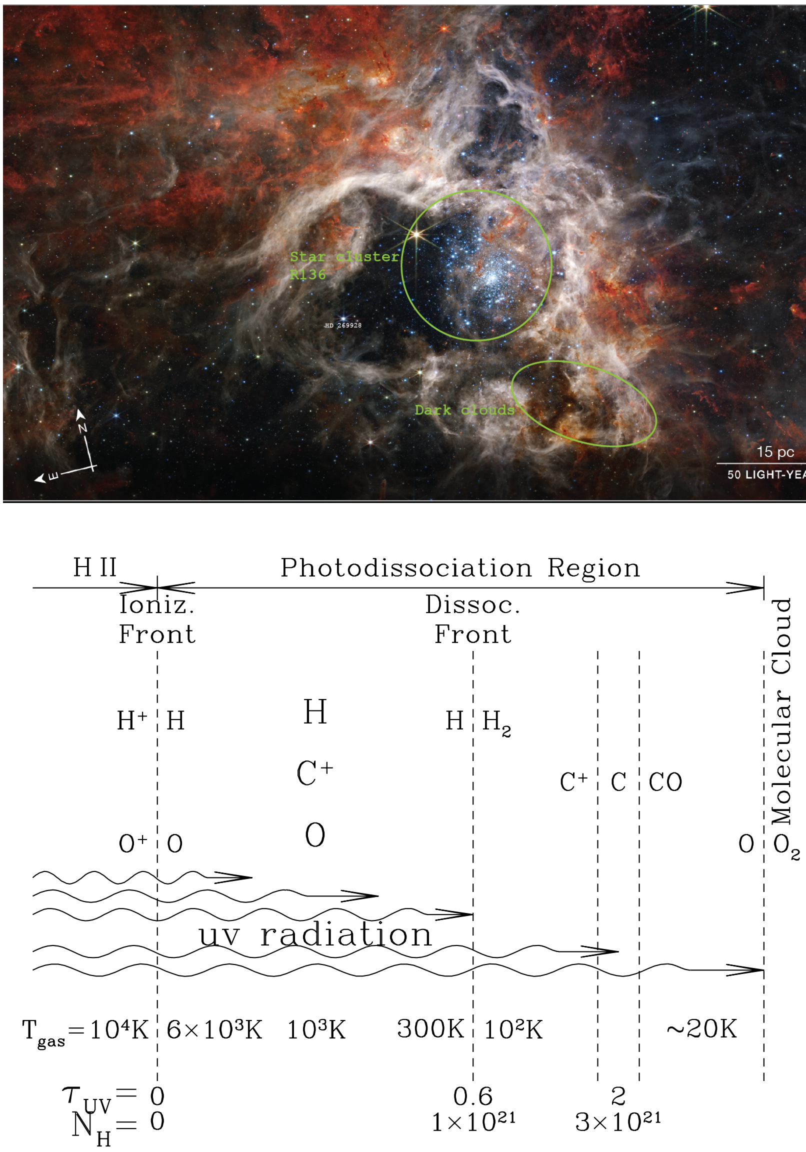

Figure 1.14 (*Top*) JWST 's NIRCam view of the Tarantula Nebula (30 Doradus), an H II region in the Large Magellanic Cloud, which is the brightest H II region in the Local Group (R. C. Kennicutt, 1984). At the centre lies the young star cluster R136. (*Bottom*) Schematic sketch of the chemistry and structure of the H II region and photodissociation region (PDR). The dominant chemical species in each region are labelled. The incident UV photons from the young massive stars in the H II region cause photo-dissociation and ionisation of H_2. Further away from the H II region, in between the ionisation front ($\sim$ 0.01 pc thick) and photo-dissociation front, recombination is efficient enough to maintain a low ionised fraction of H, and the resulting emission from the recombination is not energetic enough to re-ionise H again. Hence, the PDR is dominated by atomic hydrogen and ionised carbon C^+. Deeper into the molecular cloud, the UV flux has been sufficiently attenuated; most hydrogen is bound in molecular form, and low-J transition lines of CO serve as a good tracer of it. At the bottom, the decreasing intensity of the UV flux and the decline in gas temperature (resulting in an increase in optical depth) and density as one moves further away from the H II region are annotated. [Image credits: *Top*: NASA, ESA, CSA, STScI, Webb ERO Production Team. *Bottom*: B. T. Draine 2011]

of a galaxy encodes the ‘chemical memory’ of past star formation, nucleosynthesis, gas flows, and mass loss. Radial metallicity profiles are shaped by several competing processes: (i) Dilution by inflow of metal-poor gas (e.g. cosmological accretion, minor mergers). (ii) Enrichment by recycled, metal-rich galactic fountain flows. (iii) Metal-loaded galactic winds that preferentially remove metals from the disk. (iv) Radial gas flows driven by bars, spiral arms, clumps, or interactions with companion galaxies. Because these mechanisms operate with different efficiencies and spatial scales, the observed gradient of metallicity constrains how far gas is expelled and re-accreted and how efficiently internal radial gas transport is. Mapping chemical abundances, therefore, provides a complementary window onto the dynamical evolution of galaxies. Recent observational progress is driven by increasingly sensitive, high-resolution IFUs from the ground and space. These instruments enable mapping of a galaxy’s internal chemical gradients and kinematics in a single observation.

1.4.1 Chemical abundance from spectral lines

In this section, I will discuss the basic physics underlying the tools used to study metallicity in the gas phase of H II regions in extragalactic objects (Fig. 1.14 shows an example H II region in our local backyard). Gas-phase metallicity is particularly pertinent for studies at high redshifts, where measuring stellar metallicity is largely infeasible. Gas-phase metallicity reflects the more recent star formation history and is more sensitive to gas flow and enrichment of gas around young massive stars. In practice, the abundance of elements relative to hydrogen can be inferred by comparing the strengths of collisionally excited lines of metal ions to emission resulting from the recombination of electrons with H^+ ions.[6] Recombination (and the subsequent cascade to the ground state) is responsible for a series of hydrogen line emissions, as hydrogen does not have low-lying energy levels that can be easily excited through collisions.

Another important process is the photoionisation of the metal atoms. Photoionisation is one of the major avenues of transferring radiative energy of stars to gas in the ISM. The source of photoionising photons $AB + h\nu \rightarrow AB^+ + e^-$ could be the UV photons from young massive stars. Photoionisation can also occur in the diffuse ISM by absorbing diffuse starlight, or around the accretion disks of black holes, such as in AGN. It results in a so-called H II regions (Fig. 1.14), with temperature $T \approx 10^4\,\mathrm{K}$, and density spanning a wide range of $n_\mathrm{H} = 0.3\text{–}10^4\,\mathrm{cm}^{-3}$.

Many species of metal ions (e.g. O^{2+}, S^+, N^+) have fine structure in their electronic ground state as a result of, to first order, the spin-orbit coupling. Therefore, they have

---

[6] In H II region, electrons are the primary collider responsible for the excitation of metal ions.

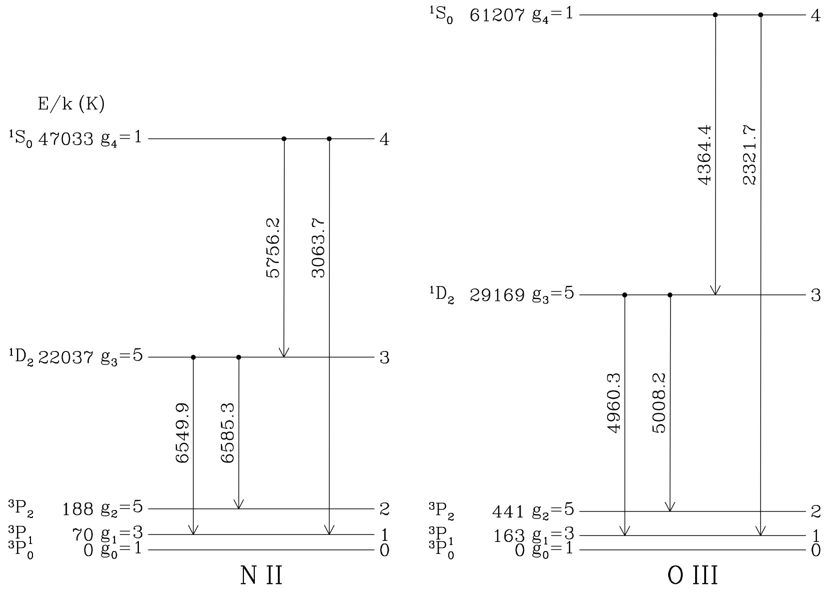

Figure 1.15 Energy levels for two $2p^2$ ions [N II] and [O III]. Transitions are labelled by vacuum wavelength. [Image adopted from B. T. Draine (2011).]

low-lying fine-structure energy states that can be collisionally excited. The subsequent de-excitation transitions are either magnetic dipole (M1) or electric-quadrupole (E2) transitions with very low Einstein A (spontaneous emission) coefficients. In low-density regions ($n_e \lesssim 10^3\,\mathrm{cm}^{-3}$) where collisional de-excitation is unimportant, such radiative decay produces the so-called forbidden lines. Since collisional processes are several orders of magnitude faster than the recombination process, collisionally excited lines are as strong as the H recombination lines, although the abundances of metals are much lower than that of hydrogen. These forbidden lines are optically thin, and among which, the lines of the M1 $^1D_2$–$^3P_{1,2}$ transitions of [O III] at $\lambda\lambda 4959, 5007$ ÅÅ and [N II] $\lambda\lambda 6548, 6583$ ÅÅ (Fig. 1.15) are among the brightest forbidden lines at optical wavelengths in the ISM, and are particularly useful for studying high redshift SFG(s). The abundances of various ions relative to H are obtained by solving the statistical equilibrium equation using collisional excitation models.

The collisional cross section for the transition from level j to level i is inversely proportional to v^2 above the energy threshold E_{ij} and is zero below. The collisional cross-section can be expressed as dimensionless collisional strength (B. T. Draine, 2011):[7]

$$\sigma_{ji}(v) = \left(\pi a_0^2\right)\left(\frac{hR_\infty}{\frac{1}{2}\,m_\mathrm{e}v^2}\right)\frac{\Omega_{ji}}{g_j} = \left(\frac{\pi h^2}{4\pi^2 m_\mathrm{e}^2 v^2}\right)\frac{\Omega_{ji}}{g_j}\,, \tag{1.22}$$

where $a_0 = h^2/4\pi m_e e^2$ is the Bohr radius, $R_\infty = \frac{2\pi^2 e^4 m_e}{h^3}$ is the Rydberg constant, and g_j is the statistical weight that describes the degree of degeneracy at level j.

The collisional excitation rate for an ensemble of electrons at temperature T_e can be obtained by averaging over the Maxwellian distribution:

$$C_{ji}(T_e) = \int_{v_\mathrm{min}}^{\infty} v\,\sigma_{ji}(v)\,f(v)\,dv = \int_{v_\mathrm{min}}^{\infty} v\,\sigma_{ji}(v)\,4\pi\left(\frac{m_e}{2\pi kT}\right)^{3/2} e^{-m_e v^2/2kT}v^2 dv \tag{1.23}$$

where $v_\mathrm{min} = \left(\frac{2E_{ij}}{m_e}\right)^{1/2}$, and E_{ij} is the energy level difference between level i and j. Substituting Eq. 1.22 into Eq. 1.23 gives

$$C_{ji} = \frac{8.629\times10^{-6}}{T_e^{1/2}}\,\frac{\Omega_{ji}}{g_j}\,\exp\!\left(-\frac{E_{ij}}{kT_e}\right)\;\mathrm{cm}^3\,\mathrm{s}^{-1}, \tag{1.24}$$

where Ω_{ji} is the collision strength. At high densities, the population distribution is dominated by collisions. By the principle of detailed balance,[8] the excitation rate from a lower state (l) to an upper state (u) is exactly balanced by the de-excitation rate from u to l:

$$n_u\, n_e\, C_{ul} \;=\; n_l\, n_e\, C_{lu}. \tag{1.25}$$

Since the population ratio of the two states is given by the Boltzmann equation, the collisional excitation and de-excitation rates are therefore related by

$$\frac{C_{lu}}{C_{ul}} = \frac{g_u}{g_l}\exp\!\left(-E_{ul}/kT_e\right), \tag{1.26}$$

where g is again the statistical weight. Assuming a two-level system and negligible ambient radiation (so that the stimulated terms can be omitted, i.e. Einstein B coefficient $= 0$), we have from the equation of statistical equilibrium:

$$n_u\left(n_e C_{ul} + A_{ul}\right) = n_l\, n_e\, C_{lu}, \tag{1.27}$$

---

[7] The equation can be understood classically by considering the conservation of energy and angular momentum of an ion-electron inelastic scattering.

[8] Still holds even if not in thermodynamic equilibrium.

where A_{ul} is the Einstein A coefficient of the transition $u \rightarrow l$. Rearranging and inserting Eq. 1.26 we have

$$\begin{aligned}
\frac{n_u}{n_l} &= \frac{n_e C_{lu}}{A_{ul} + n_e C_{ul}} && (1.28)\\
&= \frac{(g_u/g_l)\exp(-E_{ul}/kT_e)}{n_{\text{crit}}/n_e + 1} && (1.29)\\
&\approx \frac{g_u}{g_l}\exp(-E_{ul}/kT) && \text{for } n_e \gg n_{\text{crit}}\\
&\approx \left(\frac{n_e}{n_{\text{crit}}}\right)\frac{g_u}{g_l}\exp(-E_{ul}/kT) && \text{for } n_e \ll n_{\text{crit}},
\end{aligned}$$

where $n_{\text{crit}} \equiv \frac{A_{ul}}{C_{ul}}$ is the critical density, above which the population is thermalised and the relation falls back to the Boltzmann equation. When $n_e \ll n_{\text{crit}}$, the spontaneous emission $u \rightarrow l$ dominates over collisional excitation $l \rightarrow u$. The net result is the emission of photons carrying the energy E_{ul}.

Due to the low metal abundances and the small A_{ul} (and thus small n_{crit}), the forbidden lines of metal are generally optically thin ($\tau_\nu \ll 1$). Therefore, the line intensity is the integral of the emissivity along the line of sight ds, and for a bound-bound transition:

$$I_\nu = \int j_v \, ds \propto n_i A_{ij} \nu \propto n_{\text{ion}} n_e C_{ji} \exp(-E_{ji}/kT_e)\nu. \quad (1.30)$$

From this, we can already estimate the density of an ion, n_{ion}, from its emissivity, if the electron density, n_e, and electron temperature, T_e are known.

The density can be derived from doublet ratios of ions with an np^3 electron configuration. For example, the [S II] $\lambda\lambda 6716, 6731$ doublet from the transitions from ${}^2D_{5/2}$ and ${}^2D_{3/2}$ to ${}^4S_{3/2}$ of [S II], which has small energy difference. This doublet can be treated as a pair of two-level atom systems, in which the energy level difference between ${}^2D_{5/2}$ and ${}^2D_{3/2}$ is neglected. Then from Eq. 1.30, inserting Eq. 1.27, we can see that, when $n_e \ll n_{\text{crit}}$ in Eq. 1.29, the ratio of the line intensity

$$I(6717)/I(6731) = \frac{n_3}{n_2}\frac{A_{31}}{A_{21}} = \frac{C_{13}}{C_{12}}\left(\frac{n_{\text{crit},31}}{n_{\text{crit},21}}\right)\left(\frac{A_{31}}{C_{31}}\frac{C_{21}}{A_{21}}\right) = \frac{C_{13}}{C_{12}} = \frac{\Omega_{13}}{\Omega_{12}},$$

where the last equality is from Eq. 1.24; whereas when $n_e \gg n_{\text{crit}}$,

$$I(6717)/I(6731) = \frac{g_3}{g_2}\frac{A_{31}}{A_{21}}.$$

The different behaviour of line ratios in different density regimes makes such line pairs a useful indicator of density. The temperature, on the other hand, can be obtained from ratios in ions with an np^2 configuration, for example, the [O III] triplet, [O III] λ4363/ [O III]($\lambda4959 + \lambda5007$) from the ${}^1S_0 \to {}^1D_2$ and ${}^1D_2 \to {}^3P_{2,1}$ transitions. Considering the three-level atom system in Fig. 1.15, similar to Eq. 1.25, we can write the density ratios of the two upper states as

$$\frac{n_3}{n_2} = \frac{C_{13}}{C_{12}} \frac{A_{21}}{A_{31} + A_{32}}.$$

Hence, the intensity ratio of the triplet is

$$\begin{aligned}
\frac{I(4363)}{I(5007 + 4959)} &= \frac{n_3 \nu_{32} A_{32}}{n_2 \nu_{21} A_{21}} \\
&= \frac{C_{13}}{C_{12}} \frac{A_{32}}{A_{31} + A_{32}} \frac{\nu_{32}}{\nu_{21}} \\
&= \frac{\Omega_{13}}{\Omega_{12}} \exp[-(E_{31} - E_{21})/kT_e] \left(\frac{\nu_{32}}{\nu_{21}}\right) \frac{A_{32}}{A_{31} + A_{32}} \\
&= \frac{\Omega_{13}}{\Omega_{12}} \exp(-E_{32}/kT_e) \left(\frac{\nu_{32}}{\nu_{21}}\right) \frac{A_{32}}{A_{31} + A_{32}}.
\end{aligned}$$

The second last equality comes from Eq. 1.27. Hence, this line ratio can probe T_e through its $\exp(-E_{32}/kT_e)$ dependence.

With n_e and T_e known, the ionic abundance can be derived by comparing the flux of the forbidden line to the hydrogen recombination line. Eventually, the total elemental abundance can be derived by assuming an ionisation correction for the unobserved ionisation levels (e.g. L. S. Pilyugin & T. X. Thuan, 2005).

As mentioned in Sect. 1.2, dust in the ISM can significantly modify the observed spectrum through wavelength-dependent scattering and absorption. These processes are most efficient at UV and optical wavelengths, so the short-wavelength light is preferentially removed and the spectrum appears reddened. Therefore, the dust reddening effect needs to be corrected for when comparing the line ratios. Since Balmer decrement (sequence of line ratios $I(\mathrm{H}\alpha)/I(\mathrm{H}\beta)$, $I(\mathrm{H}\gamma)/I(\mathrm{H}\beta)$ and so on) are relatively insensitive to T_e and density when at low density. Therefore, comparison of the observed Balmer line ratios to theoretical line ratios is usually used to determine the degree of reddening by dust assuming a reddening law, for example, the D. Calzetti et al. (1994) law for local starburst galaxies, the J. A. Cardelli et al. (1989) law for our MW, and for SFG(s) at $z > 1.5$ with JWST spectroscopic studies (e.g. N. A. Reddy et al., 2025).

The metallicity is often referred to as the oxygen abundance relative to hydrogen, with

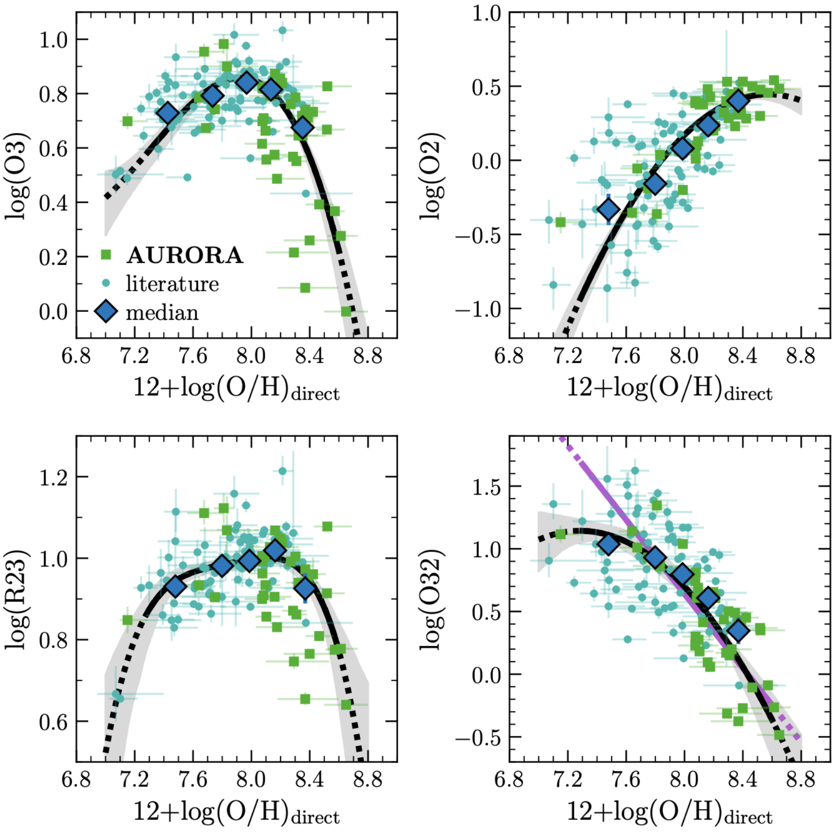

Figure 1.16 Relations between direct-T_e method metallicity and line ratios of collisionally excited lines of [O II] and [O III] to Hβ for galaxies at $2 < z < 10$. The data are obtained from NIRSpec IFU on JWST as part of the AURORA programme. [Figure credit: R. L. Sanders et al. 2025].

the following convention:

$$12 + \log(\mathrm{O/H}) \equiv 12 + \log(n_{\mathrm{O}}/n_{\mathrm{H}}), \tag{1.31}$$

defined such that H is fixed at 12 and nearly all other elements fall on a convenient positive scale. n_{O} and n_{H} are the number densities of O and H, respectively. Oxygen is often chosen because it is generally the most abundant heavy element in mass. There is also the implicit (although not always correct) assumption that the abundance of all other chemical elements scales proportionally to the solar abundance ratios. For the Sun, a commonly adopted value is $12 + \log(\mathrm{O/H}) = 8.69$ (M. Asplund et al., 2009), from the 3D hydrodynamical solar atmospheric modelling of the photospheric spectrum (see K. Lodders et al., 2009, for chondritic meteoritic values).

For high redshift studies, T_e is often not directly measurable since the T_e-sensitive auroral lines, such as [O III] $\lambda4363$, is generally too faint to detect in individual massive galaxies without stacking or extremely deep exposures. It is because massive galaxies are more metal-rich, the enhanced radiative cooling lowers T_e, which in turn suppresses T_e-sensitive auroral lines emissivity following Eq. 1.30, making their fluxes too faint to detect in individual galaxies. In such cases, observers resort to empirical 'strong-line' calibrations that relate bright nebular forbidden-line ratios (D. Alloin et al., 1979), typically normalised to Hβ or Hα to the oxygen abundance. Examples include R23, O32, Ne3O2, and N2 indices, which involve the lines [O II] $\lambda\lambda3726,3729$, [Ne III] $\lambda3869$, [O III] $\lambda5007$, [N II] $\lambda\lambda6548,6583$, as well as Hβ and Hα. These calibrations are commonly anchored to direct-T_e metallicities. Such direct-T_e calibrations had been only available for local to $z \lesssim 3.5$ systems before JWST (e.g. M. Pettini & B. E. J. Pagel, 2004; R. L. Sanders et al., 2020), which do not automatically transfer to high-z systems because of differences in ionisation parameter, ionising spectra, and N/O ratio, which also influence the relative emission line intensities.

Thanks to the sensitivity and wide spectral coverage to $\sim 5\,\mu$m of JWST, rest-frame optical strong lines can now be observed for a growing sample of galaxies at $z \gtrsim 3$. Corresponding metallicity calibrations have been derived for an ever-growing high-redshift sample (e.g. M. Curti et al., 2024; R. L. Sanders et al., 2025, and see also Fig. 1.16), making them directly applicable to the galaxies analysed in Chap. 4. Because individual diagnostics are degenerate with other parameters as mentioned, most studies combine several indicators or make use of photoionisation modelling (see review by L. J. Kewley et al., 2019; R. Maiolino & F. Mannucci, 2019). Chap. 4 will discuss these issues in more detail.

1.4.2 Metallicity gradients as proxies for chemical abundance distributions

The radial variation of a galaxy, the oxygen abundance is commonly quantified by the linear gradient of Eq. 1.31:

$$\log_{10} Z(r) = \nabla_r \log_{10}(Z) r + Z_0, \tag{1.32}$$

where $\log_{10} Z = 12 + \log_{10}(\mathrm{O/H})$, $\nabla_r \log(Z)$ is defined as the metallicity gradient with unit of $\mathrm{dex\,kpc}^{-1}$, and Z_0 is the central metallicity.

For our MW, the current $\nabla_r \log(Z) \approx -0.06\,\mathrm{dex\,kpc}^{-1}$ (from H II regions, J. E. Méndez-Delgado et al., 2022),[9] indicating a chemically richer central region compared to the outskirts. Looking at other nearby galaxies, observations from various large surveys indicate a typical

---

[9] It is a somewhat tracer-dependent value, with tracers such as H II regions, classical Cepheids and open clusters, with each tracing different timescales (R. Maiolino & F. Mannucci, 2019, and references therein).

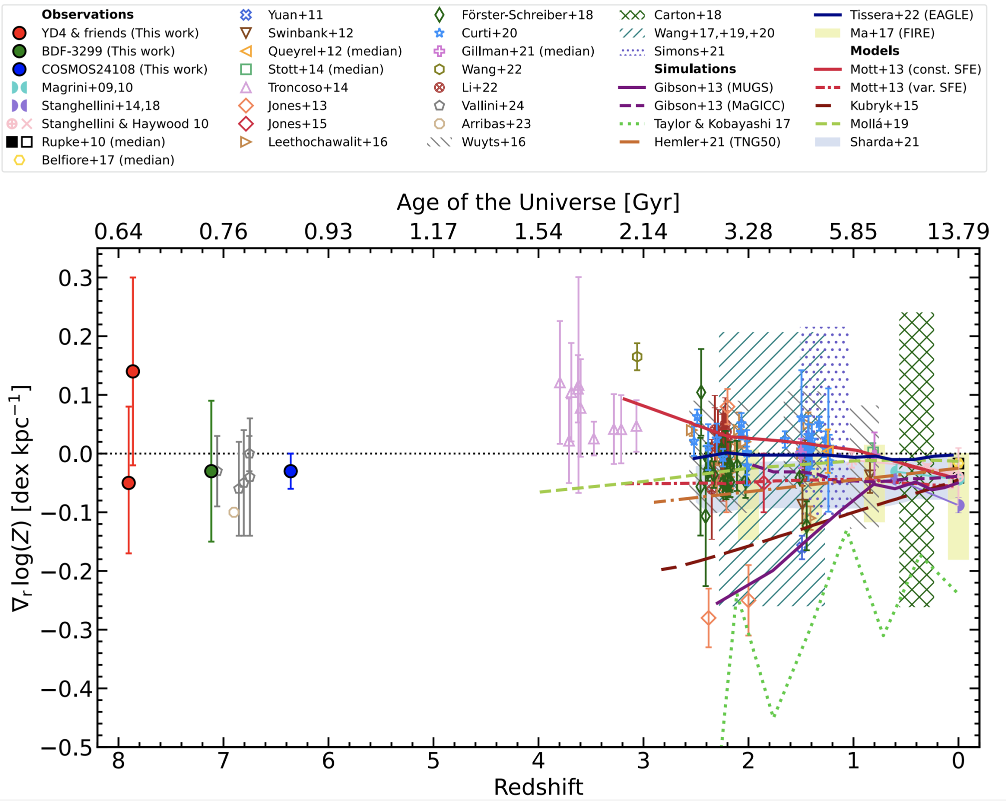

Figure 1.17 Observed and simulated cosmic evolution of metallicity gradients from local to $z = 8$, with compiled results from the literature (G. Venturi et al., 2024, and references therein.).

negative metallicity gradient ranging from ~ -0.05 to $0\,\mathrm{dex\,kpc}^{-1}$ (e.g. S. F. Sánchez et al., 2014; K. Grasha et al., 2022). The observed negative metallicity in the local Universe could be explained by an inside-out growth scenario, where the inner disk forms stars first from the high density of gas and has more time to enrich the ISM than the outer regions (e.g. F. Matteucci & P. Francois, 1989).

However, the metallicity gradient of the MW was shallower, with a value of approximately $-0.01\,\mathrm{dex\,kpc}^{-1}$, around 7.7 billion years ago ($z = 1$), based on chemical evolution models (C. Chiappini et al., 2001; L. Stanghellini et al., 2014). This implies that the metallicity gradient of the MW has steepened over time to match the currently observed value. Indeed, observations of galaxies at high-z using sensitive IFUs have revealed that a majority of these galaxies exhibit flat ($< 0.1\,\mathrm{dex\,kpc}^{-1}$) or only moderately negative or positive metallicity gradients (e.g. P. Troncoso et al., 2014; E. Wuyts et al., 2016; N. M. Förster Schreiber et al., 2018; M. Curti et al., 2020b), as shown in the literature compiled sample in Fig. 1.17.

The flatness implies the metal mixing processes inside galaxies should be efficient with a timescale shorter than that for star formation. Yet, there is no consensus on the dominant mechanism that causes this flattening, and many cosmological simulations continue to struggle to reproduce the observed trends at high redshifts (see A. M. Garcia et al., 2025, for a recent discussion).

Since disks are the dominant population of galaxies out to $z \lesssim 6$, internal secular processes are likely to be pivotal. Radial gas flows driven by gravitational torques from spiral or bar-like density waves and transfer of angular momentum by viscosity (D. Lynden-Bell & A. J. Kalnajs, 1972) can dilute the central regions. Furthermore, strong feedback in the form of galactic outflows can transport metals synthesised in central active star-forming regions to the outer disks as seen in observations (e.g. J. Chisholm et al., 2018) and simulations (e.g. X. Ma et al., 2017; P. B. Tissera et al., 2022).

Observationally, the study of metallicity gradients has long been restricted to redshifts of $z \lesssim 4$. The advent of JWST has enabled access to multiple strong rest-frame optical lines. Recent metallicity measurements based on JWST data at $z \gtrsim 6$ suggest that galaxies in the early Universe exhibit flat to positive gradients, although these findings are based on heterogeneous samples drawn from different galaxy populations (G. Venturi et al., 2024, and references therein). In particular, no measurement is available at $4 < z < 6$, let alone from a homogenous sample (Fig. 1.17). Chap. 4 will address this missing piece and place it in the broader context of the kinematic properties of the galaxies studied in Chap. 3. Together, these two chapters will provide a more comprehensive picture of the chemo-dynamical nature of the typical SFG(s) at the epochs immediately following EoR.

Thesis outline

The structure of this thesis and the scientific questions being addressed are as follows.

Chap. 2 sets out the groundwork for interpreting observational kinematics through modelling, incorporating knowledge about distant disks and observational effects.

1. How do different kinematics modelling tools, each with its own rationale, compare in terms of their recovery performance, and what are the implications of these differences for our modelling of dynamical evolution of disks?
2. What data quality is required to minimise biases introduced by modelling, and how can we optimise our modelling and observational strategies to best mitigate such biases?

In Chap. 3, I present the kinematic properties of MS SFG(s) at $4 < z < 6$, an epoch which was poorly explored with a representative galaxy sample. The study furthers our understanding of how MS SFG(s) build up in the post-reionisation era before cosmic noon and the early stages of galaxy formation. Specifically, I will address

1. What fraction of the galaxies are disks, and how do their kinematic properties, such as velocity dispersion, compare to those of lower redshifts and galaxies of different populations?
2. What are their galactic-scale dark matter fractions, and how do they compare to predictions from cosmological simulations?
3. What drives the velocity dispersion in these high-z disks?

Chap. 4 builds upon the kinematic analysis in Chap. 3, and tackles the following questions in the aspects of metallicity gradients of the sample:

1. What is the relationship between the kinematic nature of high-z galaxies and their metallicity gradients, and how do these correlations inform our understanding of metal mixing processes and timescales?
2. How do metallicity gradients vary between disk and non-disk systems? What could it tell us about the different physical processes governing metal enrichment in these systems?
3. Are there significant azimuthal variations in the metallicity gradients of high-z galaxies, and if so, what do these variations imply about the role of metal transport and localised metal enrichment processes?

I conclude with a summary and outlook with next-generation facilities in Chap. 5.

Chapter 2

Disk kinematics at high redshift: `DysmalPy`'s extension to 3D modeling and comparison with different approaches

This Chapter is a reprint of the ApJ publication Disk kinematics at high redshift: `DysmalPy`'s extension to 3D modeling and comparison with different approaches by L. L. Lee et al. (2025a); doi:10.3847/1538-4357/ad90b5. ©AAS. Reproduced by permission of the AAS.

Abstract – Spatially-resolved emission line kinematics are invaluable to investigating fundamental galaxy properties and have become increasingly accessible for galaxies at $z \gtrsim 0.5$ through sensitive near-infrared imaging spectroscopy and millimeter interferometry. Kinematic modeling is at the core of the analysis and interpretation of such data sets, which at high-z present challenges due to lower signal-to-noise ratio (S/N) and resolution compared to data of local galaxies. We present and test the 3D fitting functionality of `DysmalPy`, examining how well it recovers intrinsic disk rotation velocity and velocity dispersion, using a large suite of axisymmetric models, covering a range of galaxy properties and observational parameters typical of $z \sim 1$–3 star-forming galaxies. We also compare `DysmalPy`'s recovery performance to that of two other commonly used codes, `GalPak`$^{\mathrm{3D}}$ and $^{\mathrm{3D}}$`Barolo`, which we use in turn to create additional sets of models to benchmark `DysmalPy`. Over the ranges of S/N, resolution, mass, and velocity dispersion explored, the rotation velocity is accurately recovered by all tools. The velocity dispersion is recovered well at high S/N, but the impact of methodology differences is more apparent. In particular, template differences for parametric tools and S/N sensitivity for the non-parametric tool can lead to differences up to a factor of 2. Our tests highlight and the importance of deep, high-resolution data and the need for careful consideration of: (1) the choice of priors (parametric approaches), (2) the masking (all approaches) and, more generally, evaluating the suitability of each approach to the specific data at hand. This paper accompanies the public release of `DysmalPy`.

2.1 Introduction

Spatially-resolved kinematics provide fundamental insights into the nature, dynamical state, and mass assembly history of galaxies. Thanks to ever more powerful near-infrared/optical integral field unit (IFU) spectrographs on 4–8 m-class telescopes and millimeter interferometers (R. Bacon et al., 1995; L. Weitzel et al., 1996; F. Eisenhauer et al., 2003; J. Larkin et al., 2006; R. Sharples et al., 2013), kinematics have become a widespread tool in galaxy evolution studies at redshifts $z > 0.5$ (K. Glazebrook, 2013; N. M. Förster Schreiber & S. Wuyts, 2020). IFU studies, mainly targeting the Hα rest-optical line, comprise the most comprehensive census of resolved kinematics of massive star-forming galaxies (SFG(s)) at $z \sim 1-3$. These surveys cover well the "main sequence" (MS) of SFG(s) in stellar mass $M_\star$ vs. star formation rate SFR, which dominates the population and cosmic star formation (e.g., G. Rodighiero et al., 2011; M. T. Sargent et al., 2012; P. Madau & M. Dickinson, 2014). Resolved millimeter interferometric observations focused primarily on CO lines at $z \lesssim 4$ and on the bright [C II] $\lambda 158 \mu$m far-infrared line at $z \gtrsim 4$ in modest samples are now available for dynamical studies of the cold neutral gas. With its NIRSpec instrument in IFU mode, the *James Webb* Space Telescope (JWST), has recently opened up the way to resolved Hα kinematics mapping at $z \gtrsim 3$.

Such observations provide the most direct approach to probe the potential well and the physical processes that shape galaxies over time, including gas accretion, non-circular motions, galaxy interactions, mass and angular momentum transfer, and feedback from massive stars and active galactic nuclei (AGN). In this context, the gas velocity dispersion σ_0 and rotational-to-dispersion support $v_{\rm rot}/\sigma_0$ constitute important measures of disk structure and settling across cosmic time. Despite increasing observational efforts, results remain mixed on the amount, evolution, and origin of gas dispersion and dynamical support of distant disks.

Part of the differences may be attributed to sample selection and tracer choices. A number of studies over the past couple of decades found increasing disk dispersions and decreasing $v_{\rm rot}/\sigma_0$ towards higher redshift for samples probing mainly massive (stellar masses $M_\star \gtrsim 10^{10} M_\odot$) MS SFG(s) out to $z \sim 3$, trends that have been interpreted in the framework of marginally unstable gas-rich disks given the increasing molecular gas fraction at earlier time (see reviews by L. J. Tacconi et al., 2020; N. M. Förster Schreiber & S. Wuyts, 2020, and references therein). Other studies reported dynamically fairly cold, regular disk rotation including among infrared-luminous dusty SFG(s) and at $z \gtrsim 4$, either unlensed or strongly gravitationally lensed (e.g., J. A. Hodge et al., 2012; P. Sharda et al., 2019;

F. Fraternali et al., 2021; F. Lelli et al., 2021; F. Rizzo et al., 2021, 2022; T. Tsukui & S. Iguchi, 2021). At any given redshift, the scatter in σ_0 and $v_{\rm rot}/\sigma_0$ is substantial, even among the best data sets of MS SFG(s) (e.g., H. Übler et al., 2019). Although part of the spread in $v_{\rm rot}/\sigma_0$ at fixed redshift appears to be explained by a trend with galaxy stellar mass, it is less clear for σ_0 (e.g. S. A. Kassin et al., 2012; E. Wisnioski et al., 2015; R. C. Simons et al., 2018; H. L. Johnson et al., 2018; E. Parlanti et al., 2023; L. E. Rowland et al., 2024). Furthermore, there is a potentially inherent difference between the gas kinematics traced by warm ionized gas and colder atomic and molecular gas. Larger samples with high-resolution, high S/N data of multiple tracers for the same galaxies will be essential to establish whether, and how much, kinematic properties depend on the interstellar medium (ISM) phase (contrast D. Liu et al., 2023; E. Parlanti et al., 2023, 2024a; F. Rizzo et al., 2023, with H. Übler et al. 2018; R. Genzel et al. 2023).

Compounding the sample and tracer differences described above, the observational picture is further complicated by the use of various modeling approaches among studies. In some cases this has even led to discrepant results from the same data sets (e.g., compare K.-i. Tadaki et al. 2018, 2020 to P. Sharda et al. 2019; F. Roman-Oliveira et al. 2023b; see also F. Lelli et al. 2023). Because kinematics modeling serves as the foundation for linking observables to physical properties, tools should ideally rely on full spatial and velocity forward modeling that accounts for the appreciable beam-smearing in high-redshift data and the limited S/N due to cosmological surface brightness dimming. Several packages have been developed to this aim, including the parametric modeling codes `Dysmal`/`DysmalPy` (e.g., R. I. Davies et al., 2004a,b; R. Davies et al., 2011; G. Cresci et al., 2009; S. Wuyts et al., 2016; P. Lang et al., 2017; S. H. Price et al., 2021), `GalPak`$^{\rm 3D}$ (N. Bouché et al., 2015; N. F. Bouché et al., 2022), and the non-parametric modeling code $^{\rm 3D}$`Barolo` (E. M. Di Teodoro & F. Fraternali, 2015)[1]. Parametric models are built around analytic descriptions of the mass distribution and/or the rotation and dispersion velocities (e.g., S. Courteau, 1997), making them inherently less sensitive to S/N than non-parametric models. Moreover, parametric modeling that starts from mass models enables an immediate characterization of the mass profile and quantifies the amount of gas involved in out- or in-flowing motions. On the other hand, non-parametric models have the advantage of more flexibility in a system's description, which may deviate from common functional forms due to non-axisymmetric features and kinematic perturbations (e.g., D. H. Rogstad et al., 1974; K. G. Begeman, 1989; R. Sancisi, 2004). Each code has its strengths and has been internally benchmarked against

---

[1] Other 3D-fitting tools exist, such as `TiRiFiC` (G. I. G. Józsa et al., 2007; P. Kamphuis et al., 2015), `KinMS` (T. A. Davis et al., 2013, 2017), GPU-accelerated `GBKFIT` (G. Bekiaris et al., 2016), `BLOBBY3D` (M. R. Varidel et al., 2019), and `qubefit` (M. Neeleman et al., 2021).

observations of local galaxies, mock analytical models, and/or numerical simulations.

All these tools, however, share a common advantage: they operate in full 3D space to generate models, thereby accounting for beam smearing and projection effects in the best possible way.

In this work, we expand on S. H. Price et al. (2021) by testing the `DysmalPy`'s performance in fitting in 3D, accompanied by the first public release of the code[2]. We additionally benchmarked `DysmalPy` against two widely-used modeling tools: the parametric `GalPak`$^{\mathtt{3D}}$ and the non-parametric $^{\mathtt{3D}}$`Barolo`. For this purpose, we employ an extensive set of synthetic galaxies with known input properties subjected to various realistic observational conditions. The mock galaxies consist of intentionally simple axisymmetric disk models but with an empirically motivated range of properties. The systematic inter-comparison expands on the validation tests for the individual codes presented by S. H. Price et al. (2021, see also R. Davies et al. 2011) for `DysmalPy`, N. Bouché et al. (2015) for `GalPak`$^{\mathtt{3D}}$, and E. M. Di Teodoro & F. Fraternali (2015) for $^{\mathtt{3D}}$`Barolo`. We use modeling setups as consistently as possible between the tools and discuss the impact of our adopted choices vs. recommended or widely used ones when they differ. We focus on fits performed in 3D for IFU and interferometric observations. `GalPak`$^{\mathtt{3D}}$ was designed to only fit in 3D, while $^{\mathtt{3D}}$`Barolo` could also fit a 2D velocity field through its `2DFIT` task. `DysmalPy` has mainly been applied to fit data in 1D or 2D (e.g., major axis kinematic profiles, moment maps), but by its 3D model construction was easily adapted to fit data cubes (S. H. Price et al., 2021).

The paper is organized as follows. In Sect. 2.2, we summarize the relevant features of the three fitting codes and describe the main setups employed in our analysis. In Sect. 2.3, we describe the construction of the baseline mock data cubes used in this study. In Sect. 2.4, we compare the fitting results between the codes with the baseline setups and mock data sets and explore more deeply the impact of parametrization and treatment of S/N. In Sect. 2.5, we discuss the potential implications in studies of high-z kinematics. In Sect. 2.6, we summarize our findings. Throughout, we assume a Λ-dominated cosmology with $H_0 = 70\ \mathrm{km\,s^{-1}\,Mpc^{-1}}$, $\Omega_\mathrm{m} = 0.3$, and $\Omega_\Lambda = 0.7$. For this cosmology, $1''$ corresponds to 8.37 kpc at $z = 2$.

---

[2] Available at `https://www.mpe.mpg.de/resources/IR/DYSMALPY/index.html`

Table 2.1. Comparisons between the three software used in this study.

Software	Parametric	$V_{\rm rot}$	σ	Optimizer	References
`DysmalPy`	Yes	axisymmetric mass model(s)	turbulence	`MPFIT`/MCMC	S. H. Price et al. (2021) and references therein
`GalPak`$^{\rm 3D}$	Yes	analytic functions	turbulence+thick disk+mixing	MCMC	N. Bouché et al. (2015)
$^{\rm 3D}$`Barolo`	No	free-form	free-form	Nelder-Mead	E. M. Di Teodoro & F. Fraternali (2015)

Note. — $^{\rm 3D}$`Barolo` parameterizes the scale-height as Gaussian, sech^2 or constant

2.2 Kinematic modeling codes and setups

Complete details of `DysmalPy`, `GalPak`$^{\mathtt{3D}}$, and $^{\mathtt{3D}}$`Barolo` can be found in the references below. For the comparisons, we focus on the recovery of the main kinematic properties: the intrinsic rotation velocity $v_{\rm rot}$ and local disk velocity dispersion σ. These properties are the ones that are most directly comparable between the codes. As we are primarily interested in exploring the impact of model parametrization and parametric vs. non-parametric approaches, we maximize consistency as follows: (i) we perform the fitting in 3D space, (ii) within the architecture of the codes, we use prior on parameters, minimization algorithms, masking and weighting schemes that are as similar as possible, and (iii) we keep the number of free parameters to a minimum.

For high-z observations, beam smearing is important, S/N is modest, and the morphology of the emission line tracing kinematics can be prominently irregular due to spatial variations in dust extinction, stellar population properties, and gas distributions. To mitigate these challenges, geometric parameters are typically fixed or tightly constrained through narrow priors and the morphology is not always directly used in the fitting (especially for parametric codes that typically assume smooth axisymmetric models). This also helps to reduce well-known degeneracies (e.g., between mass and inclination), which are compounded by low resolution. Therefore, in running all codes, we fixed the center, size parameter(s), inclination (i) along the line-of-sight, and position angle (PA) of the line of nodes on the sky plane.

This intentional choice of a few degrees of freedom is an ideal case; if other parameters are fitted simultaneously (with or without priors), the outcome of all codes will be less accurate. We have verified this by additionally allowing i and $R_{\rm e,d}$ to vary freely (for `DysmalPy` and `GalPak`$^{\mathtt{3D}}$), within ranges of $\pm15^\circ$ and $\pm20\%$, respectively, with initial guesses derived from the line intensity map. We find that there is no substantial improvement in fitting accuracy, and in some cases, there are more systematic offsets from the intrinsic values, while also resulting in reduced precision. More extensive exploration will be beneficial, but we consider it as a future study.

Table 2.1 summarizes the key differences between the three packages, and Table 2.3 in Appendix 2.7 lists the setups and parameters employed for each of them. For `DysmalPy` and $^{\mathtt{3D}}$`Barolo`, we initially follow their built-in masking routine, with specific settings listed in Table 2.3. Later in Sect. 2.4.6, we swap the masks between `DysmalPy` and $^{\mathtt{3D}}$`Barolo`, allowing us to explore the effects of using a common masking approach and to assess the impact of masking on the performance of each individual code.

2.2.1 `DysmalPy`

Main features

The `Python`-based `DysmalPy`, or its parent `IDL` version `Dysmal`, is a versatile forward-modeling tool based on multi-component mass models with a long history of development. It has been employed in near-IR/optical IFU and millimeter interferometric studies of disk galaxies at high-z (e.g., R. Genzel et al., 2006, 2011, 2014b, 2017, 2020, 2023; G. Cresci et al., 2009; S. Wuyts et al., 2016; A. Burkert et al., 2016; P. Lang et al., 2017; K.-i. Tadaki et al., 2017; H. Übler et al., 2018, 2019, 2021, 2024b; S. H. Price et al., 2021; R. Herrera-Camus et al., 2022; A. Nestor Shachar et al., 2023), and of local disks (e.g., R. I. Davies et al., 2009, 2014; E. Sani et al., 2012; F. Müller-Sánchez et al., 2013; M.-Y. Lin et al., 2016). `Dysmal` has been tested, especially regarding the recovery of velocity dispersion by R. Davies et al. (2011). S. Wuyts et al. (2016), A. Burkert et al. (2016), and P. Lang et al. (2017) significantly expanded it to incorporate an improved treatment of the effects of disk finite thickness and pressure gradients and to add DM halos to the family of possible mass components. H. Übler et al. (2018) adopted the `Python` version, introducing Markov chain Monte Carlo (MCMC) posterior sampling in addition to the original least-squares minimization. S. H. Price et al. (2021) presented a substantial upgrade, including a wide set of DM halo parametrizations, radial flow motions (to represent, for instance, bar-induced inflows or feedback-driven outflows), and the ability to tie model component parameters and fit in 3D space.

A detailed description of `DysmalPy`'s model construction and optimization is given by S. H. Price et al. (2021); we focus here on the aspects that are relevant to the present paper. `DysmalPy` is based on a mass distribution from which the kinematics are computed. Mass components are defined by azimuthally symmetric parametric functions, with flexibility in terms of their number and mass-to-light ratio (M/L), as well as a common center and inclination. Baryonic components are set up in the disk framework, whereas the DM halo is spherically symmetric (and contributes no light by definition). The total circular velocity $v_{\rm c}$ in the mid-plane is obtained from those of the individual mass components (summed in quadrature), computed in the spherical approximation ($v^2_{\rm circ}(r) = GM(<r)/r$, where G is the gravitational constant and $M(<r)$ is the enclosed mass), with options to account for disk geometry with finite thickness (via the prescriptions of E. Noordermeer 2008 for oblate flattened spheroids) as well as the effects of pressure gradients and DM halo adiabatic contraction (following the formulations of A. Burkert et al., 2010). The 3D model is cylindrical, with the mid-plane radial kinematics and structure assigned to all vertical layers, with a Gaussian light distribution of standard deviation h_z.

The velocity dispersion is assumed to be locally isotropic and radially uniform, representing a dominant turbulence term σ_0. This choice is motivated by the lack of evidence for clear trends with inclination and radius in high resolution, high S/N IFU observations of extended star-forming disks at $z \sim 1-3$. Typical inferred values are significantly in excess of predicted values at large radii for (exponential) disks in hydrostatic equilibrium with constant vertical scale height h_z, $\sigma_\mathrm{d}(R) = h_z V_\mathrm{rot}(R)/R$ (e.g., R. Genzel et al. 2011; H. Übler et al. 2019; D. Liu et al. 2023; but see also, e.g., F. Rizzo et al. 2020, 2021 and F. Lelli et al. 2021 for contrasting views).

The equilibrium assumption of `DysmalPy` is admittedly simple and cannot account for merger perturbations. However, the merger fraction is $\lesssim$20% at cosmic noon (P. Madau & M. Dickinson, 2014). On the other hand, disk accretion and violent disk instability can indeed perturb the system (A. Dekel et al., 2022), potentially impacting kinematic measurements. But (i) dynamics from stars and gas at cosmic noon (H. Übler et al., 2024a) are in good agreement, suggesting that in general the impact of such perturbations is not drastic; (ii) signatures of large dynamical perturbations would be evident in residuals (along with observed velocity fields deviating substantially from spider diagrams), providing sanity checks and ways to evaluate whether an object is well described by the equilibrium assumption or not.

With the ingredients above, `DysmalPy` generates the intrinsic composite model as a 4D hypercube, summing up the components accounting for projection according to the inclination, PA, and relative flux weighting. Each cell of the hypercube contains the total model flux in the "sky" coordinates (x_sky, y_sky, z_sky) and its full line-of-sight velocity distribution, which is then collapsed along z_sky and convolved with a 3D kernel folding in the spatial point spread function (PSF) and spectral line spread function (LSF). This procedure accounts for beam smearing, velocity resolution, and broadening of the line-of-sight velocity distribution due to projection effects. The convolved data cube is the basis for fitting the observations directly in 3D or 1D/2D by applying identical profile and map extraction methods between the model and data to ensure full consistency in their comparisons. The fitting can be performed through least-squares minimization via the Levenberg–Marquardt iterative search technique (using the routine `MPFIT`; C. B. Markwardt 2009), or in a Bayesian framework through affine invariant MCMC parameter space exploration (using the `emcee` implementation of D. Foreman-Mackey 2016)[3]. Masking and weighting schemes can be applied to exclude bad pixels, low S/N data, or any region as needed by a specific application and treat the impact of oversampling if relevant. In 2D or 1D, `DysmalPy` can constrain the

---

[3] `dynesty` (S. Koposov et al., 2023), a dynamic nested sampling algorithm as an alternative Bayesian inference method to `emcee`, is now also incorporated in `DysmalPy` version 2.0.0.

free parameters using either the observed flux, velocity, and velocity dispersion or solely the kinematics.

Adopted Setups

In this work, we use version 1.8.2 of `DysmalPy`[4]. We fit models consisting of a baryonic disk, bulge, and DM halo. While this choice is motivated by the set of mock galaxies created for our tests (described in Sect. 2.3), it also allows us to cover a wide enough range of realistic RC shapes. To match as closely as possible the workings of `GalPak`$^{\texttt{3D}}$ and $^{\texttt{3D}}$`Barolo`, we keep only a minimum of free parameters in the `DysmalPy` fitting: the total baryonic mass $M_{\rm bar}$, the (turbulent) disk velocity dispersion σ_0, and the DM mass fraction within the disk's effective radius $f_{\rm DM}(<R_{\rm e})$.

The disk component is parametrized as a Sérsic profile of index $n_{\rm d} = 1$ (exponential disk) adopted for all fits, with flattening $q_{\rm d}$ and effective radius $R_{\rm e,d}$ (henceforth $R_{\rm e}$) fixed to the particular values of the fitted mock model. Similarly, the bulge component is set with a Sérsic profile of $n_{\rm b} = 4$ (de Vaucouleurs) and flattening $q_{\rm b} = 1$ identical for all fits, and $R_{\rm e,b}$ fixed to those of the mock galaxy that is modeled.

For the baryonic components, the mass is treated as a flattened 3D deprojected Sérsic profile characterized by $R_{\rm e}$ and n_d. Their total mass is left free while their relative masses are tied through the bulge-to-total ratio (B/T) fixed to the mock model value. The two-parameter NFW (Navarro, Frenk, & White, 1996) DM halo profile option is used, with concentration parameter c set to that of the input mock model, and virial mass $M_{\rm vir}$ tied to the variable $f_{\rm DM}(<R_{\rm e})$; we do not apply adiabatic contraction in our fits. The inclination is also fixed to the value of the mock model.

We start from the E. Noordermeer (2008) parametrization with thick disk geometry and apply the A. Burkert et al. (2010) corrections to $v_{\rm c}$ to account for pressure support. We use the option for a self-gravitating exponential disk with constant velocity dispersion, such that

$$V^2_{\rm rot}(R) = V^2_{\rm circ}(R) - 3.36\sigma_0^2(R/R_{\rm e}). \tag{2.1}$$

The vertical Gaussian light weighting of the disk or bulge is controlled by the scale height h_z in `DysmalPy` and is through the inverse of q:

$$h_z \equiv R_{\rm e} \cdot q/\sqrt{2\ln 2}. \tag{2.2}$$

---

[4] The publicly available version is 2.0.0, but the main functionalities are the same, and the minor differences and improvements have no impact on our results.

The denominator accounts for the conversion of full width at half maximum (FWHM) to dispersion for a Gaussian thickness profile. h_z is fixed to the true value of the mock model. The RC is always extracted from the midplane for all radial and vertical (z-direction) positions, with the vertical Gaussian light weighting.

Given the simple axisymmetric light distribution of the mock models, we fit in 3D to account simultaneously for the morphology and kinematics. We use the least-squares minimization (`MPFIT`) option. This choice is adequate given the small number of free parameters ($N_{\rm free\,params} = 3$). S. H. Price et al. (2021) showed a very good agreement between results obtained with least-squares minimization and the Bayesian MCMC approach in `DysmalPy`. We do not apply weighting but use masking to exclude low S/N data in the fits. Specifically, we mask out entire spaxels with insufficient integrated line flux S/N (S/N < 3) to avoid fitting overly masked line profiles.

2.2.2 `GalPak`$^{\rm 3D}$

Main Features

`GalPak`$^{\rm 3D}$ (N. Bouché et al., 2015) is a `Python`-based parametric forward-modeling tool in a Bayesian framework. It was the first such public tool available[5] that was designed specifically for fitting disk models directly to 3D data cubes of high-redshift galaxies and has been applied in a variety of studies from optical to mm wavelengths (e.g., C. Péroux et al., 2013; R. Bacon et al., 2015; T. Contini et al., 2016; C. A. Mason et al., 2017; M. Girard et al., 2018; K.-i. Tadaki et al., 2018; C. E. Sharon et al., 2019; J. Zabl et al., 2019, 2020, 2021; N. F. Bouché et al., 2022; L. Hogan et al., 2021; S. Huang et al., 2023; A. Puglisi et al., 2023). The original conceptual approach differs from `DysmalPy` in that the models are defined by the light distribution and kinematics, returning best-fit parameters and rotation curves that can be used for subsequent mass decomposition modeling outside of `GalPak`$^{\rm 3D}$. The code was developed with an emphasis on applications to distant low-mass galaxies and extensively tested by N. Bouché et al. (2015); N. F. Bouché et al. (2021) using parametric axisymmetric models and numerical hydrodynamical simulations. N. F. Bouché et al. (2021, 2022) upgraded the code notably to expand the set of RC parametrizations and fitting algorithms and augment its capabilities to disk-halo mass decomposition in which a multi-component mass model is first generated and sets the kinematics (more similarly to `DysmalPy`). We focus below on `GalPak`$^{\rm 3D}$'s baseline framework where kinematics define the models.

---

[5] `https://galpak3d.univ-lyon1.fr/index.html`

`GalPak`^{3D} first creates a 2D model light distribution following a choice of Sérsic radial profile parametrizations in the disk plane and vertical Gaussian, exponential, or sech^2 profiles with thickness following Eqn. 2.2. Circular velocity cubes are generated that contain the velocity components in the disk plane from parametric RCs and propagating them to the vertical layers. Several functional forms are implemented, including notably an arctan, inverted exponential, or tanh profile, motivated by typical shapes of local disk RCs, and with turnover radius R_t and maximum intrinsic rotation velocity V_max as parameters[6]. The model is then rotated according to i and PA to create a cube in projected sky plane coordinates and in wavelength, using intermediate 2D projected flux, flux-weighted mean velocity along the line-of-sight, and total line-of-sight velocity dispersion σ_tot maps. The latter combines (i) the contribution from disk self-gravity $\sigma_\mathrm{d} = h_z\, V(r)/r$, (ii) a broadening term σ_s due to mixing of velocities along the line of sight for a thick disk and computed as the flux-weighted variance of the projected circular velocities along each sightline, (iii) and an isotropic and spatially constant term σ_0 to capture additional turbulence. The three terms are added in quadrature,

$$\sigma^2_\mathrm{tot}(R) = \sigma^2_\mathrm{d}(R) + \sigma^2_\mathrm{s}(R) + \sigma^2_0. \tag{2.3}$$

Throughout, for consistent comparison with other codes, we adopt the σ value at R_e of the above total dispersion profile for `GalPak`^{3D}. The rotated data cube is then convolved with the PSF and LSF. Fitting in 3D is performed in a Bayesian framework, with a choice of several MCMC samplers. No masking nor weighting schemes are performed by `GalPak`^{3D} (N. F. Bouché et al., 2021).

Key differences between `GalPak`^{3D} and `DysmalPy` model construction that we exploit for our analysis lie in the explicit parametrization of RCs in `GalPak`^{3D} and the treatment of velocity dispersion. The former implies different families of intrinsic RC shapes. We note that the options implemented implicitly account for the effects of a DM halo, as captured by the asymptotically flat behavior of the functions to large radii.

For the velocity dispersion, `DysmalPy` explicitly considers the full velocity distribution of each spatial coordinate from 4D space, encoding both circular velocity and (turbulent) dispersion before projection of the data in 3D space. `GalPak`^{3D} approximates line broadening due to projection solely from the circular velocities, adds self-gravity and turbulence terms assuming isotropic local dispersion, and then generates the line-of-sight velocity distribution. This procedure speeds up the code but assumes Gaussianity. `DysmalPy`'s approach preserves

---

[6] For completeness, the publicly available version also has an option to calculate the circular velocity in the spherical approximation using the light distribution as a proxy for mass.

higher-order moments. In practice, at modest to low S/N and for reasonably regular morphologies and kinematics, higher-order moments are difficult to discern, and the mixing term due to projection is usually small compared to the other terms, so these aspects have little impact on our analysis. More importantly, in the regime of low turbulence, the model dispersion profile in `GalPak`$^{\mathrm{3D}}$ exhibits an appreciable radial dependence from σ_{d} that is absent from current `DysmalPy` models.

Adopted Setups

We use the publicly available version 1.32.0 of `GalPak`$^{\mathrm{3D}}$. We employ an exponential disk profile (Sérsic model with $n = 1$) with Gaussian vertical distribution of thickness tied to the disk size by Eqn. 2.2, identical to the disk component assumed for the `DysmalPy` modeling. We use an arctan RC shape with turnover radius also tied to the galaxy size via $R_{\mathrm{t}} = 0.25\,R_{\mathrm{e}}$. The free parameters in our fits are the maximum rotation velocity $V_{\max}$ and the intrinsic turbulence term σ_0, assuming flat bounded priors. Other `GalPak`$^{\mathrm{3D}}$ input parameters are the center, R_{e}, i, and PA fixed to the values of each mock galaxy modeled. We adopt the default MCMC method in `GalPak`$^{\mathrm{3D}}$, which uses a Metropolis–Hasting (MH) algorithm and a Cauchy (or Lorentzian) proposal distribution that converges faster than a Gaussian distribution thanks to its broader wings. The maximum iteration is set to 3000, which is sufficient to pass the burn-in phase; tests with a subset of our mock sample show that increasing the number of iterations does not significantly change the results.

2.2.3 $^{\mathrm{3D}}$`Barolo`

Main Features

$^{\mathrm{3D}}$`Barolo`[7] (E. M. Di Teodoro & F. Fraternali, 2015) is a non-parametric modeling tool that extends the "tilted-ring" approach from its classical 2D applications in modeling high-resolution velocity fields (e.g., D. H. Rogstad et al., 1974; T. S. van Albada et al., 1985; K. G. Begeman, 1989; J. M. van der Hulst et al., 1992) to fitting full 3D observations of disk-like systems. It was developed for a wide range of applications to emission-line data cubes, with a special emphasis on lower-resolution data. It has been widely used in studies of galaxy kinematics at high-z (e.g., E. M. Di Teodoro et al., 2016; L. Fan et al., 2019; F. Loiacono et al., 2019; M. Bischetti et al., 2021; F. Fraternali et al., 2021; S. Fujimoto et al., 2021, 2025; G. C. Jones et al., 2021; G. Sharma et al., 2021, 2022, 2025; L. Hogan et al., 2022; F. Lelli et al., 2023; A. Pope et al., 2023; A. C. Posses et al., 2023; F. Rizzo

---

[7] Available at `https://editeodoro.github.io/Bbarolo/`

et al., 2023; F. Roman-Oliveira et al., 2023b) and low–z (e.g., G. Iorio et al., 2017; P. E. Mancera Piña et al., 2019; A. Bewketu Belete et al., 2021; N. Deg et al., 2022; M. Perna et al., 2022; Y.-C. Su et al., 2022; P. Biswas et al., 2023; Y. Cao et al., 2023). Continuous developments and testings have been made since the original tool release, notably to add the `pyBBarolo` `Python` wrapper running the `C++` core code, to incorporate the option of accounting for pressure support on rotational velocities (G. Iorio et al., 2017, available since version 1.3), and to improve estimates of geometric parameters (via the `CANNUBI`[8] `Python` script; F. Roman-Oliveira et al., 2023b).

$^{\mathrm{3D}}$`Barolo` constructs a 3D disk model as a series of concentric rings characterized by their radius and width, spatial center and systemic velocity $V_{\rm sys}$, inclination and PA, rotational velocity $V_{\rm rot}$ and velocity dispersion σ, face-on gas surface density, and scale-height z_0. All details and extensive testing of the impact of spatial and spectral resolution, inclination, and S/N with data of local galaxies and mock models are presented by E. M. Di Teodoro & F. Fraternali (2015). Complementary tests using zoom-in numerical cosmological simulations are presented by F. Rizzo et al. (2022). Our analysis extends these tests mainly by expanding the explored space to regimes of higher disk velocity dispersions.

In brief, the model generation in $^{\mathrm{3D}}$`Barolo` derives from the `GALMOD` routine (F. J. Sicking, 1997) incorporated in the `GIPSY` software environment (J. M. van der Hulst et al., 1992). Each ring is randomly populated via a Monte Carlo procedure by “clouds” represented as Gaussian point sources, drawn from uniform distributions in radius (within the ring width) and azimuth, and non-uniform vertical distributions (Gaussian, sech^2, exponential, Lorentzian, or top-hat). Each ring is rotated according to its i and PA. The observed velocity distribution along the line-of-sight is computed from the combination of systemic, rotational, and random motions, splitting the clouds at each location into sub-clouds distributed around the average velocity according to the sum-squared of dispersions accounting for intrinsic random motions and the LSF. The resulting model rings are individually convolved with a 2D Gaussian PSF and normalized such that the full model surface mass density matches the observed distribution (in column density, or light as a proxy) either on a spaxel-by-spaxel basis or to the azimuthally-averaged ring flux. Normalization can be disabled, allowing either a predefined functional form for the surface density distribution to be provided or leaving it free to be fitted along with the other parameters. The effects of pressure support, if chosen to be accounted for, are computed following the classical asymmetric drift formulation (e.g., S.-H. Oh et al., 2015; G. Iorio et al., 2017).

Fitting in 3D is performed ring-by-ring via the Nelder-Mead multidimensional downhill

---

[8] `https://www.filippofraternali.com/cannubi`

simplex solver for non-analytic functions (J. A. Nelder & R. Mead, 1965). At each ring, the sum of the residuals F over individual valid pixels is passed to the minimization algorithm. Valid pixels in 3D are identified based on the source finding results through the `DUCHAMP` algorithm (M. T. Whiting, 2012), and as those exceeding a flux threshold defined by the root-mean-square (rms) noise of the cube with or without prior smoothing.

There is an option to let $^{\rm 3D}$`Barolo` automatically estimate initial guesses and to perform regularization to avoid unphysical discontinuities in the returned best-fit radial profiles when geometrical parameters (i and PA) are left free. Residuals between model M and data D values can be computed as a pseudo-χ^2 $(M-D)^2/\sqrt{D}$, the absolute difference $|M-D|$, or as $|M-D|/(M+D)$ to upweight fainter emission regions. The minimized quantity F scales the residuals by $w(\theta) = |\cos(\theta)|^m$, where m can be 0 (unweighted sum of residuals), 1 or 2 (giving increasing weight to regions along the kinematic major axis defined as $\theta = 0$).

By construction, the tilted-ring approach and the 3D implementation of $^{\rm 3D}$`Barolo` leave many degrees of freedom. This allows, for instance, capturing non-axisymmetric features such as thin disk warping or other local irregularities in high-resolution rotation curves. As stressed by E. M. Di Teodoro & F. Fraternali (2015), this flexibility must be used with caution depending on the resolution, inclination, and S/N. In applications to high-z data, fixing global parameters (such as center and systemic velocity) and adopting radially constant inclination and PA may be necessary.

Adopted Setups

We use version 1.6 of $^{\rm 3D}$`Barolo` and perform the 3D fitting through the `3DFIT` task. To keep the setup as uniform as possible between the modeling tools considered in this paper, and similar to high-z studies using $^{\rm 3D}$`Barolo`, we fix the rings to identical centers, $V_{\rm sys}$, i, PA, and Gaussian vertical surface density distribution as in Eqn. 2.2, according to the values of each modeled mock galaxy. We set the radial bin width and separation to one-third of the beam FWHM size (corresponding to a physical scale of 0.228 kpc on average for our mock galaxies), and adopt local flux normalization (i.e., on a pixel-per-pixel basis). We verified that varying the bin widths to one-half to full-size of the beam has no significant statistical effect on the results, consistent with M. R. Varidel et al. (2019). $^{\rm 3D}$`Barolo` assumes the velocity dispersion within each ring to be isotropic. For the baseline runs, we choose a masking threshold of S/N = 3 from unsmoothed data, and uniformly weighted pseudo-χ^2 residuals as the closest analogs to the procedures in `DysmalPy` and `GalPak`$^{\rm 3D}$, and discuss the impact of these choices in detail in Sect. 2.4. The rings $V_{\rm rot}$ and dispersion σ are left

Table 2.2. Range of parameters of the mock galaxy models

Parameter	[5th,95th] percentile	Constrained by
z	$[0.72, 2.43]$	RC100
$\log(M_*/M_\odot)$	$[9.9, 11.1]$	RC100
$R_{\rm e,d}$ [kpc]	$[3.2, 9.2]$	A. van der Wel et al. (2014)
$R_{\rm e,b}$ [kpc]	$[0.5, 1.1]$	P. Lang et al. (2014)
B/T	$[0.08, 0.53]$	P. Lang et al. (2014)
σ_0 [$\rm km\,s^{-1}$]	$[16.2, 88.8]$	RC100
SFR [$M_\odot\,\rm yr^{-1}$]	$[7, 121]$	J. S. Speagle et al. (2014)
$\log(M_{\rm gas}/M_\odot)$	$[10.2, 11.4]$	RC100
$f_{\rm gas}$	$[0.31, 0.63]$	RC100
i [deg]	$[28.6, 75.0]$	RC100
$\log(M_{\rm vir}/M_\odot)$	$[11.5, 12.7]$	B. P. Moster et al. (2018)
c	[3.8, 7.1]	A. A. Dutton & A. V. Macciò (2014)
$\langle {\rm S/N}(< R_{\rm e})\rangle$	$[2, 21]$	RC100
PSF FWHM [$''$]	[0.2, 1.2]	RC100
$R_{\rm e}/\mathrm{beam}_{\rm HWHM}$	$[1.3, 5.4]$	RC100

Note. — PA and LSF are kept constant at 90° and $40\,\rm km\,s^{-1}$, respectively. Other parameters are also held fixed.

free to vary within bounded intervals ($[0, 400]\,\rm km\,s^{-1}$ and $[0, 150]\,\rm km\,s^{-1}$, respectively). We do not employ the asymmetric drift correction option because our focus is on comparing the recovery of the rotation velocity $V_{\rm rot}$ (corrected for inclination and resolution), not the circular velocity $V_{\rm circ}$.

2.3 Mock galaxies set

Our primary goal is to assess the 3D self-recovery performance of `DysmalPy`. We then take it a step further by comparing `DysmalPy`'s performance against other popular 3D modelling tools, which are `GalPak`$^{\tt 3D}$ (parametric) and $^{\tt 3D}$`Barolo` (non-parametric), to understand the factors that lead to any differences between the fitting results. We thus employ a baseline set of analytical axisymmetric model disk galaxies, with exact knowledge of the intrinsic kinematic parameters of interest, $v_{\rm rot}$ and σ_0, created by `DysmalPy`. We also create variants of this suite to explore the effects of irregularities in the light distribution and of different families of rotation and dispersion profiles.

In parametric modeling, a mismatch between the assumed model and reality is inevitable. Given that `GalPak`$^{\mathtt{3D}}$ and `DysmalPy` employ different templates for $V_{\rm rot}(R)$ and $\sigma(R)$, we also create a subset of mock models using `GalPak`$^{\mathtt{3D}}$ in Sect. 2.3.3 to investigate the impact of template mismatch on `DysmalPy`. In contrast, the non-parametric $^{\mathtt{3D}}$`Barolo` should not be restricted by specific templates. Our comparison of 1000 face-on mock cubes generated by `GALMOD` (the core routine of $^{\mathtt{3D}}$`Barolo`, see Sect. 2.2.3) and `DysmalPy`, sharing the same $V_{\rm rot}(R)$ and $\sigma(R)$ profiles, reveals that the differences between the two are negligible within $1.5R_{\rm e}$ ($\lesssim 5\%$), with discrepancies primarily attributed to numerical noise. Nevertheless, to complete the comparison, we repeat the same exercise with mock cubes generated by $^{\mathtt{3D}}$`Barolo` in Sect. 2.3.4.

In the following Sections, we outline the setup for generating the mock models using `DysmalPy`, `GalPak`$^{\mathtt{3D}}$ and $^{\mathtt{3D}}$`Barolo`. The number of mock galaxies generated exceeds the currently available observational data with comparable properties. It is clear that using models "blindly" on a large set of samples can be problematic. In reality, results should be examined critically on an individual basis. Initially, we began with a limited dataset but soon discovered that it was insufficient to properly identify systematic behaviours. To address this limitation, we expanded our mock sets while maintaining a minimal number of fitted parameters. We prioritized fixing parameters that are known to be observationally uncertain and have a significant impact on the outcome, such as the dynamical center, $R_{\rm e}$, PA, and inclination, as detailed in Sect. 2.2.

2.3.1 Baseline mock models with `DysmalPy`

To explore a realistic range of disk properties and observational parameters and to ensure a sufficiently large mock data set to identify statistical trends in the recovery analysis, we build a baseline set with 9000 mock galaxies guided by the properties of 100 $z \sim 1{-}3$ MS SFG(s), the "RC100" sample discussed by A. Nestor Shachar et al. (2023). This sample has high-quality 3D kinematics from deep observations (median on-source integration time of 10.7 hr) with typical S/N of 10 per pixel in the brightest channel averaged within $R_{\rm e}$, and FWHM angular resolution from $0\farcs2$ up to $1\farcs2$ (5th and 95th percentile). RC100 is drawn from the large parent sample of the KMOS$^{\rm 3D}$ + SINS/zC-SINF near-infrared IFU surveys targeting Hα emission and the PHIBSS+NOEMA$^{\rm 3D}$ millimeter interferometric surveys of CO emission, totaling ~800 galaxies that probe well the massive population at $0.6 < z < 2.6$ over nearly two orders of magnitude in stellar mass and SFR (N. M. Förster Schreiber et al., 2009, 2018; C. Mancini et al., 2011; L. J. Tacconi et al., 2013, 2018; E. Wisnioski et al., 2015, 2019; J. Freundlich et al., 2019).

The defining properties of the mock galaxy population are the stellar mass (M_*) and redshift (z), from which all other physical properties are obtained via scaling relations and accounting for their scatter in drawing values at fixed $M_\star$ and z. We use `DysmalPy` to create the model data cubes, constructing each galaxy as baryonic thick disk+bulge with total mass $M_{\rm bar} = M_\star + M_{\rm gas}$ embedded in a spherical Navarro, Frenk, & White (1996) DM halo. Table 2.2 lists the relevant parameters for the mock galaxies' construction, and Appendix 2.8 illustrates the match to the RC100 distributions in the main parameters.

We randomly draw 9000 times from the $M_\star$ and redshift distributions of RC100, split equally between the redshift ranges $z = [0.6, 1.1]$, $[1.15, 1.8]$, and $[1.9, 2.6]$ (for which Hα falls in the YJ, H, and K near-IR atmospheric bands). We set the SFR and gas-to-baryonic mass fraction $f_{\rm molgas}$ based on the relationships for SFR(M_*, z) from J. S. Speagle et al. (2014) and $f_{\rm gas}(M_*, z, {\rm SFR})$ from L. J. Tacconi et al. (2020). The DM halo virial mass and concentration are derived from the $M_\star - M_{\rm vir}$ and $c(M_{\rm vir},z)$ relationships of B. P. Moster et al. (2018) and A. A. Dutton & A. V. Macciò (2014), respectively. The effective radius of the disk is taken from the stellar mass-size relation of A. van der Wel et al. (2014). The (stellar) bulge mass is assigned following the B/T ratios relation of P. Lang et al. (2014). The bulge effective radius $R_{\rm e,b}$ is fixed at 1 kpc and it does not emit light. Given that the observed disk velocity dispersion exhibits primarily a trend with redshift, with a large scatter and no clear dependence on physical galaxy properties (e.g., H. L. Johnson et al., 2018; H. Übler et al., 2019), for each mock model, we assign the σ_0 of the galaxy in RC100 that most closely matches it in $M_\star$, SFR, and $f_{\rm molgas}$. The inclination i is drawn randomly from the RC100 distribution. Other parameters specifying the disk and bulge components are fixed or tied to those mentioned above as described in Sect. 2.2.1.

The model cubes are created on a grid with a spaxel size of $0.''125 \times 0.''125$ over a FoV of $6.''375 \times 6.''375$, and a velocity channel width of $10\,{\rm km\,s^{-1}}$ over the range $\pm 1000\,{\rm km\,s^{-1}}$. Since for the effects of beam smearing, the number of linear resolution elements across the source is most relevant, we assign the PSF FWHM by drawing from the RC100 distribution of $R_{\rm e}$/beam, where the beam is the PSF half-width at half-maximum (HWHM). This results in a mock data set covering $R_{\rm e}$/beam from 0.93 to 8.5 ([$5^{\rm th}$,$95^{\rm th}$] percentile = $[1.3, 5.4]$). The velocity resolution is fixed and represented by a Gaussian dispersion $\sigma_{\rm instrument} = 40\,{\rm km\,s^{-1}}$. The adopted velocity resolution is higher than the σ_0 of 37% galaxies in our baseline sample. However, only 6.5% of the galaxies have $\sigma_0 < 0.5\sigma_{\rm instrument}$ and the minimum $\sigma_0/\sigma_{\rm instrument} \sim 0.3$ affects $<$ 1% of the sample. As demonstrated by E. Wisnioski et al. (2015), the presence of galaxies with velocity dispersion below the spectral resolution limit in

IFU surveys is not uncommon and will amount to ~ 30–60% error (depending on the S/N) in the recovered velocity dispersion when the resolution decreases from $\sigma_{\rm intrinsic} \approx \sigma_{\rm instrument}$ to $\sigma_{\rm intrinsic} \approx 0.3\sigma_{\rm instrument}$, compared to 20% error when $\sigma_{\rm intrinsic} > \sigma_{\rm instrument}$. Finally, random Gaussian noise is added to the model cubes to match the RC100 S/N distribution, using our adopted definition of the average flux to rms noise ratio in pixels within $R_{\rm e}$ for the velocity channel with the brightest line emission.

2.3.2 Clumpy mock models

Disks at high redshift commonly exhibit prominently clumpy or irregular light distributions. To explore how the different modeling tools respond to light-weighting effects, we created an additional suite by adding two massless clumps into 400 of the baseline mock galaxies that lie at the higher ranges of $f_{\rm molgas}$ ($\geq 50\%$) and z ($\gtrsim 1$). This subset follows the SFR and $M_{\rm bar}$ distributions of the baseline sample. The clump sizes and brightnesses are motivated by observations of (unlensed) massive $z \sim 1-3$ SFG(s) (e.g., B. G. Elmegreen et al., 2005; R. Genzel et al., 2008; N. M. Förster Schreiber et al., 2011; S. Wuyts et al., 2012, 2013; Y. Guo et al., 2015), and are consistent with the Toomre scales predicted for gravitational instabilities in high-z gas-rich turbulent disks (e.g., R. Genzel et al., 2008; A. Dekel et al., 2009b). The clumps are represented by circular Gaussian light distributions with random contributions to the total light between 2% and 6%, and effective radii of $R_{\rm e,clump} = 0.5$ kpc. They are placed randomly at galactocentric radii $0.75R_{\rm e,d} < R < 2R_{\rm e,d}$, azimuthal angles in the range $[0, 2\pi]$ on the plane of the disk, and with a minimum azimuthal angle separation of 10°. The clumps are purely light sources with no intrinsic mass or kinematics. They co-rotate with the galaxy, and the velocity dispersion corresponds to that of the host galaxy at the same location. The two clumps always differ in luminosity to ensure the final model is asymmetric in light distribution. Examples are shown in Appendix 2.8.1 Fig. 2.15.

2.3.3 Mock models with `GalPak`$^{\rm 3D}$

To test the impact of the choice of analytical prescription in kinematic modeling, we also consider a set of 500 model cubes generated with `GalPak`$^{\rm 3D}$. For simplicity, we randomly draw this subset from the full baseline sample and use the best-fit parameters returned from the `GalPak`$^{\rm 3D}$ fitting as the "true values" to compare with in the recovery analysis. We generate the input model cube by introducing Gaussian noise to the noiseless best-fit model, which mirrors the baseline model with identical spatial and spectral sampling and already incorporates beam-smearing and spectral broadening. We verified that the resulting distributions in the galaxy and observational properties are similar to those of the full baseline mock sample in terms of the total baryonic mass, size, R_e/beam, i and S/N to avoid strong biases stemming from model properties in comparing the recovery performances.

2.3.4 Mock models with $^{3\mathrm{D}}$`Barolo`

To complete the comparison, we evaluate the performance of all codes using mock galaxies generated by $^{3\mathrm{D}}$`Barolo`. Similar to Sect. 2.3.3, we utilize the 500 best-fit model cubes returned by $^{3\mathrm{D}}$`Barolo` when fitting the baseline models. The resulting distributions of physical properties are similar to those of the baseline models. We select cubes corresponding to galaxies with original S/N $\gtrsim$ 20, as the best-fit profiles of $V_\mathrm{rot}(R)$ and $\sigma(R)$ returned by $^{3\mathrm{D}}$`Barolo` are better behaved and will serve as the new intrinsic reference profiles. The new intrinsic $V_\mathrm{rot}(R)$ profiles capture a variety of shapes, ranging from rising to declining profiles. However, the new intrinsic $\sigma(R)$ profiles are no longer constant but show mild declining trends, due to the S/N sensitivity of $^{3\mathrm{D}}$`Barolo` when modeling the baseline models, as will be discussed in Sections 2.4.2 and 2.4.5. Following the same approach as in Sect. 2.3.3, we reintroduce Gaussian noise into these noiseless models (projected, beam-smeared, and spectral-broadened) to achieve an S/N distribution similar to that shown in the last panel of Fig. 2.14 in Appendix 2.8.

2.4 Model comparisons

In this section, we examine the performance of each code in recovering the rotation velocity and disk velocity dispersion of the model galaxies. Throughout, we quantify the goodness of recovery through the ratio of the best-fit value returned by the modeling tool to the known intrinsic model value, i.e., $V_\mathrm{rot,model}/V_\mathrm{rot,intrinsic}$ and $\sigma_\mathrm{model}/\sigma_\mathrm{intrinsic}$. We exclude numerical catastrophic fits that do not converge in `DysmalPy` (indicated by the `MPFIT` status or when model values hit the prior boundaries) and `GalPak`$^{3\mathrm{D}}$. We also reject $^{3\mathrm{D}}$`Barolo` fits if there are fewer than 3–4 consecutive successfully modeled rings. The latter is a conservative choice but allows us to investigate recovered radial trends. On average, all three tools achieve $\sim 80\%$ (~ 7000 of the initial 9000 baseline models) successful fits of the mock sample. The S/N, R_e/beam, i, and σ_0 distributions of the successfully modeled sample are shown in the side panels of Fig. 2.16 in Appendix 2.8.2. All three tools share very similar distributions of these parameters. However, due to variations in the consideration of catastrophic fits among different codes, the final effective samples differ. Specifically, $^{3\mathrm{D}}$`Barolo` has the fewest retained fits ($\sim$70%), most notably at low S/N and R_e/beam. Consequently, the effective

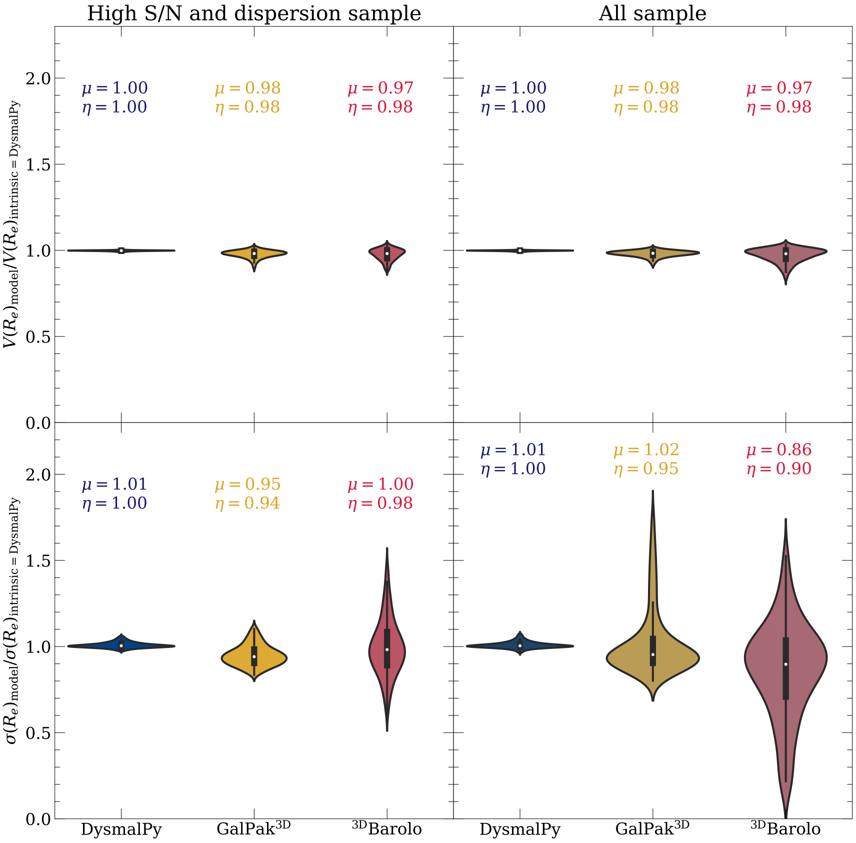

Figure 2.1 Comparison of the best-fit properties derived at the effective radius R_{e} from modeling the baseline mock data set with `DysmalPy`, `GalPak`$^{\mathrm{3D}}$, and $^{\mathrm{3D}}$`Barolo`. The results are illustrated via violin plots of the ratios of recovered to intrinsic rotation velocity $V_{\mathrm{model}}(R_{\mathrm{e}})/V_{\mathrm{intrinsic}}(R_{\mathrm{e}})$ (*upper row*), and recovered to intrinsic disk velocity dispersion $\sigma_{\mathrm{model}}(R_{\mathrm{e}})/\sigma_{\mathrm{intrinsic}}(R_{\mathrm{e}})$ (*lower row*). The mean μ and median η of each distribution is given in the plots. The *first column* shows results from samples that are less susceptible to template mismatch and signal-to-noise ratio (S/N) sensitivity issues specifically for `GalPak`$^{\mathrm{3D}}$ and $^{\mathrm{3D}}$`Barolo`, in which all codes demonstrate good recovery performance with $\mu \approx \eta \approx 1$. For the entire sample in the *second column*, the rotation velocity is still very well recovered by all three packages. The largest differences are in velocity dispersion and mainly in the scatter and asymmetry of the distributions. By construction, the properties of the baseline `DysmalPy`-generated mock data cubes are best recovered by `DysmalPy`.

samples of `DysmalPy` and `GalPak`$^{\mathrm{3D}}$ include more of the low-S/N and poor-resolution mocks.

We stress that the v_{rot} refers to the intrinsic rotation velocity, corrected for beam-smearing and inclination but not for pressure support, in order to keep the comparison as simple and consistent as possible between the modeling tools. The value of v_{rot} is directly output by all three tools. For the velocity dispersion, we adopt in all cases the total intrinsic σ corrected for the effects of beam smearing, projection, and velocity resolution. As described in Sect. 2.2, the total intrinsic σ at a given radius R corresponds to the global and radially constant σ_0 for `DysmalPy`, to the sum of disk self-gravity, line-of-sight velocity mixing, and constant turbulence for `GalPak`$^{\mathrm{3D}}$, and to the total velocity dispersion interpolated from the two closest rings to R for $^{\mathrm{3D}}$`Barolo`. These differences in implementation play a role in the results as discussed below, but beyond the fitting exercise. They also imply a different physical interpretation of the recovered dispersion that should be kept in mind.

2.4.1 Overall recovery of the baseline models

We begin by considering the rotation velocity and velocity dispersion recovered at the disk effective radius (R_{e}) for the baseline set of mock data cubes. As velocity and dispersion are not described by parametric functions in $^{\mathrm{3D}}$`Barolo`, comparing parametric modeling results from `DysmalPy` and `GalPak`$^{\mathrm{3D}}$ is less straightforward. For the rotation velocity, we use the returned intrinsic V_{rot} at R_{e} (linearly interpolated from the two nearest annuli). For the velocity dispersion, we measure the value at R_e to ensure consistency across codes. As shown in the top panel of Fig. 2.1, all three tools overall perform very well for $v_{\mathrm{rot}}(R_{\mathrm{e}})$, which is recovered within $<5\%$ in the mean μ and median η, and with small scatter of <0.04. In contrast, the distributions have larger scatter and are more asymmetric for $\sigma(R_{\mathrm{e}})$. The `GalPak`$^{\mathrm{3D}}$ results tend to underestimate the intrinsic values by 5% in the median, with a more pronounced tail extending to $\sigma_{\mathrm{model}}(R_{\mathrm{e}})/\sigma_{\mathrm{intrinsic}}(R_{\mathrm{e}})>1$ and 13% of the sample lying above one standard deviation (SD) of the mean. The velocity dispersion recovered by $^{\mathrm{3D}}$`Barolo` is $\sim 90\%$ (mean and median) of the input values, with a more extended tail towards lower values and 16% of the sample 1 SD below the mean. `DysmalPy` performs best for both v_{rot} and σ, which is unsurprising given the `DysmalPy`-generated baseline mock data set and simply reflects the better match in intrinsic and model parametrizations. The tests carried out here use the 3D-space fitting functionality of `DysmalPy`, and thus extend the validation tests performed in 1D and 2D presented by R. Davies et al. (2011) and S. H. Price et al. (2021).

2.4.2 Trends with input parameters

Next, we investigate the dominant source of scatter and asymmetry in the recovery results for the baseline data set. We searched for trends in $V_{\rm model}(R_{\rm e})/V_{\rm intrinsic}(R_{\rm e})$ and $\sigma_{\rm model}(R_{\rm e})/\sigma_{\rm intrinsic}(R_{\rm e})$ with observational parameters and galaxy physical properties, based on the Spearman's rank correlation coefficient (ρ; C. Spearman, 1904) as well as visual inspection. However, as ρ is only sensitive to monotonic trends between variables, it may not capture all possible relationships. To address this limitation, we also compare our results to the Maximal Information Coefficient (MIC) (D. N. Reshef et al., 2011), which is more adept at detecting non-single-valued functions. The MIC scores mostly agree with ρ in terms of identifying the stronger trends in our results. Therefore, we will only report ρ henceforth. The S/N, i, angular resolution, and intrinsic velocity dispersion have the largest impact on our results, consistent with previous findings from validation tests (e.g., R. Davies et al., 2011; N. Bouché et al., 2015; E. M. Di Teodoro & F. Fraternali, 2015). We thus focus on these four parameters.

Figs. 2.2 and 2.3 show 2D histograms of the distributions of recovered to intrinsic $v_{\rm rot}$ and σ (at $1R_{\rm e}$) as a function of intrinsic velocity dispersion for the full sample (excluding catastrophic fits). Different curves are overplotted to illustrate the running median trends of subsets split in terms of (i) S/N, (ii) inclination i, and (iii) $R_{\rm e}$/beam, with error bars showing 68% confidence intervals derived from bootstrapping. The dividing values correspond to the sample median values of $\mathrm{S/N} = 11$, $i = 52°$, and $R_{\rm e}/\mathrm{beam} = 3$. The variations of standard deviations are also plotted. Fig. 2.18 in Appendix 2.10 report the Spearman's ρ between the ratios $\sigma_{\rm model}(R_{\rm e})/\sigma_{\rm intrinsic}(R_{\rm e})$ and the S/N, i, $R_{\rm e}$/beam, and intrinsic σ. Fig. 2.4 is similar to Figs. 2.2 and 2.3, but shows instead the distributions of recovered to intrinsic σ vs. (i) S/N, (ii) inclination i, (iii) $R_{\rm e}$/beam and (iv) intrinsic σ directly. For the baseline models under comparison, only the light green curves (labeled $\sigma(R_{\rm e})_{\rm mock=DysmalPy}$) are pertinent. Other trends will be addressed in subsequent sections.

Rotation velocity

Fig. 2.2 indicates that there is overall a minor impact of the parameters considered on the recovered $V_{\rm rot}(R_e)$. $R_{\rm e}$/beam has the largest impact on the results, causing the slight tail towards lower values in $V_{\rm rot}(R_e)$ for `GalPak`$^{\rm 3D}$ and $^{\rm 3D}$`Barolo` in Fig. 2.1, but this is a very small effect. In our tests, the reliability of all three tools in recovering $v_{\rm rot}(R_{\rm e})$ is fairly robust against varying S/N over the range explored. Closer inspection shows that at lower S/N, the scatter becomes larger for $^{\rm 3D}$`Barolo` for which the standard deviation in $V_{\rm model}(R_{\rm e})/V_{\rm intrinsic}(R_{\rm e})$ increases from $\mathrm{SD} = 0.04$ at $\mathrm{S/N} \gtrsim 11$ to 0.09 at $\mathrm{S/N} < 11$.

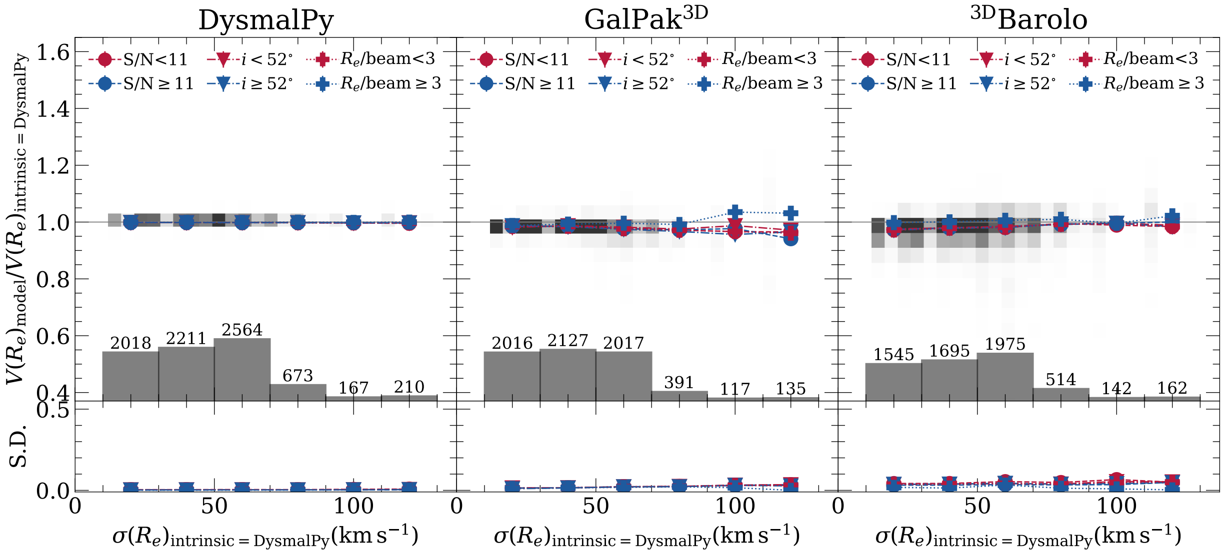

Figure 2.2 Comparison of best-fit to intrinsic rotation velocity derived at R_e from modeling the baseline mock models with `DysmalPy` (*left*), `GalPak`^{3D} (*middle*) and ^{3D}`Barolo` (*right*). The $V_\mathrm{model}(R_\mathrm{e})/V_\mathrm{intrinsic}(R_\mathrm{e})$ is plotted as a function of the `DysmalPy` model intrinsic (and radially constant) velocity dispersion σ_0. The gray-scale background image illustrates the density distributions of the full set of models, and the overplotted curves correspond to running median trends for different subsets split by S/N, inclination, and R_e/beam as labeled in each panel. Error bars associated with the data points are the 68% confidence interval for the medians derived from bootstrapping. The gray histograms give the number of galaxies included in each $\sigma(R_e)$ bin. The panels in the *bottom* row are the associated standard deviation (S.D.) values of each $\sigma(R_e)$ bin for each subset. Overall, all three modeling tools recover well the intrinsic $v_\mathrm{rot}(R_\mathrm{e})$, with no significant dependence on S/N, disk inclination, and angular resolution in the regimes tested by our models.

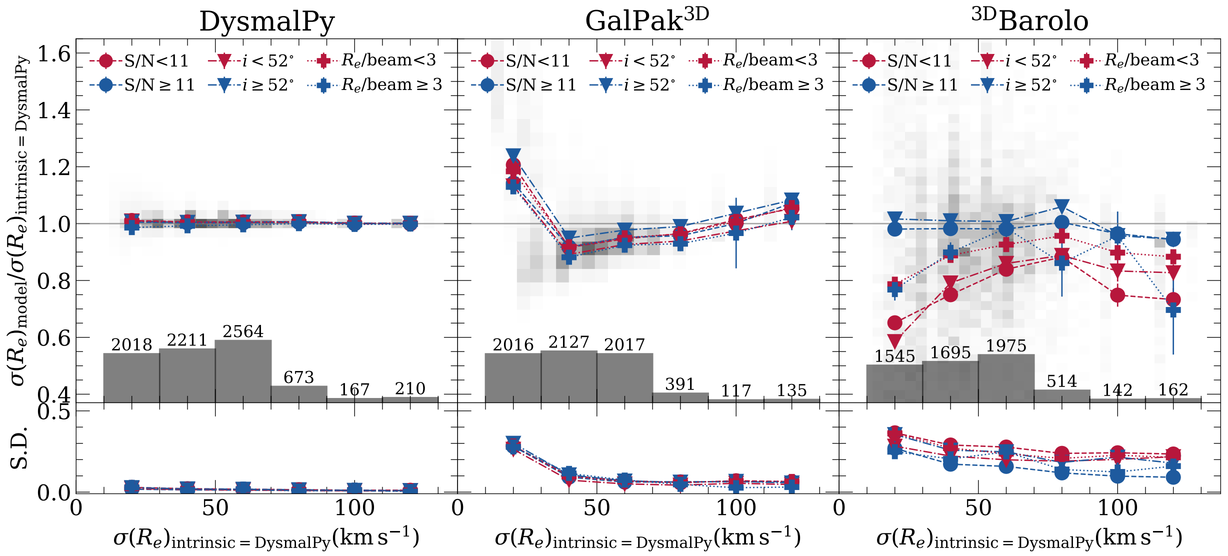

Figure 2.3 Similar to Figure 2.2, but for the ratio of $\sigma_{\mathrm{model}}(R_{\mathrm{e}})/\sigma_{\mathrm{intrinsic}}(R_{\mathrm{e}})$ as a function of `DysmalPy`-generated model intrinsic velocity dispersion σ_0. The large typical overestimate by `GalPak`$^{\mathrm{3D}}$ at the lowest σ_0 values is a direct result of the template mismatch between the constant and radially varying profiles adopted by `DysmalPy` and `GalPak`$^{\mathrm{3D}}$, respectively. This effect is much reduced as σ_0 increases and there is little dependence on S/N, i, and R_{e}/beam. For $^{\mathrm{3D}}$`Barolo` the curves show that the large scatter reflects, in part, a fairly strong dependence on S/N and i.

Velocity dispersion

Fig. 2.3 shows stronger trends in median recovered velocity dispersion with different behavior for `GalPak`$^{\mathrm{3D}}$ and $^{\mathrm{3D}}$`Barolo`. For `DysmalPy`, the weak or absent trends in median values and for different subsets are partly attributable to the match in parametrization between mock models and fitted models. Taken at face value, the R_{e}/beam may play the most important role, but the correlation is weak ($\rho = 0.24$).

For `GalPak`$^{\mathrm{3D}}$, the strongest sensitivity is to the intrinsic dispersion. The most salient feature is the "L-shaped" trend with an upward tail at $\sigma_0 < 30\,\mathrm{km\,s^{-1}}$ regardless of S/N, i, and R_{e}/beam. About a quarter ($\sim 26\%$) of the baseline sample falls into this regime and is the main cause of the asymmetric distribution in Fig. 2.1. The overestimated dispersion at low $\sigma_{\mathrm{intrinsic}}$ is the direct consequence of the different velocity dispersion parametrizations between `GalPak`$^{\mathrm{3D}}$ and `DysmalPy`. To visualize this behavior, in Fig. 2.5 we compare the profiles (corrected for beam smearing) of the best-fit `GalPak`$^{\mathrm{3D}}$ models for two baseline mock data sets with high $\sigma_0 = 53\,\mathrm{km\,s^{-1}}$ and low $\sigma_0 = 13\,\mathrm{km\,s^{-1}}$. At higher velocity dispersion, the radially-dependent σ_{d} term is sub-dominant, and `GalPak`$^{\mathrm{3D}}$ better matches the uniform dispersion through its radially-constant turbulent term. On the other hand, when σ_0 is low `GalPak`$^{\mathrm{3D}}$ has more difficulty recovering the value around R_{e} because σ_{d} more strongly dominates out to larger radii.

For ^{3D}`Barolo`, the recovered $\sigma(R_e)$ is comparably affected by S/N and i, typically leading to an underestimate of the intrinsic velocity dispersion driving the asymmetric distribution shown in Fig. 2.1. Although globally, there is only a weak correlation with median intrinsic σ, the results for the $S/N < 11$ and $i < 52°$ subsets exhibit a stronger dependence with more pronounced downturns at both low and high dispersion ends. That both S/N and i can affect ^{3D}`Barolo` modeling results have been discussed previously (e.g., E. M. Di Teodoro & F. Fraternali, 2015; C. Bacchini, 2020; N. Deg et al., 2022). The sensitivity to intrinsic σ could be related to these two factors. At higher velocity dispersions, the line flux is spread over more velocity channels, resulting in a lower S/N per pixel in the brightest channel (our adopted definition of S/N). At lower velocity dispersions, the line emission gets narrower, especially at lower inclinations, potentially leading to the overmasking of line wings in velocity from the ^{3D}`Barolo` algorithm and underestimating the line width. Masking effects are discussed in more detail in Sect. 2.4.6 (see also R. Davies et al., 2011).

For all three tools, we find little difference in the median trends as a function of angular resolution but note that this could be due to the limited range probed by our mock models: the R_e/beam varies only from 1.4 to 7.2, with a median of 3. For ^{3D}`Barolo`, these results are consistent with a very modest dependence on the angular resolution for similar ranges of R_e/beam reported by E. M. Di Teodoro & F. Fraternali (2015) and F. Rizzo et al. (2022), based on different test models.

The tightness of the distributions is different between the three tools, as evidenced by the lower panels in Fig. 2.3. The scatter systematically decreases from low to high S/N and angular resolution regimes mainly for `DysmalPy` and ^{3D}`Barolo`. For `DysmalPy`, the scatter (in standard deviation) ranges from ~ 0.06 at $S/N < 11$ and $R_e/\mathrm{beam} < 3$ to ~ 0.03 at $S/N > 11$ and $R_e/\mathrm{beam} > 3$. For ^{3D}`Barolo`, the corresponding drop is from about 0.36 to 0.23 as S/N increases, with comparable scatter from low to high R_e/beam. There is no significant change in scatter for either parameter in `GalPak`^{3D}.

2.4.3 Light-weighting effects tested with clumps

One of the potential advantages of ^{3D}`Barolo` over `DysmalPy` and `GalPak`^{3D} is that its surface brightness distribution can take an arbitrary form, whereas `DysmalPy`[9] and `GalPak`^{3D} assume a smoothly varying and axisymmetric analytic distribution. Since accounting for the effects of beam smearing is driven by the smearing of the underlying flux profile, if

---

[9] `DysmalPy` is capable of modeling clumps, but here we are interested in benchmarking its performance against `GalPak`^{3D} which offers smooth model only.

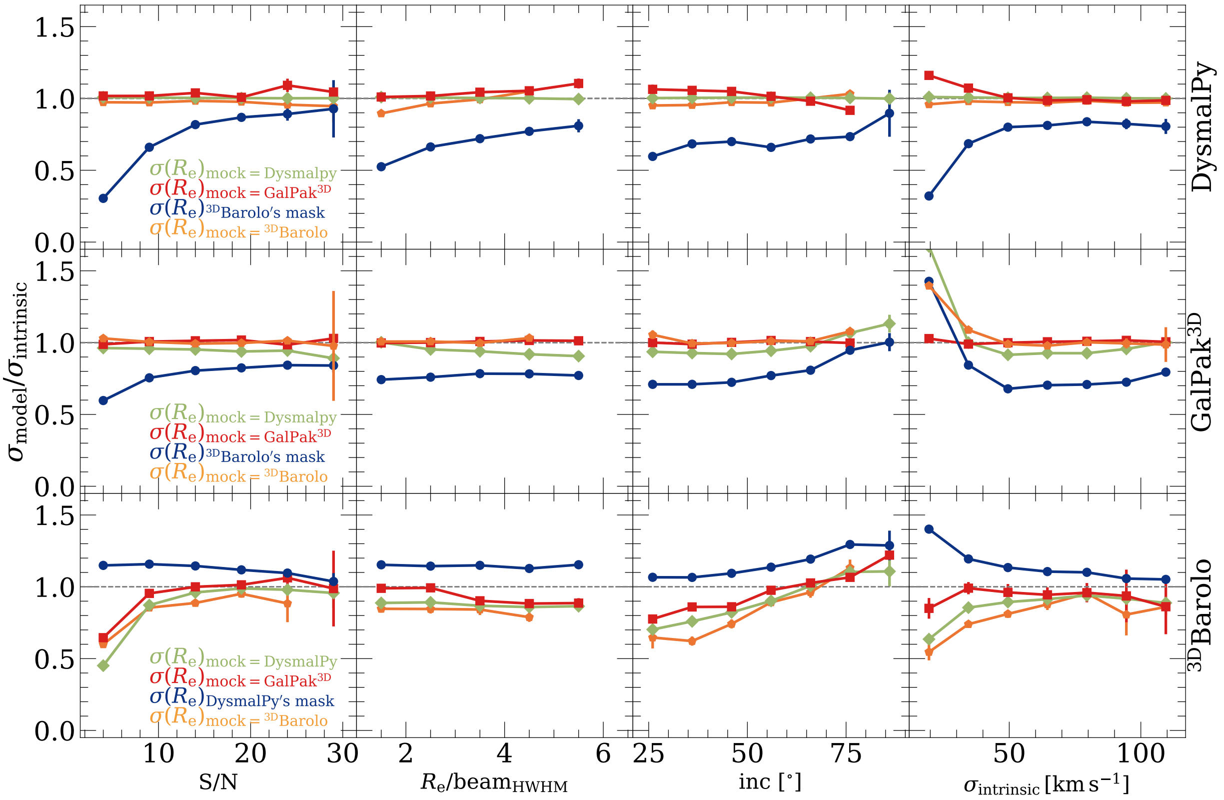

Figure 2.4 An expansion of Figure 2.3 to show the ratios of recovered ($\sigma_{\rm model}$) and intrinsic ($\sigma_{\rm intrinsic}$) velocity dispersions against 4 different parameters, signal-to-noise ratio (S/N) (*first column*), ratio between the effective radius and beam in half-width-half-maximum (HWHM) (*second column*), inclination (i) (*third column*) and intrinsic dispersion ($\sigma_{\rm intrinsic}$) (*fourth column*). Intrinsic values correspond to baseline models unless specified by "mock=`GalPak`$^{\rm 3D}$" or "mock=$^{\rm 3D}$`Barolo`". In such case, $\sigma_{\rm intrinsic}$ would be the value taken at R_e of the total intrinsic dispersion profile of `GalPak`$^{\rm 3D}$ or $^{\rm 3D}$`Barolo`, respectively. The colored curves are the running median of their corresponding distributions as labeled, with errors representing 68% confidence interval derived by bootstrapping. $^{\rm 3D}$`Barolo`-recovered $\sigma_{\rm model}$ shows positive dependence on i and S/N, with the latter converging to the intrinsic values when S/N $\gtrsim 8$. For comparison, we show the same plot with only S/N ≥ 11 mocks in Figure 2.19 in Appendix 2.11. Trends persist across different $\sigma_{\rm model}$ definitions, even with `GalPak`$^{\rm 3D}$- or $^{\rm 3D}$`Barolo`-generated models. The source of such S/N dependence is due to $^{\rm 3D}$`Barolo` spectral overmasking, and if the same masking is applied to `DysmalPy` and `GalPak`$^{\rm 3D}$ when modeling, a similar asymptotic trend (light green curves) is also recovered. S/N dependency in $^{\rm 3D}$`Barolo` vanishes (although now with systematic overestimate) when `DysmalPy`'s masking is adopted. Dependence on i persists nevertheless. `GalPak`$^{\rm 3D}$ and `DysmalPy` show negligible S/N and $R_{\rm e}$/HWHM dependencies. Dependency on $\sigma_{\rm intrinsic}$ is attributed to template mismatch, as detailed in the main text.

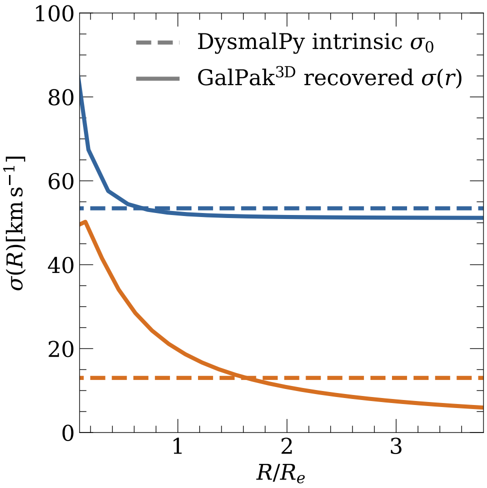

Figure 2.5 Examples of velocity dispersion profiles $\sigma(r)$ derived by `GalPak`^{3D} (*solid*) (beam-smearing corrected) and the intrinsic profiles (*dashed*) of two mock samples at high (*orange*) and low (*blue*) intrinsic dispersion constructed by `DysmalPy`. In high intrinsic dispersion conditions, `GalPak`^{3D}'s dispersion profile coincides with the intrinsic dispersion value around R_e, while in low intrinsic dispersion conditions, the radially dependent disk self-gravity term dominates and causes the intrinsic dispersion value at R_e to be overestimated compared to a model that adopts a flat intrinsic dispersion profile.

the underlying flux distribution is clumpy, `DysmalPy` and `GalPak`^{3D} may recover the main kinematic properties less accurately. We focus on the velocity dispersion, which is the property most sensitive to modeling approach and tool. We find similarly good performance in $v_{\rm rot}$ recovery among the three codes as in the case of the smooth mocks.

We present the recovery performance of the three codes in $\sigma_{\rm model,clumpy}/\sigma_{\rm intrinsic}$ for comparison with the smooth mocks $\sigma_{\rm model,smooth}/\sigma_{\rm intrinsic}$ in 1D histograms along the y- and x-axes of Fig. 2.6, respectively. The systematic scatter between the two cases is comparable for `GalPak`^{3D} and ^{3D}`Barolo`, while `DysmalPy` exhibits slightly more overestimation in the case of clumpy galaxies compared to smooth galaxies. To isolate the pure effect of asymmetric light distribution introduced by light clumps versus axisymmetric effects, we consider light clumps to affect the model fitting if $\sigma_{\rm model,clumpy}/\sigma_{\rm intrinsic}$ differs from $\sigma_{\rm model,smooth}/\sigma_{\rm intrinsic}$ by more than the average fitting error of the same galaxy returned by the respective code. In Fig. 2.6, those outside the shaded region around the one-to-one line would meet this criterion. Data points are color-coded based on the primary factor that most strongly correlates with the σ recovery: $\sigma_{\rm intrinsic}$ for `GalPak`^{3D}, and S/N for ^{3D}`Barolo`.

Of the three tools, `DysmalPy` is the most affected by light clumps, with $\sim 30\%$ of the models differing by more than the fitting error. They tend to happen for intrinsically low dispersion. The fraction drops to $\sim 12\%$ and $\sim 5\%$ for `GalPak`^{3D} and ^{3D}`Barolo`, respectively.

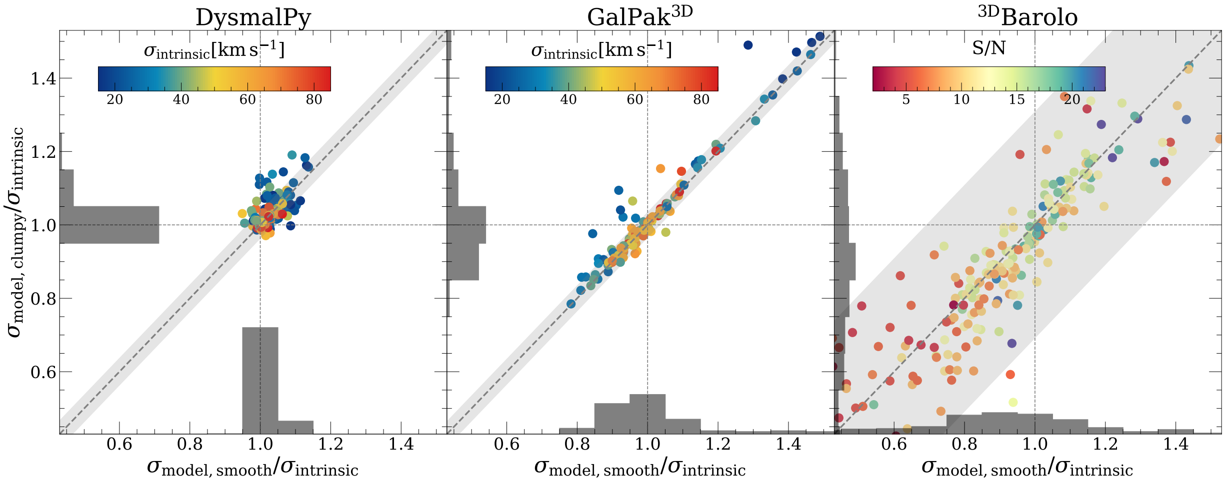

Figure 2.6 Comparison plots of velocity dispersions recovered from clumpy mock galaxies ($\sigma_{\rm model,clumpy}$) and those from smooth galaxies with otherwise identical properties ($\sigma_{\rm model,smooth}$) by `DysmalPy` (*left*), `GalPak`$^{\rm 3D}$ (*middle*) and $^{\rm 3D}$`Barolo` (*right*). The gray histograms along the x- and y-axis are the distributions of ratios between the recovered and intrinsic values for smooth and clumpy galaxies, respectively. The colors of the points represent the intrinsic velocity dispersion ($\sigma_{\rm intrinsic}$) in the *left* and *middle* panels, while the *right* panel shows signal-to-noise (S/N). The choice of colors for `GalPak`$^{\rm 3D}$ and $^{\rm 3D}$`Barolo` is determined by the parameters that exhibit the strongest correlation with the recovered σ in the smooth galaxies sample. The shading around the one-to-one line represents the typical fitting errors of the respective codes. The points that lie along the one-to-one line are those not affected by the presence of clumps, and those lying outside the shading are more affected. For `DysmalPy`, `GalPak`$^{\rm 3D}$, and $^{\rm 3D}$`Barolo`, roughly 30%, 12%, and 5% of the points lie outside the shaded regions, respectively. In other words, *relative to their typical fitting uncertainties*, the parametric models are more affected by light clumps. As for the smooth axisymmetric models, the scatter for the non-parametric modeling is larger towards lower S/N.

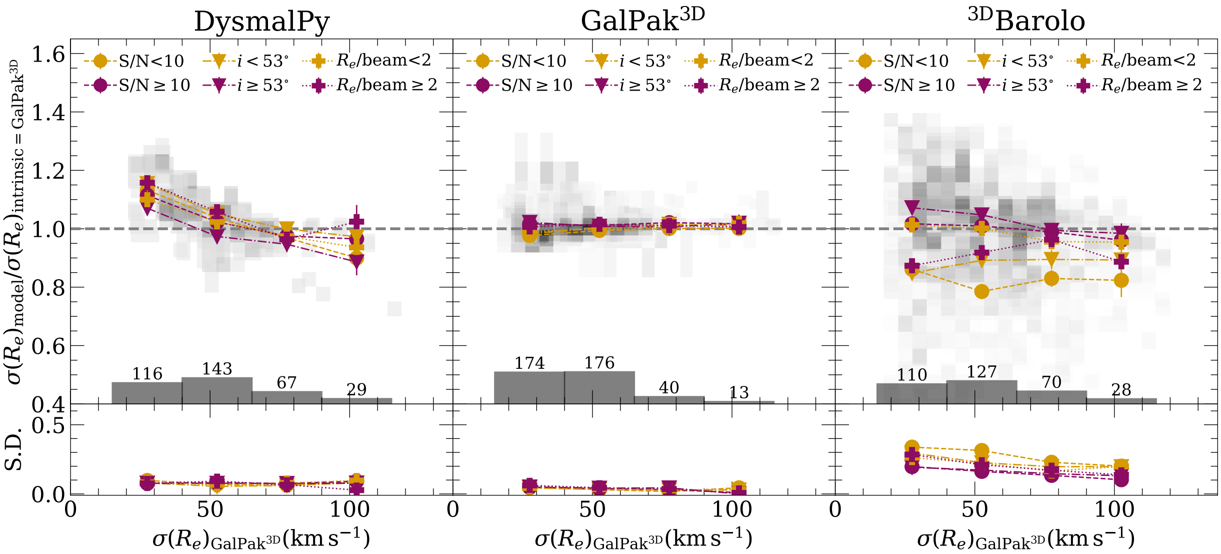

Figure 2.7 Similar to Fig. 2.3, but for `GalPak`^{3D} generated mocks. Due to the inherent template mismatch between `DysmalPy` and `GalPak`^{3D} as explained in the main text, `DysmalPy` in the *left* panel tends to overestimate the dispersion values when the intrinsic values are low, whereas `GalPak`^{3D} could accurately recover the intrinsic values at all ranges. In the *right* panel, ^{3D}`Barolo` shows a similar behavior as before, with a comparable dependence on the signal-to-noise, but with an overall better recovery when compared to Figure 2.3.

The scatter, however, is large for ^{3D}`Barolo`. Although ^{3D}`Barolo` is less systematically affected by clumps relative to the fitting errors, it is also less accurate in our recovery exercise. In cases of clumpy galaxies, the Bayesian kinematic modeling tool `Blobby3D` (M. R. Varidel et al., 2019; M. Varidel & S. Croom, 2023) could be a potentially preferable choice, as it was more specifically designed to treat irregular clumpy systems. Testing this code against others, as done here, would be valuable but is beyond the scope of this paper.

2.4.4 Impact of parametrization

We now examine the results when using `GalPak`^{3D}-generated mock data sets. We focus on the recovery of the velocity dispersion around R_e to compare the performance of the codes when galaxies have a radially-dependent dispersion. The results are plotted in Fig. 2.7, where the reference model intrinsic dispersion $\sigma(R_e)_\mathrm{gp}$ now corresponds to the total dispersion at R_e including the hydrostatic equilibrium, line-of-sight velocity mixing, and turbulence terms (Eqn. 2.3) but excluding any broadening by beam smearing. For convenience, we denote the results from modeling the `GalPak`^{3D} mock models with `DysmalPy`, `GalPak`^{3D}, and ^{3D}`Barolo` below as dy(gp), gp(gp), and bb(gp), and those from modeling the `DysmalPy`-generated

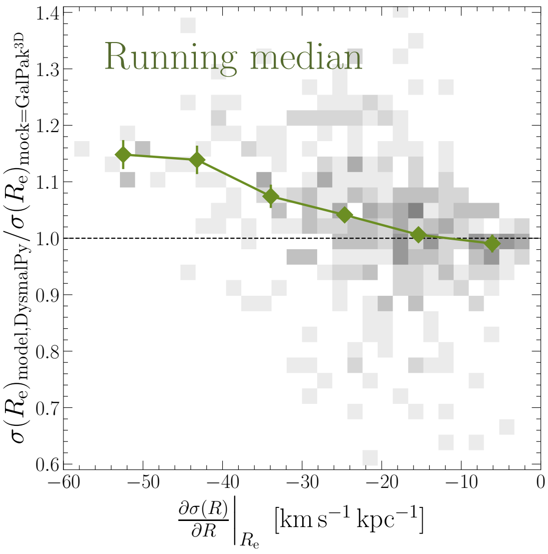

Figure 2.8 Similar to the leftmost panel of Figure 2.7, but with no distinction on signal-to-noise, inclination and resolution. The x-axis is replaced by the gradient of the intrinsic `GalPak`$^\mathtt{3D}$ dispersion profile at the effective radius R_e: $\frac{\partial\sigma(R)}{\partial R}\Big|_{R_\mathrm{e}}$.

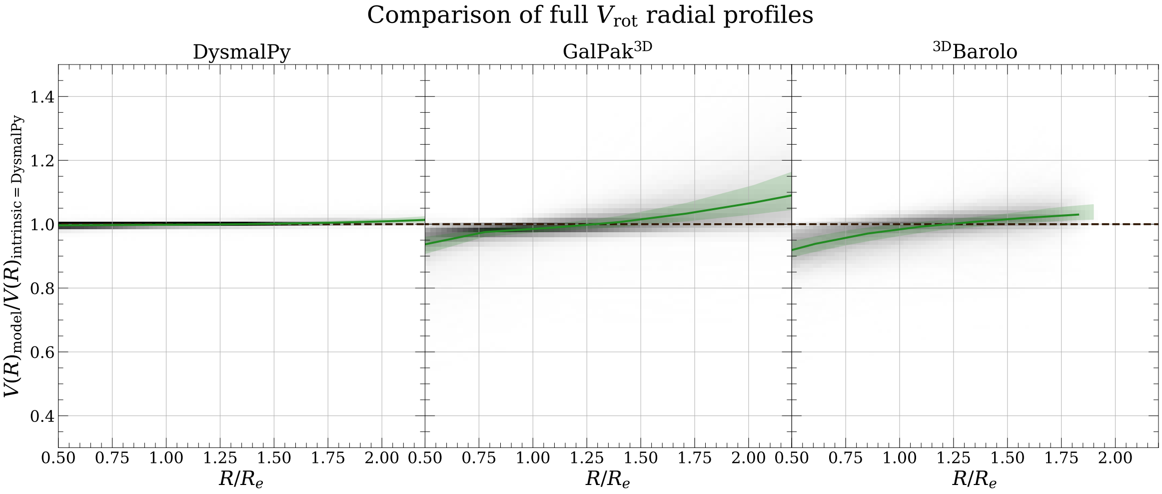

Figure 2.9 Running medians of the ratios between model and intrinsic rotation velocity $(V(R)_\mathrm{model}/V(R)_\mathrm{intrinsic})$ of `DysmalPy` (*left*), `GalPak`$^\mathtt{3D}$ (*middle*), $^\mathtt{3D}$`Barolo` (*right*) in the range of $[0.5, 2.2]R_e$, where R_e is the effective radius. The light green shading represents 1σ spread from the nominal median trend.

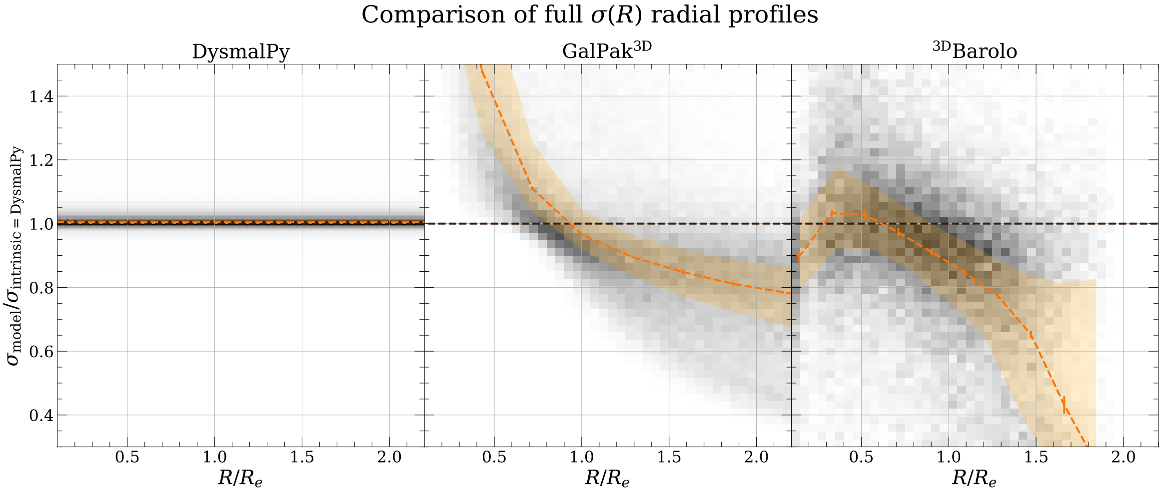

Figure 2.10 Similar to Figure 2.9 but for velocity dispersions ($\sigma_{\text{model}}/\sigma_{\text{intrinsic}}$) of `DysmalPy` (*left*), `GalPak`$^{\text{3D}}$ (*middle*), $^{\text{3D}}$`Barolo` (*right*) in the range of $[0.1, 2.2]R_e$, where R_e is the effective radius. The errors of the running medians are the 95% confidence interval derived by boot-strapping. The shading indicates 1–σ spread. In the *left* panel, `DysmalPy` shows an excellent recovery of the intrinsic values with minimal scatter, as template match is maximized. In the *middle* panel, the decreasing trend is primarily due to the mismatch between `DysmalPy`'s flat dispersion profile and the centrally peaked profile of `GalPak`$^{\text{3D}}$, as evidenced by the opposite trend in the *left* panel in Figure 2.11 (see Section 2.4.2 for details). In the *right* panel, $^{\text{3D}}$`Barolo` underestimates the intrinsic values at radii $\gtrsim R_e$. As discussed in Section 2.4.2, given the strong dependence of $^{\text{3D}}$`Barolo` performance on signal-to-noise (S/N), the observed trends are most likely caused by decreasing S/N at increasing radii from the centers.

baseline mock models as dy(dy), gp(dy), and bb(dy).

Because of the different analytical prescriptions, now the `GalPak`$^{\texttt{3D}}$ fits perform better than those with `DysmalPy`, as expected. In both mock sets, there is no significant correlation in the median $\sigma_{\rm model}(R_{\rm e})/\sigma_{\rm intrinsic}(R_{\rm e})$ trend with S/N, i, $R_{\rm e}$/beam, The pronounced tail of systematically overestimated $\sigma(R_{\rm e})$ at low intrinsic dispersion observed for gp(dy) is now absent in the gp(gp) fits.

For the fits with `DysmalPy`, the median $\sigma_{\rm model}(R_{\rm e})/\sigma_{\rm intrinsic}(R_{\rm e})$ now shows a systematic behavior reflecting again the template mismatch as seen in Fig. 2.5. At intrinsic velocity dispersions $\lesssim 50\,{\rm km\,s^{-1}}$, `DysmalPy` typically overestimates the dispersion at $R_{\rm e}$ by up to ~ 10–15% in the median (a lesser effect than the sharp and steep tail in the case of gp(dy) discussed in Sect. 2.4.2). The effect reverses to a typical underestimate at $\sigma_{\rm intrinsic} \gtrsim 50\,{\rm km\,s^{-1}}$ by a few up to $\sim 10\%$. This behavior can be explained by the relative contribution to the overall profile of the radially-dependent $\sigma_{\rm d}$ term in `GalPak`$^{\texttt{3D}}$ (Eqn. 2.3), which contributes more importantly and over a wider radial range at lower $\sigma(R_e)_{\rm gp}$.

To illustrate the sensitivity of `DysmalPy` to the slope of the intrinsic dispersion profile, Fig. 2.8 plots the $\sigma_{\rm model}(R_{\rm e})/\sigma_{\rm intrinsic}(R_{\rm e})$ for dy(gp) as a function of the intrinsic gradient at $R_{\rm e}$ of the model, $\left.\frac{\partial\sigma(R)}{\partial R}\right|_{R_{\rm e}}$. The Figure shows that more generally, by construction `DysmalPy` will have a tendency to overestimate the dispersion in the case of radially declining intrinsic dispersion when the slope around $R_{\rm e}$ is $\left.\frac{\partial\sigma(R)}{\partial R}\right|_{R_{\rm e}} \lesssim -30\,{\rm km\,s^{-1}\,kpc^{-1}}$, which is a fairly steep slope compared to local CO studies (e.g., C. D. Wilson et al., 2011).

$^{\texttt{3D}}$`Barolo` recovered values at $R_{\rm e}$ are slightly less underestimated than bb(dy) by 5% in median of $\sigma(R_e)_{\rm model}/\sigma(R_e)_{\rm intrinsic}$. The trends and scatter in Fig. 2.7 show no significant difference compared to Fig. 2.3 when S/N ≥ 10 and $\sigma_{\rm intrinsic} \gtrsim 40\,{\rm km\,s^{-1}}$. The smaller scatter and overall slightly better recovery of $^{\texttt{3D}}$`Barolo` stem from its improved performance when $\sigma_{\rm intrinsic} \lesssim 40{\rm km\,s^{-1}}$, as demonstrated in Fig. 2.4: when $\sigma_{\rm intrinsic} \lesssim 40{\rm km\,s^{-1}}$, it was underestimated by $\sim 25\%$ when baseline (`DysmalPy`-generated) models were used, and now this has improved to $\sim 5\%$. There is an overall slightly milder dependence with respect to S/N, as also reflected in Fig. 2.4.

Finally, a comparison with mocks generated using $^{\texttt{3D}}$`Barolo` reveals consistent trends for all codes, similar to those observed in the case of baseline models (orange lines in Fig. 2.4). $^{\texttt{3D}}$`Barolo` displays similar trends with S/N, $R_{\rm e}$/beam, i, and $\sigma_{\rm intrinsic}$. The persistent S/N trend of $^{\texttt{3D}}$`Barolo` is unsurprising, as it is not limited by any template assumption, and S/N sensitivity is universal regardless of intrinsic profiles. In other words, as long as the S/N is insufficient, $^{\texttt{3D}}$`Barolo` would tend to underestimate the σ. In contrast, `GalPak`$^{\texttt{3D}}$ still suffers from the template mismatch problem, as seen in the baseline models recovery,

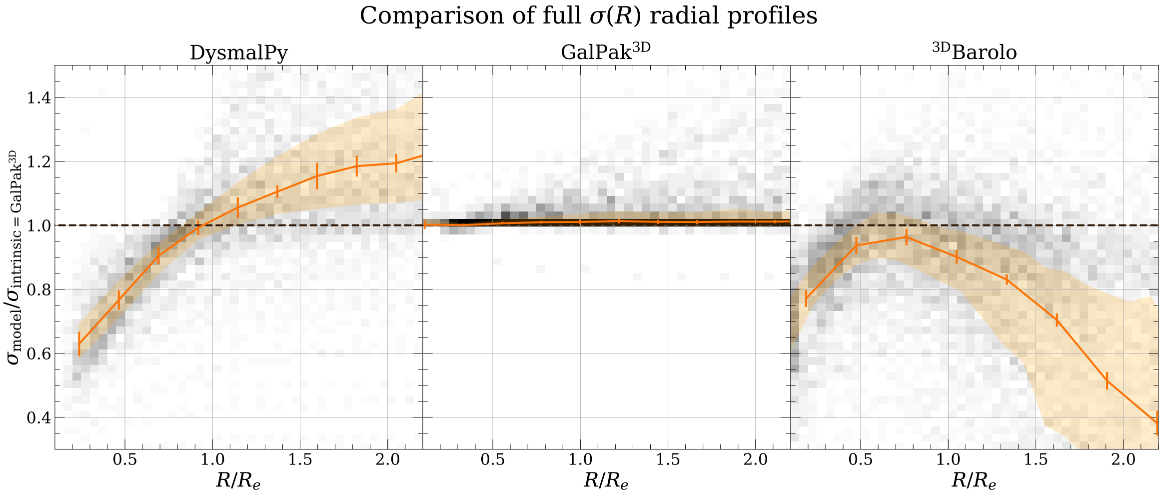

Figure 2.11 Similar to Figure 2.10, but the mock galaxies are generated by `GalPak`$^{\texttt{3D}}$. The increasing trend in the *left* panel, opposite to the decreasing trend in the *middle* panel of Figure 2.10, is due to the template mismatch that is described in detail in the main text (see also Figure 2.5 for the difference in profile shapes). `GalPak`$^{\texttt{3D}}$ recovers itself excellently with the running median close to unity up to large radii, albeit with a larger scatter. $^{\texttt{3D}}$`Barolo` exhibits a similar radial trend as in the same panel in Figure 2.10.

characterized by the same “L-shaped” tail at the low dispersion end, albeit to a lesser extent. This is because most intrinsic profiles have declining slopes, but are much shallower than the profile assumed in `GalPak`$^{\texttt{3D}}$ (Eqn. 2.3). Meanwhile, `DysmalPy` performs similarly to the baseline models, but with a slightly stronger dependence on R_e/beam and i. This additional exercise highlights once again the limitations of parametric modeling when the assumed template deviates substantially from the truth. In such cases, non-parametric modeling may be more effective, although it requires a higher S/N.

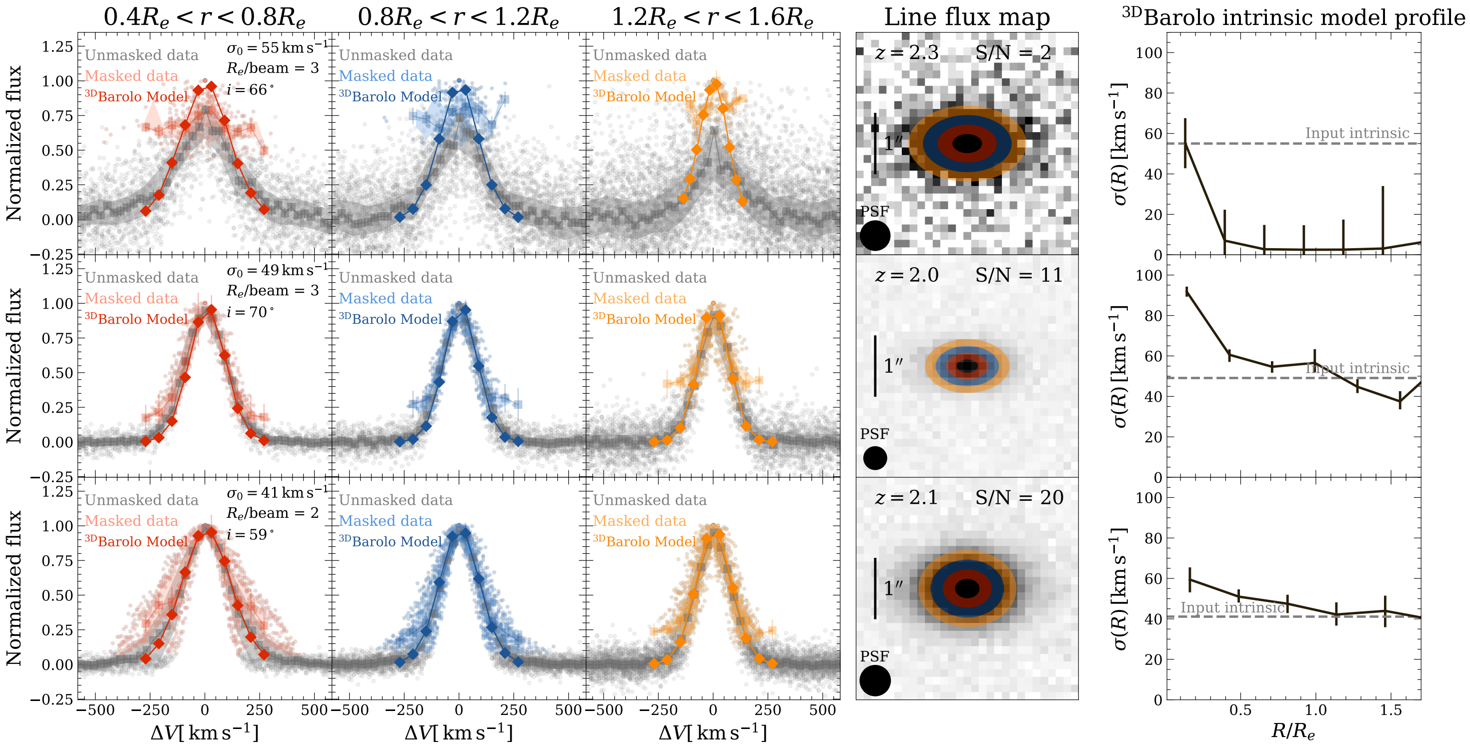

Figure 2.12 Velocity-shifted spectra of three `DysmalPy`-generated mock galaxies, extracted from spaxels in 3 radial elliptical bins annotated on top of the *first three* columns. The spectra of the original unmasked mock data cube are represented by individual gray points, while the ^{3D}`Barolo`-masked spectra (hereafter, masked data) are shown in pale red, blue, and orange points for each radial bin, respectively, across 3 different S/N levels (S/N=$[2, 11, 20]$) in each row. The axis ratio of the bins is determined by 2D Sérsic fitting of the line flux map displayed in the *fourth* column, overlaid with the color-coded radial bins. The curves with squares and shading overlay on the spectra are the median trends, and the central 68% of the full distributions for both the unmasked and masked data. The solid curves with diamond markers represent the velocity-shifted spectra extracted from the ^{3D}`Barolo`'s model. The *fifth* column shows the model intrinsic (accounted for observational effects) dispersion profile of the respective galaxies, with radii normalized to the effective radius R_e. At large radii, the line profile can be severely under-sampled because of marginal S/N, where in the extreme case, only the brightest few pixels remain to determine the line width. This causes a systematic underestimation of the line width at large radii. Consequently, across all three galaxies, a clear radially declining trend is evident in the recovered dispersion profiles, with the steepest drop observed in the lowest S/N model. The position-velocity diagrams and channel maps of these three galaxies are shown in Figures 2.20 and 2.21 in Appendix 2.12, respectively.

2.4.5 Further insights from full radial profiles

We have discussed so far the recovery of $V_{\rm rot}$ and σ by the three codes at $1R_e$. Here we explore the full radial profiles of $V_{\rm rot}$ and σ of the three codes. The full $V_{\rm rot}$ and σ profiles would be essential in mass decomposition, one of the key applications of kinematic modeling.

Fig. 2.9 shows the running medians and 1-σ spread of $V_{\rm rot,model}/V_{\rm rot,intrinsic}$ over the radial range $[0, 2.2]R_e$ for each of the packages for the baseline models. Because the same parametric models are used, `DysmalPy` recovers itself well. `GalPak`$^{\tt 3D}$ shows monotonically increasing median values and scatter from small to larger radii. The template mismatch between `GalPak`$^{\tt 3D}$ and `DysmalPy` becomes more apparent when $R \gtrsim 1.25R_e$, as the choice of arctan in `GalPak`$^{\tt 3D}$ only accommodates rising to flat shapes, in comparison with `DysmalPy` multicomponent mass models, which can take on a variety of RC shapes, from rising to flat to declining. For $^{\tt 3D}$`Barolo`, the median increases with radius, albeit more mildly and with a smaller scatter. Too few galaxies are modeled by $^{\tt 3D}$`Barolo` at $\gtrsim 2R_e$, so values are not plotted in this range. Overall, $^{\tt 3D}$`Barolo` recovers the intrinsic $V_{\rm rot}(R)$ within $\lesssim 10\%$ accuracy, thanks to the flexibility of the tilted-ring approach that can adjust to any shape of the $V_{\rm rot}(R)$ RC. The mild increasing trend is likely attributed to two factors (i) known limitation of $^{\tt 3D}$`Barolo` when applied to thick disk (see Sect. 7.1 in G. Iorio et al. (2017)) (ii) residual beam smearing correction in $^{\tt 3D}$`Barolo` as noted in M. R. Varidel et al. (2019). Factor (i) is in general true for tilted-ring modeling as also discussed in Sect. 4.5 in G. I. G. Józsa et al. (2007) for `TiRiFiC`. Both of these effects would underestimate the inner velocity gradient while overestimating it at the outer disk.

Similarly, we compare the radial variation of σ in Fig. 2.10 for the recovery of the baseline models and Fig. 2.11 for the `GalPak`$^{\tt 3D}$ generated mocks. As expected, `DysmalPy` and `GalPak`$^{\tt 3D}$ show very good self-recovery when modeling their respective mocks. The expected template mismatch signatures are apparent when `GalPak`$^{\tt 3D}$ models the baseline mocks, and vice versa, as reflected by the declining trend in the middle panel of Fig. 2.10 and rising trend in the left panel of Fig. 2.11, both with a typical transition radius at $\sim R_e$. Comparing σ at R_e as we did in the previous discussion should generally reduce the effect of template mismatch, albeit the scatter is still significant.

The non-parametric $^{\tt 3D}$`Barolo` shows consistent radially declining behavior regardless of the mock model suite. $^{\tt 3D}$`Barolo` best recovers the input σ at $0.75R_{\rm e}$. At $1R_{\rm e}$, σ is typically underestimated by $\sim$10–15% and worse at larger radii, accompanied by larger scatter. The S/N rapidly decreases with radius in the models, and $^{\tt 3D}$`Barolo`'s sensitivity to S/N becomes increasingly apparent at larger radii. We discuss the implications of this trend on estimates of intrinsic velocity dispersion based on the full-fitted dispersion profile in Sect. 2.5. Towards smaller radii, the systematic overestimate in σ and the small but systematic underestimate in $V_{\rm rot}$ is the result of its tilted-ring approach. The approach constrains parameters for each ring independently and is unable to account for disk thickness accurately. This limitation is discussed in detail in, for example, Sect. 5.1.2 of F. A. Roper et al. (2023) and G. Iorio et al. (2017).

2.4.6 Effect of masking in the recovery of σ

We next explore an alternative masking routine in $^{\rm 3D}$`Barolo`. We did not apply smoothing before generating the mask to boost consistency across codes (by specifying `SEARCH` in the `MASK` option), which is also the default option in $^{\rm 3D}$`Barolo`. Nonetheless, `SEARCH` is commonly used in the literature (e.g., G. Sharma et al., 2021; L. Hogan et al., 2022; F. Rizzo et al., 2023; A. Pope et al., 2023; F. Roman-Oliveira et al., 2023b). Another popular choice is `SMOOTH&SEARCH` (e.g., P. E. Mancera Piña et al., 2020; F. Fraternali et al., 2021; F. Lelli et al., 2023), where $^{\rm 3D}$`Barolo` first smooths the data cube before calling the source finding algorithm. Repeating our recovery tests instead using `SMOOTH&SEARCH` masking (with default option `FACTOR=2`, which doubles the beam size) shows little difference in best-fit results, with similar trends obtained without smoothing illustrated in Fig. 2.4. A more detailed inspection of $^{\rm 3D}$`Barolo` indicates that both masking routines often lead to over-masking in velocity, with only a few of the brightest channels being passed to the fitting algorithm. We verified that this behavior remains with different choices of `MINCHANNELS` in the `SEARCH` routine.

To illustrate the impact of spectral masking on low S/N data more clearly, we present spectra extracted from individual pixels from inner to outer regions (in elliptical annuli with axis ratio of the bins set by 2D Sérsic fitting of the line flux map) of three selected galaxies in Fig. 2.12. These galaxies share similar $R_{\rm e}$/beam, inclination ($\sim 60°$–$70°$), and redshifts ($z \sim 2$) but differ in S/N, from low S/N (S/N = 2) to high S/N (S/N = 20). The spectra are shifted in velocity space to align with a common normalized emission line peak, and we refer to them as "velocity-shifted spectra" to distinguish them from more typical integrated spectra extracted in circular aperture. The gray points and the solid line with square markers represent the individual velocity-shifted spectrum and the running median trends of this ensemble of the spectrum. The data left after masking is applied are shown in colored points with the running median trend overlaid. The solid-colored curves are the median trends of the velocity-shifted spectra extracted from the $^{\rm 3D}$`Barolo` model cube. The recovered $\sigma(R)$ profiles by $^{\rm 3D}$`Barolo` are shown in the last column of Fig. 2.12. Additionally, we provide the position-velocity (PV) diagrams extracted using the

`PVSLICE` task in $^{\rm 3D}$`Barolo`, as well as channel maps at every 4 channels in Figs. 2.20 and 2.21, respectively, in Appendix 2.12. We also show those from `DysmalPy` and `GalPak`$^{\rm 3D}$in addition to $^{\rm 3D}$`Barolo` results. These diagnostics are supplementary to Fig. 2.12 to demonstrate the quality of the fitted model, particularly for $V_{\rm rot}$, but Fig. 2.12 is more informative of the effects of masking on velocity dispersion.

At higher S/N, the impact of spectral masking is minimal, and the recovered dispersion profile at large radii closely resembles the intrinsic constant profile. The upward trends (second and third panels in the last column) towards the inner region could be due to residual correction of beam smearing, consistent with the behavior in Fig. 8 in E. M. Di Teodoro & F. Fraternali (2015) for similar inclinations.

At lower global S/N or towards larger radii within the same galaxy, the aggressive clipping of high- and low-velocity wings below the same specified S/N inevitably leads to underestimating the true velocity dispersion. Within the same galaxy, this could manifest as an apparent radially declining profile, as illustrated in the first and second panels in the last column. Indeed, as noted already in E. M. Di Teodoro & F. Fraternali (2015), a satisfactory fit at low S/N typically requires a channel count ranging from 8 to 12, depending on the spatial resolution, and the source should be detected over multiple channels with S/N $\gtrsim 3$. This highlights the importance of validating model results with direct data-based measurements, particularly at large radii, similar to the velocity-shifted spectra presented here.

To further investigate the effects of spectral masking, we exchanged the masks between `DysmalPy` and $^{\rm 3D}$`Barolo`. Given that `DysmalPy` determines the mask based on the integrated S/N along a spaxel, it does not apply spectral masking, ensuring the same number of channels are modeled for every included spaxel, following the recommendation of R. Davies et al. (2011). We multiplied the mock cube with `DysmalPy`'s mask and set `MASK` to `NONE` in $^{\rm 3D}$`Barolo`. To complement the test, we repeat the same exercise for `GalPak`$^{\rm 3D}$ by multiplying the input mock cubes by the $^{\rm 3D}$`Barolo`'s masks. When such a mask is used in $^{\rm 3D}$`Barolo` and S/N approaches ~ 30, $^{\rm 3D}$`Barolo` and `DysmalPy` generated masks are in good agreement. If the mask generated by $^{\rm 3D}$`Barolo` is applied to `DysmalPy` and `GalPak`$^{\rm 3D}$, we recover a similar trend with S/N as in $^{\rm 3D}$`Barolo` when its mask is used. Overall, the S/N dependence of $^{\rm 3D}$`Barolo`'s recovery of σ vanishes, as evidenced by the flat trend with S/N in Fig. 2.4 (leading to a very low Spearman's and MIC scores). Contrary to the previous underestimation trends, the systematic overestimation observed now is likely due to $^{\rm 3D}$`Barolo`'s sensitivity to the available valid pixels for modeling when S/N is limited.

In summary, we tested (1) `SMOOTH&SEARCH` masking, (2) vary the `MINCHANNELS` parameter, and (3) `DysmalPy` masking (entire spaxel masking using integrated S/N). We found no significant difference in recovery trends and scatter for (1) and (2), and the dependence on S/N was appreciably reduced when (3) was adopted.

This simple experiment underscores the critical role of masking in σ recovery across all codes, with non-parametric methods exhibiting particular sensitivity. The general impact of masking has been extensively discussed in a similar context, notably by R. Davies et al. (2011), N. Deg et al. (2022), and Sect. 7.3 (Fig. 14) in W. J. G. de Blok et al. (2024). It is unsurprising that fitting is affected by the data to which the fitting is applied. Whether and how (e.g., `DysmalPy` and $^{\text{3D}}$`Barolo`) or not (e.g. `GalPak`$^{\text{3D}}$) masking is applied, this aspect should be taken with extra care when analyzing and interpreting fitting results.

Since all codes yield good agreement toward very high S/N, regardless of the masking routine, deeper integration data is ideal for reducing systematic differences across different codes.

2.4.7 Effect of alternative settings in the recovery of σ for $^{\text{3D}}$`Barolo`

To maintain consistency in comparing the best-fit results of the three kinematic modeling tools discussed in this paper, we adopted settings for $^{\text{3D}}$`Barolo` that come closest to those implemented in `DysmalPy` and `GalPak`$^{\text{3D}}$. However, these are not necessarily those most commonly employed in the literature. This pertains in particular to the metric employed for the goodness of fit and the masking procedure. First, we experiment with a different residual function for minimization in $^{\text{3D}}$`Barolo`. While there are three options listed in Sect. 2.2.3, we opted for the pseudo-χ^2: $(M-D)^2/\sqrt{D}$. The default option in $^{\text{3D}}$`Barolo`, the absolute difference $|M-D|$, is also a common choice in the literature (e.g., F. Lelli et al., 2023; A. C. Posses et al., 2023). Similar to our findings using other minimization settings, our results reveal a similar trend with S/N and other parameters regardless of the residual function used.

2.5 Implications for the physical properties of high-z galaxies

The recovery tests presented in this paper were performed with sets of 3D mock models covering a realistic range of galaxy properties for massive MS SFG(s) at $z\sim1$–3, and representative observational parameters with emphasis on higher S/N than many current observations. Intentionally, we used very large suites of simple axisymmetric models and a minimum of free parameters to robustly assess trends and scatter in the relative performance of the tools and to reduce the impact of known degeneracies affecting all modeling approaches (e.g., between mass and inclination).

Tests based on observations would be very informative, but for high-z galaxies the intrinsic parameters would themselves be derived from modeling and thus would require the highest resolution and S/N possible. Very few such data sets currently exist as they rely on very deep observations (difficult to obtain) or very bright targets (rare). Data of local disk galaxies at very high S/N and resolution enable a better characterization of intrinsic kinematics, but because of the different conditions prevailing at higher redshift (higher accretion rates, cold gas fractions, and star formation rates; smaller disk sizes), local disks may not provide the most realistic templates at high-z. Numerical cosmological simulations of galaxy evolution may better capture the conditions and complexities of real high-z disks, although their use is not straightforward. Complications include the mismatch in how properties are derived between simulations and observations, and the reliance on sub-grid recipes that are typically tuned to reproduce the final stage of present-day galaxy properties (see discussions by, e.g., S. Wellons et al. 2020 and H. Übler et al. 2021).

Nevertheless, our experiments highlight a key aspect that should be kept in mind when interpreting high-z kinematics data, especially in the context of two key applications: challenges determining the disk velocity dispersion and the resulting implications for mass decomposition. Our tests suggest that it remains difficult to pin down the disk velocity dispersion to better than $\sim 20-50\%$ depending on the tool considered, unless there is a close match between the true and the assumed model profile and the S/N per spatial pixel at the line peak velocity is above 10 over a sufficiently large and well resolved radial range. In `DysmalPy`, the intrinsic velocity dispersion (σ_0) is assumed to be isotropic and spatially constant across disks, representing a dominant turbulence term. This assumption was empirically motivated by high S/N, adaptive optics (AO) assisted IFU observations of Hα resolved on ~ 1 kpc scales of large $z \sim 2$ MS SFG(s) from the SINS/zC-SINF survey, after accounting for instrumental and beam smearing effects through modeling (R. Genzel et al., 2017; H. Übler et al., 2019). In those galaxies, no significant spatial variation was observed in derived intrinsic velocity dispersion beyond the innermost radii (where residual beam smearing could still play a role) out to a few R_e. Similarly, no evidence for appreciable radial variations in intrinsic dispersion to $\sim 10\,$kpc was found from modeling of a much larger sample of 240 $z \sim 1-3$ MS SFG(s) with deep integrations in excellent near-IR seeing of $\approx 0\farcs5$ from the KMOS^{3D} survey (S. Wuyts et al., 2016).

As the dispersion values derived for these galaxies are large ($> 30\,\mathrm{km\,s^{-1}}$), in line with expectations in the framework of gas-rich marginally (un)stable disks with the typically high f_{molgas} at high redshift, the contribution from self-gravity for radially decreasing mass densities is sub-dominant (see Fig. 2.5) and would be difficult to discern as it would be small and apparent only in the innermost regions. If the full velocity dispersion is intrinsically declining, as considered by F. Rizzo et al. (2020, 2021), any significant radial gradient would have left a measurable systematic trend in the observed dispersion profiles and residuals in the best-resolved galaxies examined by R. Genzel et al. (2017) and H. Übler et al. (2019), which was not observed.

Ideally, non-parametric modeling would be best suited to examine galaxies' dispersion profiles. Some past studies reported radially declining velocity dispersion using $^{3\mathrm{D}}$`Barolo` (e.g., F. Lelli et al., 2021; F. Rizzo et al., 2023; F. Roman-Oliveira et al., 2023b), with profiles similar to those of local H I and CO studies (e.g., R. Boomsma et al., 2008; D. Tamburro et al., 2009; C. D. Wilson et al., 2011; K. M. Mogotsi et al., 2016). If so, this highlights the challenge of distinguishing radial variations due to the intrinsic profile versus the potential impact of S/N and beam smearing. In this context, we note that our recovery tests compared σ at a fixed radius between the tools, taken as R_e in Sections 2.4.1–2.4.3, to maximize consistency. The common convention for calculating σ from $^{3\mathrm{D}}$`Barolo` modeled profiles includes taking the mean or median value of all modeled rings or, less commonly, the average of the two outermost rings (e.g., E. M. Di Teodoro et al., 2016; G. Iorio et al., 2017; F. Fraternali et al., 2021; F. Lelli et al., 2021; M. Neeleman et al., 2023; F. Rizzo et al., 2023; F. Roman-Oliveira et al., 2023b; G. Sharma et al., 2025). Repeating our exercise using the former two definitions, we find no significant difference in trends identified when using the value around $1R_e$.

Determinations of the intrinsic velocity dispersion of high-z disks are important in the context of disentangling the drivers of disk gas turbulence (stellar feedback, gas transport induced by internal gravitational/disk instabilities or by external accretion), the relative contribution of which is thought to vary with redshift (e.g., M. R. Krumholz et al., 2018; R. Genzel et al., 2011; C.-L. Hung et al., 2019; O. Ginzburg et al., 2022; E. Jiménez et al., 2023). It is also of interest in terms of the disk thickness, as more pressure support implies geometrically thicker disks such that elevated dispersion in high-z disks may be linked to the formation of today's thick disk components (e.g., B. G. Elmegreen & D. M. Elmegreen, 2006; F. Bournaud et al., 2009). Moreover, if hydrostatic equilibrium holds, radially constant disk dispersion should imply disk flaring at larger radii. Ultimately, substantially higher sensitivity and both angular and velocity resolution would be needed to accurately pin down disk velocity dispersions and their evolution at high redshift. In the meantime, one way forward could be to obtain deep data at (sub-)kpc resolution and $R \gtrsim 10000$ (instrumental LSF of $\sigma \lesssim 15\,\mathrm{km\,s^{-1}}$) of low-inclination galaxies, reducing the contribution to emission line broadening from projected rotation and even allowing model-independent estimates directly from observed line widths.

Knowledge of the velocity dispersion and its profile is also important for dynamical mass estimates and mass modeling. Since the rotation velocity curve $v_{\rm rot}(R)$ is fairly well recovered by all three tools, as long as the pressure support is small (i.e., $v_{\rm rot}$ approximates $V_{\rm circ}$ as a tracer of the full potential well), results for $M_{\rm dyn}$ and mass decomposition derived from `DysmalPy`, `GalPak`$^{\rm 3D}$, and $^{\rm 3D}$`Barolo` kinematic modeling should agree very well for the same assumptions on the underlying mass distribution. However, if dispersions are elevated, and especially relative to $v_{\rm rot}$, results based on modeling with the different tools may lead to different conclusions. This could arise from possible significant misestimates in recovered velocity dispersion depending on template mismatch (for parametric models like `DysmalPy` and `GalPak`$^{\rm 3D}$), and on the S/N regime and inclination (most relevant for $^{\rm 3D}$`Barolo`). The other important reason lies in the treatment of the pressure support, which can differ between studies (e.g., A. Burkert et al., 2016; G. Iorio et al., 2017; M. Kretschmer et al., 2021; S. H. Price et al., 2021; G. Sharma et al., 2021). Additional factors are obviously the specific choice for the mass model component(s).

Empirically-motivated pressure support corrections and well-constrained mass components from high-z data of stars, warm and cold gas distributions, and kinematics would be ideal but may need to await future more powerful and efficient observational capabilities. At the very least, deep observations probing as far out as possible in radius will help by providing better leverage for the relative contributions of DM and baryons, and sub-kpc resolution can tighten constraints on the inner core/bulge component. Independent observations of multiple ISM phases are valuable in augmenting the constraints, giving better priors for the gas (which makes up an important fraction of the baryonic component at high-z), and complementing each other in tracing radial coverage and mitigating optical depth effects. These are within reach of current facilities; time estimates for typical massive MS SFG(s) with ERIS, ALMA and NOEMA imply on-source integration of $\sim 10--20$ hours, and such deep observations already carried out demonstrate their potential (e.g., R. Genzel et al., 2017, 2020, 2023; H. Übler et al., 2018; A. Nestor Shachar et al., 2023; A. Puglisi et al., 2023). Even stellar kinematics are feasible up to at least $z \sim 1$ (e.g., J. van Houdt et al., 2021; C. M. S. Straatman et al., 2022; H. Übler et al., 2024a) for very deep integrations.

2.6 Summary

We have assessed the 3D kinematic recovery performance of the kinematics modeling tool `DysmalPy`, which is publicly released as part of this work. We also compared its performance with two other packages whose methodologies are based on different motivations but share the similarity of being 3D forward-modeling algorithms: `GalPak`$^{\texttt{3D}}$ and $^{\texttt{3D}}$`Barolo`. We simulated a large number of mock disk galaxies matching the galaxy parameter space and S/N and resolution distributions of a sample of deep $z \sim 1-3$ MS SFG(s) (RC100; A. Nestor Shachar et al., 2023), which includes high-quality kinematics data sets from near-IR IFU and mm interferometry. Our experiment intentionally kept a minimum number of free parameters to help highlight the root causes of potential differences in different modeling approaches to mitigate them in applications to real data. We focussed on evaluating the reliability in recovering the important kinematics properties: $V_{\rm rot}$ and σ. We summarize the key results as follows:

1. Recovery of $V_{\rm rot}$ at R_e is largely independent of the choice of modeling tool (e.g., Fig. 2.1 in Sect. 2.4.1). In terms of recovery of the full $V_{\rm rot}$ profile, unsurprisingly, template mismatch can affect parametric modeling with `DysmalPy` and `GalPak`$^{\texttt{3D}}$ whereas $^{\texttt{3D}}$`Barolo` can accommodate different $V_{\rm rot}$ shapes more easily (Sect. 2.4.5).

2. The recovery of $\sigma_{\rm model}/\sigma_{\rm intrinsic}$ from different tools can vary significantly depending on $\sigma_{\rm intrinsic}$, S/N, and i (Sect. 2.4.2). The disagreement between `GalPak`$^{\texttt{3D}}$ and `DysmalPy` can be primarily explained by the inherent template mismatch (Sect. 2.4.4, Fig. 2.7 and 2.8). The flexibility of $^{\texttt{3D}}$`Barolo` is hampered by its stringent demand on S/N, which is challenging to fulfill for high-z galaxies with typical allocated observing time. Aspects to be cautious about include:

    - the choice of parametric functions, for example, constant vs. radially varying velocity dispersion profile. The choice should be informed ideally from empirical evidence, which is still scarce at $z \gtrsim 1$;
    - the flexibility of non-parametric methods comes with higher S/N requirements for a robust recovery. If S/N is insufficient, tilted-ring modeling is more sensitive to the masking choice.

3. The presence of light clumps (Sect. 2.4.3) can affect the results from parametric models due to the inflexibility of the analytic light profile. Non-parametric modeling, on the other hand, is less systematically affected by asymmetric light distributions, although we find there is still a large scatter in the recovered-to-intrinsic values. The non-parametric model flexibility is still primarily hindered by poor sensitivity in low S/N samples.

Based on our recovery exercise, we strongly recommend that, before applying any modeling to real data, it is crucial to assess the impact of

- any prior assumptions on radial kinematics profiles, especially when these are parametrized (intrinsically or otherwise);
- masking using model-independent diagnostics, such as the example shown in Fig. 2.12;
- S/N on the recovered properties, especially towards the outer edges of the detected regions;

These steps additionally help to gauge whether the adopted template and the resulting modeled values deviate significantly from the data, thereby mitigating template mismatch and S/N sensitivity issues, as discussed above.

The mock models used in this paper are idealized in many respects: they are axisymmetric, and the center, PA, and i are known (fixed in modeling). Those quantities are, however, difficult to recover in reality from low S/N and resolution data with highly irregular light distributions. In our study, we only tested one out of many possible scenarios of asymmetry by introducing a fixed number of light clumps. Real galaxies, however, can possess a range of different features, such as rings and bars. Nevertheless, our exercise of using simple mock models here should shed light on the discrepancies of the measured kinematic quantities, especially the velocity dispersion across studies, when the same set of galaxies is analyzed.

In light of the significant difference in recovering the velocity dispersion between different modeling approaches, we need standardized metrics and modeling assumptions for accurate comparisons between different samples. Only then can we assess robustly the evolution of disk velocity dispersion with redshift, and correlations with stellar mass, star formation activity, and other galaxy properties.

Obtaining a subset of galaxies with enhanced spectral resolution and higher S/N to larger radii is crucial for constraining whether velocity dispersion varies radially. This information is pivotal for selecting an appropriate template in parametric modeling. Deep observations with radio interferometers such as NOEMA and ALMA are well-suited for that purpose. The near-IR IFU ERIS on the Very Large Telescope is also ideal, affording a spectral resolution capability of $R \sim 11000$ and, combined with AO, a high spatial resolution with a high Strehl ratio. High S/N and resolution are as important as sample size for characterizing the global velocity dispersion of high-z disks, spatial variations, and the origin of scatter among galaxies.

ACKNOWLEDGMENTS

We thank the anonymous referee for the constructive comments. We are very grateful for the useful discussions and insightful comments at various stages of this work by Tim de Zeeuw, Stéphane Courteau, Nathan Deg, Nicolas Bouché, Emily Wisnioski, Jianhang Chen and Minju Lee. N.M.F.S. and J.M.E.S. acknowledge financial support from the European Research Council (ERC) Advanced Grant under the European Union's Horizon Europe research and innovation programme (grant agreement AdG GALPHYS, No. 101055023). HÜ gratefully acknowledges support by the Isaac Newton Trust and by the Kavli Foundation through a Newton-Kavli Junior Fellowship.

SOFTWARE

DysmalPy (R. I. Davies et al., 2004a,b; R. Davies et al., 2011; G. Cresci et al., 2009; S. Wuyts et al., 2016; P. Lang et al., 2017; S. H. Price et al., 2021), GalPak$^{\mathrm{3D}}$ (N. Bouché et al., 2015), $^{\mathrm{3D}}$Barolo (E. M. Di Teodoro & F. Fraternali, 2015), Numpy (C. R. Harris et al., 2020), MPFIT (C. B. Markwardt, 2009), Scipy (P. Virtanen et al., 2020), Matplotlib (J. D. Hunter, 2007), corner (D. Foreman-Mackey, 2016), Astropy (Astropy Collaboration et al., 2013), Imfit (P. Erwin, 2015), minepy (D. Albanese et al., 2012).

2.7 Appendix A – Mock models setup

Table 2.3 lists the names and priors of the parameters in each code for the modeling as performed in this work. There are in total 3, 2 and 2 free parameters in `DysmalPy`, `GalPak`$^{\mathrm{3D}}$ and $^{\mathrm{3D}}$`Barolo`, respectively.

Table 2.3. Parameters and Priors used in this study.

Software [method, $N_{\rm free}$]	Parameters [unit]	`Parameters Names`	Priors/Values	`Input Priors/Options`
`DysmalPy` [mpfit, 3]	PA [deg]	`pa`	[90]	`pa=90` `pa_fixed=True`
	Inclination [deg]	`inc`	[True value]	`inc_fixed=True`

	$\log{(M_{\rm bar}/M_\odot)}$	`total_mass`†	[8.0,13.0]	`total_mass=10.5`
				`total_mass_bounds=8.0 13.0`
				`total_mass_fixed=False`
				`pressure_support=True`
				`noord_flat=True`

	$R_{\rm e,d}/(h_z\sqrt{2\ln 2})$	`invq_disk`	[True value]	*
	$R_{\rm e,b}/(h_z\sqrt{2\ln 2})$	`invq_bulge`	[True value]	*
	$R_{\rm e,d}$ [kpc]	`r_eff_disk`	[True value]	`r_eff_disk_fixed=True`
	$R_{\rm e,b}$ [kpc]	`r_eff_bulge`	[True value]	`r_eff_bulge_fixed=True`
	B/T	`bt`	[True value]	`bt_fixed=True`
	h_z [kpc]	`sigmaz`	Tied to $R_{\rm e,d}$	`sigmaz_fixed=False` `zheight_tied=True`

	$f_{\rm DM}$	`fdm`	[0,1]	`fdm=0.5`
				`fdm_fixed=False`
				`fdm_bounds=0.0 1.0`

	σ_0 [km s^{-1}]	`sigma0`	[0,150]	`sigma0=40`
				`sigma0_fixed=False`
				`sigma0_bounds=0.0 150.0`

	$\log{(M_{\rm vir}/M_\odot)}$	`mvirial`	Tied to $f_{\rm DM}$	`mvirial_tied=True`
				`mvirial_fixed=True`
				`adiabatic_contract=False`
				`halo_profile_type=NFW`

Table 2.3 (cont'd)

Software [method, $N_{\rm free}$]	Parameters [unit]	`Parameters Names`	Priors/Values	`Input Priors/Options`
				`include_halo=True`
	$c_{\rm halo}$	`halo_conc`	[True value]	`halo_conc_fixed=True`
	PSF [″]	`psf_fwhm`	[True value]	`psf_type=Gaussian`
	LSF [km s^{-1}]	`sig_inst_res`	40	`use_lsf=True`
				`data_inst_corr=True`
	Masking	`auto_gen_3D_mask`		`True`
	Integrated S/N threshold	`auto_gen_mask_snr_int_flux_thresh`	3	`3`
	Light distribution: Sérsic	`fitflux`	True	`True`
	Disk Sérsic index ($n_{\rm d}$)	`n_disk`	Exponential	`1`
	Bulge Sérsic index ($n_{\rm b}$)	`n_bulge`	de Vaucouleurs	`4`
`GalPak`$^{\rm 3D}$ [mcmc, 2]	PA [deg]	`fixed.pa`[a]	[90]	`90`
	Inclination [deg]	`fixed.inclination`	[True value]	*
	σ_0 [km s^{-1}]	`velocity_dispersion`[b]	[0,150]	`0,150`
				`dispersion_profile='thick'`[c]
	$V_{\rm max}$ [km s^{-1}]	`maximum_velocity`[b]	[50,400]	`50,400`
				`rotation_curve='arctan'`[c]
	$R_{\rm e}$ [″]	`fixed.radius`	[True value]	*
	$R_{\rm turn}$ [″]	`fixed.turnover_radius`	[0.25$R_{\rm e}$]	`radius/4`
	PSF [″]	`fwhm`[d]	[True value]	*
	LSF [km s^{-1}]	`fwhm`[d]	40 × 2.3548	`94.192`
	Light distribution	`type`	Sèrsic	`ModelSersic`
		`flux_profile`	Exponential	`exponential`
		`thickness_profile`	Gaussian	`gaussian`
	$(h_z\sqrt{2\ln 2})/R_{\rm e}$	`aspect`	[True value]	`*`
$^{\rm 3D}$`Barolo` [Nelder-Mead, 2[‡]]	PA [deg]	`PA`	[90]	`DELTAPA=0`

Table 2.3 (cont'd)

Software [method, $N_{\rm free}$]	Parameters [unit]	`Parameters Names`	Priors/Values	`Input Priors/Options`
	Inclination [deg]	`INC`	[True value]	`DELTAINC=0`
	Gaussian disk scale height h_z [$''$]	`Z0=*`	[True value]	`LTYPE=1`
	$V_{\rm rot}(r)$ [$\rm km\,s^{-1}$]	`VROT=200`	[0,400]	`DELTAVROT=200`
				`VSYS=0`
				`ADRIFT=False`
	$\sigma(r)$ [$\rm km\,s^{-1}$]	`VDISP=40`	[0,150]	`MINVDISP=0`
				`MAXVDISP=150`
	Free parameters	`FREE`	$V_{\rm rot}(R)$, $\sigma(R)$	`FREE=VROT VDISP`
	PSF [arcsec]	`BEAMFWHM`	[True value]	*
	LSF [channels]	`LINEAR`[e]	40/10	4
	Masking/source finding	`MASK`		`SEARCH`
		`SNRCUT`	3	3
		`SEARCH`	True	`True`
	Light distribution (normalization)	`NORM`		`LOCAL`
	Scale height profile	`LTYPE`	Gaussian	1
	Weighting function	`WFUNC`	Uniform	0
	Minimization function	`FTYPE`	chi-square	1

Note. — The x, y, z centroid positions are fixed to the known values for all packages. The parameters not listed here are either not relevant for the fitting, e.g. plotting styles, or we use the default values. Conversion between arcsecond and kpc is based on the specified cosmology.

[a] `fixed = GalaxyParameters().copy()`, which is then assigned to the argument `known_parameters` in `GalPaK3D.run_mcmc()`.

[b] The lower and upper values are assigned to `min_boundaries` and `max_boundaries`, respectively, as a `GalaxyParameters` object. These boundaries are then passed as arguments with matching names to `GalPaK3D.run_mcmc()`.

[c] As arguments of `DefaultModel()` and serves as an argument in `GalPaK3D.run_mcmc()`.

[d] As the argument of `GaussianPointSpreadFunction()` and `GaussianLineSpreadFunction()`, respectively, and are passed to `Instrument()`, which eventually assigned to object `GalPaK3D`.

[e] In unit of number of channels.

[†] Total baryonic mass.

[‡] For each ring.

2.8 Appendix B – Distributions of mock galaxies' parameters

Fig. 2.13 shows the distribution of the `DysmalPy`-generated baseline set of model galaxies in M_*, SFR, $f_{\rm gas}$, and $M_{\rm vir}$. Fig. 2.14 plots the distribution of z, σ_0, i, $R_e/{\rm beam}_{\rm HWHM}$, and S/N (in the brightest spectral channel and averaged over spaxels within $R_{\rm e}$). In both figures, histograms compare the distributions of the baseline models with those of the RC100 disks, and the median values are indicated. The baseline sample's M_*, SFR, z, R_e/beam are statistically equivalent to the RC100 sample with K-S score $\lesssim 0.07$. In other parameters, although the K-S score is larger, the median values are in close agreement.

2.8.1 Appendix B.1 – Clumpy sub-sample

Fig. 2.15 displays the integrated line intensity maps (0th-moment) of 12 randomly selected clumpy mocks generated by `DysmalPy`.

2.8.2 Appendix B.2 – Covariant distributions of parameters

Fig. 2.16 shows the covariant distributions of i, $R_{\rm e}$/beam, and S/N for the baseline set of model galaxies. The contours indicate $[1, 2, 3]\sigma$ of the distributions. Round-shaped contours imply the distributions are sufficiently randomized and not expected to introduce substantial biases in the analysis. The histograms compare the original distribution of the full baseline set, as well as of the successfully modeled subsets by `DysmalPy`, `GalPak`$^{\tt 3D}$, and $^{\tt 3D}$`Barolo`, indicating no important bias in the recovery analysis is introduced by the failed or excluded fits.

2.9 Appendix C – Ratios between $V_{\rm rot}$ and σ

Fig. 2.17 is the same as Fig. 2.2 and Fig. 2.3 but showing the ratios of recovered and intrinsic $V(R_{\rm e})/\sigma(R_{\rm e})$ for the `DysmalPy`-generated baseline models.

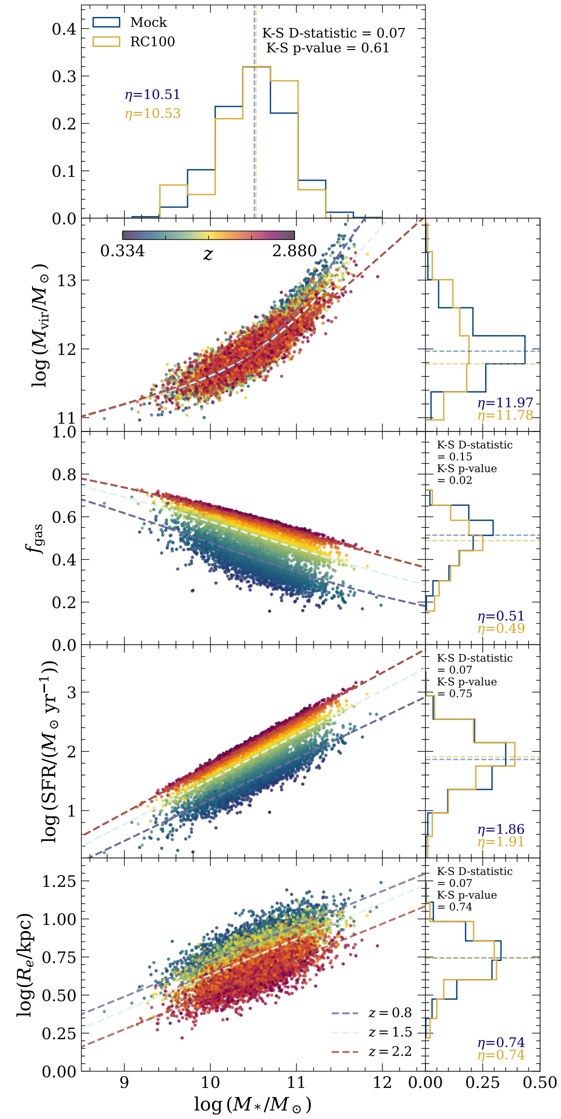

Figure 2.13 Distributions of stellar mass M_*, star formation rate (SFR), gas fraction ($f_{\rm gas}$) and virial mass $M_{\rm vir}$ of the baseline set of model galaxies generated with `DysmalPy`. The mock galaxy properties are guided by the parameter space coverage of the RC100 sample of A. Nestor Shachar et al. (2023), and derived from scaling relations as described in Sec. 2.3 and listed in Table 2.2. The empirical relations are plotted in dashed lines colored by redshifts. The mock sample (blue) is compared with the RC100 sample (yellow) in the histograms, annotated also by the Kolmogorov-Smirnov (K-S) statistic scores and the medians.

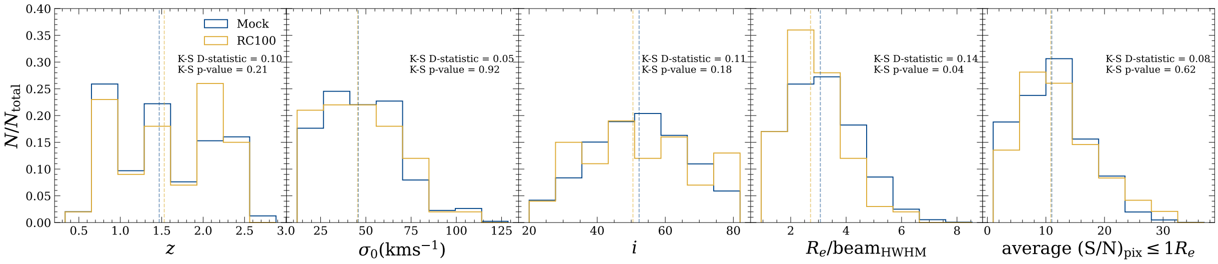

Figure 2.14 The distributions of redshift (z), velocity dispersion (σ_0), inclination (i), number of resolution elements within R_e ($R_e/\mathrm{beam}_{\mathrm{HWHM}}$) and signal-to-noise (S/N) of RC100 and the baseline mock sample. D-statistics and the associated p-value from the two-sample Kolmogorov-Smirnov (K-S) test are also shown to illustrate the resemblance of the resulting mock galaxies distribution and RC100.

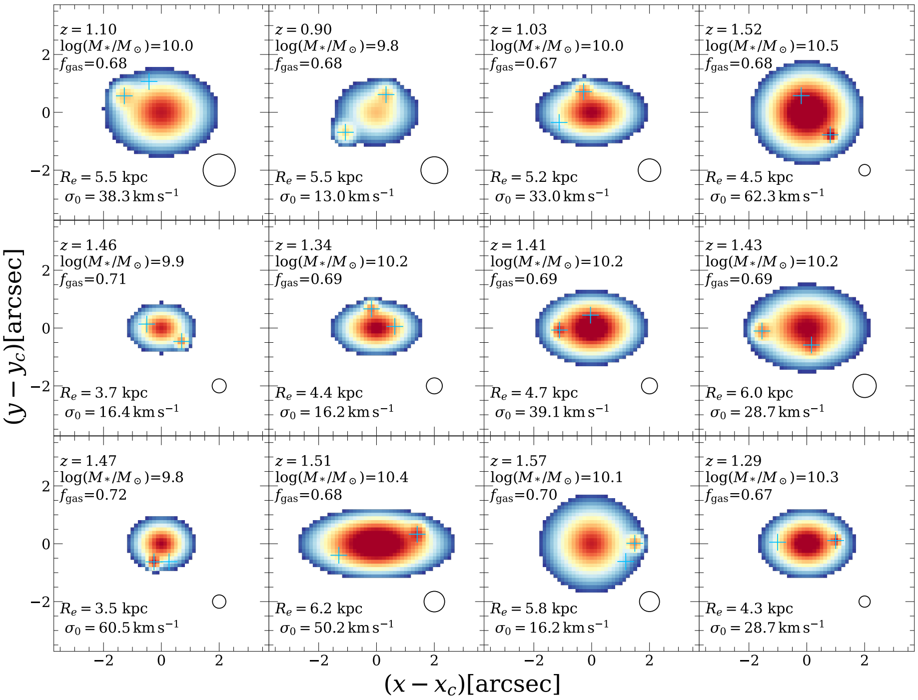

Figure 2.15 A gallery showing the (noiseless) zeroth moment maps of 12 selected clumpy galaxies out of a total of 500, created using `DysmalPy`. The color map represents the light intensity from blue to red. Cyan crosses mark the locations of the clumps. The beam size is shown at the bottom right corner of each panel. The properties of the smooth galaxy component are also listed on the left.

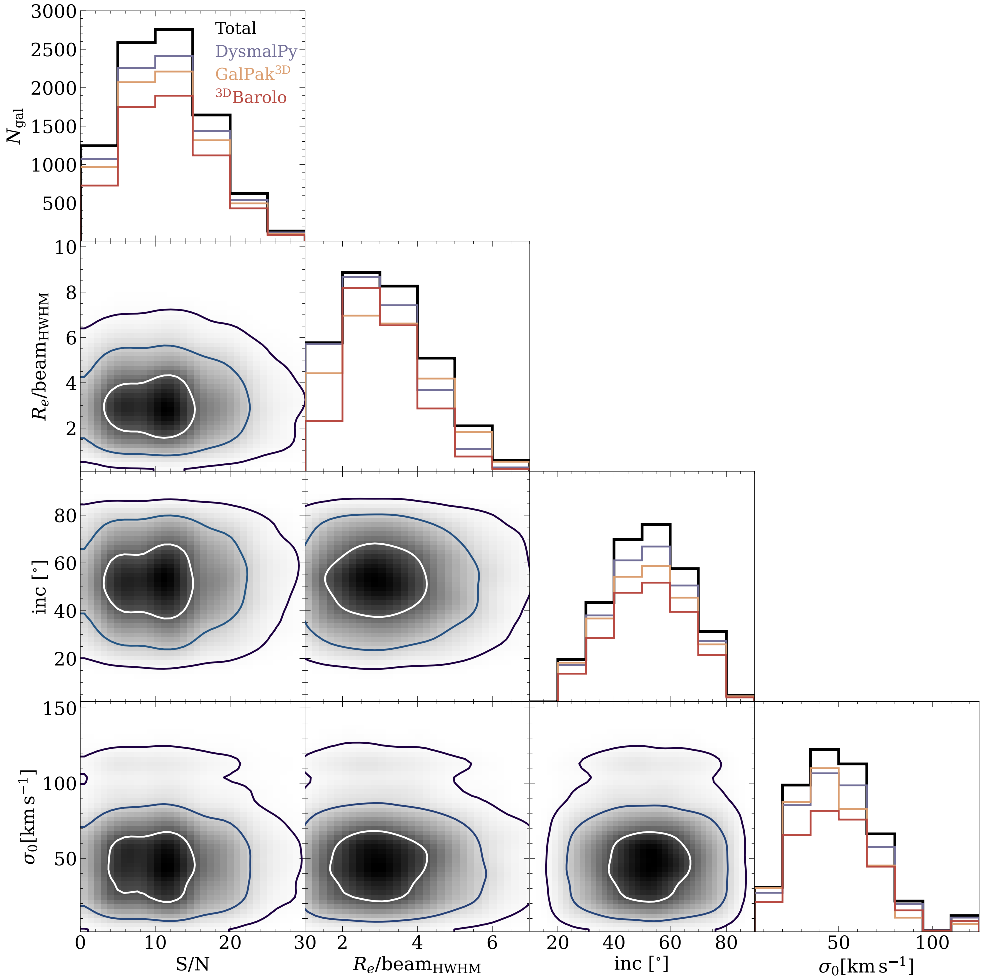

Figure 2.16 Corner plot showing the covariance distributions of velocity dispersion σ_0, inclination i, the number of resolution elements in one effective radius R_e/beam$_{\rm HWHM}$ and signal-to-noise ratio (S/N) used for the baseline mock sample. The contours correspond to $[1, 2, 3]\sigma$ of the distributions. The histograms indicate the individual distributions of the original baseline samples and the successfully modeled samples by `DysmalPy`, `GalPak`$^{\rm 3D}$, and $^{\rm 3D}$`Barolo`, respectively, in black, violet, orange, and red.

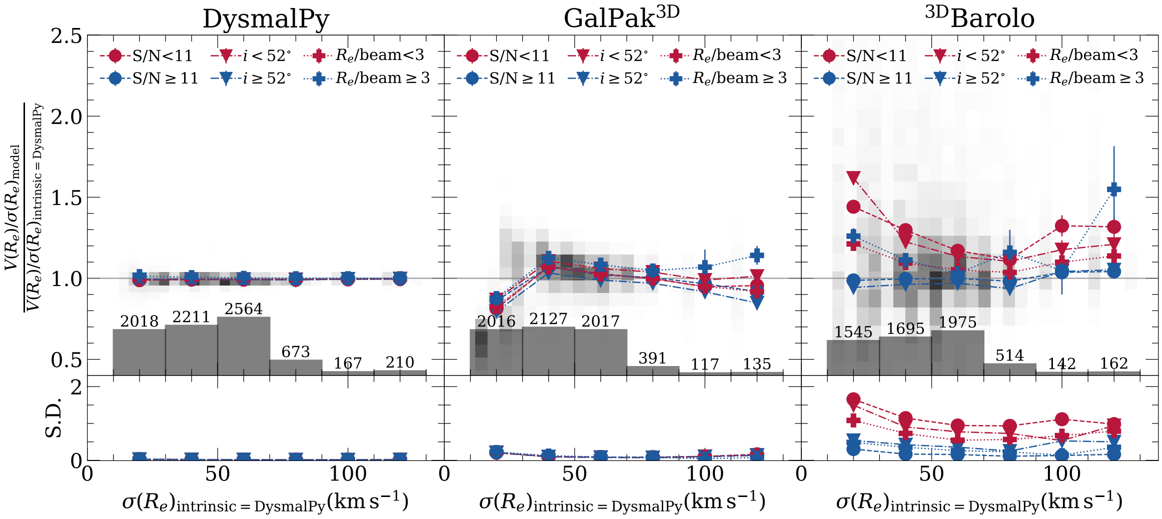

Figure 2.17 Comparisons between the recovered and intrinsic ratios of rotation velocity over velocity dispersion, evaluated at the effective radius ($V(R_{\rm e})/\sigma(R_{\rm e})$), for the baseline `DysmalPy`-generated mocks. The 2D histograms in the background represent the distribution of the parameters. The choices of line styles and markers for the running median curves are identical to Figure 2.2 and Figure 2.3. Given that $V(R_e)$ is satisfactorily recovered (Section 2.4.2) by all three codes, the primary factor responsible for most of the systematic biases in $V(R_{\rm e})/\sigma(R_{\rm e})$ lies in the recovered $\sigma(R_{\rm e})$. In the case of `GalPak`$^{\rm 3D}$ (*middle*), the predominant overestimation of σ occurs when intrinsic $\sigma < 30, {\rm km}, {\rm s}^{-1}$, where the self-gravity term becomes dominant (see Figure 2.8), leading to the underestimation of $V(R_e)/\sigma$ in the same regime. As for $^{\rm 3D}$`Barolo` (*right*), $V(R_{\rm e})/\sigma(R_{\rm e})$ is most overestimated when the signal-to-noise (S/N) is lower than 11, a result of the underestimated $\sigma(R_{\rm e})$.

2.10 Appendix D – Spearman's and MIC's correlation matrices

Fig. 2.18 shows the Spearman's ρ between the ratio $\sigma_{\rm model}(R_{\rm e})/\sigma_{\rm intrinsic}(R_{\rm e})$ and the S/N, i, $R_{\rm e}$/beam, and intrinsic σ for the `DysmalPy`-, `GalPak`$^{\rm 3D}$- and $^{\rm 3D}$`Barolo`-generated model set.

2.11 Appendix E – Recovery of σ of high-S/N mocks

To supplement Fig. 2.4, Fig. 2.19 shows the same median trends of σ recovery but focuses only on the S/N ≥ 11 recovery.

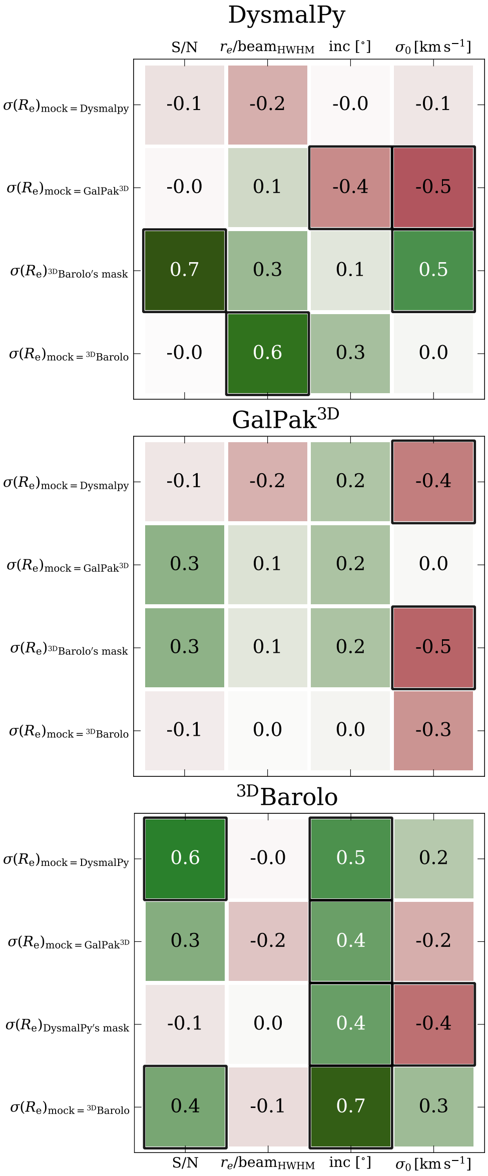

Figure 2.18 Spearman rank correlation matrix showing the strength of correlations between quality of σ recovery and the signal-to-noise (S/N), number of beams in an effective radius ($R_{\rm e}$/beam), inclination angle (i), and intrinsic velocity dispersion ($\sigma_{\rm intrinsic}$). Four cases are shown here: (i) baseline `DysmalPy`-generated mock models ($\sigma(R_{\rm e})_{\rm mock=\texttt{DysmalPy}}$), (ii) `GalPak`$^{\rm 3D}$ mock models ($\sigma(R_{\rm e})_{\rm mock=\texttt{GalPak}^{3D}}$), (iii) $^{\rm 3D}$`Barolo`'s masking applied in `DysmalPy` and `GalPak`$^{\rm 3D}$ ($\sigma(R_{\rm e})_{^{3D}\texttt{Barolo}\text{'s mask}}$) and vice versa for `DysmalPy`'s masking applied in $^{\rm 3D}$`Barolo` ($\sigma(R_{\rm e})_{\ \texttt{DysmalPy}\text{'s mask}}$), and (iv) $^{\rm 3D}$`Barolo` mock models($\sigma(R_{\rm e})_{\rm mock=^{3D}\texttt{Barolo}}$). The quality of σ recovery is represented by the ratio $\sigma(R_{\rm e})_{\rm model}/\sigma(R_{\rm e})_{\rm intrinsic}$ as in the main text, but here for simplicity, the y-axis label shows only the numerator. The black boxes highlight moderate or stronger correlations with absolute Spearman score ≥ 0.4. Unless "mock = `GalPak`$^{\rm 3D}$" or "mock = $^{\rm 3D}$`Barolo`" is indicated, the intrinsic dispersion value $\sigma(R_{\rm e})_{\rm intrinsic}$ is always that of the baseline mock models generated by `DysmalPy`.

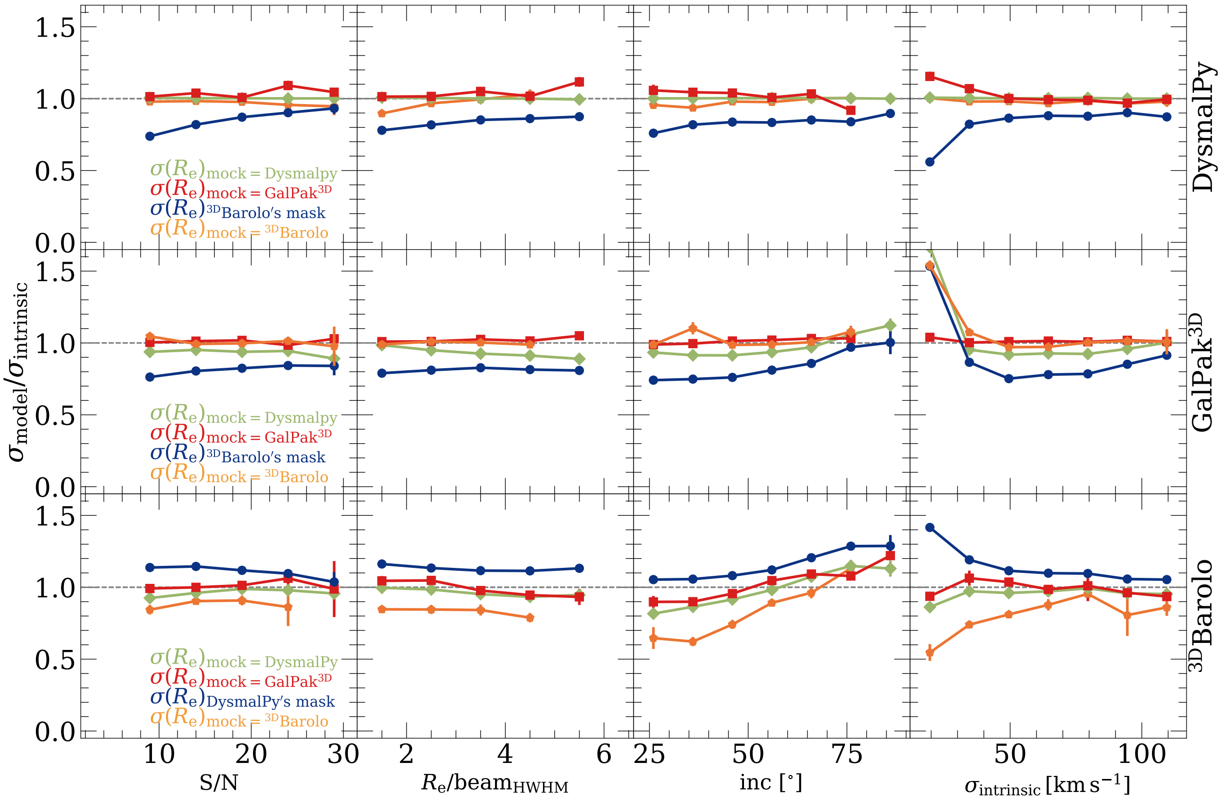

Figure 2.19 Similar to Figure 2.4 but only including mock models with signal-to-noise (S/N) ≥ 11.

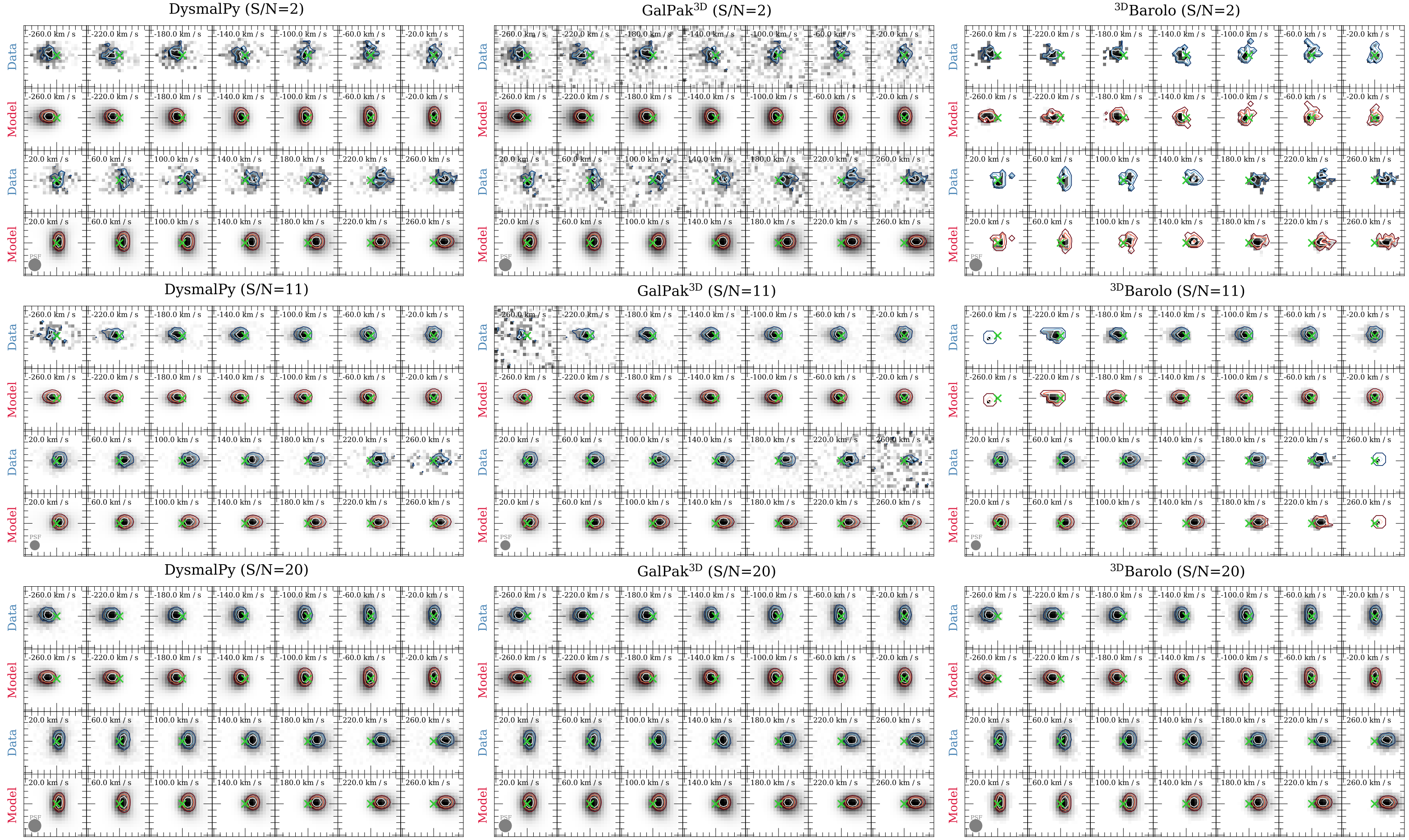

Figure 2.20 Channel maps in step of $40\,\mathrm{km\,s^{-1}}$ of the three example galaxies in Figure 2.12, arranged in order of increasing signal-to-noise (S/N) ratio from top to bottom, similar to Figure 2.12. The *second* and *fourth rows* of each panel display the model channel maps, overlaid with red contours, from the respective codes as labeled. Note that the channel width of the mocks is $10\,\mathrm{km\,s^{-1}}$, so the maps shown here represent every 4 channels.

2.12 Appendix F – PV diagrams and channel maps

We show in Figures 2.20 and 2.21 the channel maps at every 4 channels and PV diagrams of the three example galaxies in Fig. 2.12, respectively. The PV diagrams are extracted using `PVSLICE` task in $^{\mathrm{3D}}$`Barolo`, and are derived from the data cube masked by each of the respective codes, namely `DysmalPy` and $^{\mathrm{3D}}$`Barolo`.

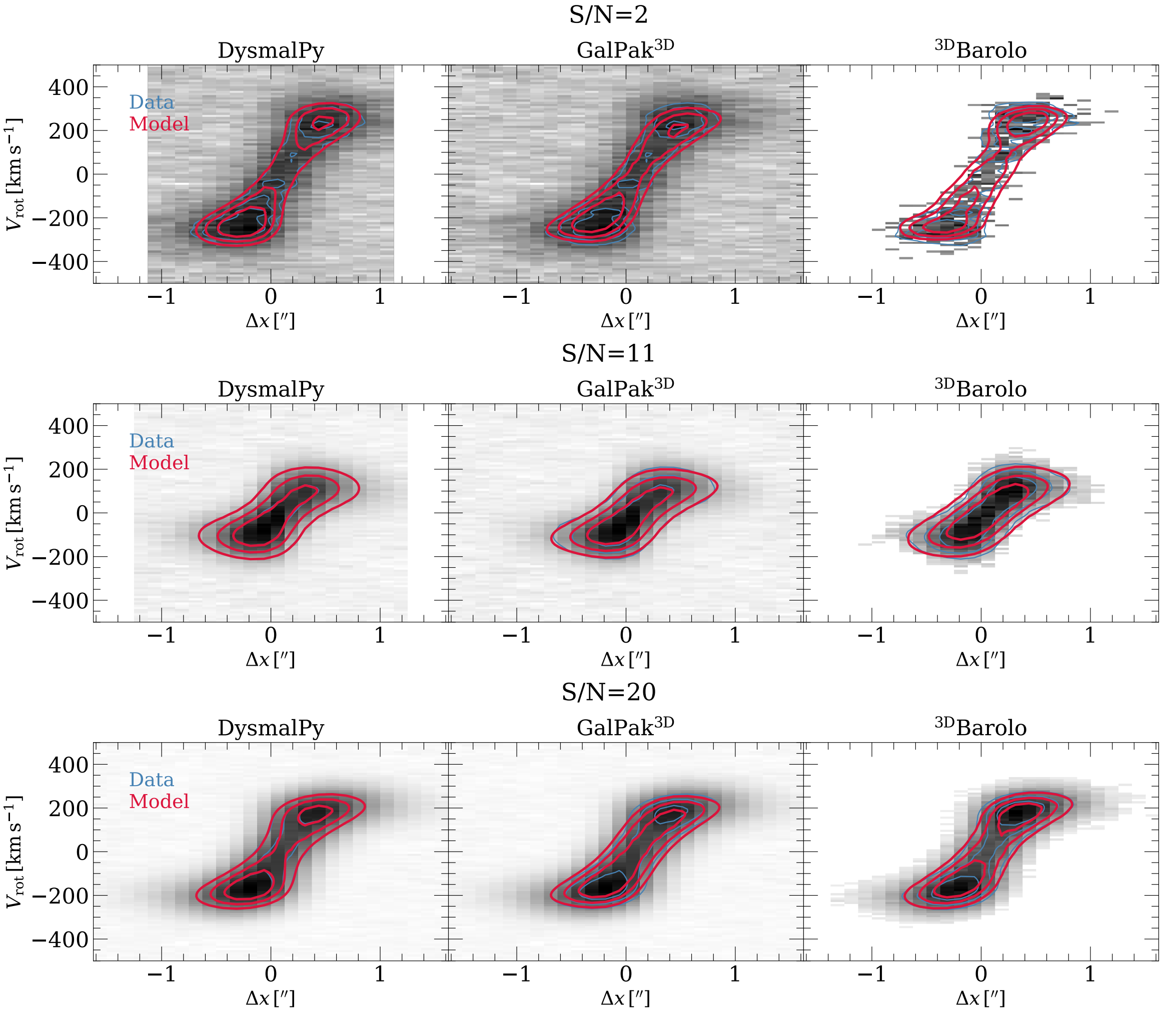

Figure 2.21 Position-velocity (PV) diagrams for the three example galaxies in Figure 2.12 arranged in increasing signal-to-noise (S/N) from top to bottom. The background image shows the PV diagram extracted from the data, masked by the respective codes for `DysmalPy` and ^{3D}`Barolo`, with the blue contours overlaid. The red contours are those of the PV diagrams of the model from the annotated codes.

Chapter 3

The ALMA-CRISTAL survey: Resolved kinematic studies of main sequence star-forming galaxies at $4 < z < 6$

This Chapter is a reprint of the A&A publication The ALMA-CRISTAL survey: Resolved kinematic studies of main sequence star-forming galaxies at $4 < z < 6$ by L. L. Lee et al. (2025b); doi:10.1051/0004-6361/202555362. ©EDP Sciences. Reproduced with permission from EDP Sciences.

Abstract – We present a detailed kinematic study of a sample of 32 massive ($9.5 \leqslant \log(M_*/\mathrm{M}_\odot) \leqslant 10.9$) main sequence star-forming galaxies (MS SFG(s)) at $4 < z < 6$ from the ALMA-CRISTAL programme. The data consist of deep (up to 15 hr observing time per target), high-resolution ($\sim$1kpc) ALMA observations of [C II]158μm line emission. This dataset allowed us to carry out the first systematic, kiloparsec-scale (kpc-scale) characterisation of the kinematics nature of typical massive SFG(s) at these epochs. We find that $\sim$50% of the sample are disk-like, with a number of galaxies located in systems of multiple components. Kinematic modelling reveals these main sequence disks exhibit high-velocity dispersions (σ_0), with a median disk velocity dispersion of $\sim 70\,\mathrm{km\,s^{-1}}$ and $V_{\mathrm{rot}}/\sigma_0 \sim 2$, which is consistent with dominant gravity driving. The elevated disk dispersions are in line with the predicted evolution based on Toomre theory and the extrapolated trends from $z \sim$ 0–2.5 MS star-forming disks. The inferred dark matter (DM) mass fraction within the effective radius $f_{\mathrm{DM}}(< R_{\mathrm{e}})$ for the disk systems decreases with the central baryonic mass surface density. This is consistent with the trend reported by kinematic studies at $z \lesssim 3$; roughly half the disks display $f_{\mathrm{DM}}(< R_{\mathrm{e}}) \lesssim 30\%$. The CRISTAL sample of massive MS SFG(s) provides a reference of the kinematics of a representative population and extends the view onto typical galaxies beyond previous kpc-scale studies at $z \lesssim 3$.

3.1 Introduction

Studying the kinematics of high-redshift galaxies offers a direct tracer of the distribution of stars, gas, and dark matter (DM) on galactic scales. Observations at multiple epochs provide constraints on the evolution of the contribution of rotation and turbulence to the dynamical support of galaxies. Therefore, galaxy kinematics serve as a powerful probe of the dominant mechanisms governing the growth and structural formation of galaxies, with processes including gas accretion, non-circular motions, galaxy interactions, and feedback.

Thanks to the advent of near-infrared (NIR) integral field units (IFU) and slit spectroscopy on 8–10m telescopes (e.g. F. Eisenhauer et al., 2003; R. Sharples et al., 2013), ionised gas kinematics from rest-frame optical emission lines have become routinely accessible at cosmic noon $z \sim 1$–3. This has enabled the census of resolved kinematics of massive star-forming galaxies (SFG(s)) at $z \sim 1$–3 on the main sequence (MS) of star-forming galaxies (SFG(s), e.g. N. M. Förster Schreiber et al., 2009; S. A. Kassin et al., 2012; E. Wisnioski et al., 2015), which dominate the population and cosmic star formation rate density (P. Madau & M. Dickinson, 2014). The cold gas kinematics of the same population of galaxies traced primarily via CO lines are increasingly available through the Atacama Large Millimeter/submillimeter Array (ALMA) and Northern Extended Millimetre Array (NOEMA) and employed in a number of recent studies (H. Übler et al., 2018; A. Nestor Shachar et al., 2023; F. Rizzo et al., 2023; D. Liu et al., 2023).

The general findings at $z \lesssim 3$ suggest that a majority of disks among massive (stellar masses $M_\star \gtrsim 10^{10} M_\odot$) SFG(s) have increasing gas velocity dispersion, σ_0, and decreasing rotational-to-dispersion support, $V_{\rm rot}/\sigma_0$, towards higher redshift. These findings are in line with the increase of galactic gas mass fractions, which play an important role in the emergence of the 'equilibrium growth' model of galaxy evolution (see reviews by L. J. Tacconi et al., 2020, and references therein) in the framework of marginally stable gas-rich disks (e.g. R. Genzel et al., 2008; A. Dekel et al., 2009b; A. Dekel & A. Burkert, 2014; A. Zolotov et al., 2015; O. Ginzburg et al., 2022). These works have highlighted the important role of internal processes, alongside accretion and merging, in galaxy stellar mass and structural build-up during the peak epoch of cosmic star formation activity around $z \sim 2$ (see e.g. reviews by K. Glazebrook, 2013; N. M. Förster Schreiber & S. Wuyts, 2020).

The exploration of kinematics beyond cosmic noon at $z > 3$ has been opened by facilities such as ALMA and NOEMA, primarily via the bright [C II]$^2P_{3/2}$–$^2P_{1/2}$ ([C II]158μm, hereafter [C II]) line emission. The [C II] line serves as a key coolant for the interstellar

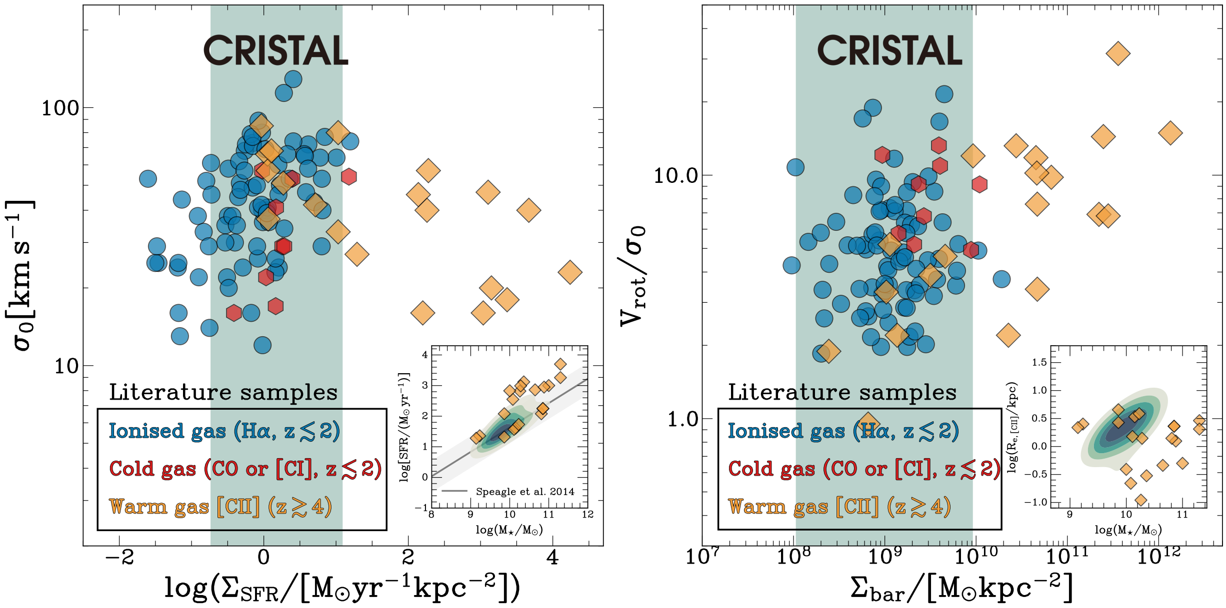

Figure 3.1 Parameter space of the CRISTAL sample in terms of surface densities of star formation rate ($\Sigma_{\rm SFR}$, left) and baryons ($\Sigma_{\rm bar}$, right). For comparison, the $z \sim 2$ MS galaxies observed in Hα (blue circles) and CO (red hexagons) by A. Nestor Shachar et al. (2023) are also shown. The inset of the left and right panels show the SFR-$M_\star$ and [C II]-sizes-$M_\star$ distributions of CRISTAL (green contour) and other studies at $z \gtrsim 4$ (yellow diamonds) (M. Neeleman et al., 2020; F. Rizzo et al., 2020, 2021; F. Fraternali et al., 2021; R. Herrera-Camus et al., 2022; E. Parlanti et al., 2023; F. Roman-Oliveira et al., 2023a), respectively. The solid line in the left inset is the MS relation from J. S. Speagle et al. (2014) at $z = 5$, with the shading representing ±0.5 dex offset from the relation. For the purposes of illustration, the values of CRISTAL shown on the plots are adopted from ALPINE (M. Béthermin et al., 2020; A. L. Faisst et al., 2020c; O. Le Fèvre et al., 2020). CRISTAL provides a higher-resolution sample of MS SFG(s) that fills up the parameter space currently poorly explored by existing $z \gtrsim 4$ samples observed with [C II], which predominantly comprises starburst and compact galaxies.

medium (ISM; e.g. M. G. Wolfire et al., 2003). Its relatively low ionisation potential of 11.3 eV (compared to 13.6 eV for hydrogen) allows [C II] to arise from various ISM phases, primarily from the photo-dissociation regions (PDRs; e.g. L. Vallini et al., 2015; P. C. Clark et al., 2019). Consequently, the [C II] line is an ideal tracer for kinematics, enabling measurements reaching well beyond the effective radii of these early galaxies (e.g. F. Lelli et al., 2021; G. C. Jones et al., 2021; T. Tsukui & S. Iguchi, 2021; H. Umehata et al., 2025).

So far, studies suggest that disks appear to be sub-dominant among the bulk of SFG(s) at $z \sim 4$–7 (from rest-UV-selected samples, e.g. R. Smit et al. 2018; O. Le Fèvre et al. 2020; G. C. Jones et al. 2021; R. Herrera-Camus et al. 2022; A. C. Posses et al. 2023). While some of them appear to be quite turbulent, high-resolution observations of small samples of individual galaxies, primarily IR-luminous dusty SFG(s), reveal the existence of dynamically cold disks at those early epochs (e.g. P. Sharda et al., 2019; F. Fraternali et al., 2021; F. Lelli et al., 2021; F. Rizzo et al., 2021; T. Tsukui & S. Iguchi, 2021; F. Roman-Oliveira et al., 2023a; L. E. Rowland et al., 2024). Larger, more systematic samples covering typical galaxies, such as those provided by ALPINE ($4 < z < 6$; O. Le Fèvre et al. 2020; M. Béthermin et al. 2020; A. L. Faisst et al. 2020c) and REBELS ($7 < z < 8$; R. J. Bouwens et al. 2022), are available, albeit at lower spatial resolution and shallower depths. Nevertheless, the typical SFG(s) targeted by ALPINE formed an ideal sample for high-resolution follow-up studies, providing the motivation for the CRISTAL ([C II] Resolved ISM in STar forming galaxies with ALMA) survey.

CRISTAL is designed to address four primary science goals: (i) kinematics, (ii) outflows, (iii) spatial distribution of the ISM and star formation, and (iv) the ISM conditions.

R. Herrera-Camus et al. (2022) presented a pilot study of the kinematics of one of the CRISTAL galaxies, HZ4 (CRISTAL-20). A. Posses et al. (2025) and K. Telikova et al. (2025) presented detailed case studies of the kinematics of CRISTAL-05 and CRISTAL-22, respectively, and highlighted the improvement in kinematics modelling of complex systems, thanks to higher resolution. The outflow properties of one of the CRISTAL galaxies are presented in R. L. Davies et al. (2025) and the overall outflow demographics through stacking in J. E. Birkin et al. (2025). Works addressing goals (iii) and (iv) are presented in J. Li et al. (2024a), I. Mitsuhashi et al. (2024), V. Villanueva et al. (2024), R. Ikeda et al. (2025), N. E. P. Lines et al. (2025), and M. Solimano et al. (2025). We refer to the overview survey paper by R. Herrera-Camus et al. (2025) for more details. In this paper, we present a systematic study of the kinematics of the CRISTAL sample.

The structure of this paper is as follows. In Sect. 3.2, we describe the sample selection and data reduction process. Sect. 3.3 presents the classification of the kinematic types and Sect. 3.4 discusses the disk fraction of CRISTAL galaxies. Sect. 3.5 discusses the kinematic properties of the disks from forward modelling, along with a comparison with literature results in the context of the dynamical evolution of MS SFG(s). Sect. 3.6 investigates the intrinsic velocity dispersion of CRISTAL disks in the broader context of the dynamical evolution of galaxies with redshift, exploring possible drivers of turbulence, in particular, gravitational instabilities and stellar feedback. In Sect. 3.7, we discuss the DM fraction within the effective radius of the CRISTAL disks, and its dependence on the circular velocity and baryonic surface density. Sect. 3.8 presents a brief discussion on the properties of non-disk galaxies. Finally, Sect. 4.7 summarises the key findings and outlines ways forward to improve constraints on the nature and kinematics of $z \sim 4$–6 galaxies.

Throughout, we adopted a flat ΛCDM cosmology with $H_0 = 70\,\mathrm{km\,s^{-1}\,Mpc^{-1}}$, and

$\Omega_m = 0.3$. Physical size is always reported in physical kiloparsecs (pkpc), but we use kpc henceforth for brevity. Where relevant, we quote the rest-frame air wavelengths unless specified otherwise.

3.2 Data and sample selection

3.2.1 Galaxy sample

The full CRISTAL sample is presented by R. Herrera-Camus et al. (2025). In brief, the survey builds on an ALMA Cycle-8 Large Program (2021.1.00280.L; PI: R. Herrera-Camus), targeting [C II] emission of 19 MS SFG(s) drawn from ALPINE (O. Le Fèvre et al., 2020), selected at $\log(M_\star/\mathrm{M}_\odot) \geqslant 9.5$ and within a factor of 3 of the MS in their specific SFRs ($\mathrm{sSFR}/\mathrm{sSFR(MS)} \leqslant 3$). At the higher resolution of the CRISTAL ALMA observations, some of these sources split into separate components. This sample was expanded with six systems satisfying the same criteria taken from pilot programmes and the literature (see details in R. Herrera-Camus et al., 2025). There are 39 galaxies in the final CRISTAL sample in total.

The sample studied here consists of the 32 galaxies near the MS that have sufficient S/N and are sufficiently well-resolved to perform quantitative measurements and model their kinematic properties. Table 3.1 lists the galaxies included in this kinematics sample, along with their redshifts, coordinates, stellar masses ($M_\star$) and SFRs, as well as the beam size and sensitivity of the ALMA data sets. Fig. 3.1 shows the range of $M_\star$, SFRs, and surface densities in SFR and baryonic masses (Σ_{SFR} and Σ_{bar}) covered by the CRISTAL MS SFG(s), in comparison to those drawn from selected detailed kinematics studies of disks at lower redshifts in ionised and cold molecular gas, and literature work at $z \gtrsim 4$ from [C II] data (M. Neeleman et al., 2020; F. Rizzo et al., 2020, 2021; F. Fraternali et al., 2021; R. Herrera-Camus et al., 2022; E. Parlanti et al., 2023; F. Roman-Oliveira et al., 2023a). CRISTAL MS SFG(s) are distinct from most existing samples that predominantly comprise starburst or compact galaxies, allowing for more direct comparisons to $z \sim 1$–3 kinematics studies of MS star-forming disks at lower redshifts (e.g. E. Wisnioski et al., 2015, 2019; R. Genzel et al., 2020; A. Nestor Shachar et al., 2023; A. Puglisi et al., 2023). For the purpose of the figures, we adopted the values from the ALPINE catalogues (M. Béthermin et al., 2020; A. L. Faisst et al., 2020c; O. Le Fèvre et al., 2020) to demonstrate the original sample selection. We adopted the values given in Table 3.1 for our subsequent analysis in this work.

Table 3.1. Properties of the 32 galaxies in kinematics sample of ALMA-CRISAL

CRISTAL ID	Full name	$z_{\rm [CII]}$	R.A. (°)	Decl. (°)	$\log\,(M_\star/{\rm M}_\odot)$ (dex)	$\log\,[{\rm SFR}/({\rm M}_\odot\,{\rm yr}^{-1})]^{\rm a}$ (dex)	Beam size	Cube Noise$^{\rm b}$ (mJy beam^{-1})
01a	DC_842313	4.554	150.2271	2.5762	10.65	2.31	$0\farcs42\times0\farcs47$	0.13
01b	. . .	4.530	150.2282	2.5745	9.81	1.71	$0\farcs42\times0\farcs47$	0.13
02	DC_848185, HZ6, LBG-1	5.294	150.0896	2.5864	10.30	2.25	$0\farcs45\times0\farcs55$	0.13
03	DC_536534, HZ1	5.689	149.9719	2.1182	10.40	1.79	$0\farcs68\times0\farcs82$	0.15
04a	vc_5100822662	4.520	149.7413	2.0809	10.15	1.89	$0\farcs57\times0\farcs75$	0.18
04b	vc_5100822662	4.520	149.7414	2.0813	8.91	0.63	$0\farcs57\times0\farcs75$	0.16
05	DC_683613, HZ3	5.541	150.0393	2.3372	10.16	1.83	$0\farcs31\times0\farcs38$	0.16
06a	vc_5100541407	4.562	150.2538	1.8094	10.09	1.62	$0\farcs45\times0\farcs54$	0.13
06b	. . .	4.562	150.2542	1.8097	9.19	1.07	$0\farcs45\times0\farcs54$	0.13
07a	DC_873321, HZ8	5.154	150.0169	2.6266	10.00	1.89	$0\farcs49\times0\farcs74$	0.18
07b	. . .	5.154	150.0166	2.6268	. . .	. . .	$0\farcs49\times0\farcs74$	0.18
07c	. . .	5.155	150.0134	2.6271	10.21	1.92	$0\farcs49\times0\farcs74$	0.18
08	vuds_efdcs_530029038	4.430	53.0793	-27.8771	9.85	1.88	$0\farcs54\times0\farcs80$	0.17
09a	DC_519281	5.575	149.7537	2.0910	9.84	1.51	$0\farcs33\times0\farcs36$	0.16
10a	DC_417567, HZ2	5.671	150.5172	1.9290	9.99	1.86	$0\farcs44\times0\farcs48$	0.09
10a-E	. . .	5.671	150.5186	1.9304	. . .	. . .	$0\farcs44\times0\farcs48$	0.09
11	DC_630594	4.439	150.1358	2.2579	9.68	1.57	$0\farcs38\times0\farcs47$	0.22
12	CG_21	5.572	53.0498	-27.6993	9.30	0.98	$0\farcs42\times0\farcs58$	0.12
13	vc_5100994794	4.579	150.1715	2.2873	9.65	1.51	$0\farcs44\times0\farcs52$	0.18
14	DC_709575	4.411	149.9461	2.3758	9.53	1.45	$0\farcs11\times0\farcs12$	0.15
15	vc_5101244930	4.580	150.1986	2.3006	9.69	1.44	$0\farcs36\times0\farcs42$	0.17
16a	CG_38	5.571	53.0662	-27.6901	9.60	1.30	$0\farcs42\times0\farcs58$	0.14

Table 3.1 (cont'd)

CRISTAL ID	Full name	$z_{\text{[CII]}}$	R.A. (°)	Decl. (°)	$\log(M_\star/\mathrm{M}_\odot)$ (dex)	$\log[\mathrm{SFR}/(\mathrm{M}_\odot\,\mathrm{yr}^{-1})]^{\mathrm{a}}$ (dex)	Beam size	Cube Noise[b] ($\mathrm{mJy\,beam^{-1}}$)
19	DC_494763	5.233	150.0213	2.0534	9.51	1.45	$0\farcs31\times0\farcs40$[c]	0.15
20[d]	DC_494057, HZ4	5.545	149.6188	2.0518	10.11	1.82	$0\farcs41\times0\farcs45$	0.06
21[d]	HZ7	5.255	149.8769	2.1341	10.11	1.80	$0\farcs32\times0\farcs35$	0.22
22a[d]	HZ10	5.653	150.2471	1.5554	10.35	2.13	$0\farcs27\times0\farcs34$	0.22
22b[d]	HZ10	5.653	150.2469	1.5554	...		$0\farcs27\times0\farcs34$	0.22
23a[e]	DC_818760	4.560	150.4786	2.5421	10.55	2.50	$0\farcs25\times0\farcs30$	0.35
23b[e]	DC_818760	4.562	150.4790	2.5421	10.46	1.72	$0\farcs25\times0\farcs30$	0.35
23c[e]	...	4.565	150.4778	2.5421	...	...	$0\farcs25\times0\farcs30$	0.35
24[e]	DC_873756	4.546	150.0113	2.6278	10.53	2.06	$0\farcs26\times0\farcs31$	0.46
25[e]	vc_5101218326	4.573	150.3021	2.3146	10.90	2.75	$0\farcs25\times0\farcs30$	0.38

[a] Adopted from J. Li et al. (2024a) and I. Mitsuhashi et al. (2024). They are in broad agreement with the values inferred from existing $L_{\text{[CII]}}$-SFR relations as demonstrated by J. Li et al. (2024a) and references therein.

[b] Cube noise are measured in cubes with $20\,\mathrm{km\,s^{-1}}$ channel width.

[c] Briggs-weighted data is used.

[d] CRISTAL pilot targets.

[e] From ALMA archive.

Note. — DC, vc, and CG stand for the following: DEIMOS_COSMOS, vuds_cosmos and CANDELS_GOODSS, respectively. CRISTAL-01c, 07d, 09b, 10b, 16b, 17, 18 are not included in this study because they are either too faint for kinematics analysis or not detected. SMG J1000+0234 and CRLE are excluded because they are starburst galaxies. A full table with all CRISTAL source is available in Table 1 of R. Herrera-Camus et al. (2025).

3.2.2 ALMA observations and data

We refer to R. Herrera-Camus et al. (2025) for the observation setup. In brief, each observation was reduced using the standard `CASA` (Common Astronomy Software Applications; CASA Team et al. 2022) pipeline. Each cube was continuum-subtracted in the *uv* plane, resulting in a line-only, continuum-free data cube. For the kinematics modelling, we used the cubes with channel with of $20\,\mathrm{km\,s^{-1}}$ and natural weighting.[1] We did not apply the 'JvM' correction (S. Jorsater & G. A. van Moorsel, 1995) in our analysis, as it mostly affects the measurement of integrated properties.

3.2.3 Space-based ancillary data

All of the galaxies in the kinematics sample benefit from high-resolution broad-band optical to mid-IR imaging obtained with the *Hubble* Space Telescope (HST) and, in most cases, also the *James Webb* Space Telescope (JWST). Covering stellar continuum emission at rest-frame UV to near-IR wavelengths, this imaging data provides important complementary information for a full morpho-kinematic classification and important priors in the dynamical modelling of [C II] kinematics. These data sets were reduced in a homogeneous fashion for the CRISTAL sample, as described by J. Li et al. (2024a) and R. Herrera-Camus et al. (2025).

3.3 (Morpho)-kinematic classification

In this section, we describe the classification of the galaxies from the CRISTAL kinematics sample. We used several methods devised for applications to IFU and interferometric observations of high-redshift galaxies, with a comparable S/N and resolution as our ALMA data. We determined the final classification by combining the results from each method detailed in Sects. 3.3.1–3.3.5. We assigned two points to three metrics (PV, kinemetry, and spectro-astrometry) and one point to $V_{\mathrm{obs}}/2\sigma$ and morphological information, amounting to eight points.

Table 3.2 compiles the relevant measurements and resulting classification. Appendix 3.10 provides details of the individual galaxies. In summary, the systems in the CRISTAL sample can be broadly classified into three general groups:

---

[1] Except for CRISTAL-19, in which the higher resolution Briggs-weighted (robust = 0.5) cubes have sufficient S/N. There is, however, no significant difference in the kinematics modelling results between the natural-weighted and Briggs-weighted cubes.

Table 3.2. Kinematic Classification and Properties of CRISTAL galaxies

ID	Classification[a]	PA$_k$[b] (°)	$V_{obs}/2$[c] (km s^{-1})	$V_{obs}/2\sigma_{int}$[d]	f_{molgas}[e]	K_{asym}[f]	Disk Score[g] (Total: 8)
01a	Non-Disk	295.6	116.54 ± 26.56	0.41 ± 0.09	$0.10^{+0.21}_{-0.06}$	0.29 ± 0.05	3
01b	Non-Disk	325.8	54.54 ± 5.64	0.46 ± 0.12	…	0.63 ± 0.78	3
02	Disk	126.9	65.19 ± 6.24	0.45 ± 0.04	$0.43^{+0.21}_{-0.11}$	0.23 ± 0.03	5
03	Best Disk	126.6	50.0 ± 11.99	0.35 ± 0.09	$0.13^{+0.14}_{-0.06}$	0.15 ± 0.03	7
04a	Non-Disk	171.5	47.16 ± 13.87	0.58 ± 0.17	$0.39^{+0.25}_{-0.12}$	0.71 ± 0.12	1
04b	Non-Disk	207.9	27.6 ± 20.78	0.68 ± 0.51	…	0.54 ± 0.15	1
05a	Disk	…	…	…	$0.39^{+0.29}_{-0.13}$	…	…[h]
05b	Non-Disk	…	…	…	…	…	…[h]
06a	Non-Disk	268.0	44.18 ± 2.09	0.57 ± 0.03	$0.51^{+0.26}_{-0.13}$	2.10 ± 0.28	3
06b	Disk	79.0	48.11 ± 7.29	0.56 ± 0.09	…	0.35 ± 0.17	5
07a	Disk	359.0	83.3 ± 6.03	0.88 ± 0.08	$0.43^{+0.28}_{-0.13}$	0.20 ± 0.03	5
07b	Non-Disk	66.8	63.37 ± 15.79	0.62 ± 0.16	…	0.84 ± 0.15	3
07c	Non-Disk	32.0	100.56 ± 19.01	0.91 ± 0.18	$0.21^{+0.20}_{-0.09}$	0.81 ± 0.42	4
08	Best Disk	123.0	110.43 ± 28.70	0.94 ± 0.25	$0.63^{+0.29}_{-0.13}$	0.18 ± 0.06	7
09a	Disk	170.0	84.27 ± 59.79	0.63 ± 0.45	$0.74^{+0.32}_{-0.12}$	0.25 ± 0.27	6
10a	Non-Disk	226.0	127.79 ± 24.82	0.78 ± 0.16	$0.73^{+0.23}_{-0.11}$	0.36 ± 0.06	3
10a-E	Disk	123.0	30.54 ± 15.88	0.32 ± 0.16	…	0.35 ± 0.03	6
11	Best Disk	335.0	63.19 ± 45.60	0.45 ± 0.32	$0.73^{+0.23}_{-0.11}$	0.13 ± 0.05	8
12	Disk	34.3	25.72 ± 18.66	0.43 ± 0.31	$0.67^{+0.43}_{-0.15}$	0.45 ± 0.08	7
13	Non-Disk	17.0	145.26 ± 13.16	0.96 ± 0.11	$0.63^{+0.27}_{-0.13}$	0.37 ± 0.03	4
14	Non-Disk	61.9	73.79 ± 27.03	0.55 ± 0.20	$0.78^{+0.23}_{-0.10}$	0.49 ± 0.33	3
15	Best Disk	308.2	37.27 ± 3.89	0.28 ± 0.03	$0.41^{+0.27}_{-0.13}$	0.51 ± 0.22	7
16	Non-Disk	14.0	52.58 ± 9.06	0.44 ± 0.08	$0.69^{+0.35}_{-0.14}$	2.78 ± 0.70	1
19	Best Disk	313.0	110.58 ± 37.79	0.89 ± 0.31	$0.70^{+0.27}_{-0.12}$	0.17 ± 0.32	8
20	Best Disk	17.0	68.31 ± 13.26	0.73 ± 0.14	$0.47^{+0.35}_{-0.15}$	0.14 ± 0.08	8
21	Non-Disk	41.0	27.82 ± 18.31	0.19 ± 0.12	$0.59^{+0.28}_{-0.13}$	2.17 ± 1.43	4
22a	Disk	…	…	…	$0.71^{+0.28}_{-0.12}$	…	…[i]
22b	Non-Disk	…	…	…	…	…	…[i]
23a	Non-Disk	354.0	45.79 ± 1.27	0.40 ± 0.02	$0.40^{+0.23}_{-0.12}$	1.12 ± 0.29	3
23b	Disk	260.0	51.31 ± 2.32	0.34 ± 0.02	$0.25^{+0.18}_{-0.09}$	0.21 ± 0.02	6
23c	Best Disk	45.0	92.78 ± 4.82	0.83 ± 0.06	$0.17^{+0.13}_{-0.07}$	0.17 ± 0.04	8
24	Non-Disk	60.0	140.69 ± 22.69	0.43 ± 0.07	$0.51^{+0.06}_{-0.05}$	0.38 ± 0.11	4
25a	Non-Disk	309.0	60.03 ± 30.54	0.61 ± 0.31	…	0.45 ± 0.10	4
25b	Non-Disk	335.0	98.95 ± 26.06	0.86 ± 0.23	…	0.32 ± 0.08	4

[a] Classification of the sample based on the Disk Score.

[b] Position angle along the kinematic major axis pointing to the blue side.

[c] Half difference between the observed maximum and minimum velocities: $V_{obs}/2 = (V_{max} - V_{min})/2$.

[d] Ratios between (c) and the [C II] integrated line widths σ_{int}.

[e] Molecular gas fraction inferred in Appendix 3.12 for systems with dust continuum detection

[f] Asymmetry measure of the velocity and velocity dispersion fields following K. L. Shapiro et al. (2008) demarcation.

[g] The sum of points from the metrics outlined in Sects. 3.3.1–3.3.5, with the following scheme: Best Disk if Disk Score $\geqslant 7$, Disk if 5–6, and Non-Disk if $\leqslant 4$.

[h] See A. Posses et al. (2025).

[i] See K. Telikova et al. (2025).

1. Best Disk (22%): Score $\geqslant 7$. These are clear disks with no clear sign of nearby interacting companions within a projected distance of ~ 20 kpc in the HST, JWST, and ALMA data. The velocity gradients are monotonic with a well-defined kinematic position angle ($\mathrm{PA_k}$), and the location of steepest slope coinciding with a central peak in observed velocity dispersion, defining the kinematic centre.

2. Disk (28%): Score = 5–6. They show features of a rotating disk, but also irregularities. These systems meet most criteria but exhibit some deviations from one or the other pure disk rotation features. Except for two cases, they belong to systems with visible companions in both [C II] and HST or JWST imaging data.

3. Non-Disk (50%): The rest of the systems with a score of $\leqslant 4$. They do not have an apparent velocity gradient across $\geqslant 2$ beams and no centralised dispersion peak. Some of them have a visible companion.

3.3.1 Position-velocity diagrams

We extracted position-velocity (p-v) diagrams from the original reduced data cubes along the kinematic major axis ($\mathrm{PA_k}$), defined as the direction of the largest observed velocity difference across the source. The width of the synthetic slit is equal to the FWHM of each beam, which was taken to be the geometric average of the major and minor axes values listed in Table 3.1. The slit was positioned to pass through the dynamical centre of the galaxies. We then integrated the light along the spatial direction perpendicular to the slit orientation. These p-v diagrams are presented in Figs. 3.19 to 3.25 in Appendix 3.10. For visualisation purposes, we median-filtered the p-v diagrams with a kernel size of 3 pixels.

We classified a system as disk-like if there are no detached and distinct velocity structures in the p-v diagrams. This metric contributes to two points in the disk score in Table 3.2. We did not consider deviations (e.g. CRISTAL-02 and 08) from a standard S-shape as indicative of a merger, as they may instead reflect the possible origin of non-circular gas flow, which could be common for gas-rich systems at higher redshifts.

3.3.2 Kinematics profiles and $V_{\mathrm{obs}}/2\sigma_{\mathrm{int}}$

The ratio between the full observed velocity difference across a source (V_{obs}) and the source-integrated line width (σ_{int}) has been used as a proxy to distinguish systems with dominant support from rotational and orbital motions versus random motions (e.g. N. M. Förster Schreiber et al., 2009; E. Wisnioski et al., 2015). The V_{obs} and σ_{int} values can be

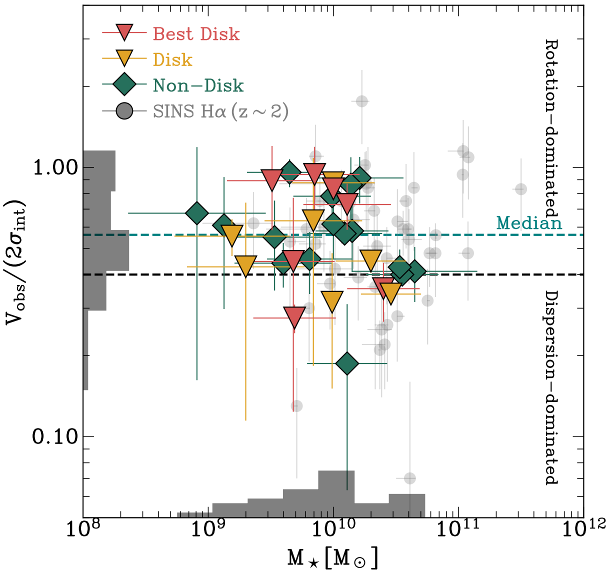

Figure 3.2 Ratios of observed half velocity gradient $V_{\rm obs}/2$ and integrated line width ($\sigma_{\rm int}$) of [C II] as a function of stellar mass $M_\star$. The black horizontal dashed line represents the distinction value ($V_{\rm obs}/2\sigma_{\rm int} = 0.4$), which demarcates the boundary between rotation- and dispersion-dominated systems, as commonly used in the literature.

measured from the data, without the need for beam-smearing or inclination corrections. The boundary at $V_{\rm obs}/2\sigma_{\rm int} = 0.4$ adopted in previous work, based on mock disk models, is also applicable for the typical range of galaxy sizes relative to beam sizes for our sample.

We measured the integrated line width, $\sigma_{\rm int}$, from spatially integrated spectra extracted from the reduced data cubes. The cubes are at the original spatial and spectral resolution and with the channel size of $\Delta V = 20\,{\rm km\,s^{-1}}$. The circular apertures for the extraction are positioned at the light centre of the galaxies, determined from the [C II] line maps, in order to capture the contributions from both velocity gradients and local velocity dispersion to $\sigma_{\rm int}$. The apertures' sizes roughly followed those determined by R. Ikeda et al. (2025). We then summed the spectra of individual pixels within the apertures to obtain the integrated spectrum. The extracted spectra are shown in the last column of Figs. 3.19 to 3.25 in Appendix 3.10.

We fitted the spectrum with a single Gaussian with `emcee` (D. Foreman-Mackey et al., 2013) to extract the line widths, except for CRISTAL-02, where we fit a double Gaussian profile as there is a broad component possibly associated with an outflow (R. L. Davies et al., 2025). The emission from the narrow component is always the one used in this analysis.

The fitted values of integrated line widths ($\sigma_{\rm int}$([C II])) are annotated in Figs. 3.19

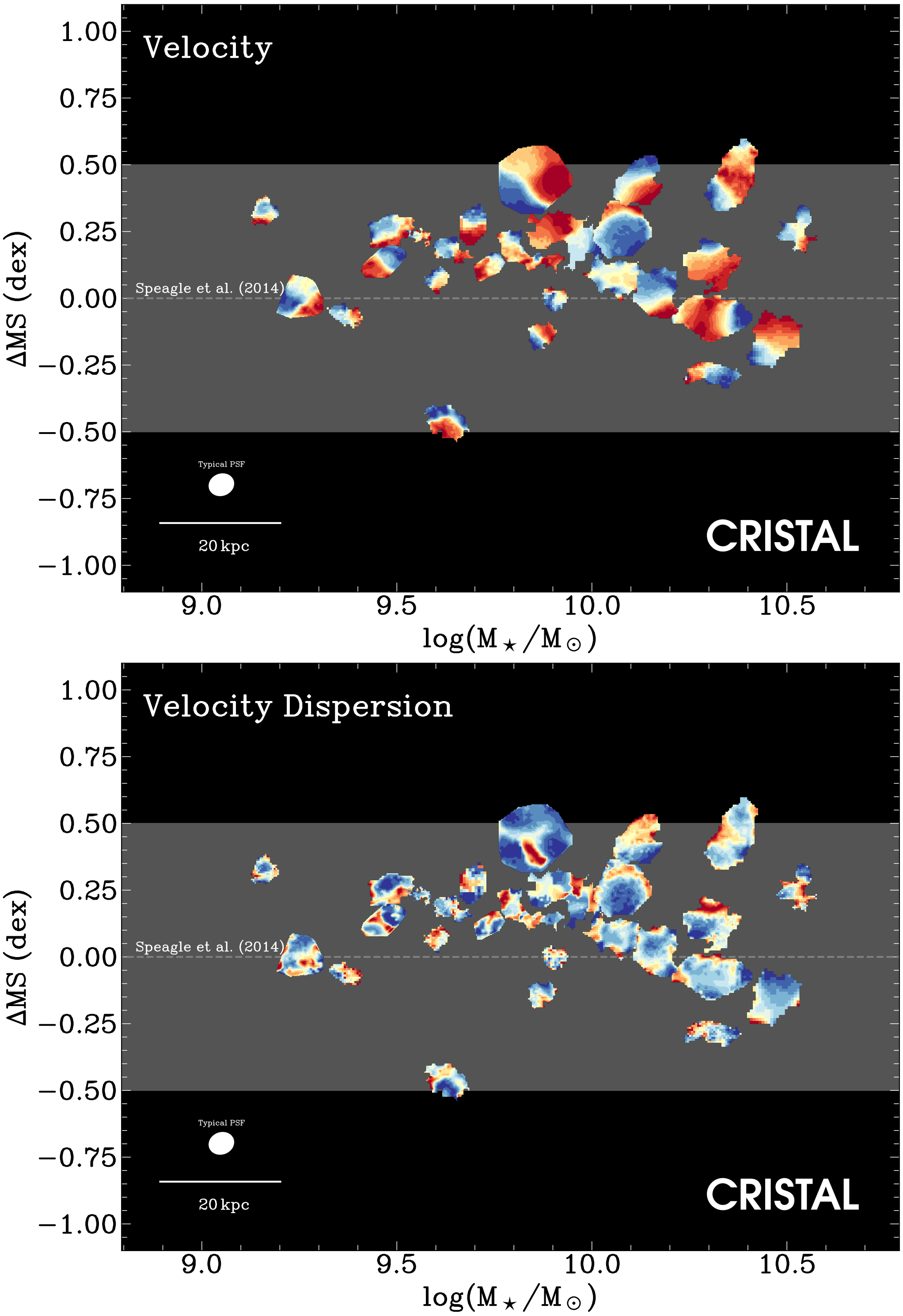

Figure 3.3 Velocity (*Top*) and velocity dispersion (*bottom*) fields of CRISTAL galaxies placed on the ΔMS offset relative to the J. S. Speagle et al. (2014) main-sequence (MS) relation. The velocity and dispersion fields correspond to that derived from the [C II] emission described in § 3.3.3. For the velocity fields, the colour coding represents the relative velocity of the line emission with respect to the systemic velocity. For the dispersion fields, the colour coding indicates the widths (in standard deviation) of the 1D Gaussian fitted to the spectra of individual spaxels. All sources are shown in the same field of view of 3″ (∼20 kpc at $z \sim 5$). The median beam size (0.″43×0.″36) with position angle (104° counter-clockwise from north) is shown at the bottom left; the individual values are listed in Table 3.1.

to 3.25 along with the best-fit model overlaid on the extracted spectra. Uncertainties of $\sigma_{\rm int}$([C II]) are taken as the $[16, 84]$-th percentile (1σ) bounds of the marginalised posterior distributions. We stress that the $\sigma_{\rm int}$ quantity determined here does not represent the local intrinsic disk velocity dispersion, but rather a global measure of the dynamical support combining rotation and orbital motions as well as random motions.

The value of $V_{\rm obs}$ is defined as the maximum observed velocity difference $V_{\rm obs} = V_{\rm max} - V_{\rm min}$. We extract velocity profiles from the p-v diagrams obtained in Sect. 3.3.1 by fitting a single Gaussian profile column-by-column (i.e., collapsed emission of the velocity channels at the same position) using again `emcee` (D. Foreman-Mackey et al., 2013). A one-pixel-wide vertical pseudo-slit is moved along the position axis. The centroids and widths of the fitted Gaussian models would then be the velocity and velocity dispersion at the locations of the slits. Finally, the extracted profiles were down-sampled by averaging to a resolution of one-half to one-fourth of the beam FWHM. The velocity and velocity dispersion profiles can then serve as an input for the dynamical modelling in Sect. 3.5.

We list the $V_{\rm obs}/2\sigma_{\rm int}$ of our sample in Table 3.2. We plot in Fig. 3.2 the distribution of $V_{\rm obs}/2\sigma_{\rm int}$ as a function of the stellar mass. For comparison, we show the values for the SINS Hα IFU sample at $z \sim 2$ (N. M. Förster Schreiber et al., 2009). The median $V_{\rm obs}/2\sigma_{\rm int}$ of all samples is 0.56. For the Best Disk, Disk and Non-Disk samples, the median values are 0.73, 0.45, and 0.57, respectively.

We observe that many Non-Disk systems have $V_{\rm obs}/2\sigma_{\rm int} > 0.4$, which can be attributed to the fact that mergers may exhibit a substantial projected velocity gradient from orbital motions, depending on the orientation of the merging system. While the $V_{\rm obs}/2\sigma_{\rm int}$ ratio is useful, especially in cases where the sources are less well resolved, it is not sufficient to unambiguously distinguish disks from mergers. Therefore, this metric contributes only one point to the disk score, as reported in Table 3.2.

3.3.3 Velocity and velocity dispersion maps and their asymmetry

To derive the flux, velocity, and velocity dispersion maps, we fitted a single Gaussian profile to the [C II] emission line of each spaxel in the continuum-subtracted line cube in velocity units, with the amplitude, mean and standard deviation of the profile as free parameters. In the resulting [C II] kinematic maps, we masked pixels with $\mathrm{S/N} < 3$ and pixels resulting in unphysical outlier values. For the velocity map, we determined the systemic velocity of the galaxy by symmetrising the red-shifted and blue-shifted peak velocities. Fig. 3.3 displays the derived velocity and velocity dispersion maps, plotted in the $M_\star$ versus offset from the MS in SFR. The line flux, velocity, and velocity dispersion maps of individual galaxies are shown in the fourth and fifth columns of Figs. 3.19 to 3.25 in Appendix 3.10.

Under the assumption of a single Gaussian profile, our fits primarily capture the narrower line emission component dominated by star formation. Such single-component fits of individual pixel spectra will scarcely be sensitive to possible emission from broader lines originating, e.g. from outflowing gas as long as the amplitude of the broad component is sufficiently low (e.g. N. M. Förster Schreiber et al., 2018). Examination of our CRISTAL data shows this is the case for all galaxies considered here except for CRISTAL-02, where more prominent outflow components are detected (R. L. Davies et al., 2025). In the kinematic maps of these galaxies, the regions (largely outside of the main body of the sources) are masked out for quantitative analysis.

We then use kinemetry (D. Krajnović et al., 2006) to quantify asymmetries in the velocity and velocity dispersion maps of our galaxies. We followed the method described by K. L. Shapiro et al. (2008) for applications in studies of galaxy kinematics at $z \sim 2$ (see also, e.g. A. M. Swinbank et al., 2012a; R. Genzel et al., 2023).

Kinemetry allows us to perform a Fourier analysis on the velocity and dispersion maps, decomposed into concentric ellipses, with the centre, position angle (PA), and inclination determined a priori through methods detailed in Sect. 3.3.1. Given the limited S/N and angular resolution of our data, we fixed the centre, $\mathrm{PA_k}$, and inclination to the adopted values in Sects. 3.3.1 and 3.5, respectively. We also required at least 75% of valid pixels in an annulus. We followed the Fourier expansion up to the fifth-order term, similar to K. L. Shapiro et al. (2008).

We used the demarcation set by K. L. Shapiro et al. (2008) at $K_{\mathrm{asym}} = \sqrt{(v_{\mathrm{asym}}^2 + \sigma_{\mathrm{asym}}^2)} = 0.5$, above which the system is classified as a merger and below which is a disk. The values of v_{asym} and σ_{asym} are dimensionless measurements of the average higher-order kinematic coefficients in the Fourier expansion relative to the coefficients corresponding to the regular rotation.

We plot the v_{asym} and σ_{asym} of the CRISTAL galaxies in Fig. 3.4. There are 20 and 10 galaxies (out of 30 with measurements) that fall into the ‘disk’ and ‘merger’ regime, respectively, according to the fiducial $K_{\mathrm{asym}} = 0.5$. Some Disks and Non-disks (according to the overall classification) overlap in the region around the boundary, which can reflect intrinsic deviations from pure circular motions caused by minor merging, non-axisymmetric structures such as bars and spirals, even in the absence of interactions, noise in kinematic maps or incomplete coverage of the objects due to regions with lower S/N and fainter surface brightness, beam smearing, or a combination of these factors. For illustrative purposes, we indicate in Fig. 3.4 the band corresponding to $K_{\mathrm{asym}} = 0.3$ to 0.9, for the simulated galaxies used by K. L. Shapiro et al. (2008), to calibrate the threshold would result in 6% higher

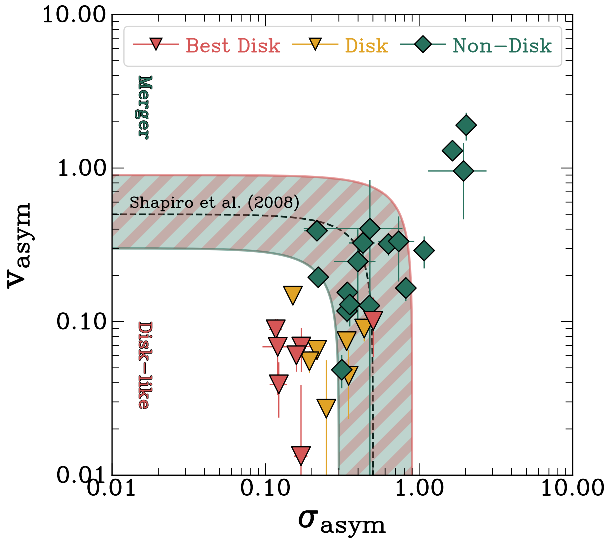

Figure 3.4 Asymmetry measure of the velocity and velocity dispersion fields for the CRISTAL galaxies from `Kinemetry` (D. Krajnović et al., 2006). The black dashed line represents the demarcation in K. L. Shapiro et al. (2008) at $K_{\rm asym} = 0.5$. With this metric alone, we classify a system as disk-like if it falls below the dashed line and as a merger if it falls above. Over half of the samples fall below the dashed line. The pink ($K_{\rm asym} = 0.9$) and green ($K_{\rm asym} = 0.3$) lines indicate the modified demarcations.

merger fraction or 3% higher disk fraction, respectively. Adopting the fiducial threshold for CRISTAL, we classified galaxies with $K_{\rm asym} \leqslant 0.5$ as a disk, counting for two points in the disk score from this metric.

3.3.4 Spectro-astrometry

We also applied spectro-astrometry (SA) to classify our sample. This technique, commonly used to study compact, marginally resolved stellar binary systems (e.g. J. W. Christy et al., 1981; J. M. Beckers, 1982) was successfully applied to IFU observations of high-z galaxies (e.g. A. Gnerucci et al., 2010; M. Perna et al., 2025). SA operates on the principle that closely spaced sources with projected separation below the angular resolution element can be spectrally separated if their relative velocities differ. This technique leverages the 3D information in data cubes and can be especially useful in retrieving velocity gradients when beam smearing is important.

For each velocity channel map, we derived the spatial offsets along the X and Y directions by fitting a 2D Gaussian without any a priori assumptions of the kinematics major axis. In cases where multiple emission peaks were observed and separated by multiple beams in FWHM, we fitted multiple 2D Gaussians to the emission blob. We derived the positional uncertainty following Eq. (1) in J. J. Condon et al. (1998), which depends on the amplitude of the emission and the beam size, in addition to the formal fitting errors. We show the locus traced by the SA measurements in the sixth column in Figs. 3.15 to 3.18 in Appendix 3.10, overlaid on either HST or JWST colour images.

For a galaxy to be considered Best Disk, its SA locus should be unidirectional, i.e., moving along monotonically in one direction, as in the case of CRISTAL-15 and 20 (Fig. 3.15). However, for systems with non-circular motion, the loci would deviate from a straight line near the centre, as in the case of CRISTAL-02 and 08, but would overall follow a single direction. In all cases, the overall direction of the velocity gradients agrees with the velocity map with consistent $\mathrm{PA_{kin}}$. For Non-disks, the SA loci would exhibit a more zig-zag shape, characterised by sudden changes in opposite direction; when companions are present, the loci show discontinuities with abrupt jumps from one location to another, often separated by one to two resolution elements.

The inherent nature of SA results in uneven spatial sampling, while spectral sampling remains constant. The spectral resolution of our SA measurement is naturally determined by the channel width, which is set at $20\,\mathrm{km\,s^{-1}}$. We did not consider a wider channel width, such as e.g. $50\,\mathrm{km\,s^{-1}}$ because it would have poorly compromised spectral sampling for several sources with observed velocities $v_{\mathrm{obs}} < 200\,\mathrm{km\,s^{-1}}$ (Table 3.2). In the case of Non-Disk sources, which could potentially be mergers, there could be a few channels with emission peaks that are spatially close to each other. Although this may appear to be a spatial sampling that is too high on the SA curve, we have chosen to retain these data, as they could indicate unresolved line-of-sight mergers.

The fainter outer regions of the sources, often associated with the most blue- or redshifted emission, tend to have too low S/N for a robust centroid measurement. Consequently, the full velocity gradient may not be probed for some of our targets.

This metric adds two points to the disk score in Table 3.2.

3.3.5 Morphology of rest-frame UV-optical and [C II] line emission

We complement the kinematic classification methods described in the previous sections with morphological information. We consider the HST along with JWST/NIRCam data and [C II] data. The longest wavelength NIRCam filter F444W corresponds to the rest-frame optical emission ($\lambda = 0.7\,\mu$m) at $z = 5$, redwards of the Balmer break, in contrast to the rest-frame 0.3 μm provided by HST/F160W. The depth of the JWST data varies across the sample, with CRISTAL-08, 11, 13, and 15 being the deepest.

We considered the source multiplicity in our inspection of the imaging data. In most cases, our ALMA data already indicate the single or multiple nature of the galaxies, with 14 of the multiple systems associated with Non-Disks according to the kinematic criteria applied in Sects. 3.3.1–3.3.4. The higher angular resolution of JWST can provide a more detailed view of the morphology and deblending unresolved companions within the ALMA beam that could explain the observed perturbations in the [C II] kinematics. We emphasise that the companions we defined in Table 3.1 are unlikely to be multiple clumps within a single galaxy, as their closest separations is on average $\sim 8\,\mathrm{kpc}$, ranging from 5 to 10 kpc, which is much larger than the typical size of SFG(s) at $z \sim 5$ (R. G. Varadaraj et al., 2024; T. B. Miller et al., 2025). We further stress that multiplicity on scales of a few kpc could be ambiguous, as clumpy disks may mimic multiple systems, especially if the sensitivity is insufficient to detect a fainter host galaxy underlying bright clumps.

The first two columns of Figs. 3.15 to 3.18 present a comparison between HST and JWST colour-composite images. We observe a marked difference between the rest-frame optical and UV images of galaxies in CRISTAL-01a, 07c, 08, 11, 12, 13, 16, 24, and 25. For systems CRISTAL-02 and 04a, the rest-frame optical resembles that in the UV. However, all galaxies retain their substructures or clumpy appearance. The single-pair classification using the [C II] and HST-based morphologies of R. Ikeda et al. (2025) are unchanged with the additional information from JWST data, and the multiplicity remains the same.

To highlight the clumpiness and substructures, we subtracted the F444W image by a smooth Sérsic (J. L. Sérsic, 1968) model in Appendix 3.11. The clumpy appearance of CRISTAL-02, 08, and 15 is apparent in the residual images shown in Fig. 3.26. Since many of the galaxies were not well-fitted by a Sérsic model, we did not consider the difference between JWST (or HST) morphological PA and $\mathrm{PA_{kin}}$ (defined in Sect. 3.3.1) as a disk criterion because the former was not well-constrained.

There are systems with visible [C II] companions or extended emission, such as CRISTAL-01b, 12, and 13, but no associated counterparts in either HST or JWST images. This suggests that we are still missing the more evolved stellar population due to extinction or simply fainter emission with the shallow NIRCam data. Therefore, we consider the imaging data as complementary but not decisive evidence for the kinematic nature. With the visual inspection of JWST and HST images, alongside [C II] line maps, we classify a system as a disk if it is a single-component system with smooth underlying emission, possibly featuring bright clumpy substructures that are closely spaced (typically within $\lesssim 2\,\mathrm{kpc}$, generally consisting of more than two clumps). Additionally, there should be no detectable companion within $\lesssim 20\,\mathrm{kpc}$ across the observed wavelengths. This contributes one point towards the disk score.

3.4 Disk fraction

Considering systems with a disk score of $\geqslant 5$, the total disk fraction among the 32 CRISTAL kinematics samples is $50 \pm 9\%$ ($N = 16$), encompassing both Best Disk and Disk (Table 3.2). The Best Disk and Disk categories make up $22 \pm 7\%$ ($N = 7$) and $28 \pm 8\%$ ($N = 9$) of the sample, respectively. The errors are binomial errors. The distribution of these types is shown in the inset in Fig. 3.5. The disk fraction in our study is higher than that reported in the previous ALPINE work (O. Le Fèvre et al., 2020), which found that for the overlapping CRISTAL sample, $\lesssim 40\%$ of systems are classified as 'rotator' or 'extended dispersion dominated', with only $< 20\%$ being the former, and the remaining systems being classed as 'pair-mergers'.

The 50% disk fraction of CRISTAL ($4.4 < z < 5.7$) is consistent with morphological studies based on NIRCam/JWST data, which reveal a high fraction of disks of $\sim 35\%$ on average across studies (L. Ferreira et al., 2023; C. Jacobs et al., 2023; J. S. Kartaltepe et al., 2023; M. Huertas-Company et al., 2024; J. H. Lee et al., 2024; V. Pandya et al., 2024; C. Tohill et al., 2024). A smaller sample using JWST/MIRI also supports this finding (L. Costantin et al., 2025). These results suggest an early establishment of the Hubble sequence (L. Ferreira et al., 2023; D. Xu & S.-Y. Yu, 2024; M. Huertas-Company et al., 2025).

In particular, we compare our CRISTAL disk fraction with L. Ferreira et al. (2023), a morphological study of $\sim 4{,}000$ galaxies from the CEERS survey, classified in rest-frame optical observed with JWST. Fig. 3.5 plots our disk fractions against their evolutionary trend. For consistency, we select galaxies from L. Ferreira et al. (2023) in the same mass and ΔMS ranges as our kinematic sample, using the galaxy parameters from the CANDELS-EGS catalogue of M. Stefanon et al. (2017). We did not apply surface-brightness corrections to the fractions as we compared them with the direct fraction from our kinematic classification. Figure 3.5 shows these derived morphology-based disk fractions over $z \sim 1$–6; our kinematics-based disk fraction for the CRISTAL MS SFG(s) is in very good agreement.

The presence of Disk (disks in an interacting system) is perhaps not surprising, as hinted from simulation (see also the classic example of M51); gravitational interactions between galaxies and the presence of rotating disks are not inherently contradictory (V. Springel & L. Hernquist, 2005; B. Robertson et al., 2006). The rotation of a disk is relatively resilient to minor mergers. For gas-rich systems, the stellar disk can rapidly reform and sustain itself through the formation of new stars from the remaining gas, even if the pre-existing stellar disk is destroyed in the process (H. Übler et al., 2014; N. Peschken et al., 2020; D. Sotillo-Ramos et al., 2022).

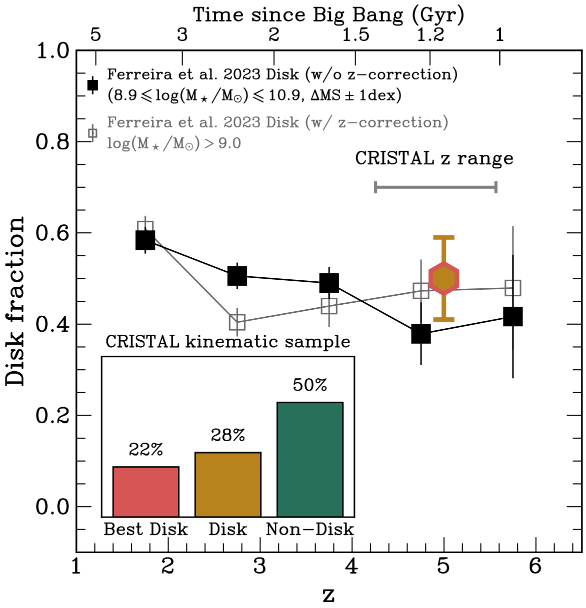

Figure 3.5 Comparison of the CRISTAL total disk fraction (yellow hexagon with red outline) to the mass-selected sample from L. Ferreira et al. (2023) based on CRISTAL mass range. The grey curve with square markers shows the ‘redshift-corrected’ trend of their high-mass bin. To more fairly compare with our sample, we further selected so that their star formation rates are within 1 dex from the J. S. Speagle et al. (2014) MS relation. The grey horizontal line indicates the redshift range of CRISTAL ($4.4 < z < 5.7$). The black solid curve with square markers represents the redshift evolution of disk fraction as reported by L. Ferreira et al. (2023) before their application of ‘redshift corrections’, which primarily account for surface-brightness effects in higher redshift objects. It would be a more equal comparison since we do not apply any such correction to the CRISTAL disk fraction. The inset shows the distribution of Best Disk, Disk, and Non-disk among the CRISTAL sample.

3.5 Kinematics modelling and properties of the disk sample

3.5.1 Forward modelling with `DysmalPy`

To extract the intrinsic kinematics and mass distribution of CRISTAL disks, we used the public forward-modelling code `DysmalPy`[2] (R. I. Davies et al., 2004a,b; G. Cresci et al., 2009; R. Davies et al., 2011; S. Wuyts et al., 2016; P. Lang et al., 2017; S. H. Price et al., 2021; L. L. Lee et al., 2025a). Table 3.5.1 reports the best-fit results. We refer to the earlier cited works for a detailed description of `DysmalPy`. In short, it is a forward modelling tool that starts from a parametrised input mass distribution to establish the best-fit models for the data. The models consist of a baryonic disk, bulge (optional), and DM halo. The disk component is parametrised as a Sérsic profile of index $n_\mathrm{d} = 1$ (exponential disk) adopted for all fits, with flattening q_d and effective radius $R_\mathrm{e,disk}$.

The baryonic disk component was assumed to be a thick oblate disk, treated as a flattened spheroid of intrinsic axis ratio $q = c/a$, and the rotation curve (RC) was derived accordingly following the E. Noordermeer (2008) parametrisation. We assumed the velocity dispersion is locally isotropic and radially uniform, representing a dominant turbulence term, σ_0.

We adopted the A. Burkert et al. (2010) pressure support (asymmetric drift) correction to circular velocity V_circ. We used the option for a self-gravitating exponential disk with constant velocity dispersion $\sigma(R) = \sigma_0$, such that

$$V^2_\mathrm{rot}(R) = V^2_\mathrm{circ}(R) - 3.36\sigma_0^2(R/R_\mathrm{e}). \tag{3.1}$$

We note that the pressure support corrections derived from local galaxies (J. J. Dalcanton & A. M. Stilp, 2010) and from simulations of high-z galaxies (M. Kretschmer et al., 2021) predict more moderate corrections (see N. F. Bouché et al., 2022; S. H. Price et al., 2022). As discussed below, due to the lack of empirical evidence of strong radially varying velocity dispersions in SFG(s) at cosmic noon, here we choose to adopt the A. Burkert et al. (2010) prescription derived for isotropic dispersion and self-gravitating disks.

---

[2] `https://www.mpe.mpg.de/resources/IR/DYSMALPY`

Table 3.3. Best-fit properties from our dynamical models.

ID	$\log_{10}(M_{\rm tot}/{\rm M}_\odot)^a$	${R_{\rm e,disk}}^b$	${\rm B/T}^c$	$V_{\rm rot}(R_{\rm e})^d$	${\sigma_0}^e$	$f_{\rm DM}(R_{\rm e})^f$	i^g	$R_{\rm out}/{R_{\rm e,disk}}^h$	$R_{\rm out}/{\rm beam}^i$
02	$10.5^{+0.1}_{-0.2}$	$2.7^{+0.5}_{-0.5}$	$0.1^{+0.1}_{-0.1}$	$129.0^{+36.6}_{-37.2}$	$67.1^{+7.8}_{-2.4}$	$0.07^{+0.31}_{-0.06}$	[47.0]	3.0	5.5
03	$10.4^{+0.1}_{-0.2}$	$1.5^{+0.9}_{-0.2}$	[0.0]	$165.3^{+20.6}_{-65.5}$	$77.8^{+28.5}_{-0.2}$	$0.09^{+0.28}_{-0.08}$	[67.0]	2.3	1.6
06b	$10.5^{+0.1}_{-0.3}$	$1.8^{+0.7}_{-0.7}$	[0.3]	$136.3^{+44.6}_{-136.3}$	$80.8^{+12.5}_{-6.4}$	$0.08^{+0.46}_{-0.07}$	[43.0]	2.3	2.6
07a	$10.2^{+0.4}_{-0.2}$	$3.0^{+0.9}_{-1.0}$	$0.1^{+0.1}_{-0.1}$	$132.6^{+41.7}_{-73.5}$	$63.1^{+5.0}_{-7.2}$	$0.62^{+0.28}_{-0.29}$	[54.7]	1.4	2.2
08	$10.5^{+0.3}_{-0.2}$	$3.4^{+0.9}_{-0.9}$	$0.1^{+0.1}_{-0.1}$	$183.6^{+50.2}_{-61.0}$	$62.4^{+10.9}_{-12.8}$	$0.52^{+0.28}_{-0.29}$	[46.0]	2.6	4.1
09	$10.4^{+0.1}_{-0.6}$	$1.2^{+0.2}_{-0.2}$	$0.1^{+0.1}_{-0.0}$	$153.1^{+70.0}_{-153.1}$	$93.2^{+26.2}_{-13.2}$	$0.08^{+0.52}_{-0.07}$	[55.0]	3.1	3.7
10a-E	$10.3^{+0.0}_{-0.2}$	[1.3]	[0.0]	$111.8^{+40.3}_{-20.6}$	$79.2^{+13.1}_{-9.0}$	$0.05^{+0.27}_{-0.04}$	[80.0]	2.2	2.2
11	$10.6^{+0.1}_{-0.3}$	$1.5^{+0.6}_{-0.9}$	[0.0]	$160.3^{+47.9}_{-98.9}$	$107.8^{+16.7}_{-12.2}$	$0.10^{+0.27}_{-0.09}$	[82.0]	2.9	3.3
12	$9.7^{+0.1}_{-0.1}$	[1.5]	[0.0]	$69.6^{+32.9}_{-69.6}$	$48.5^{+14.8}_{-14.8}$	$0.43^{+0.12}_{-0.12}$	[58.0]	2.6	2.7
15	$10.5^{+0.1}_{-0.5}$	[1.7]	[0.1]	$117.8^{+45.1}_{-117.8}$	$100.5^{+27.0}_{-1.0}$	$0.17^{+0.35}_{-0.16}$	[65.0]	2.4	3.3
19	$10.5^{+0.1}_{-0.4}$	$2.3^{+0.4}_{-0.2}$	$0.1^{+0.1}_{-0.1}$	$156.0^{+50.3}_{-81.5}$	$70.3^{+12.0}_{-7.4}$	$0.18^{+0.45}_{-0.13}$	[65.0]	1.7	3.7
20	$10.3^{+0.2}_{-0.1}$	$3.5^{+0.9}_{-0.6}$	[0.0]	$98.7^{+37.2}_{-33.9}$	$61.2^{+3.8}_{-6.7}$	$0.43^{+0.10}_{-0.37}$	[64.4]	1.5	4.2
23b	$9.8^{+0.1}_{-0.1}$	$1.4^{+0.2}_{-0.2}$	[0.0]	$93.3^{+24.2}_{-27.1}$	$66.8^{+2.0}_{-2.5}$	$0.57^{+0.09}_{-0.11}$	[60.9]	2.5	3.9
23c	$9.2^{+0.1}_{-0.3}$	$0.4^{+0.1}_{-0.1}$	$0.1^{+0.2}_{-0.1}$	$114.4^{+17.3}_{-34.8}$	$56.5^{+11.0}_{-15.7}$	$0.53^{+0.23}_{-0.05}$	[73.5]	9.2	3.7

Note. — From (a) to (h) are the best-fit (maximum a posteriori) parameters from `DysmalPy` modelling. Values in square brackets are fixed. The rotation velocity in (d) is the intrinsic total (baryons and dark matter) velocity defined in Equation 3.1. Inclinations in (g) are inferred from the JWST/F444W image, except for CRISTAL-10a, 20 and 23, which we infer from [CII] line flux map due to lack of NIRCam data. The gas fraction $f_{\rm molgas}$ listed in (h) is estimated using the method outlined in Appendix 3.12 for galaxies with available dust continuum measurements. The 1σ uncertainties from (a) to (f) are the distance to the shortest interval containing 68% of the marginalised posterior for each parameter (See Appendix A.2 in S. H. Price et al. 2021). The ratios in (h) and (i) represent the outermost measurable radius $R_{\rm out}$ (maximum radius on either the approaching or receding side) relative to the disk effective radius $R_{\rm e,disk}$ and the beam size in half-width-half-maximum, respectively. Best-fit values of CRISTAL-05 and 22a are presented in A. Posses et al. (2025) and K. Telikova et al. (2025), respectively.

We chose the two-parameter NFW (Navarro, Frenk, & White, 1996) profile for the DM halo. The virial mass, $M_{\rm vir}$, is tied to the variable $f_{\rm DM}(< R_{\rm e})$. The initial guess of $M_{\rm vir}$ is set by the expected value from the stellar-mass-halo-mass (SMHM) scaling relation from abundance matching (B. P. Moster et al., 2018), and $\log(M_{\rm vir}/{\rm M}_{\odot}) \in [11.7, 12.1]$. We then allow $M_{\rm vir}$ to vary by tying it to $f_{\rm DM}$. The concentration parameter $c_{\rm vir}$ is fixed at a value following the $M_{\rm vir}$–$c_{\rm vir}$ relation from A. A. Dutton & A. V. Macciò (2014), such that $c_{\rm vir} \in [3.4, 3.6]$. We did not apply adiabatic contraction in our fits (A. Burkert et al., 2010).

`DysmalPy` assumes an isotropic velocity dispersion profile $\sigma(R) = \sigma_0$. It is motivated by empirical results from MS SFG(s) at $z \sim 1$–3 (e.g. R. Genzel et al., 2011; S. Wuyts et al., 2016; H. Übler et al., 2019; D. Liu et al., 2023), in which $\sigma(R)$ do not show strong trends with inclination and radius in high-resolution and high-S/N IFU observations, after accounting for beam-smearing effects. They also do not exhibit significant residuals after subtracting a constant profile, which would otherwise justify using a more complicated model for the dispersion profile. The σ_0 is sensitive to the masking of spectral channels, especially for the S/N of the CRISTAL data (R. Davies et al., 2011; W. J. G. de Blok et al., 2024; L. L. Lee et al., 2025a). Overly aggressive masking, which removes the fainter wings of the line emission, can result in a bias towards lower σ_0 values. To avoid this bias entirely, we did not apply masking along the spectral axis. Instead, we evaluate the integrated S/N for each spaxel, and if the S/N falls below a threshold of ~ 3, we mask the entire spaxel.

The inclination (i) of the galaxies is inferred from the intrinsic axis ratio of the JWST/NIRCam F444W image when available, or from the [C II] line emission map if not. The F444W-inferred inclinations are, on average, 10° more face-on than those inferred from the [C II] line emission map suggesting a possible overestimation of inclination when using the [C II] line emission map alone, even after accounting for beam convolution due to the elongated beam sizes and shapes.

The inclination is then derived from the axis ratio (ϵ) using the equation

$$\cos^2(i) = (\epsilon^2 - \epsilon_0^2)/(1 - \epsilon_0^2), \tag{3.2}$$

where ϵ_0 is the intrinsic axis ratio which we assume to be 0.25 (e.g. E. Wisnioski et al., 2019). The median inclination is 54°, which is essentially the same as the average over a population of randomly oriented disks (D. R. Law et al., 2009).

We simultaneously fit the 1D velocity and dispersion profiles extracted in Sect. 3.3.2 along the kinematic major axis. This approach is preferred for our data over 2D and 3D methods, the latter are more demanding in terms of per-spaxel S/N and are more sensitive to non-circular motions. Since this work primarily focuses on the first-order kinematics of disks, the 1D approach is sufficient since the motion along the major axis best captures these properties (e.g. P. C. van der Kruit & R. J. Allen, 1978; R. Genzel et al., 2017, 2020; S. H. Price et al., 2021). The extended radial coverage provided by the 1D method allows us to constrain σ_0 at larger distances from the central region, thereby mitigating the effects of beam smearing and helping to resolve degeneracies in the model parameters, particularly those related to the relative contributions of baryons and DM to the observed RCs.

As demonstrated by S. H. Price et al. (2021) for $z \sim 1$–2.5 MS galaxies, such a 1D approach is in broad agreement with 2D modelling. We additionally verified that the 3D and 1D methods agree within $\sim 10\%$ if the per-pixel S/N within the effective radius is on average $\gtrsim 20$ within R_e, and in the worst case $\sim 20\%$ if S/N $\lesssim 3$. We note that while the terms 1D and 2D refer to the method of profile extraction from the data, `DysmalPy` always construct the model cube in full hypercube space when accounting for beam-smearing, projection, and spectral-broadening effects, as described above, irrespective of the extraction approach, and the full 3D information is used to identify the kinematic major axis. The model profile is then extracted from a 3D model cube in the same fashion as the data profiles are extracted from the observed data cube (see Fig. 6 in S. H. Price et al. 2021).

Since for all galaxies, the resolution and S/N of our data cannot provide constraints on many parameters, we leave four parameters free: (i) the baryonic mass $\log_{10}(M_\mathrm{bary}/\mathrm{M}_\odot)$, (ii) the disk effective radius $R_\mathrm{e,disk}$ (kpc), (iii) the enclosed DM fraction $f_\mathrm{DM}(< R_\mathrm{e,disk})$, and (iv) the velocity dispersion σ_0 ($\mathrm{km\,s^{-1}}$). We employ Gaussian priors for $\log_{10}(M_\mathrm{bary}/\mathrm{M}_\odot)$, with a standard deviation of 1 dex centred on the sum of the stellar mass reported in J. Li et al. (2024a) and I. Mitsuhashi et al. (2024) and the molecular gas mass derived in Appendix 3.12. For $R_\mathrm{e,disk}$ (henceforth R_e), we adopted Gaussian priors of standard deviation 1 kpc, centred on the fitted value of R_e of the [C II] emission measured in R. Ikeda et al. (2025). For CRISTAL-10a-E, 12 and 15, the quality of the data was not sufficient to

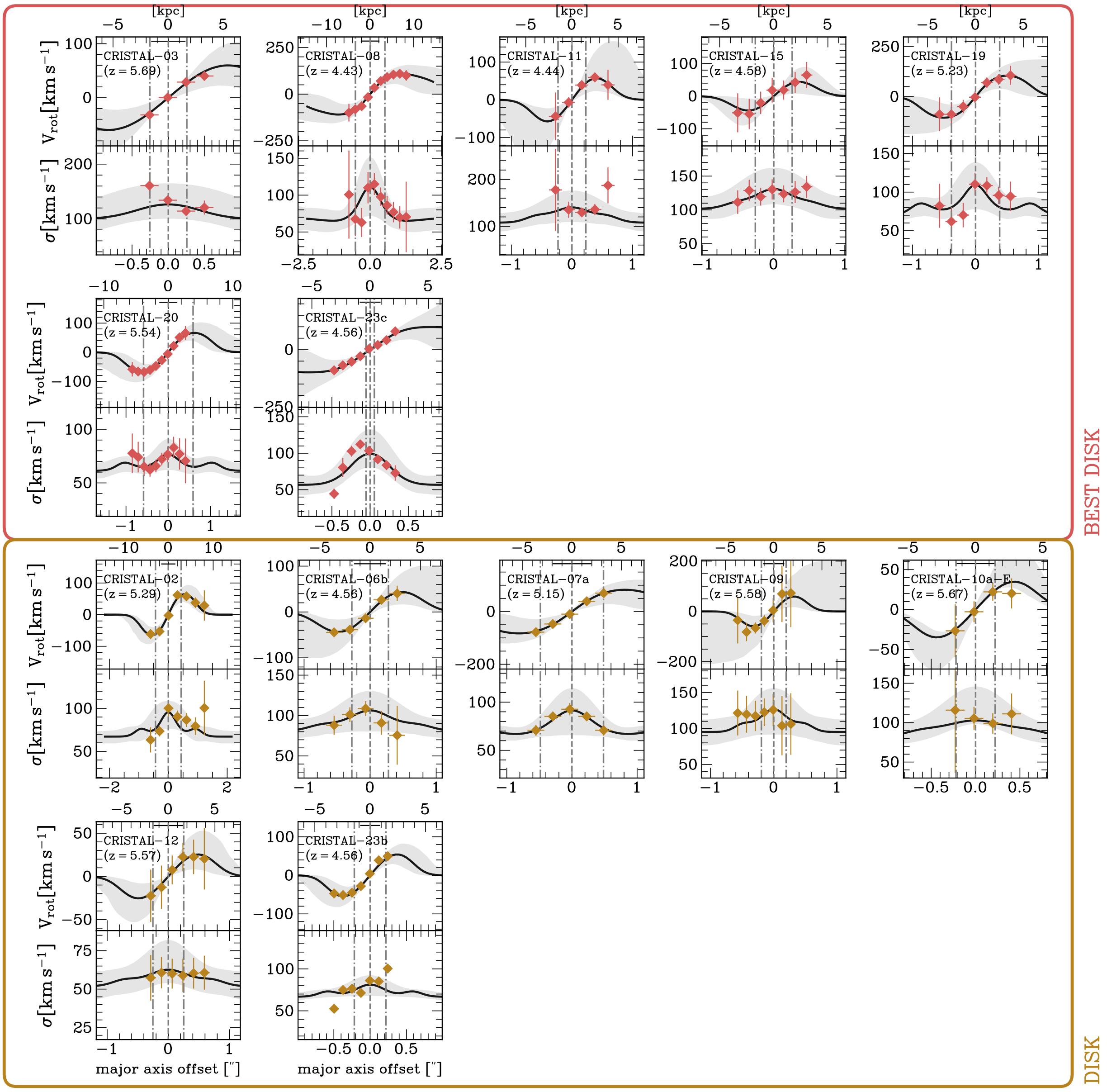

Figure 3.6 Observed rotation curves (RCs) of the CRISTAL disk sample. The RCs are the fitted line velocity centroids of the position-velocity diagram extracted along the kinematic major axis. The RCs are grouped according to their kinematics types. The black curves are the extracted 1D model (in the same way as data) from the best-fit 3D model cube from `DysmalPy`. The 3D model cubes are projected and convolved with the beam, which gives rise to the apparent central peak in the velocity dispersion profile and the shallower velocity profiles. The two symmetric grey vertical lines about the dynamical centre indicate the effective radius. The synthesised beam size is shown as the horizontal black line at the top. CRISTAL-05 and 22a belong to Disk, their velocity profiles are shown in A. Posses et al. (2025) and K. Telikova et al. (2025), respectively.

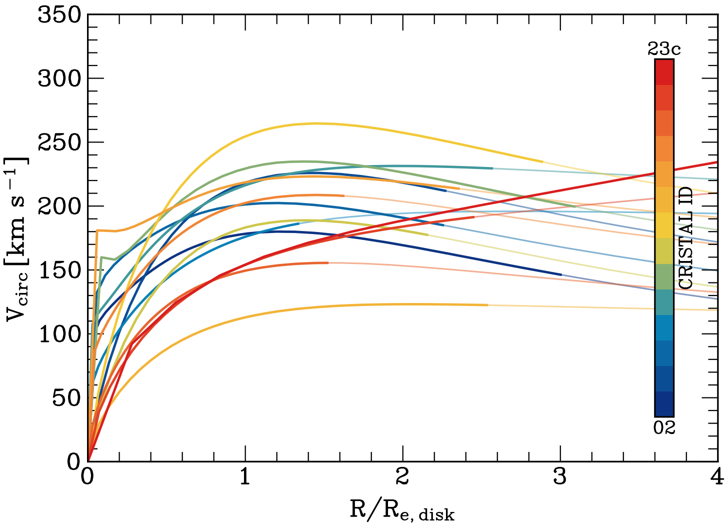

Figure 3.7 Intrinsic total circular velocity profiles $V_{\rm circ}(R/R_{\rm e,disk})$ of all CRISTAL disks, corrected for beam-smearing and projection effects. Colours in ascending order represent the CRISTAL ID (first column in Table 3.5.1). The individual $V_{\rm circ}(R)$ of baryons and DM are presented in Figure 3.28 in Appendix 3.14. Thin, lighter coloured lines indicate the radial range beyond which the data are not covered.

constrain the $R_{\rm e}$, we fix $R_{\rm e}$ to the [C II]-based radius. The prior range was tailored for each galaxy but generally spans $[0, 10]$ kpc. We assumed flat bounded priors for the intrinsic dispersion $\sigma_0 \in [20, 200]\,{\rm km\,s^{-1}}$ and DM fraction, $f_{\rm DM}(< R_{\rm e,disk}) \in [0, 1]$. Finally, we fixed the geometrical parameters i and PA inferred from Eq. (3.2) and Sect. 3.3.1, respectively. Other parameters were either tied, such as the disk scale height (through $R_{\rm e}$) and halo virial mass (through $f_{\rm DM}$), or fixed. We ran `DysmalPy` with the `emcee` sampler, employing 512 walkers and a minimum of 200 burn-in steps followed by 1000 iterations. For all our fits, the final acceptance fraction is between 0.2 and 0.5 (mean = 0.32) and the chain is run for $> 10\times$ (mean $= 23\times$) the maximum estimated parameter autocorrelation time (D. Foreman-Mackey et al., 2013).

We began the first modelling without the bulge component, given that the F444W/NIRCam data show no strong indication of a bulge based on the relatively low Sérsic indices (Appendix 3.11). For some galaxies, we observed a fair level of residuals between the data and the best-fit velocity and dispersion models in the central region, which could be evidence of a concentrated mass distribution deviating from the pure exponential disk profile. We therefore introduced a small, low-mass de Vaucouleurs bulge component with a fixed Sérsic index ($n_{\rm bulge} = 4$) and an effective radius ($R_{\rm e,b} \leqslant 1$ kpc).

We iteratively incremented the bulge-to-total ratio B/T in steps of 0.1. For all but 2

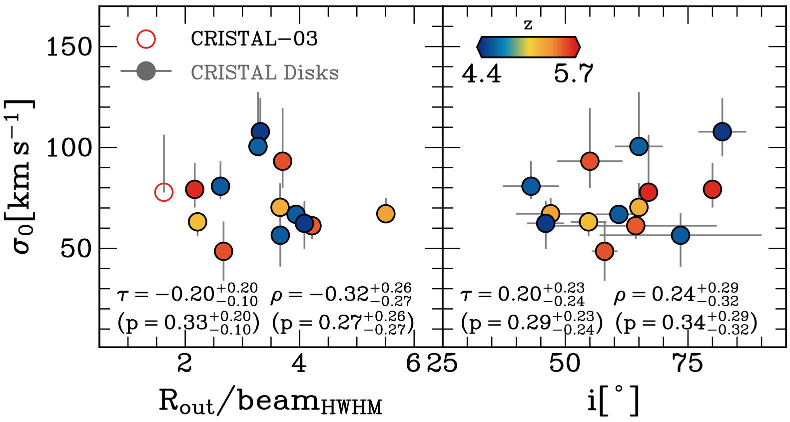

Figure 3.8 Intrinsic velocity dispersion, σ_0, as a function of the number of resolution elements within the outermost measurable radius, $R_{\rm out}$, and inclination (i). The Spearman and Kendall rank correlation coefficients (ρ and τ, respectively) do not indicate a significant correlation of σ_0 with the inclination and resolution effects, although the uncertainties in both the coefficients and p-value are large. CRISTAL-03, which has $R_{\rm out}/{\rm beam}_{\rm HWHM} = 1.6$ is excluded in the correlation analysis in Sect. 3.6.2.

cases, a value of $B/T = 0.1$ led to the best fit in terms of reduced-χ^2. For two galaxies, the preferred value is $B/T \geqslant 0.3$ (CRISTAL-06b, as well as CRISTAL-05 modelled by A. Posses et al. 2025).

We compare in Fig. 3.6 the observed and best-fit (projected and beam-smeared) model RCs for the CRISTAL disks. The intrinsic circular velocity profiles $V_{\rm circ}(R)$ of the models are shown in Fig. 3.7, with the maximum radial coverage of the data indicated. Fig. 3.28 in Appendix 3.14 shows the intrinsic σ_0, circular velocity profiles of the DM and the baryonic components. For all systems, except CRISTAL-01b, 07a, 08, 19, 23b, and 23c, we observe a fall-off of circular velocities, indicative of masses dominated by the baryonic components. We will discuss the DM fractions of the samples later in Sect. 3.7.

We examined the potential dependence of σ_0 on the angular resolution relative to the galaxies' sizes and i. Table 3.5.1 lists the ratios of $R_{\rm out}$ to the beam size (geometric average of the values in Table 3.1) in terms of half-width-half maximum (beam$_{\rm HWHM}$). $R_{\rm out}$ represents the outermost radius at which we can reliably extract velocity and dispersion profiles using the method described in Sect. 3.3.2. Overall, the kinematics profiles are traced out to $\sim$1.5–3$R_{\rm e}$ ($\sim 9\,R_{\rm e}$ for CRISTAL-23c), with $R_{\rm out}/{\rm beam}_{\rm HWHM} \sim 2$–4 (5.5 for CRISTAL-02). L. L. Lee et al. (2025a) has tested these requirements are sufficient to recover $V_{\rm rot}$ and σ_0 with a large suite of mock galaxies having comparable angular resolution and S/N to the CRISTAL data, provided that the adopted parametric profiles are close to the intrinsic profiles.

We performed Spearman and Kendall rank correlation tests (Fig. 3.8) to investigate the relationships between σ_0–$R_{\rm out}/{\rm beam}_{\rm HWHM}$ as well as σ_0–i. We do not detect significant correlations in either case (similarly for σ_0–$R_{\rm e}/{\rm beam}_{\rm HWHM}$). The small sample size, however, would only allow us to detect stronger correlations if present.

We conservatively exclude the least-resolved CRISTAL-03 in the correlation analysis in Sect. 3.6.2, which has $R_{\rm out}/{\rm beam}_{\rm HWHM} = 1.6$. For this galaxy, the 5× better angular resolution NIRSpec/JWST data reveal a consistent rotational pattern in Hα (W. Ren et al., 2025, and D. Gomez-Espinoza et al., in prep.).

3.6 Disk turbulence and dynamical support

3.6.1 Comparison to other samples and redshift trends

To put the CRISTAL disks' kinematics in the context of dynamical evolution over cosmic time, we present in Fig. 3.9 the intrinsic dispersion, σ_0, and the dynamical support from $V_{\rm rot}/\sigma_0$, compared with literature values from local to distant galaxies up to $z \lesssim 8$. The data points are coded according to the MS offset, ΔMS, of the galaxies, and different symbols distinguish measurements based on tracers of atomic, cold molecular, warm, and ionised gas phases.

The literature compilation is listed in Appendix 3.13 Table 3.5. It includes studies of local galaxies and local analogues observed in H I, CO, Hα or [O II], as well as unlensed and lensed galaxies at $0.5 < z < 4$ traced by CO, [C I], Hα, [O III] or [C II], and at $z \geqslant 4$ traced by Hα, CO, [C II], [O III], or [C III]. We only consider the systems classified as disk-like. We exclude those measurements with uncertainties in σ and $V_{\rm rot}$ greater than 50%, but include all disks in CRISTAL without this cut.

The definition and methodology employed for $V_{\rm rot}$ and σ_0 vary between studies. In cases where $V_{\rm rot}$ is not available at $R_{\rm e}$ is not available, $V_{\rm rot}$ is taken as the maximum velocity $V_{\rm max}$ or $V_{\rm rot}(2.2R_{\rm e})$. For parametric modelling, the profiles adopted for $V_{\rm rot}$ include arctan and the multi-parameter function from S. Courteau (1997). The definition of σ also varies across literature; for non-parametric modelling, such as using $^{\rm 3D}$`Barolo` (E. M. Di Teodoro & F. Fraternali, 2015) or `KinMS` (T. A. Davis et al., 2013, 2017), it would be either the median or the mean of the radial profile; for parametric modelling, which assumed either a constant profile $\sigma(R) = \sigma_0$, $\sigma(R) = \sigma_0 \exp(-R/R_\sigma)$ or other functions, we adopt the σ_0 or the median in the latter cases, following the choice of the original authors. The literature values are also a mix of data obtained from various observational methods, including IFU,

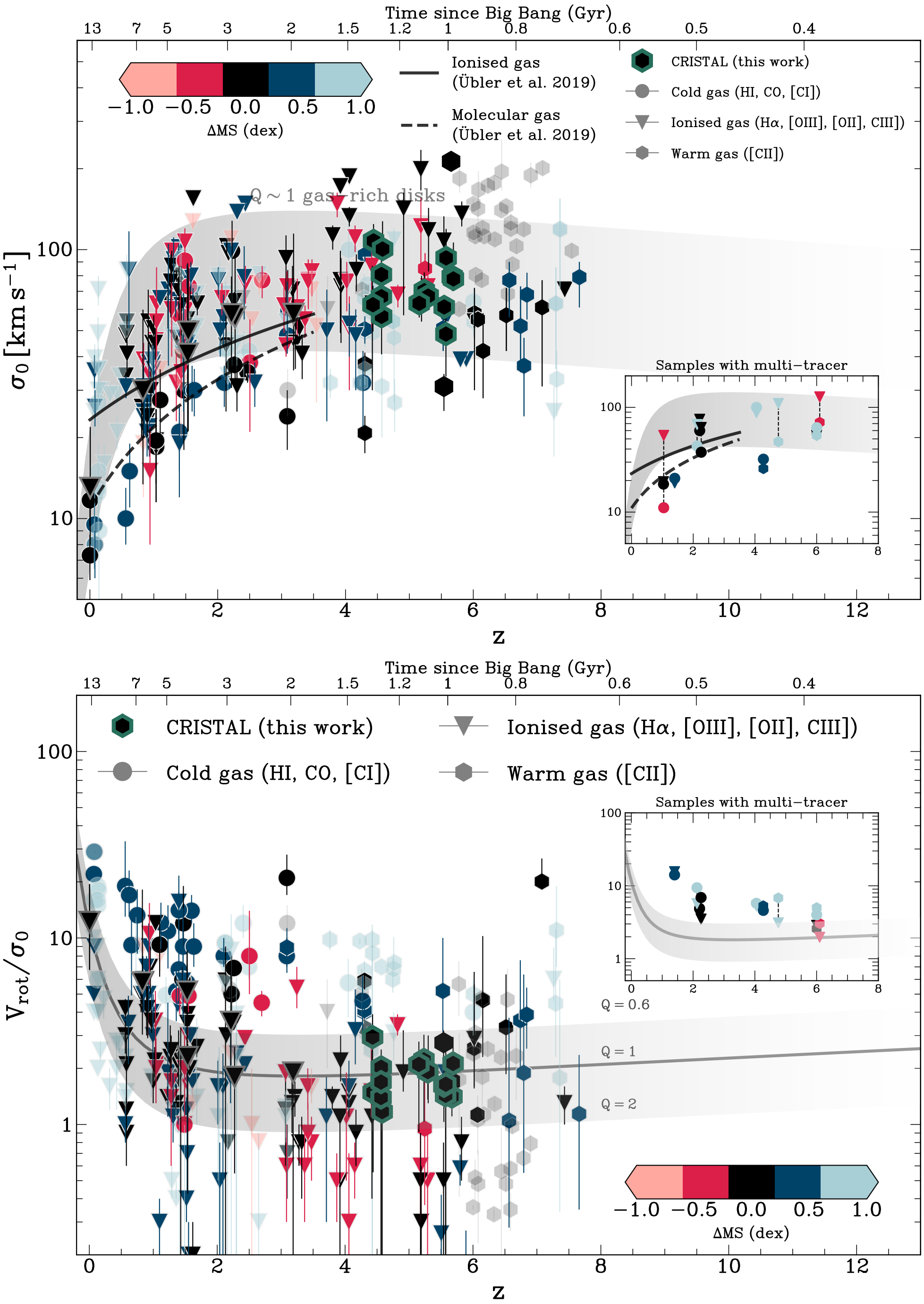

Figure 3.9 Dynamical evolution of high-z galaxies. *Top*: Intrinsic velocity dispersion σ_0 as a function of redshift for our disk sample (black hexagons with green outline) compared with the literature values (see Appendix 3.13 Table 3.5). *Bottom*: Same but for the ratio between rotational velocity and σ_0, $V_{\rm rot}/\sigma_0$. The solid and dashed black lines are the H. Übler et al. (2019)'s best-fit relations for galaxies at $z < 4$, for ionised and cold molecular gas, respectively. Where available, the points are colour-coded by their main-sequence offset ΔMS relative to the J. S. Speagle et al. (2014) relation, otherwise in grey. The insets shows the literature sample (see Table 3.6) of the same galaxy with two gas tracers tracing different phases. The insets include the galaxies with large uncertainties which are omitted in the main plots. The grey shading encloses the corresponding range in σ_0 and $V_{\rm rot}/\sigma_0$ for $Q \in [0.6, 2.0]$. The definition of the Toomre Q parameter is presented in Sect. 3.6.3.

interferometry, and slit spectroscopy. The slit-based method tends to give higher σ values than the other two (H. Übler et al., 2019). Different CO transitions can also trace gases with various kinematic and spatial properties.

We recalculate ΔMS using the relation of J. S. Speagle et al. (2014), extrapolated to the redshift range of the samples. Recent studies of the star-forming MS at $z \gtrsim 5$, utilising JWST imaging data, have provided support for this extrapolated relationship (M. P. Koprowski et al., 2024; J. W. Cole et al., 2025). When available, the stellar mass $M_\star$ values are taken directly from the literature, which was derived from spectral energy distribution (SED) fitting using various tools and assuming different initial mass functions (IMFs) or decomposition of RC. In cases where $M_\star$ is not reported, we estimate it from the dynamical and gas mass ($M_\star = M_{\rm dyn} - M_{\rm gas}$).

In Fig. 3.9, the literature values of σ_0 in ionised and molecular gas tracers are both displaying an overall increasing trend with redshift. For MS galaxies up to $z \sim 4$, the trends are well-described by the best-fit relations derived by H. Übler et al. (2019). Qualitatively, extrapolating these relations matches the evolutionary trend at even higher redshifts for the MS galaxies and agrees well with the CRISTAL values. On the other hand, some starburst galaxies observed with [C II] at similar epochs lie below the extrapolated relationships.

Sample selection differences between studies could partly explain the large spread in σ_0 (and $V_{\rm rot}/\sigma_0$). As extensively discussed by E. Wisnioski et al. (2025), the interpretation of the dispersion should also consider the different ISM phases probed by the various kinematic tracers and, relatedly, the varying contributions of different gas phases to the [C II] line emission as a function of $\Sigma_{\rm SFR}$ and other properties (e.g. D. Cormier et al., 2019; M. G. Wolfire et al., 2022; R. Ikeda et al., 2025). To better understand the potential dependence on ISM phases, it is essential to study the same object using multiple tracers; currently, this has only been done for a limited number of samples (Table 3.6), as highlighted in the insets of Fig. 3.9.

Compared to unlensed MS SFG(s) observed with [C II] at similar epochs, CRISTAL disks have comparable values of σ_0 within uncertainties, with a median difference of $11\,{\rm km\,s^{-1}}$, and a lower $V_{\rm rot}/\sigma_0$ by 0.8 in median. This is possibly because CRISTAL disks are less massive in $M_\star$ than the literature samples by an average of 0.15 dex. Given the mass-dependence of $V_{\rm rot}/\sigma$ in simulations that span a wider dynamic range (e.g. A. Dekel et al., 2020; M. Kohandel et al., 2024) than allowed by our data, the lower mass of our sample may explain the lower $V_{\rm rot}/\sigma_0$ values. When compared with the same population observed in ionised gas, now possible thanks to JWST, CRISTAL disks are in very good agreement with the 'gold' sample in A. L. Danhaive et al. (2025), with median differences of only $\sim 2\%$ in σ_0 and $\sim 10\%$ in $V_{\rm rot}(R_{\rm e})/\sigma_0$.

On the other hand, compared with the lensed samples, CRISTAL disks have higher σ_0, by $34\,\mathrm{km\,s^{-1}}$ in median, and significantly lower $V_{\mathrm{rot}}/\sigma_0$ by -6. In particular, the lensed samples tend to be starburst galaxies, and have smaller sizes (with R_{e} typically $\lesssim 1.5\,\mathrm{kpc}$, see also Fig. 3.1) that are $\sim 50\%$ and $\sim 70\%$ smaller than the unlensed galaxies and CRISTAL disks, respectively. The starburst and compact nature of these galaxies suggests that they have experienced a distinct assembly history (S. M. Stach et al., 2018; C. C. Hayward et al., 2021), differing from that of the more typical galaxy populations in CRISTAL.

3.6.2 Trends with galaxy properties

We explored any existing trends with the galaxy properties, including molecular gas mass fraction (f_{molgas}), stellar mass ($M_\star$), MS offset (ΔMS), SFR surface density (Σ_{SFR}), and molecular gas mass (M_{gas}). Fig. 3.10 plots the derived σ_0 and $V_{\mathrm{rot}}/\sigma_0$ as a function of these properties for the CRISTAL disk sample. We quantify the correlations by computing Spearman's ρ and Kendall's τ, and their p-values to assess the significance of any possible correlations. The resulting coefficients and the p-values with confidence intervals are annotated in Fig. 3.10.

For σ_0, the strongest correlation observed is with f_{molgas}. The $V_{\mathrm{rot}}/\sigma_0$ value appears to be primarily correlated with ΔMS. No other obvious trend was detected with the other galaxy properties. The dependence of σ_0 with f_{molgas} is in line with expectations for marginally stable, gas-rich disks as discussed in Sect. 3.6.1. The trend between $V_{\mathrm{rot}}/\sigma_0$ and ΔMS may reflect an underlying dependence on Σ_{bar} (see also the right panel of Fig. 3.1). However, although the correlation coefficient ρ between $V_{\mathrm{rot}}/\sigma_0$ and Σ_{bar} is ~ 0.5, the large accompanying p-value suggests that more precise size measurements are required to confirm this relationship. Clearly, the CRISTAL disk sample is small, and only the strongest correlations can be discerned. Future larger samples of near MS SFG(s) at $z \sim 4$–6 will be important to strengthen the results, such as the literature compilation efforts by E. Wisnioski et al. (2025).

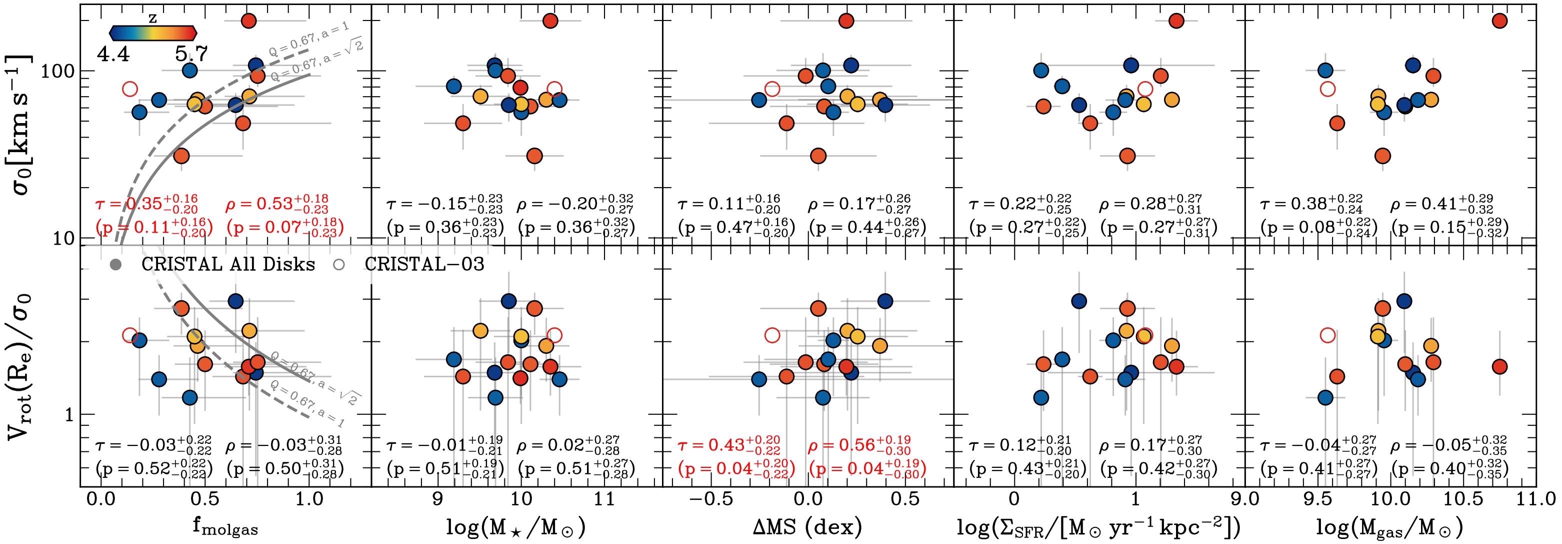

Figure 3.10 Intrinsic velocity dispersion (σ_0) and the ratio of rotation velocity at the effective radius ($V_{\rm rot}(R_{\rm e})$) to intrinsic velocity dispersion (σ_0) as a function of five galaxy properties: molecular gas fraction ($f_{\rm molgas}$), stellar mass ($\log(M_*/M_\odot)$), offset from the main sequence (ΔMS), star formation rate surface density ($\Sigma_{\rm SFR}$), and molecular gas mass ($\log(M_{\rm gas}/M_\odot)$). The dashed and solid grey curves in the first column are the predicted trends based on Equation 3.3 with Q fixed at $Q_{\rm crit} = 0.67$, with $a = 1$ and $a = \sqrt{2}$, respectively. The Kendall and Spearman's rank correlation coefficients (τ and ρ) and their corresponding p-values are shown alongside the 1-σ percentile errors. Taken σ_0 at face values, it shows a tentative correlation (highlighted in red) with $f_{\rm molgas}$, while $V_{\rm rot}(R_{\rm e})$ correlates most significantly with ΔMS. The most poorly resolved galaxy CRISTAL-03 (empty red circle), with an extent covered by < 2 beams, is excluded from the correlation analysis. The limited statistics and narrow parameter range of our data lead to large uncertainties in the correlation coefficients and their p-values, and the trends should be interpreted with caution.

3.6.3 Turbulence in the framework of marginally Toomre-stable disks

The observed evolutionary trend of σ_0 and $V_{\rm rot}/\sigma_0$ discussed above has been attributed to the increasing gas fraction at higher redshifts (e.g. L. J. Tacconi et al., 2010, 2020), as predicted by the Toomre theory. The correlation of σ_0 with $f_{\rm molgas}$ for the CRISTAL disks discussed above is also in line with expectations for marginally stable gas-rich disks. In this framework, the stability of the disks against fragmentation and local gravitational collapse is directly linked to the level of turbulence in the ISM. Turbulence is driven by both *ex-situ*, such as accretion from the cosmic web, and *in-situ*, including radial flows and clump migration, which release gravitational potential energy. This creates a self-regulating cycle that maintains the disk in a state of marginal stability. Following Eq. (3) in R. Genzel et al. (2014a) (see also, H. Übler et al., 2019; R. Genzel et al., 2011, 2023; D. Liu et al., 2023), the classical A. Toomre (1964) parameter Q can be formulated as

$$Q_{\rm gas} \approx \frac{\sigma_0 \kappa}{\pi G \Sigma_{\rm gas}} = \left(\frac{\sigma_0}{v_c}\right)\left(\frac{a}{f_{\rm gas}}\right), \tag{3.3}$$

where the epicyclic frequency is $\kappa = \sqrt{R d\Omega^2/dR + 4\Omega^2}$ and $\Omega = V_{\rm rot}/R$. The constant a depends on the rotational structure of the disk: $a = \sqrt{1}$ for Keplerian-like rotation and $a = \sqrt{2}$ for a disk with constant rotational velocity. For a quasi-stable thick gas disk , $Q_{\rm crit} = 0.67$ (e.g. M. Behrendt et al., 2015). The two panels in the first column of Fig. 3.10 plot the predicted trends of $\sigma(f_{\rm gas})$ and $V_{\rm rot}/\sigma(f_{\rm gas})$ based on Eq. (3.3) with $Q = Q_{\rm crit}$ and $a = \sqrt{1...2}$, taking into account that some RCs show a drop-off. Overall, there is a good match between the predicted trend and the CRISTAL values.

Specifically, taking the median values of CRISTAL disks, $\sigma_0/v_c = 70/200 = 0.4$ and $f_{\rm molgas} \sim 0.5$. The corresponding values of $Q_{\rm gas}$ is then 0.6, and the entire sample has Q in the range $[0.4, 2.0]$, indicating that the CRISTAL disks are, on average, marginally gravitationally stable. The Q values are broadly similar to the results of H. Übler et al. (2019) for their $z \sim 1$–3 samples. The similar Toomre Q values inferred for MS SFG(s) from $z \sim 5$ to $z \sim 1$ in MS SFG(s) suggest that this galaxy population has grown in a marginally stable and self-regulating manner for at least 5 billion years of cosmic time.

From a broader evolutionary perspective based on the Toomre theory for gas-rich disks, the observed trends from the literature, combined with CRISTAL, are in remarkably good agreement. The grey bands in both panels of Fig. 3.9 show the prediction in the Toomre framework for the evolution of dispersion for $\log(M_\star/{\rm M}_\odot) = 10.0$ galaxies with $Q_{\rm crit} \in [0.4, 2.0]$ and $v_c = 200\,{\rm km\,s^{-1}}$. These values are appropriate for the CRISTAL disk sample (and differ from more massive samples studied at lower redshifts, e.g. E. Wisnioski et al. 2015). The gas fraction $f_{\rm molgas}$ adopted evolves according to the scaling relation in L. J. Tacconi et al. (2020) which is a function of stellar mass, SFR, and size. The SFR and size evolution with redshift is determined from the J. S. Speagle et al. (2014) MS relation and A. van der Wel et al. (2014) mass-size relation. CRISTAL galaxies have $f_{\rm molgas}\sim 51\%$, consistent with the expected value from L. J. Tacconi et al. (2020)'s relation at $z=5$ for $M_\star = 10^{10}\,{\rm M}_\odot$, which is $\sim$53% (see discussions in Appendix 3.12).

3.6.4 Drivers of the gas turbulence

To explore the relative contribution of star formation- versus gravitational instability-driven turbulence in CRISTAL disks, we compare our results with the analytic model of M. R. Krumholz et al. (2018). This model combines stellar feedback and gravitational processes to drive turbulence, incorporating prescriptions for star formation, stellar feedback, and gravitational instabilities into a unified 'transport+feedback' framework. In the model, gas is in vertical hydrostatic equilibrium and energy equilibrium, with energy losses through turbulence decay balanced by energy input from stellar feedback and the release of gravitational energy via mass transport through the disk. Based on the model, there is a critical value of gas velocity dispersion (σ_g), $\sigma_{\rm sf}$, at which the amount of turbulence can be sustained by star formation alone, without the need for gravitational instability or radial transport. In such a case, σ_g is related to $\sigma_{\rm sf}$ by (Eq. (39) in M. R. Krumholz et al. 2018)

$$\begin{aligned}\sigma_{\rm g} = \sigma_{\rm sf} \equiv & \frac{4 f_{\rm SF}\epsilon_{\rm ff}}{\sqrt{3 f_{g,P}}\,\pi\eta\phi_{\rm mp}\phi_Q\phi_{\rm nt}^{3/2}}\left\langle\frac{p_*}{m_*}\right\rangle \\ & \cdot \max\left[1, \sqrt{\frac{3 f_{g,P}}{8(1+\beta)}}\,\frac{Q_{\rm min}\phi_{\rm mp}}{4 f_{g,Q}\epsilon_{\rm ff}}\,\frac{t_{\rm orb}}{t_{\rm sf,max}}\right].\end{aligned} \tag{3.4}$$

Following Table 3 in M. R. Krumholz et al. (2018) for high-z galaxies, the fraction of ISM in the star-forming molecular phase, $f_{\rm SF}$, is set to 1.0; $t_{\rm SF,max} = 2\,{\rm Gyr}$; the fractional contribution of gas to the mid-plane pressure and Q, $f_{g,P}$ and $f_{g,Q}$, respectively, are both assumed to be 0.7; the slope index of the RC, $\beta = d\ln v_\phi / d\ln r$, is set to 0.0 (i.e., flat), in which v_ϕ is the circular velocity $V_{\rm circ}$; the Toomre parameter, Q, is fixed at 1, following the fiducial value. The orbital period $t_{\rm orb} = 2\pi r/V_{\rm circ} \in [30, 120]\,{\rm Myr}$, and is adjusted to the values of our sample. The other values that we adopt are listed in Table 3.7 in Appendix 3.15. The σ_g from Eq. (3.4) is therefore $\sim 10\,{\rm km\,s^{-1}}$. Dispersion much larger than this critical value ($\gtrsim 20\,{\rm km\,s^{-1}}$) requires gravitational instability or radial mass transport for moderate SFR.

In the 'transport+feedback' model, the star formation rate surface density $\Sigma_{\rm SFR}$ and the gas velocity dispersion σ_g can be related following (Eq. (59) in M. R. Krumholz et al. 2018) as

$$\begin{aligned}\Sigma_{\rm SFR} =& f_{\rm SF}\frac{\sqrt{8(1+\beta)}f_{g,Q}}{GQ}\frac{\sigma_g}{t_{\rm orb}^2} \\ &\cdot \max\left[\frac{8\epsilon_{\rm ff}f_{g,Q}}{Q}\sqrt{\frac{2(1+\beta)}{3f_{g,P}\phi_{\rm mp}}}, \frac{t_{\rm orb}}{t_{\rm SF,max}}\right],\end{aligned} \tag{3.5}$$

while for the 'feedback-only' (fixed Q) model (Eq. (61) in M. R. Krumholz et al. 2018), we have

$$\Sigma_{\rm SFR} = \frac{8(1+\beta)\pi\eta\sqrt{\phi_{\rm mp}\phi_{\rm nt}^3}\phi_Q}{GQ^2\langle p_*/m_*\rangle f_{g,P}}\frac{\sigma_{\rm g}^2}{t_{\rm orb}^2}. \tag{3.6}$$

In Fig. 3.11, we show the σ_0–$\Sigma_{\rm SFR}$ measurements of CRISTAL disks, compared with the 'transport+feedback' and 'feedback only' model of M. R. Krumholz et al. (2018).[3] For reference, we also compare σ_0 and SFR in Appendix 3.15. Overall, our results are broadly consistent with the 'feedback+transport' model of M. R. Krumholz et al. (2018), which suggests that the high-velocity dispersion of normal SFG(s) can be predominantly attributed to the release of gravitational energy from mass transport across the disk.

This result differs from some previous studies at similar epochs, which found that star formation feedback alone can sustain the observed dispersion in starburst-like galaxies (e.g. F. Roman-Oliveira et al., 2023a; L. E. Rowland et al., 2024). However, our analysis of CRISTAL MS disks, characterised by modest star formation activity, indicates that a different dominant mechanism drives turbulence in the ISM of MS SFG(s).

The result is nevertheless consistent with the weak correlation of σ with global or local SFR ($\Sigma_{\rm SFR}$) of our sample as shown in Sect. 3.6.2. Such a weak correlation is also found in R. Genzel et al. (2011); H. L. Johnson et al. (2018) and H. Übler et al. (2019) for cosmic noon galaxies (after redshift normalisation), and in the nearby universe (e.g. B. G. Elmegreen et al., 2022). This is also in agreement with the theoretical works (e.g. R. Shetty & E. C. Ostriker, 2012; C.-G. Kim & E. C. Ostriker, 2018), which have derived a weak dependence of gas velocity dispersion on the supernova explosion rate.

We note, however, that for CRISTAL-05 with its relatively low $\sigma_0 \approx 31\,{\rm km\,s^{-1}}$ and $\Sigma_{\rm SFR} = 8.5\,{\rm M_\odot\,yr^{-1}\,kpc^{-2}}$ (SFR $= 68\,{\rm M_\odot\,yr^{-1}}$), the stellar feedback-only model would better

---

[3] For CRISTAL-23c in which the $\Sigma_{\rm SFR}$ is not available, we adopt the $\Sigma_{\rm SFR,IR}$ from M. Béthermin et al. (2023) as a lower limit, although the contribution from unobscured star formation is not significant.

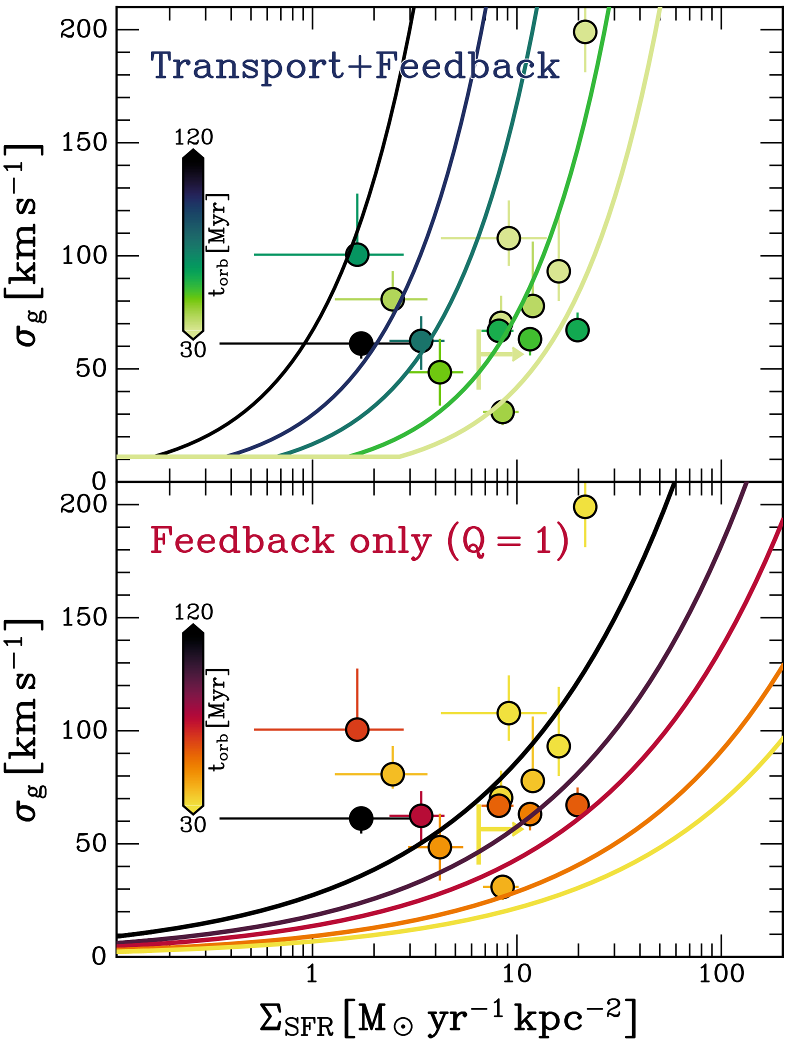

Figure 3.11 σ_0 vs $\Sigma_{\rm SFR}$ of CRISTAL disks compared with analytical models from M. R. Krumholz et al. (2018). The solid lines in the upper panel show the σ_0 values predicted from the Transport+Feedback model with orbital period $t_{\rm orb} = [30, 120]$ Myr. Similarly for the lower panel but for the 'Feedback-only' model. The results are broadly consistent with the 'feedback+transport' model, suggesting that the elevated velocity dispersion of normal star-forming galaxies at this epoch requires additional gravitational energy from mass transport across the disk.

match the observed values of σ_0 and Σ_{SFR} (and SFR), suggesting that different mechanisms among the disk sample may contribute to varying degrees of the observed velocity dispersion, as seen also in simulations (e.g. E. Jiménez et al., 2023). Additionally, spatial variation of different mechanisms within a single galaxy is also possible, but the resolution of our data is currently insufficient to reveal such variation conclusively. In the future, higher resolution observations of kinematics and SFR maps would enable to test more directly the coupling (or lack thereof) between σ_0 and stellar feedback. Other simulation works also show that stellar feedback can sustain higher dispersions compared to the M. R. Krumholz et al. 2018's analytical treatment (A. Gatto et al., 2015; M. E. Orr et al., 2020; T.-E. Rathjen et al., 2023). The relative contribution of stellar feedback versus gas transport depends on halo mass and redshift, in which gas transport plays a more dominant role in the high redshift systems (O. Ginzburg et al., 2022).

3.7 Exploration of galactic DM fraction and mass budget

On the galactic scale, CRISTAL disks tend to be baryonic-dominated, with low f_{DM} at R_{e} (Table 3.5.1), having a median value of 18% (mean = 27%), comparable to or less than maximal disks ($f_{\mathrm{DM}} \coloneqq 28\%$ T. S. van Albada et al., 1985), albeit with significant scatter among the samples that span a wider range from a few % to $\sim$ 60%. In comparison, the Galaxy's $f_{\mathrm{DM}}(R_{\mathrm{e}}) = 0.38 \pm 0.1$ (J. Bovy & H.-W. Rix, 2013; J. Bland-Hawthorn & O. Gerhard, 2016).

The radial profiles of f_{DM} of CRISTAL disks are shown in Fig. 3.28, which is defined in `DysmalPy` as [4]

$$f_{\mathrm{DM}}(< R) \coloneqq V^2_{\mathrm{circ,DM}}(R)/V^2_{\mathrm{circ,tot}}(R). \tag{3.7}$$

We observe a tentative inverse relationship between $f_{\mathrm{DM}}(R_{\mathrm{e}})$ and circular velocity (V_{circ}) in Fig. 3.12, which is pressure-support corrected (Eq. (2.1)), and similarly for the baryonic surface density Σ_{bary} based on the values in Tables 3.1 and 3.2. This trend is similar to that observed in A. Nestor Shachar et al. (2023) for cosmic noon MS SFG(s). Such an inverse correlation is well-established for local SFG(s), where the most DM-dominated disks are those with low Σ_{bary} and V_{circ} (e.g. T. P. K. Martinsson et al., 2013a,b; S. Courteau & A. A. Dutton, 2015, and references therein). We also compare our results to S. Wuyts et al. (2016),

---

[4] We note that in our analysis, f_{DM} at $R_{e,\mathrm{disk}}$ is a free parameter — by instead calculating the total halo mass given the specified baryonic mass distribution and $f_{\mathrm{DM}}(R_{\mathrm{e,disk}})$, the full f_{DM} radial profile for each galaxy is then computed given the best-fit parameters (M_{bar}, $R_{\mathrm{e,disk}}$, f_{DM} enclosed within R_{e}, and σ_0).

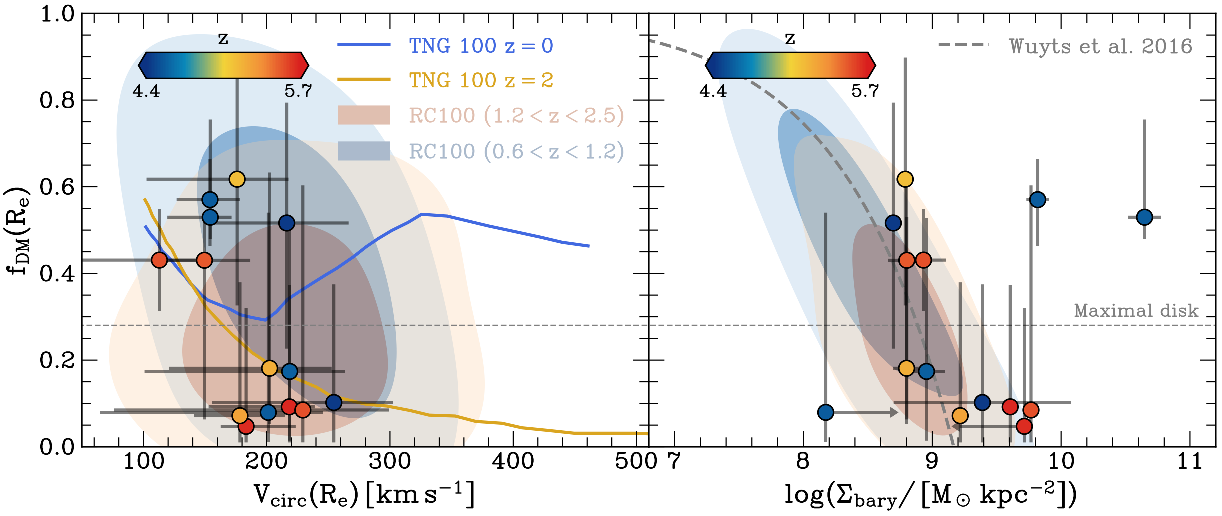

Figure 3.12 Dark matter (DM) fraction $f_{\rm DM}$ as a function of the circular velocity at the effective radius ($V_{\rm circ}(R_{\rm e})$, *left*) and baryonic surface density ($\Sigma_{\rm bary}$) (*right*). The yellow and blue curves show the TNG100 (without adiabatic contraction) relations at $z = 0$ and $z = 2$ (M. R. Lovell et al., 2018), respectively. The pale blue and yellow shading are measurements from RC100 at $z < 2.5$ (A. Nestor Shachar et al., 2023). The grey dashed curve is the best-fit relation of $z \sim 2$ star-forming galaxies from S. Wuyts et al. (2016). The CRISTAL sample statistics suggest a tentative anti-correlation with $f_{\rm DM}(R_{\rm e})$ and $\Sigma_{\rm bary}$, although individual galaxy uncertainties are limited by the data depth. The horizontal dashed line denotes $f_{\rm DM}$ for a maximal disk $f_{\rm DM} := 28\%$ (T. S. van Albada et al., 1985). In the *right* panel, the two symbols plotted with only limit arrows represent CRISTAL-10a-E (upper limit) and CRISTAL-06b (lower limit). The stellar mass is only for CRISTAL-10a as a whole, which includes CRISTAL-10a-E, while no gas mass is available for CRISTAL-06b.

who derived $f_{\rm DM}$ at the inner disk by subtracting the sum of stellar and gas masses from the dynamical mass obtained from RCs of 240 galaxies, assuming $f_{\rm bary} = M_{\rm bary}/M_{\rm dyn} = 1 - f_{\rm DM}$. We find that most of the CRISTAL disks follow the S. Wuyts et al. (2016) relation on the $\Sigma_{\rm bary}$–$f_{\rm DM}$ plane, except for CRISTAL-23b and 23c, which are both disk-like galaxies in an interacting system.

The low $f_{\rm DM}(R_{\rm e})$ of our sample is broadly consistent with the general trend of decreasing DM fraction towards higher redshifts. Fig. 3.13 shows the median $f_{\rm DM}(R_{\rm e})$ of our sample aligns with the extrapolated trend toward higher redshift from A. Nestor Shachar et al. (2023) and S. Wuyts et al. (2016), when considering a sample matched in $M_{\rm bary}$ and ΔMS. Both $f_{\rm DM}$ are below the expectations from the TNG100 simulation from M. R. Lovell et al. (2018). This could be due to the insufficient physical resolution of large-scale cosmological simulations to resolve sub-galactic processes (H. Übler et al., 2021) and the effect of adiabatic contraction (G. R. Blumenthal et al., 1986). The possible drivers of DM deficit in MS SFG(s) have been discussed thoroughly by, e.g. R. Genzel et al. 2020 and A. Nestor Shachar et al. 2023. It is potentially linked to kinetic heating due to the efficient transport of baryons to central regions in gas-rich systems (e.g. A. El-Zant et al., 2001), and/or strong feedback processes redistributing DM to larger radii (e.g. J. Freundlich et al., 2020). One example is CRISTAL-02, which has $f_{\rm DM}(< R_{\rm e}) < 0.1$ and drives a vigorous outflow detected in [C II] (R. L. Davies et al., 2025).

The widely scattered distribution in Fig. 3.13 with large errors associated with individual galaxies prevents a definite conclusion on the physical origin of this distribution. We investigated whether the inhomogeneous radial coverage of the RCs (Fig. 3.7) could systematically drive up the $f_{\rm DM}(R_{\rm e})$ for galaxies with limited radial coverage. However, we do not find a straightforward one-to-one correspondence between $f_{\rm DM}(R_{\rm e})$ and the ratio of $R_{\rm out}/R_{\rm e}$ (Kendall's $\tau = -0.19^{+0.23}_{-0.25}$, $p = 0.32^{+0.23}_{-0.25}$).

We emphasise that $f_{\rm DM}$ is measured at the effective radius, and we lack constraints on the DM distribution on the halo scale ($\gg R_{\rm e}$) with our current data, except for the very compact CRISTAL-23c. Extrapolating the DM mass from the inner disk to the virial scale with an NFW distribution would result in an unphysically large baryon fraction larger than the cosmic baryon fraction (R. Genzel et al., 2017). As discussed in Sect. 3.5.1, the intrinsic, circular velocities would also depend on the assumption of the pressure support corrections, which would explain the differences found in the literature (cf. G. Sharma et al. 2021 with, e.g. R. Genzel et al. 2020; S. H. Price et al. 2021 and A. Nestor Shachar et al. 2023). If we were to assume a non-constant σ, such as an exponential decline, for the pressure support correction, rather than using Eq. (2.1), the correction to $V_{\rm rot}$ would be even larger (Eq. (12) in S. H. Price et al., 2022), leading to a more steeply declining $V_{\rm circ}$, which would further

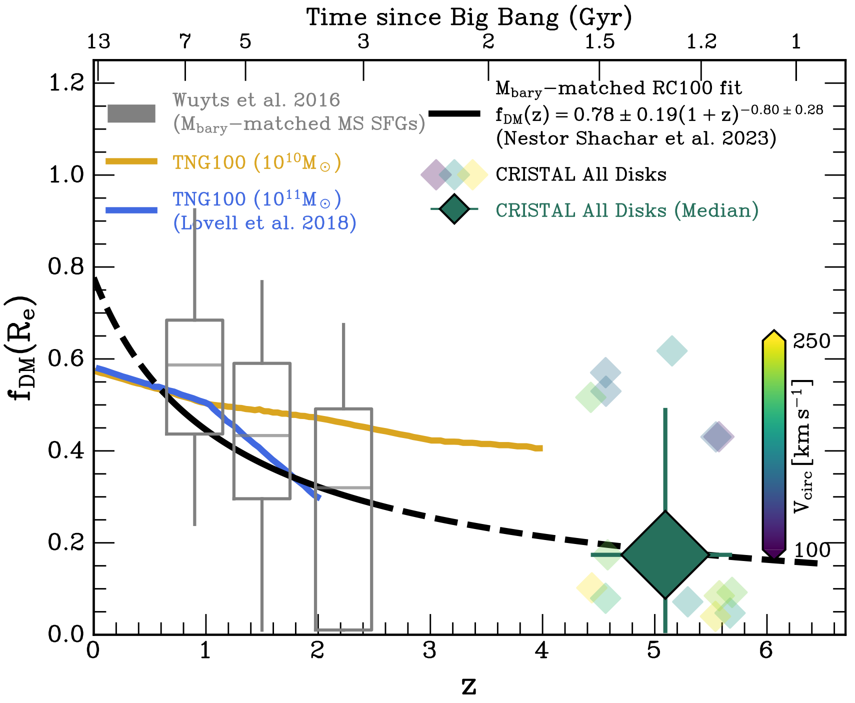

Figure 3.13 DM fraction at effective radius, $f_{\rm DM}(R_{\rm e})$, as a function of redshift. The $f_{\rm DM}(R_{\rm e})$ of individual CRISTAL disks ($4 < z < 6$) are represented by small diamonds, colour-coded by their $V_{\rm circ}(R_{\rm e})$. For comparison, we include lower redshift studies around $z = 2$ from S. Wuyts et al. (2016) (grey box-and-whisker) and the best-fit relation to the RC100 data set (A. Nestor Shachar et al., 2023) (black solid line for the redshift range covered and dashed line for the extrapolated range). For both observational studies, we consider only SFG(s) on the MS and the baryonic mass $M_{\rm bary}$ matched within 0.3 dex of the CRISTAL disks. The new best-fit relation to RC100, using the $M_{\rm bary}$-matched sample, is shown in the legend. The trends predicted from the TNG100 simulation for $M_* = 10^{10} M_\odot$ and $M_* = 10^{11} M_\odot$ are shown in yellow and blue, respectively (M. R. Lovell et al., 2018). Overall, the CRISTAL disks tend to be baryon-dominated on galactic scales, with a median DM fraction of $\sim 18\%$ (large green diamond) that is tentatively consistent with the extrapolated relation based on RC100. However, there is a significant scatter in the values among the sample, partly driven by the scattered distributions of circular velocity $V_{\rm circ}(R_{\rm e})$ (and $\Sigma_{\rm bary}$) shown in Figure 3.12.

exacerbate the discrepancies between our observations and simulations.

Although we have adopted the NFW profile for the DM profile, the $f_{\rm DM}(< R_{\rm e})$ results for the sample change less than 10% (in terms of absolute difference) for alternative DM mass profile assumption, such as the two-power halo (2PH) profile (J. Binney & S. Tremaine, 2008) with a variable inner slope. Improved constraints on the DM fraction in the future would benefit from deeper observations of individual galaxies and/or kinematic stacking analysis (e.g. P. Lang et al., 2017; A. L. Tiley et al., 2019).

3.8 Nature of Non-Disks

The origin of the kinematic perturbations in the Non-Disk subset of the sample could arise from galaxy interactions and mergers. Most Non-Disks, except CRISTAL-21, 24 and 25, have visible companions already in the HST and/or JWST images alone, and the one classified as Non-Disk is, in most cases, the less luminous and less massive for those with available mass measurement. The higher non-disk fraction among the CRISTAL kinematic sample compared to samples of typical MS SFG(s) at lower redshift may not be surprising in view of the increase in merger rates with redshift from both observational work (K. Duncan et al., 2019; M. Romano et al., 2021; Q. Duan et al., 2025; D. Puskás et al., 2025; T. Shibuya et al., 2025) and numerical simulations (V. Rodriguez-Gomez et al., 2015; A. Pillepich et al., 2019; J. A. O'Leary et al., 2021). It will be interesting to investigate the environment of the galaxies in greater detail in a future study, allowing us to quantify, for instance, the interaction strengths from neighbouring systems. More complete redshift identification around the CRISTAL galaxies will be necessary for that purpose.

3.9 Summary and outlook

In this work, we present a kinematic study of a sample of MS SFG(s) at redshift $4 < z < 6$ from the ALMA-CRISTAL programme. The angular resolution of the sensitive [C II] ALMA observations enables the characterisation of the kinematics of galaxies at a scale of $\sim 1\,$kpc. We classified the galaxies primarily based on their kinematic features traced by [C II] using a variety of methods that have been applied in lower redshift studies, supplemented by morphological information from HST and JWST imaging (Sect. 3.3). We found that $50 \pm 9\%$ of the galaxies in our sample are disk-dominated (Sect. 3.4), with over half of them located in systems of multiple components, which differs from the more isolated environment of lower redshift disks. We fitted the kinematics of the disks using fully forward-modelled

3D kinematic models (Sect. 3.5). Our kinematic modelling reveals the following important properties of the CRISTAL MS disks:

1. They have a high contribution of turbulence relative to rotational support, with a median disk velocity dispersion of $\sim 70\,\mathrm{km\,s^{-1}}$ and $V_{\mathrm{rot}}(R_{\mathrm{e}})/\sigma_0$ of ~ 2 (Sect. 3.6.1).
2. Their high-velocity dispersions are consistent with the predicted evolution based on Toomre theory and the extrapolated evolutionary trends based on detailed studies of cosmic noon to lower redshift galaxies (Sect. 3.6.1).
3. Their tentative correlation between gas mass and velocity dispersion provides hints that the high dispersion is sustained by gravitational instability, but it is unclear whether this is a local or global phenomenon (Sect. 3.6.2).
4. They tend to have a low DM fraction, with a median of $f_{\mathrm{DM}}(< R_{\mathrm{e}}) \approx 18\%$, while spanning a significant range from $\sim 5\%$ to $\sim 60\%$; the median value is in broad agreement with the extrapolated trend based on studies of lower redshifts, albeit with large scatter (Sect. 3.7).

The deep, high-resolution ALMA observations of [C II]158μm line emission from the CRISTAL programme allowed us to carry out a first systematic census of the kinematics of typical MS star-forming galaxies at $z \sim 4$–6. The brightness of [C II] along with its sensitivity to the multi-phase ISM make it an ideal probe of the gas motions (among other properties) over a large extent of galaxies encompassing cold molecular gas, ionised, and photodissociation regions. These properties facilitate measurements reaching the outskirts of galaxies. As observations of rest-optical line emission originating from the warm ionised gas phase become available from JWST IFU follow-up of CRISTAL targets, direct comparisons will become possible. This will be important especially with regard to the issue of gas turbulence. As discussed in this work (Sect. 3.6) and in the literature (e.g. M. Girard et al., 2021; T. Ejdetjärn et al., 2022; M. Kohandel et al., 2024; E. Wisnioski et al., 2025), it would greatly benefit from measurements in multiple tracers for the same objects. Another outlook enabled by CRISTAL-ALMA and JWST-IFU synergies is the connection between spatial variations in terms of the gas-phase metallicity and kinematics, which will be the subject of a forthcoming study.

Acknowledgments

We thank the anonymous referee for the constructive feedback which improves the clarity of the work. L.L.L. is thankful for the stimulating discussions with M. Bureau, Q. Fei, S. Pastras, W.

Maciejewski and E. Wisnioski at the various stages of this work. L.L.L. thanks A. Nestor for providing the data tables for Fig. 3.12. N.M.F.S. and J.C. acknowledge financial support from the European Research Council (ERC) Advanced Grant under the European Union's (EU's) Horizon Europe research and innovation programme (grant agreement AdG GALPHYS, No. 101055023). H.Ü. acknowledges funding by the EU (ERC APEX, 101164796). Views and opinions expressed are, however, those of the author(s) only and do not necessarily reflect those of the EU or the ERC. Neither the EU nor the granting authority can be held responsible for them. R.H-C. thanks the Max Planck Society for support under the Partner Group project 'The Baryon Cycle in Galaxies' between the Max Planck for Extraterrestrial Physics and the Universidad de Concepción. M.A. and R.H-C. also gratefully acknowledge financial support from ANID - MILENIO - NCN2024_112. M.A., R.J.A., R.H-C., M.S. and K. Telikova acknowledge support from ANID BASAL FB210003. R.J.A. was supported by FONDECYT grant number 1231718. R.B. acknowledges support from an STFC Ernest Rutherford Fellowship [grant number ST/T003596/1]. R.L.D. is supported by the Australian Research Council through the Discovery Early Career Researcher Award (DECRA) Fellowship DE240100136 funded by the Australian Government. T.D-S. acknowledges the research project was supported by the Hellenic Foundation for Research and Innovation (HFRI) under the '2nd Call for HFRI Research Projects to support Faculty Members & Researchers' (Project Number: 03382) I.D.L. acknowledges funding from the ERC under the EU's Horizon 2020 research and innovation program DustOrigin (ERC-2019-StG-851622) and from the Flemish Fund for Scientific Research (FWO-Vlaanderen) through the research project G0A1523N. R.I. is supported by Grants-in-Aid for Japan Society for the Promotion of Science (JSPS) Fellows (KAKENHI Grant Number 23KJ1006). T.N. acknowledges the support of the Deutsche Forschungsgemeinschaft (DFG, German Research Foundation) under Germany's Excellence Strategy - EXC-2094 - 390783311 of the DFG Cluster of Excellence 'ORIGINS'. M.S. was financially supported by Becas-ANID scholarship #21221511. K. Tadaki acknowledges support from JSPS KAKENHI Grant No. 23K03466. K. Telikova was supported by ALMA ANID grant number 31220026. V.V. acknowledges support from the ALMA-ANID Postdoctoral Fellowship under the award ASTRO21-0062. This paper makes use of the following ALMA data: ADS/JAO.ALMA#2021.1.00280.L, 2017.1.00428.L, 2012.1.00523.S, 2018.1.01359.S, 2019.1.01075.S. ALMA is a partnership of ESO (representing its member states), NSF (USA) and NINS (Japan), together with NRC (Canada), NSC and ASIAA (Taiwan), and KASI (Republic of Korea), in cooperation with the Republic of Chile. The Joint ALMA Observatory is operated by ESO, AUI/NRAO and NAOJ. This work is based in part on observations made with the NASA/ESA/CSA James Webb Space Telescope and NASA/ESA Hubble Space Telescope. The data were obtained from the Mikulski Archive for Space Telescopes (MAST) at the Space Telescope Science Institute, which is operated by the Association of Universities for Research in Astronomy, Inc., under NASA contract NAS 5-03127 for JWST and NAS 5–26555 for HST. The specific observations analysed can be accessed via 10.17909/2gpc-vd24. Support to MAST for these data is provided by the NASA Office of Space Science via grant NAG5–7584 and by other grants and contracts. Some of the data products presented herein were retrieved from the Dawn JWST Archive (DJA). DJA is an initiative of the Cosmic Dawn Center (DAWN), which is funded by the Danish National Research Foundation under grant DNRF140.

SOFTWARE

This work made use of the following Python packages: `Astropy` (Astropy Collaboration et al., 2022), `corner` (D. Foreman-Mackey, 2016), `DysmalPy` (R. I. Davies et al., 2004a,b; R. Davies et al., 2011; G. Cresci et al., 2009; S. Wuyts et al., 2016; P. Lang et al., 2017; S. H. Price et al., 2021; L. L. Lee et al., 2025a), `emcee` (D. Foreman-Mackey et al., 2013), `Imfit` (P. Erwin, 2015), `Matplotlib` (J. D. Hunter, 2007), `Numpy` (C. R. Harris et al., 2020), `pymccorrelation` (P. A. Curran, 2014; G. C. Privon et al., 2020), `Trilogy` (D. Coe et al., 2012), and `Scipy` (P. Virtanen et al., 2020).

3.10 Appendix A – Global properties of individual galaxies

For each galaxy individually, we briefly comment below on its global properties and its overall kinematic classification, based on the methods described in Sect. 3.3. Detailed properties of CRISTAL-05 and 22 are presented in A. Posses et al. (2025) and K. Telikova et al. (2025), respectively. Figs. 3.15 to 3.18, from left to right, display the JWST, HST colour-composite images, the [C II] line emission, velocity and velocity dispersion maps. The velocity locus measured with SA in Sect. 3.3.4 is overlaid on either the JWST or HST colour images in the rightmost column. The sizes and transparencies of these overlays are proportional to the positional uncertainty error. Figs. 3.19 to 3.25 show additionally the p-v diagrams along the kinematic major and minor axes and the integrated spectrum. Where applicable, the quoted distance between companions is always projected.

CRISTAL-01a: Non-Disk, identified in ‘multi-UV’ in R. Ikeda et al. (2025) with HST data, JWST further supports that it is interacting with a massive neighbour SMG J1000+0234 and a companion at its north-east. It is also consistent with the multiple peaks in the integrated spectrum. The velocity field displays a gradient along the morphological minor axis observed in imaging data. This could suggest that this system is in its later phase of the merger, and the misaligned gradient may be a signature of gas inflow triggered by the merger. The interaction of the members in the CRISTAL-01 system is studied in more detail in M. Solimano et al. (2025).

CRISTAL-01b: Non-disk, with a pair of interacting systems, situated approximately $\sim 48\,\mathrm{kpc}$ south-east of CRISTAL-01a. The binary nature is conspicuous in both HST and JWST images, with the two components separated by a distance of $\sim 7\,\mathrm{kpc}$. The [C II] line map shows emission south of the eastern companion. There is an apparent spatial offset between the [C II] emission and the stellar component of the western companion, possibly originating from the gas that is being stripped away in the interaction. Although the eastern companion exhibits a velocity gradient transitioning from north to south, its dispersion appears disrupted, with elevated peaks in the north-eastern region.

CRISTAL-02: Disk, whose system is also known as the LBG-1 in D. A. Riechers et al. (2014). The SMG AzTEC-3 ($z = 5.298$) $\sim 90\,\mathrm{kpc}$ away is also detected in [C II] at the edge of FoV. There is an overall isovelocity pattern consistent with disk rotation. The receding side is influenced by the interaction with the lower-mass satellite galaxy, resulting in a velocity reversal at the very north. The p-v diagram shows excess emission in high-velocity wings near the centre, which is associated with an outflow as evidenced in the integrated spectrum in Fig. 3.21. NIRSpec/JWST data ($R \sim 1000$) further confirms the biconical outflow signature (R. L. Davies et al., 2025). Considering the outflow and the interacting companion in the north, we therefore fit the emission in the p-v diagram (method detailed in Sect. 3.3.1) with a broad and a narrow component (Fig. 3.14). We attribute the narrower line to the bulk rotation motion, and the velocity and dispersion profiles derived from it are used in the analysis in Sect. 3.5.1. By removing the broad component, we effectively minimise the contributions from the outflow and the satellite galaxy.

CRISTAL-03: Best Disk, where the velocity gradient appears to align with the overall morphological PA of the HST and JWST images, but not with that of [C II], especially at the outer isophotes due to the protrusion at the south-west. Although this galaxy is the most poorly resolved in our sample, the NIRSpec/JWST data with $5\times$ better angular resolution reveal a consistent rotational pattern in Hα (W. Ren et al., 2025). This galaxy is also flagged as the most evident candidate for an AGN, which could potentially account for the protruded [C II] emission towards the south-west, and the slight deviation from the unidirectional SA locus in Fig. 3.15.

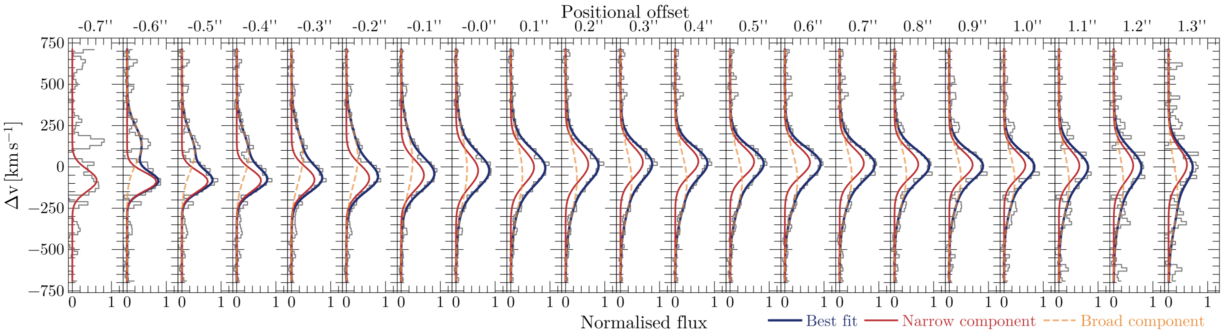

Figure 3.14 Two-component Gaussian fit (blue thick line) of CRISTAL-02 emission profile along each column in the position-velocity (p-v) diagram (grey lines) extracted along the kinematic major axis. The underlying p-v diagram from which the profiles are extracted is shown in Figure 3.21. We assumed the narrow component (red) to trace the bulk rotation motion of the gas, which was then used for subsequent kinematics modelling, while the broad component (orange) is associated with the outflow and the interacting companion in the north (at offset $\gtrsim 0\farcs8$). For other galaxies, we assume a single Gaussian profile using the same extraction method.

CRISTAL-04a: Non-Disk, with a velocity gradient running from south to north and elevated dispersion along the zeroth velocity contour. However, the velocity isocontours deviate substantially from a spider diagram, and the p-v diagram along the major axis is primarily flat. The perturbation is most likely due to its recent minor-merger interaction with CRISTAL-04b (mass ratio ∼17:1, R. Herrera-Camus et al. 2025). CRISTAL-04a and CRISTAL-04b are identified as a 'pair' in R. Ikeda et al. (2025).

CRISTAL-04b: Non-Disk, where a blob of faint [C II] emission ∼ 10 kpc north of CRISTAL-04a that does not show a clear rotating signature. It could comprise two smaller substructures, as evidenced by the [C II] line map and the JWST images.

CRISTAL-06a: Non-Disk that is possibly a counter-rotating binary merger of two disks, where we observe a reversal in velocity gradient along the major axis, yet the individual components remain spatially unresolved at the current resolution. This system was also classified as a pair-merger in association with CRISTAL-06b in O. Le Fèvre et al. (2020) and is the only multiple-[C II] system in R. Ikeda et al. (2025). Alternatively, it could be a single disk with the approaching side at the east perturbed by CRISTAL-06b, as hinted by a velocity dispersion that peaks where the gradient is steepest. R. Ikeda et al. (2025) identified the multi-[C II] nature within CRISTAL-06a, while CRISTAL-06a and CRISTAL-06b are identified as a 'pair' in R. Ikeda et al. (2025).

CRISTAL-06b: Disk, located ~ 10 kpc north-east of CRISTAL-06a with its velocity and dispersion fields consistent with a rotating disk. The slightly twisted velocity isocontours are likely a result of the perturbation from CRISTAL-06a, which is 8× more massive (R. Herrera-Camus et al., 2025).

CRISTAL-07a: Disk that exhibits a clear velocity gradient from north to south, but the northern part is perturbed by its interaction with CRISTAL-07b (mass ratio ∼2:1) in the early phase. In the kinematics modelling, we symmetrise the velocity dispersion profile from the receding and approaching sides (following A. Posses et al. 2025) to reduce the impact of the interaction on the intrinsic dispersion, as the receding side is much less perturbed.

CRISTAL-07b: Non-Disk, which is an interacting neighbour with CRISTAL-07a separated by ~ 8 kpc; there is an overall velocity gradient stretching from east to west, but the isovelocity contours are more disrupted compared to CRISTAL-07a due to its lower mass. CRISTAL-07a and CRISTAL-07b are identified as a 'pair' in R. Ikeda et al. (2025), while CRISTAL-07 as a whole was classified as a pair-merger in O. Le Fèvre et al. (2020).

CRISTAL-07c: Non-Disk that is an interacting system of comparable masses located at 140 kpc west of CRISTAL-07a and CRISTAL-07b.

CRISTAL-08: Disk that exhibits a remarkably smooth velocity gradient, although there is a change of isovelocity contours PA from south to west (visible also in the SA locus), likely due to non-circular motion along the minor axis (R. Herrera-Camus et al., in prep.). The velocity dispersion peaks at the south-west corner, away from the morphological centre and peak of the [C II] line emission; The JWST colour image shows a very clumpy appearance (see also the F444W residual image in Fig. 3.26) similar to the galaxy in T. S. Tanaka et al. (2024) at $z = 4.91$, with clumps of various colours distributed from 8 o'clock to 2 o'clock positions. The Disk classification is consistent with the 'rotating disk' classification in O. Le Fèvre et al. (2020). R. Herrera-Camus et al. (2025) will present the detailed properties of the clumps.

CRISTAL-09: Disk observed as a compact object in the HST image, JWST reveals extended stellar light in the south-west at faint levels. The extended stellar component is more apparent in the residual left after subtracting a Sérsic model (Fig. 3.26). [C II] data provides tentative evidence of disk rotation but is still limited by the angular resolution and S/N. This system was classified as a pair-merger in O. Le Fèvre et al. (2020).

CRISTAL-10a: Non-Disk, for which no JWST image is available. Based on the HST data, R. Ikeda et al. (2025) classified it as a multi-UV system, with the two UV components separated by $\sim 5.5\,\mathrm{kpc}$. [C II] line map shows a consistent separation of the two components. Consider the two components as one system, it exhibits a monotonic velocity gradient from north-east to south-west across the two components, with a prominent dispersion peak where the velocity gradient is steepest. However, the Gaussian fit errors at the dispersion peak are large due to low S/N. SA locus and p-v diagram reveal an abrupt velocity jump between the east (CRISTAL-10a-E) and west components, with a clear gap in the velocity structure, coinciding with that in the HST image. This suggests that the velocity gradient is plausibly driven by the orbital motion of the two components. Notably, this system shows a strong [C II]/FIR deficit (R. Herrera-Camus et al., 2025), with prominent dust continuum emission where [C II] emission is weakest, particularly around the southern parts of both components. While this could indicate that the CRISTAL-10a and CRISTAL-10b are substructures of a single larger system, the [C II] kinematics does not support the interpretation for now, so we classify the system as a Non-Disk.

CRISTAL-10a-E: Disk that makes up the eastern component of CRISTAL-10a. Despite being in a potentially interacting system, it shows a very promising disk-rotating signature in its own velocity and dispersion maps. The SA locus and p-v diagram resemble a disk-like system but also exhibit features indicative of interaction with the western component.

CRISTAL-11: Disk, for which we observed a velocity gradient from south-east to north-west, with a dispersion peak near the morphological centre. The kinematic PA is aligned with the morphological PA in both JWST and HST images with a difference of $< 10°$. However, the north-west region appears more dust-attenuated and has a distinct colour compared to the south-east, suggesting a possible merger of the two systems. Higher resolution data would be required to discern the true nature of this system. Nevertheless, based on the available data, we maintain our classification as a Disk. O. Le Fèvre et al. (2020) classified this system as ‘extended and dispersion-dominated’.

CRISTAL-12: Disk that is the least massive system among CRISTAL, with a shallow velocity gradient. It is classified as ‘compact’ in O. Le Fèvre et al. (2020) and, even with our higher resolution data, it remains poorly resolved, with only a tentative velocity gradient from west to east. There is a faint [C II] emission blob $\sim 4\,\mathrm{kpc}$ away in the north-west, but no visible counterpart in HST and JWST images. This emission is linked to the elevated dispersion in the north-west. This feature is also seen in other Disk systems, CRISTAL-02, 15, 19 (and 03, although poorly resolved), which may suggest an outflow origin of the gas. However, except for CRISTAL-02, deeper data will be required to confirm this speculation.

CRISTAL-13: Non-Disk that was already noted by R. Ikeda et al. (2025) about its multi-UV appearance in HST, JWST images further reveal the intriguing structure of the eastern and western components. The compact western source is dominated by an older stellar population (N. E. P. Lines et al., 2025) situated adjacent to a clumpy, blue eastern tail. The clump properties are addressed in R. Herrera-Camus et al. (2025). While both the velocity and dispersion maps exhibit characteristic signatures of a rotating disk, the p-v diagrams along both the major and minor axes show features that deviate substantially from typical disk-like rotation. SA indicates receding motion along the blue tail, suggesting that this system is likely the result of a merger between the western and eastern sources.

CRISTAL-14: Non-Disk, for which we observed an apparent velocity gradient from north-east to south-west. However, a centralised dispersion peak is absent. Furthermore, the p-v diagrams do not display the characteristic patterns associated with disk-like rotation. Both HST and JWST images reveal a western component with a distinct colour that is faint in [C II]. The [C II] emission predominantly traces the eastern component, which contributes the majority of the velocity gradient. Therefore, it is likely that this system is similar to CRISTAL-13, with the eastern source being in a close encounter with the western source.

CRISTAL-15: Best Disk, where we observe a velocity gradient from south-east to north-west, which agrees with the unidirectional locus traced by SA. An extended [C II] structure is present at the north-east of the kinematic minor axis, which could indicate slow outflowing gas (see also CRISTAL-12), as there is no significant broad emission component in the integrated spectrum. The ‘root’ of this extended structure is also co-spatial with the elevated dispersion in the dispersion map. JWST data reveal three clumps of bluer colour embedded within a redder disk, which is also more evident in the F444W residual image in Fig. 3.26. We notice that the peak-to-peak velocity difference of CRISTAL-15 is only $50\,\mathrm{km\,s^{-1}}$, and our ALMA data cube is binned to $20\,\mathrm{km\,s^{-1}}$, which barely samples the velocity gradient. The data cube binned to $10\,\mathrm{km\,s^{-1}}$ is too low S/N for robust extraction of the RC and dispersion profile. As a result, the derived velocity dispersion in Sect. 3.5 for CRISTAL-15 may still be contaminated by the contribution of the unresolved velocity gradient.

CRISTAL-16a,b: Non-Disk that is similar to CRISTAL-01b and CRISTAL-06, this system is an interacting pair consisting of at least two companions, CRISTAL-16a and CRISTAL-16b, separated by a distance of $\sim 5.3\,\mathrm{kpc}$. The eastern companion, CRISTAL-16a, appears to be composed of two clumps separated by $\lesssim 2\,\mathrm{kpc}$, similar to CRISTAL-02, although it is unclear whether these clumps represent separate galaxies in a merger, or multiple star formation clumps within a galaxy. The [C II] line map reveals two barely resolved emission peaks co-spatial with the two companions of CRISTAL-16a. When considering CRISTAL-16a as a whole, the global velocity gradient is aligned with the morphological minor axis. Interestingly, the zeroth-velocity contour coincides with the dispersion peaks, suggesting a possible scenario in which two disk-like systems are approaching each other along their respective minor axes. The JWST/F444W image (Fig. 3.26) reveals a conceivable connecting 'bridge' between the north-east and south-west clumps within CRISTAL-16a, providing further evidence for an interaction. CRISTAL-16b is too faint in [C II] for kinematics extraction. Overall, the CRISTAL-16a system bears similarities to CRISTAL-07a and 07b, but perhaps with a different orbital configuration. However, the individual components remain spatially unresolved at the current resolution.

CRISTAL-19: Best Disk, where the velocity map, SA locus and p-v diagram all show a coherent velocity gradient with little deviation from symmetry. The dispersion peak coincides with the position of the steepest velocity gradient. There is no evidence of a physically associated neighbour in the available data. Despite having a high intrinsic dispersion ($\sigma_0 = 65\,\mathrm{km\,s^{-1}}$), the system's $V_{\mathrm{rot}}/\sigma_0 \approx 2.2$ ratio indicates it is not dispersion-dominated, contrary to the classification in O. Le Fèvre et al. (2020).

CRISTAL-20: Best Disk that is one of the CRISTAL pilot galaxies first studied by R. Herrera-Camus et al. (2022), which also presented its outflow properties. The velocity map shows the typical rotating pattern of a disk, while the dispersion map shows the expected outflow signature at the north-west. SA aligns uni-directionally with the observed gradient in the velocity map; p-v diagrams along the major axis show a clean S-shape, while along the minor axis, no velocity gradient is seen, indicative of a classical disk. E. Parlanti et al. (2025) presented the NIRSpec/JWST data of the ionised gas outflow traced by [O III]λ5007 Å and a merger scenario based on the ionised gas.

CRISTAL-21: Non-Disk, where the velocity gradient is from north to south, but the dispersion map shows multiple peaks. The SA locus also displays a chaotic distribution within the central region, which could indicate unresolved line-of-sight mergers. It is consistent with the very elongated shape of the p-v diagram, stretching from $-500\,\mathrm{km\,s^{-1}}$ to $500\,\mathrm{km\,s^{-1}}$ within the central $\sim 2\,\mathrm{kpc}$ region, indicative of an absence of a global velocity gradient. Although this could also be caused by a strong outflow at the centre, T. S. Lambert et al. (2023) found no evidence of outflows from the system, as indicated by the absence of a broad secondary component in the [C II] spectrum. Instead, the observed disturbed gas and dust emission, combined with its kinematic structure, suggest that the system is in a late-stage merger. NIRCam/JWST images reveal a blue 'clump' located at the east side of the [C II] light centre, which could be the merger companion.

CRISTAL-23a: Non-Disk that is one of the companions (source C) in the 'triple-merger' system was first studied in detail by G. C. Jones et al. (2021). As noted by G. C. Jones et al. (2021), it is in proximity to the massive protocluster PC1 J1001+0220 (B. C. Lemaux et al., 2018). Since it lies along the major axis of the protocluster and is only $\sim 3.5\,\mathrm{Mpc}$ from the north-east component of this protocluster, it could be associated with the system in a filamentary structure. Because of a different slit angle chosen, we observe a velocity gradient from north to south of this source, in contrary to G. C. Jones et al. (2021). The p-v diagram, however, exhibits substantial broadening along the velocity axis in the central region, which is inexplicable by a disk origin (e.g. an outflow).

CRISTAL-23b: Disk, labelled as 'source E' in G. C. Jones et al. (2020). The velocity gradient exhibits a clear east-west orientation, consistent with SA analysis. The velocity dispersion is elevated around the zero-velocity contour. The p-v diagram along the major axis displays a characteristic disk profile, whereas the minor axis p-v diagram shows a slight deviation, likely attributed to the ongoing interaction with CRISTAL-23a.

CRISTAL-23c: Disk that was also noted by T. Devereaux et al. (2024). It is the least luminous of the three sources in the CRISTAL-23 system and is likely to be rotating. It is separated from CRISTAL-23a and 23b in velocity by $\sim 300\,\mathrm{km\,s^{-1}}$ and spatially by $18\,\mathrm{kpc}$. The velocity and dispersion map of this galaxy showed signs of disk rotation but is slightly perturbed by its interaction with CRISTAL-23a and 23b. It is the 'source W' in G. C. Jones et al. (2020).

CRISTAL-24: Non-Disk, with multiple dispersion peaks in the dispersion map; the SA does not show a large-scale velocity gradient, with a closely spaced locus suggesting a line-of-sight merger, which is further supported by the almost vertical position-velocity diagram along the major axis. Morphological and kinematic studies by T. Devereaux et al.

(2024) rejected the outflow scenarios. This galaxy has the largest integrated line width, $\sigma_{\rm int} \approx 300\,{\rm km\,s^{-1}}$. Although CRISTAL-07 is 130 kpc (projected) away, it is not associated with CRISTAL-24 with a redshift difference of $\Delta z \approx 0.6$.

CRISTAL-25: Non-Disk, for which T. Devereaux et al. (2024) previously dismissed the merger scenario based on the HST morphology and dust continuum emission; however, the disjoint velocity structure in the p-v diagram, the well-defined velocity gradients of each component (Fig. 3.25), with the northern component displaying a clear dispersion peak, could be indicative of a merger.

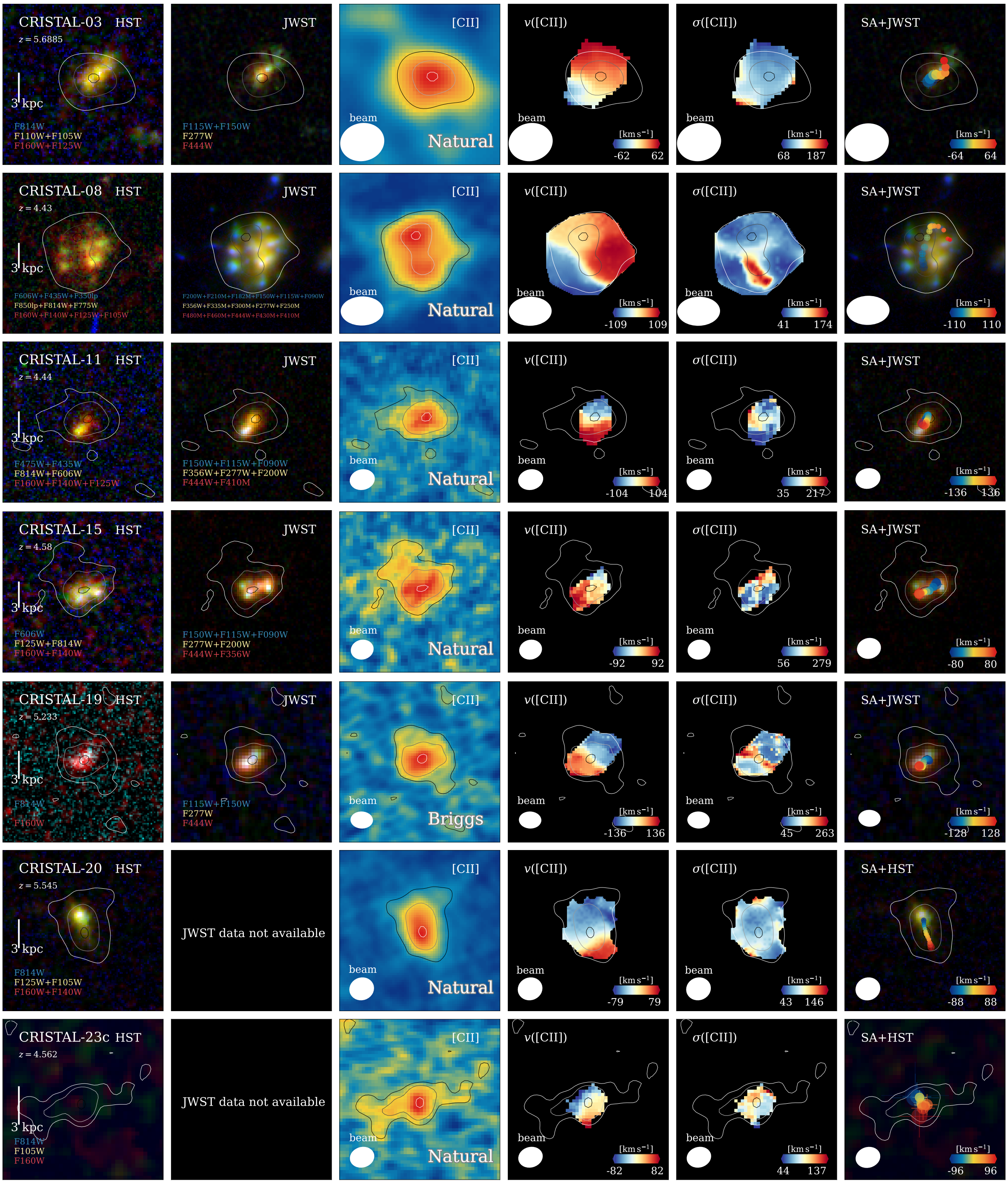

Figure 3.15 Gallery showing the multi-wavelength properties of the Best Disks. The first column displays the colour-composite images from HST, and if available, NIRCam/JWST images are shown in the second column. The third to fifth columns are ALMA images of [CII] emission, shown as line intensity, velocity, and velocity dispersion maps. The velocity and velocity dispersion maps are obtained by pixel-by-pixel single Gaussian fitting to the natural-weighted line cube, binned at $\Delta V = 20\,\mathrm{km\,s^{-1}}$ spectral resolution. They are *not* corrected for spectral broadening, beam-smearing and projection. The last column shows the spectro-astrometry (SA) measurement overlaid on HST (or NIRCam/JWST if available) colour images, in which the sizes and transparencies of the points are proportional to the positional uncertainties derived using Equation 1 in J. J. Condon et al. (1998). For all panels, the contours correspond to the intensities of the [C II] line map, plotted from 1.5σ to 3σ.

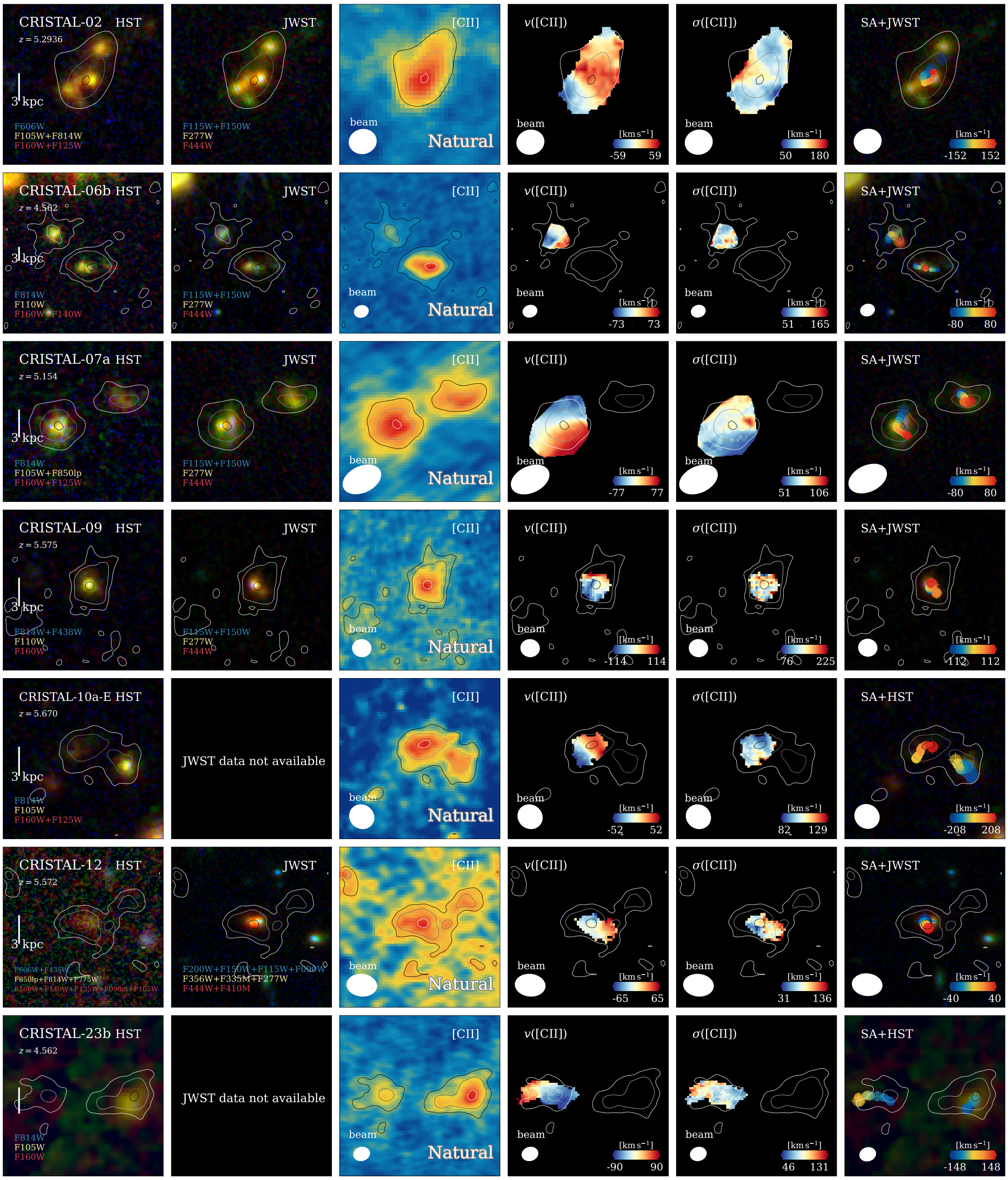

Figure 3.16 Same as Figure 3.15, but for the Disk.

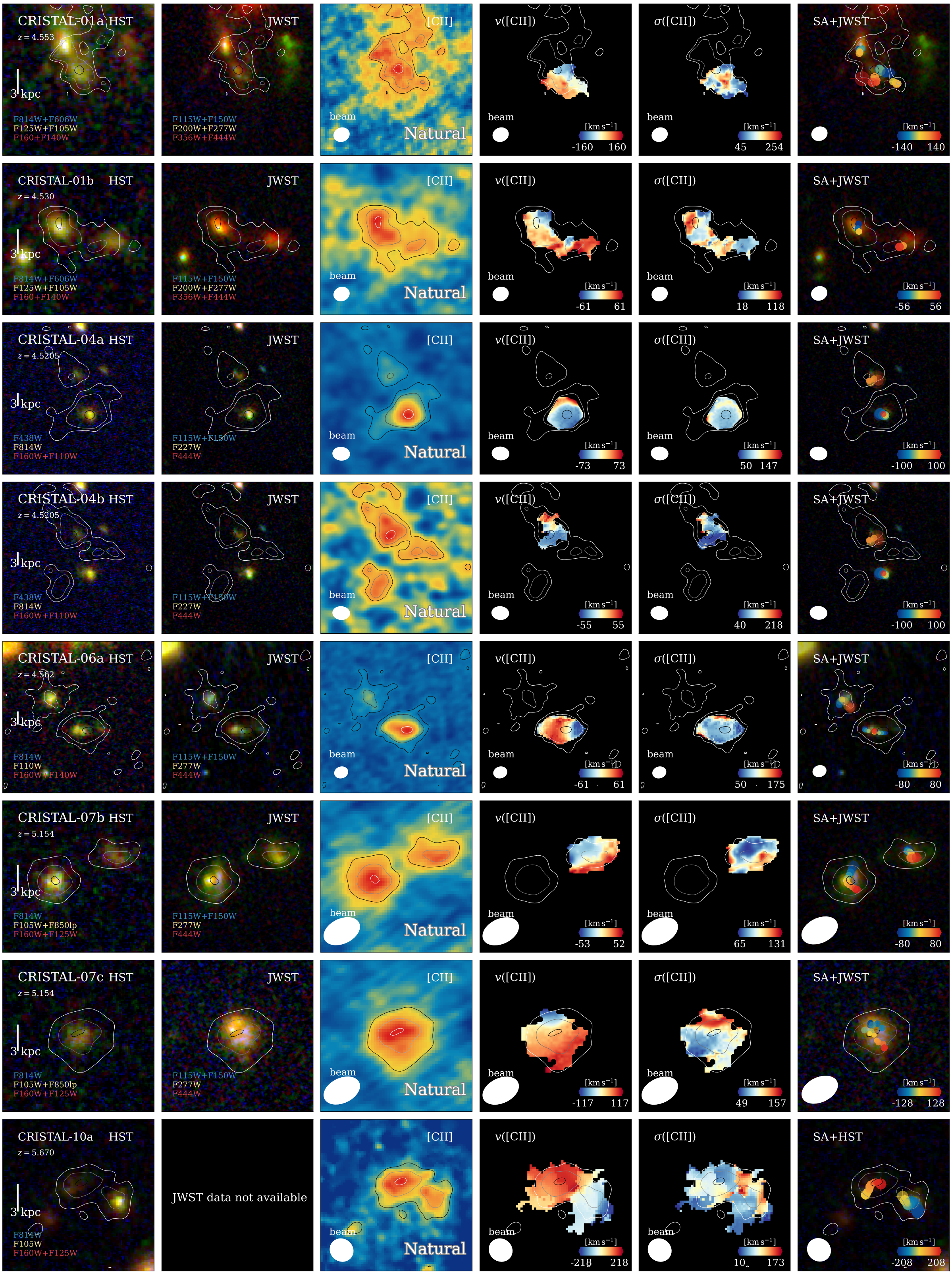

Figure 3.17 Same as Figure 3.15, but for the Non-Disk. For CRISTAL-01a and 04b, we subtract the bright companions to improve visual contrast.

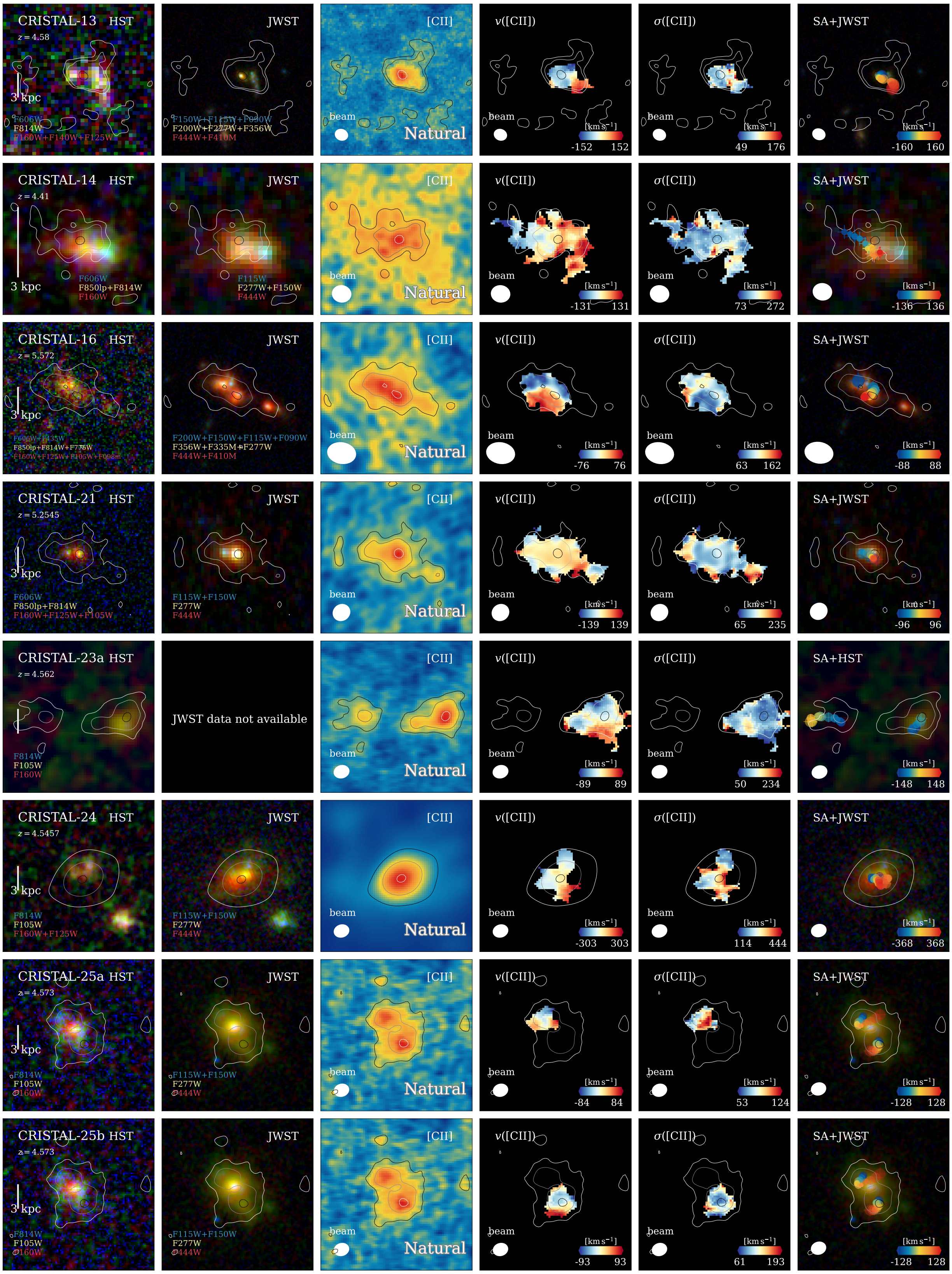

Figure 3.18 *(Continued.)*

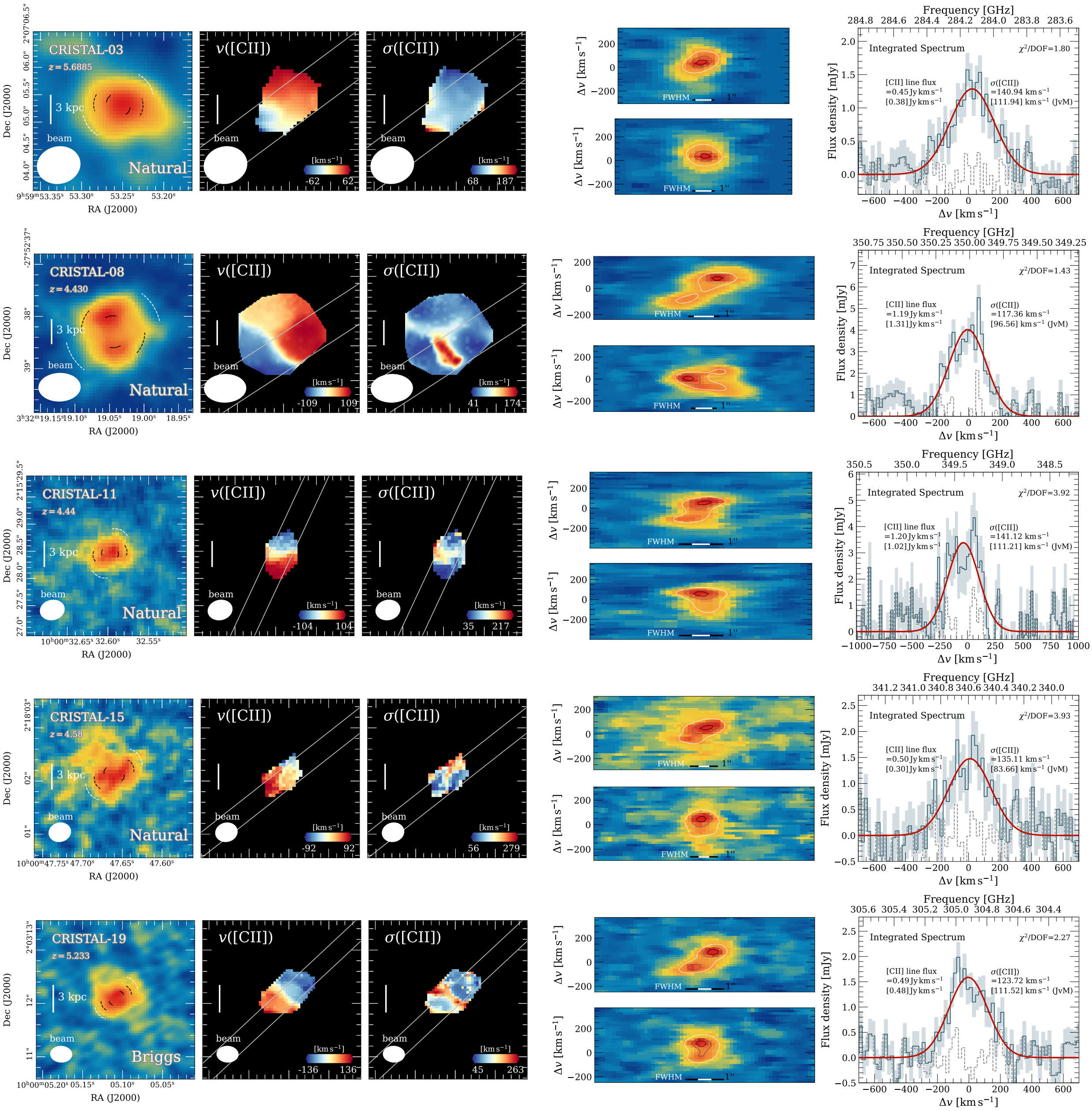

Figure 3.19 [CII] line maps, velocity maps, dispersion maps, position-velocity (p-v) diagrams (with median filtering applied for visual purposes), integrated spectra and shifted spectra of the Best Disk. In the [CII] line maps, the dashed pairs of arcs delineating the emission indicate the disk's apparent morphological position angle ($\mathrm{PA_m}$, black) and the kinematic major axis (white). The solid pair of arcs represents the intrinsic $\mathrm{PA_m}$ after correcting for the beam. In the p-v diagrams, the black and white horizontal bars correspond to $1''$ and the synthesised beam FWHM, respectively.

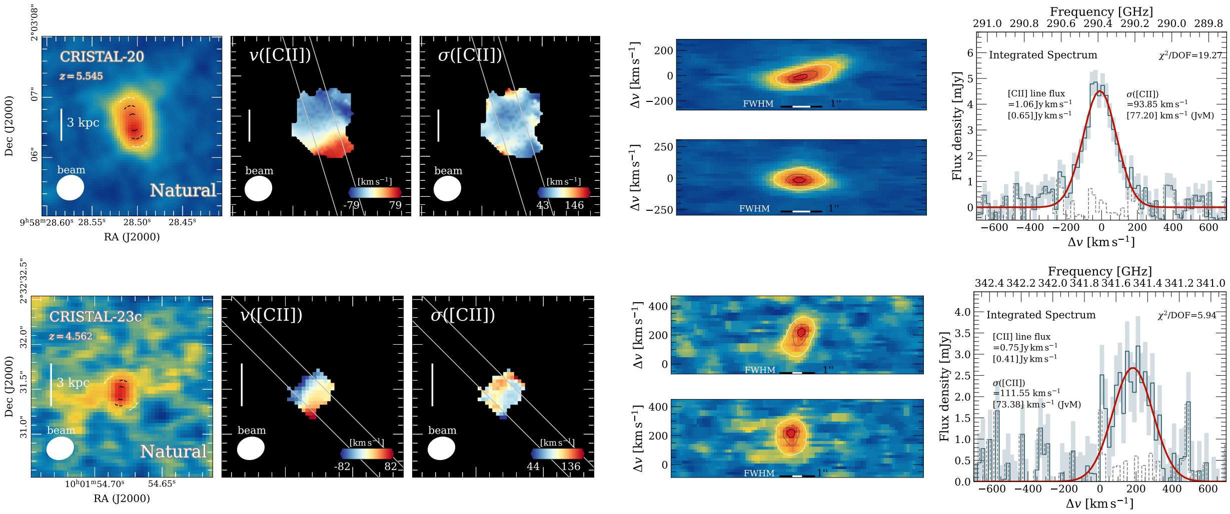

Figure 3.20 *(Continued.)*

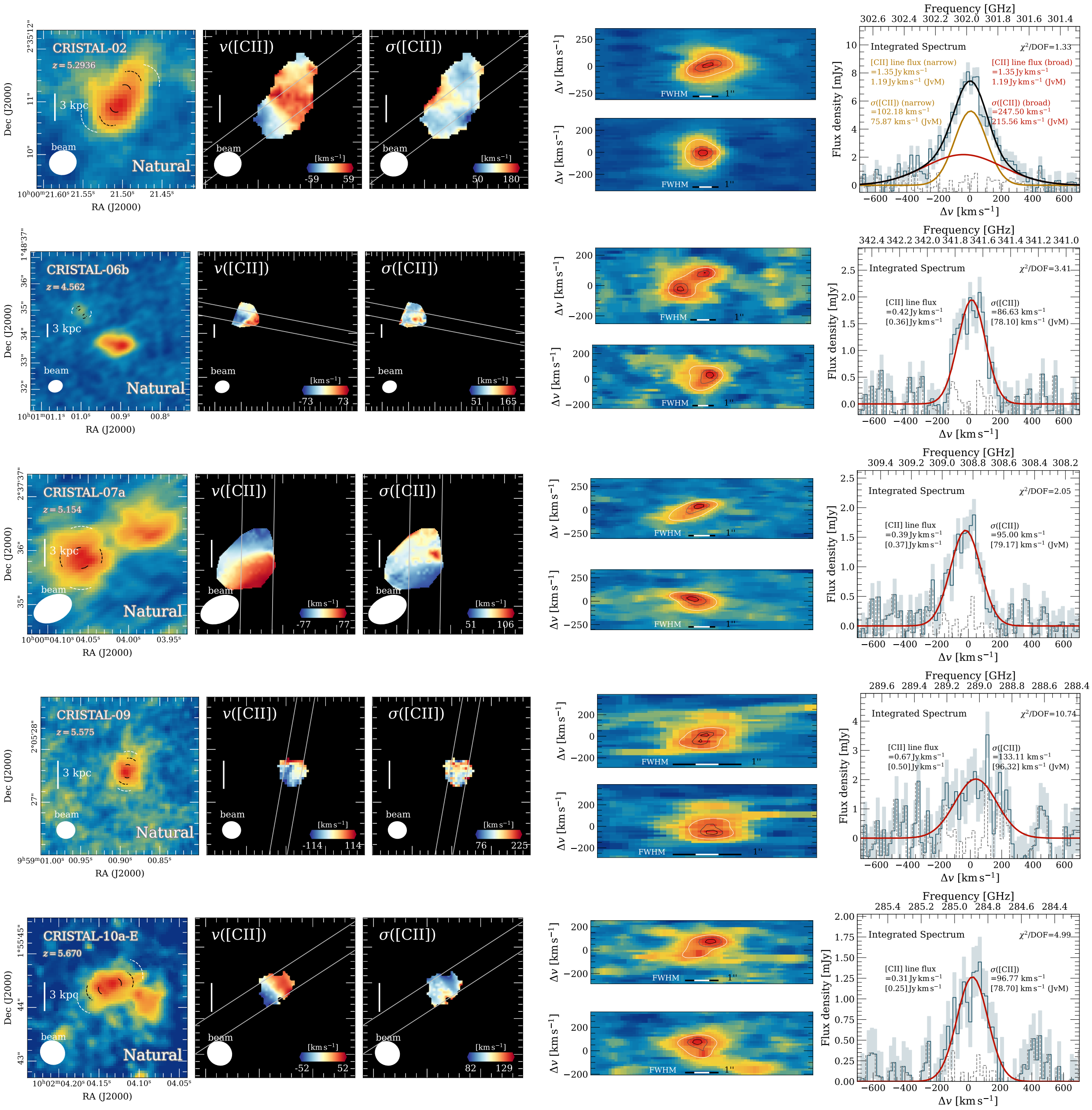

Figure 3.21 Same as Figure 3.19, but for the Disk.

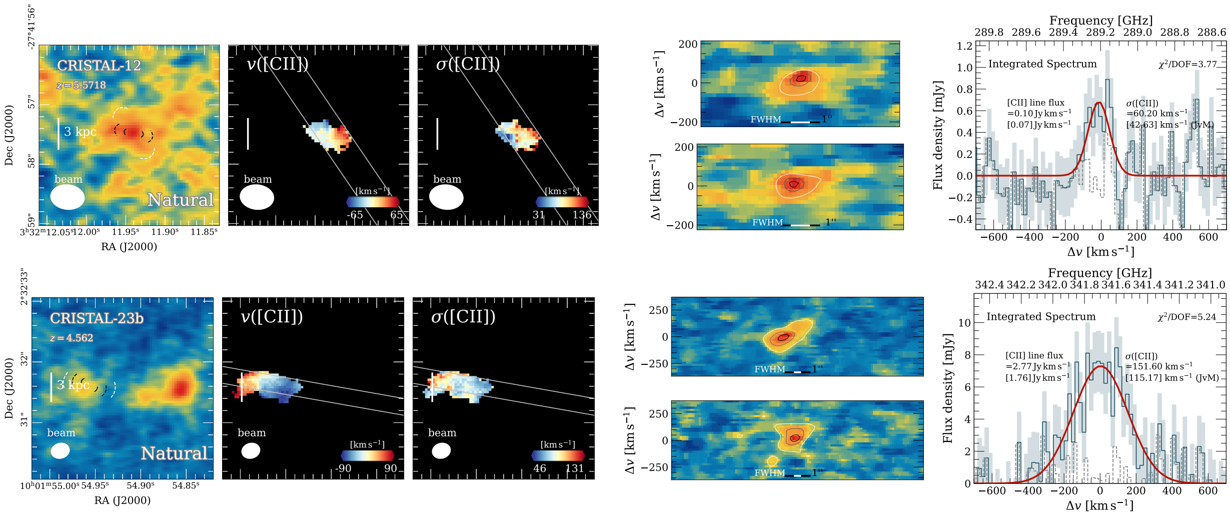

Figure 3.22 *(Continued.)*

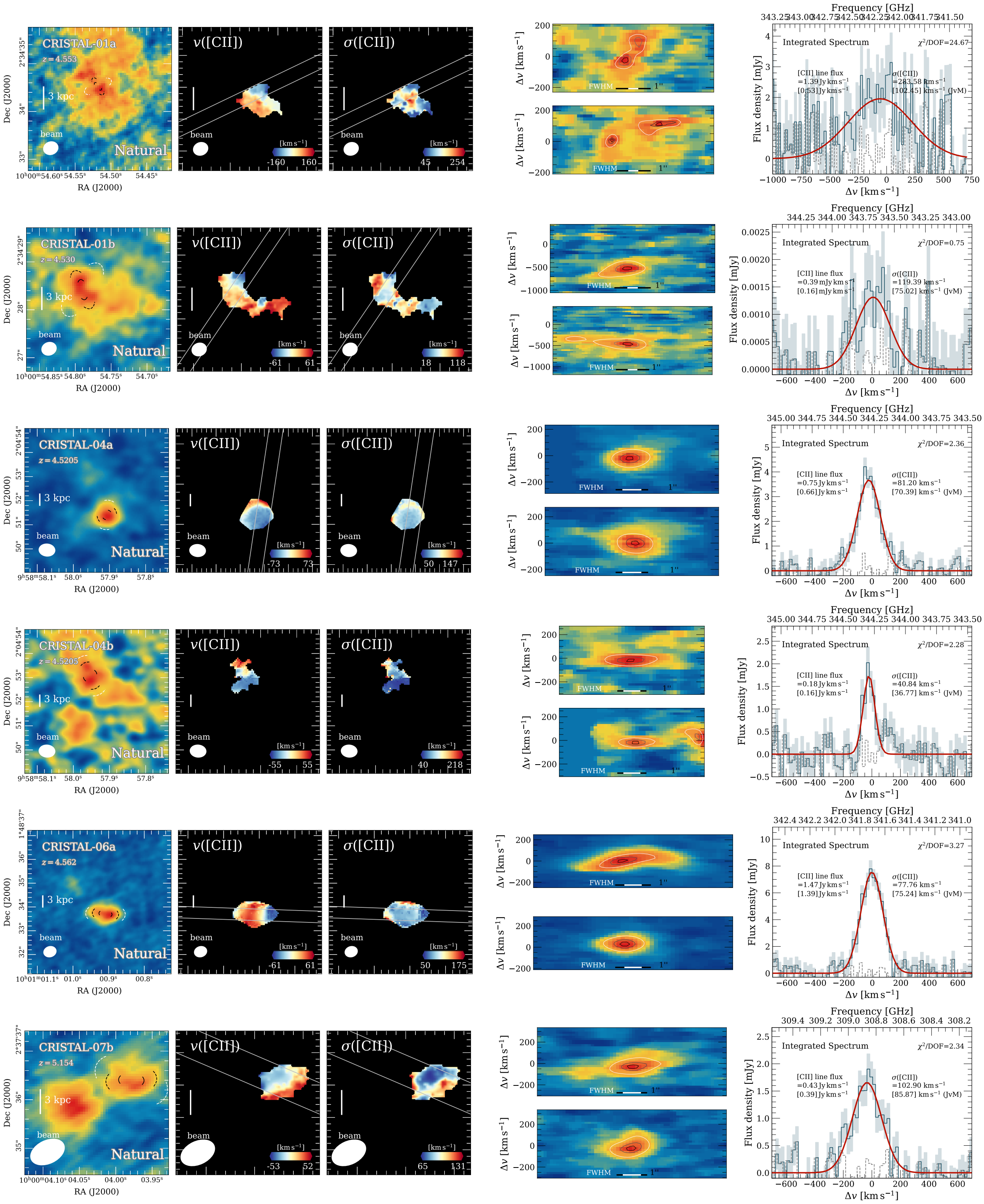

Figure 3.23 Same as Figure 3.19, but for the Non-Disk. For CRISTAL-01a and CRISTAL-04b, the bright companions are subtracted from the line maps for better visual contrast.

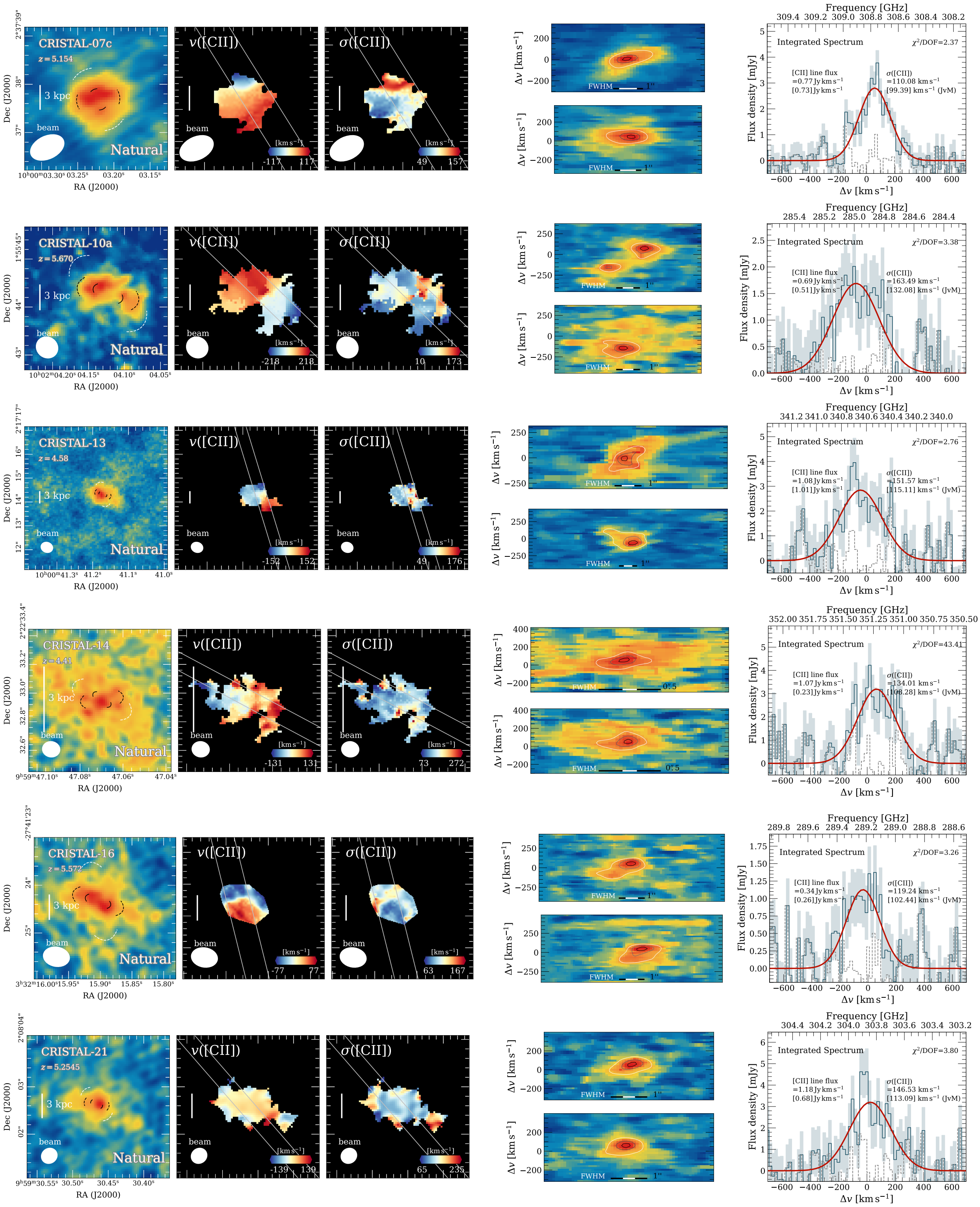

Figure 3.24 *(Continued.)*

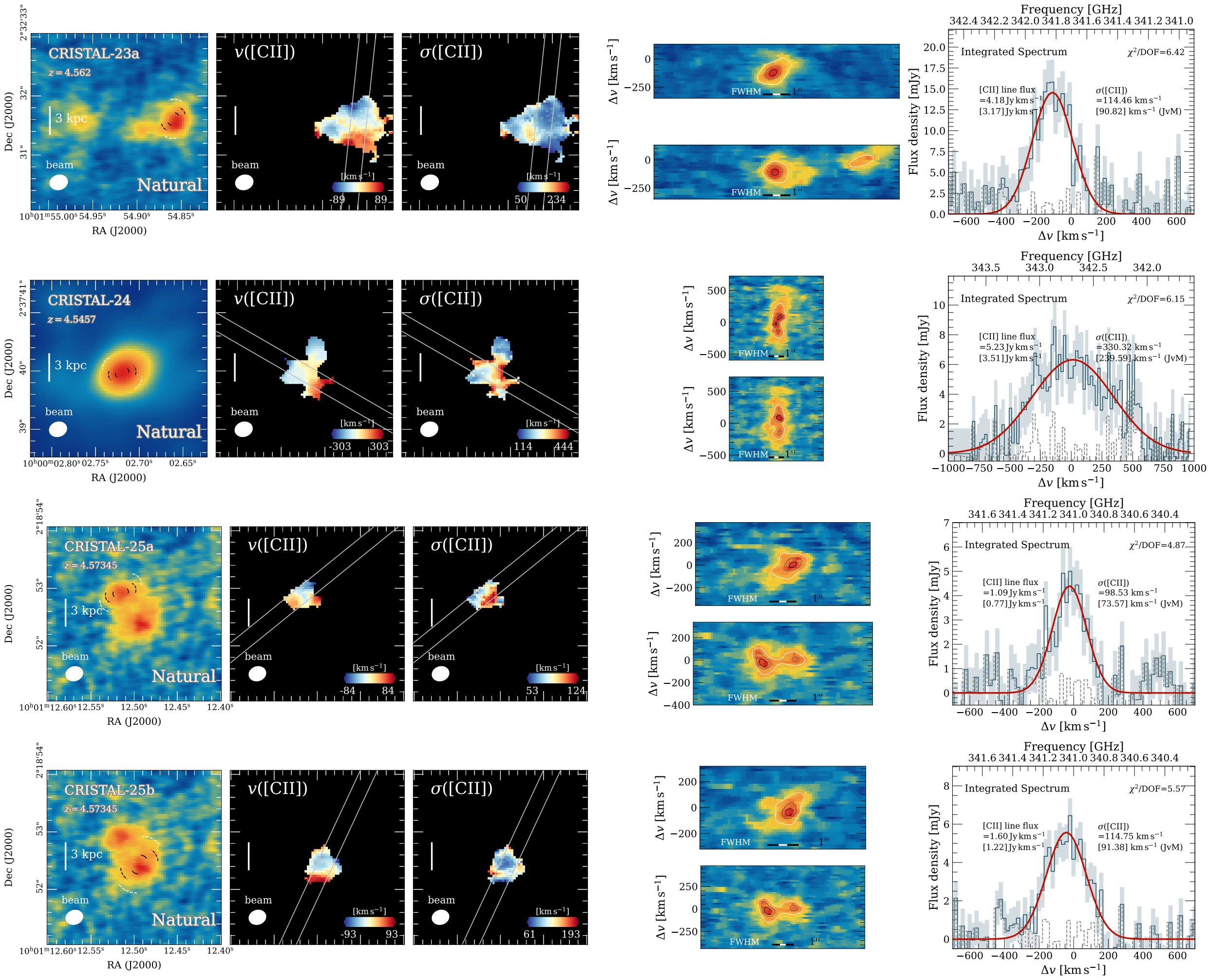

Figure 3.25 *(Continued.)*

3.11 Appendix B – Structural parameters fit of NIRCam/F444W images

We fit the 2D light distributions of the galaxies observed with NIRCam/JWST F444W with `imfit` (P. Erwin, 2015), accounting for the PSF. The PSF model adopted is described in J. Li et al. (2024a). We assume a Sérsic profile with variable Sérsic index n and fixed $n = 1$. When left free, n freely varies within $[0.5, 6]$. We also let the effective radius (R_e), the ellipticity $e = 1 - b/a$, and the position angle (PA) of the major axis as free parameters. Table 3.4 lists the best-fit structural parameters of the galaxies for variable n. Average Sérsic index and effective radius are $\langle n \rangle = 1.1 \pm 0.2$, $\langle R_{\mathrm{e}_{4.4\mu\mathrm{m}}} \rangle = 1.46 \pm 0.04\,\mathrm{kpc}$, respectively. The effective radius is $\sim 1.5\times$ that of the rest-frame UV emission $\langle R_{\mathrm{e}_\mathrm{UV}} \rangle \approx 0.98\,\mathrm{kpc}$ (for the same sources considered, R. Ikeda et al., 2025). Our $\langle R_{\mathrm{e}_{4.4\mu\mathrm{m}}} \rangle$ is comparable to that of the dust continuum emission $\langle R_{\mathrm{e}_\mathrm{dust}} \rangle \approx 1.78\,\mathrm{kpc}$ (I. Mitsuhashi et al., 2024), but is smaller than the [CII] sizes $\langle R_{\mathrm{e}_{[\mathrm{CII}]}} \rangle \approx 1.9\,\mathrm{kpc}$ (R. Ikeda et al., 2025). Fixing $n = 1$ in our fit gives $\langle R_{\mathrm{e}_{4.4\mu m}} \rangle = 1.77\,\mathrm{kpc}$. For consistency, we used the result of $n = 1$ R_e as the initial guess for the dynamical modelling.

For comparison, A. van der Wel et al. (2014), which covers $0 < z < 3$ galaxies observed in the H_{160} band, the expected value for SFG(s) extrapolated to $z = 5$ and $\log M_*/\mathrm{M}_\odot = 10$ is 2.4 kpc, our $R_{\mathrm{e}_{4.4\mu m}}$ is on average 40% smaller, but is still within the ~ 0.2 dex scatter at $z \approx 3$.

3.12 Appendix C – Molecular gas fractions f_molgas

Previous studies of MS SFG(s) at $z \sim 1$–3 have shown that their gas kinematics are closely tied to their molecular gas content (e.g. E. Wisnioski et al., 2015; H. Übler et al., 2019) inferred from scaling relations. We similarly explore the relationship between the kinematic properties of CRISTAL disks and their gas fractions in Sects. 3.6.1–3.6.2. As a first step, we need to estimate the gas content of our sample galaxies.

Measuring the gas content of CRISTAL galaxies using CO emission, which is a well-calibrated H_2 tracer at low-z, is challenging in our case due to the cosmic dimming effect and typically low metallicities of galaxies, exacerbated by the higher temperature of the cosmic microwave background for lower–J transitions ($T_\mathrm{CMB}(z) = 2.73(1 + z)\,\mathrm{K}$). Furthermore, the lack of multi-band observations for all galaxies, which would be necessary to constrain the full far-infrared (FIR) SED shape (e.g. M. Béthermin et al., 2015; M. Kaasinen et al., 2019),

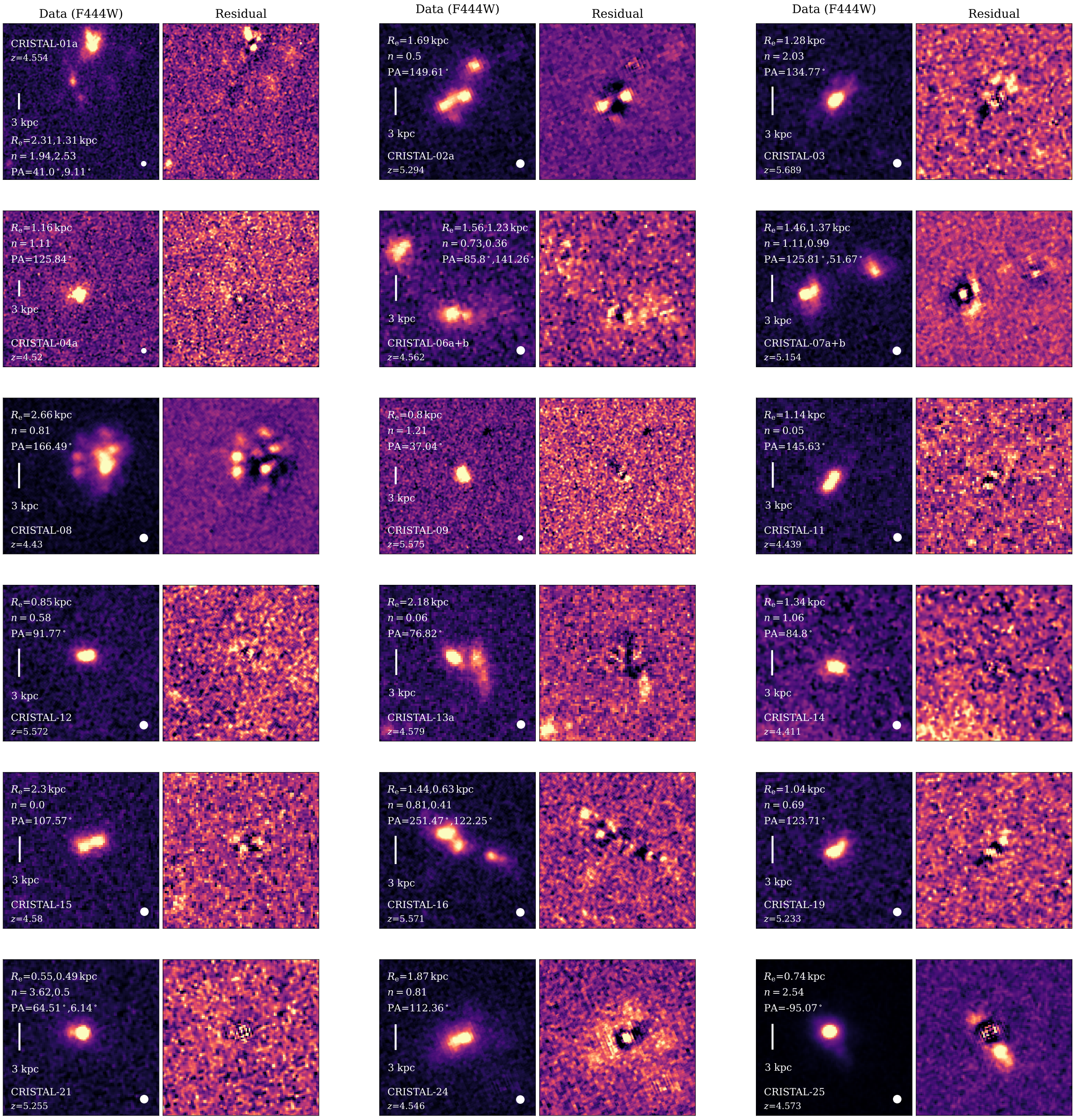

Figure 3.26 Examples of Sérsic fits and residuals of CRISTAL galaxies observed in JWST/F444W (rest-frame 0.7 μm at $z \sim 5$). North is up for all images. For galaxies with multiple components, we simultaneously fit all components, each characterised by a single Sérsic profile. The resulting half-light radii ($R_{\rm e}$), Sérsic indices (n), and position angles (PA, measured counter-clockwise from the north) are listed in Table 3.4 and annotated in the figures in order of increasing $R_{\rm e}$. Except in a few cases, such as CRISTAL-09, 12, and 14, the residuals exhibit clumpy structures and asymmetries in the light distributions due to multiple discrete clumps.

Table 3.4. Rest-frame optical to near-IR (F444W) structural parameters fitted by `imfit`

ID	R_{e}[a] (kpc)	n[b]	e[c]	PA[d] (°)	i[e] (°)
01a	1.3	2.5	0.00	…[†]	…[†]
	2.3	1.9	0.51	9	64
02	1.7	0.5	0.30	150	48
03	1.3	2.0	0.57	135	69
04a	1.2	1.1	0.04	…[†]	…[†]
04b	2.8	1.5	0.00	…[†]	…[†]
06a	1.6	0.7	0.61	86	72
06b	1.2	0.4	0.25	141	43
07a	1.5	1.1	0.26	126	44
07b	1.4	1.0	0.27	52	45
07c	1.6	0.4	0.24	33	42
08	2.7	0.8	0.29	166	46
09	0.8	1.2	0.39	37	55
11	1.1	0.1	0.71	146	82
12	0.9	0.6	0.43	92	58
13a	2.2	0.1	0.64	77	75
14	1.3	1.1	0.36	85	52
15	2.3	0.0	0.62	108	73
16a	1.4	0.8	0.32	251	49
	0.6	0.4	0.22	122	40
16b	1.5	1.3	0.55	70	67
19	1.0	0.7	0.54	124	66
21	0.6	3.6	0.18	65	36
	0.5	0.5	0.10	6	26
24	1.9	0.8	0.46	112	60
25	0.7	2.5	0.20	85	39

[a] Intrinsic half-light radius.

[b] Sérsic index.

[c] Intrinsic ellipticity ($e = 1 - b/a$).

[d] Position angle (counter-clockwise from north).

[e] Inclination inferred from Equation 3.2.

[†] The ellipticity is too low.

Note. — Targets with two entries are fitted with a double-Sérsic profile. CRISTAL-10, 20, 23 systems do not have NIRCam data available.

means that the only feasible estimator for most galaxies in CRISTAL[5] is to infer gas masses from the single-band dust continuum emission measured in the Rayleigh-Jeans (R-J) tail of the FIR SED following the method of N. Scoville et al. (2016, 2017).

With the rest frequencies probed by the Band-7 (343.5 GHz) continuum data and if we adopt $\lambda_0 = 100\,\mu$m similar to A. L. Faisst et al. (2020a), which is the wavelength where optical depth reaches unity, and single dust temperature of $T_{\rm dust} = 50\,$K (see discussion below), then we can assume the R-J regime criterion is still satisfied and the optically-thin approximation is valid. We measure the dust continuum fluxes on the image directly using the curve-of-growth method. They are in general good agreement with I. Mitsuhashi et al. (2024).

We infer the gas mass $M_{\rm gas}$ from the observed flux density $S_{\nu_{\rm obs}}$ of the Band-7 dust continuum ($\lambda_{\rm obs} \approx 850$–$1050\mu$m) in the R-J regime following Eq. (3) in L. J. Tacconi et al. (2020):

$$\begin{aligned}\left(\frac{M_{\rm gas}}{1\times10^{10}M_\odot}\right) = &\left(\frac{S_{\nu_{\rm obs}}D_{\rm L}^2}{\rm mJy\,Gpc^2}\right)\times(1+z)^{-(3+\beta)}\times\left(\frac{\delta_{\rm gd}}{150}\right)\\ &\times\left(\frac{\nu_{\rm obs}}{352\,\rm GHz}\right)^{-(2+\beta)}\times\left(\frac{6.7\times10^{19}}{\alpha_{\rm dust,0}}\right)\\ &\times\frac{\Gamma_0}{\Gamma_{\rm R-J,\nu_{\rm obs}}}.\end{aligned} \tag{3.8}$$

We introduced the R-J departure coefficient $\Gamma_{\rm R-J}$ back to Eq. (3.8) to account for the deviation of dust temperature from 25 K, which was originally used in L. J. Tacconi et al. (2020). $\Gamma_{\rm R-J}$ is defined as (Eq. (6) in N. Scoville et al. 2016)

$$\Gamma_{\rm R-J}(T_{\rm d},\nu_{\rm obs},z) = \frac{h\nu_{\rm obs}(1+z)/kT_{\rm d}}{e^{h\nu_{\rm obs}(1+z)/kT_{\rm d}}-1}. \tag{3.9}$$

The Γ_0 factor in Eq. (3.8) is taken at $z = 0, T_{\rm d} = 50\,$K (see below) and at the respective $\nu_{\rm obs}$ for different observations. On average, the coefficient $\langle\frac{\Gamma_0}{\Gamma_{\rm R-J,\nu_{\rm obs}}}\rangle \sim 2.4$.

We adopt a dust temperature[6] $T_{\rm d} = 50$K, based on V. Villanueva et al. (2024) FIR SED modelling of CRISTAL-22, which benefits from the continuum data observed at multiple bands (but see also M. Béthermin et al. 2020; A. L. Faisst et al. 2020a and L. Sommovigo

---

[5] Data from Very Large Array (VLA) observations of CO(2-1) are available for CRISTAL-22 (HZ10) and CRISTAL-02 (LBG-1).

[6] This temperature is luminosity-weighted, as the mass-weighted temperature is not available, see N. Scoville et al. (2016) and N. Scoville et al. (2017) for the discussion of the resulting difference in the dust mass between the two temperatures.

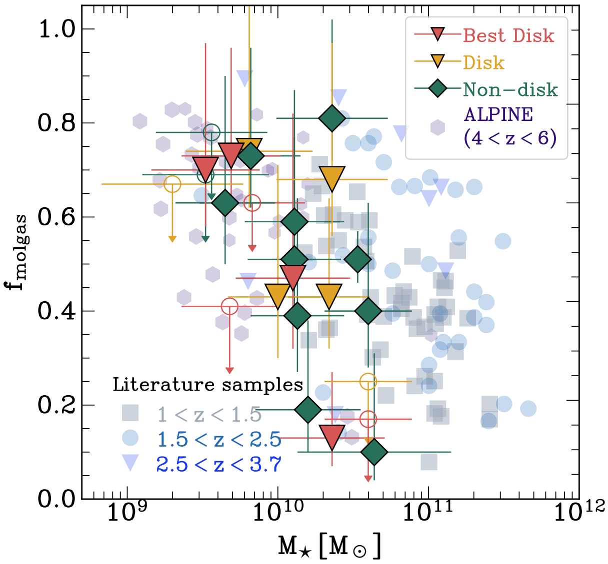

Figure 3.27 Molecular gas fraction, $f_{\rm molgas}$, (Equation 3.10) as a function of stellar mass as inferred from the Band-7 dust continuum based on Equation 3.8. The points are colour-coded by their classifications described in Section 3.3. The empty circles represent upper limits. The median gas fraction of the CRISTAL sample is ~ 0.5. Our measurements are in broad agreement with those reported by M. Dessauges-Zavadsky et al. (2020) for the ALPINE samples (purple hexagons), in which we both observe a similar slope of dependence of $f_{\rm molgas}$ on $M_\star$, similar to that of the lower redshifts $1 \lesssim z \lesssim 6$ star-forming galaxies compiled by M. Dessauges-Zavadsky et al. (2020) and references therein (light grey to blue markers).

et al. 2022). We assume a dust emissivity index[7] of $\beta = 1.8$, the suggested value by N. Scoville et al. (2016) based on the findings of the Planck Collaboration et al. (2011). Such a choice is close to the value of $\beta = 2$ measured by V. Villanueva et al. (2024). We adopt the R-J luminosity-to-mass ratio $\alpha_{\rm dust,0} = 6.7 \times 10^{19}\,{\rm erg\,(s\,Hz\,M_\odot)^{-1}}$. Assuming $\alpha_{\rm dust,0} = 8 \times 10^{19}\,{\rm erg\,(s\,Hz\,M_\odot)^{-1}}$ following L. J. Tacconi et al. (2020) [8] would result in lower $M_{\rm gas}$ by $\lesssim 0.1$ dex in median.

The gas-to-dust ratio, $\delta_{\rm gd} := \frac{M_{\rm gas}}{M_{\rm dust}}$, anti-correlates with metallicity (Eq. (10) in R. Genzel et al. (2015), see also A. K. Leroy et al. (2011) and L. J. Tacconi et al. (2018)). We estimate metallicity using the mass-metallicity relation (MZR) inferred from NIRSpec/JWST data of galaxies at $z = 4$–10 by K. Nakajima et al. (2023), which applies to galaxies with masses in the range $10^{7.5} < M_\star < 10^{9.5}$. We extrapolate the MZR to cover the more massive galaxies in our sample. Our sample's average metallicity $\langle 12 + \log({\rm O/H})\rangle = 8.27 \pm 0.05$, and the corresponding gas-to-dust ratio coefficient is $\langle \delta_{\rm gd}/150 \rangle = 2.20^{+0.22}_{-0.24}$. The uncertainties

---

[7] β is frequency-dependent but is not constrained by our data.

[8] L. J. Tacconi et al. (2020) assumes lower $\alpha_{\rm CO}$ and $X_{\rm CO}$ than N. Scoville et al. (2016)'s.

represent the scatter in the K. Nakajima et al. (2023)'s relation, which would translate to no more than 0.05 dex difference to the final $M_{\rm gas}$.

We note that individual gas-phase metallicities (except for CRISTAL-08, 21, and 23) can be determined from rest-frame optical strong line ratios using NIRSpec/JWST data ($R = 1000$), and the values are consistent with our adopted metallicities. A more detailed discussion of these results will be presented in A. Faisst (in prep.) and S. Fujimoto et al. (in prep.). E. Parlanti et al. (2025) presented the metallicity measurement of CRISTAL-20 (HZ4) which is $12 + \log({\rm O/H}) \sim 8.3$.

Based on the $M_{\rm gas}$ derived above, Fig. 3.27 and Table 3.5.1 show the gas fraction of the CRISTAL sample. We define the gas fraction as

$$f_{\rm molgas} := \frac{M_{\rm gas}}{M_{\rm gas} + M_{\rm stars}}. \tag{3.10}$$

The median gas fraction $f_{\rm molgas} = 0.51$. This is also consistent with the expected value from L. J. Tacconi et al. 2020's relation at $z = 5$ for $M_* = 10^{10} M_\odot$, which is ~ 0.53. For CRISTAL-22, our measured $f_{\rm molgas} = 0.71^{+0.28}_{-0.12}$ is consistent with that inferred by R. Pavesi et al. (2019) from VLA CO(2-1) data. For CRISTAL-01a, 08, 12, 14, 15, 16, 23b, 23c, the measured $f_{\rm molgas}$ are upper-limits because the dust continuum fluxes are below the S/N threshold defined in I. Mitsuhashi et al. (2024). There is insufficient co-spatial dust emission for CRISTAL-04b and 07b, so we have no $f_{\rm molgas}$ measurement for those. The stellar mass $M_\star$ are based on SED fitting results presented in J. Li et al. (2024a) for those sources with NIRCam/JWST images; if not, then we adopt the values from I. Mitsuhashi et al. (2024).

Our $f_{\rm molgas}$ measurements, regardless of their kinematics types, are in good agreement with M. Dessauges-Zavadsky et al. (2020) (purple hexagons in Fig. 3.27), which measured $f_{\rm molgas}$ for the ALPINE sample based on (i) [C II] emission following A. Zanella et al. (2018) (ii) rest-frame 850 μm extrapolated from the FIR SED template of M. Béthermin et al. (2017) and (iii) dynamical mass assuming virialised spherical systems. We also recover a steep relation between $f_{\rm molgas}$ and the stellar mass of the systems, similar to the lower-redshift studies following the same selection in M. Dessauges-Zavadsky et al. (2020) and references therein.

Inferring $M_{\rm gas}$ with the method described above is subject to several important caveats. Firstly, the assumption that the Band-7 continuum lies on the R-J tail is sensitive to the adopted single dust temperature, $T_{\rm d} = 50$ K. If $T_{\rm d}$ is lower, the R-J assumption breaks down, particularly for the highest-redshift sources in our sample. Using $T_{\rm d} = 25$ K would increase $M_{\rm gas}$ by ~ 0.5 dex. Furthermore, we lack information on the mass-weighted $T_{\rm d}$. The absence of longer wavelength data implies that we are neglecting a dominant colder component of the dust. Additionally, the adopted values for $\alpha_{\rm dust,0}$ and $\delta_{\rm gd}$ are based on lower-redshift measurements and calibrations, although $M_{\rm gas}$ appears to be relatively insensitive to these values within the possible range.

An alternative method for estimating $M_{\rm gas}$ is by using the [C II] luminosity. If we apply the relation from A. Zanella et al. (2018) (their Eq. (2)), we find that the resulting $M_{\rm gas}$ is systematically higher by 0.23 dex (in terms of the median), but still within the 0.3 dex scatter of the relation. We also observe a significant correlation between the dust- and [C II]-inferred $M_{\rm gas}$ values (with Kendall's $\tau = 0.56^{+0.12}_{-0.14}$, $p \ll 0.05$).

Overall, varying our assumptions and using different methods will very likely lead to higher $M_{\rm gas}$ and $f_{\rm molgas}$ values, which, as a corollary, a lower Toomre Q values, as inferred from Eq. (3.3) in Sect. 3.6.3. This would not change the main findings, namely, that CRISTAL disks are gravitationally (un)stable and the correlations discussed in Sect. 3.6.2. However, the statistical significance of the correlations would be weaker given the more uncertain $M_{\rm gas}$ and $f_{\rm molgas}$.

3.13 Appendix D – Literature sample of $V_{\rm rot}$ and σ

Table 3.5 lists the literature samples discussed in Sect. 3.6.1 and shown in Fig. 3.9.

Table 3.5. Compilation of literature references for rotational velocity and velocity dispersion from local to $z \lesssim 8$ galaxies.

Gas phase (Tracer(s))	Reference
$z \leqslant 0.5$	
Cold/Atomic (H I, CO)	K. M. Mogotsi et al. 2016 (THINGS)*
	M. Girard et al. 2021 (DYNAMO)**
Ionised (Hα, [O II])	B. Epinat et al. 2008 (GHASP)
	M. Girard et al. 2021 (DYNAMO)**
$0.5 < z < 4$	
Cold/Atomic (CO, [C I])	A. M. Swinbank et al. 2011†
	F. Lelli et al. 2018
	M. Kaasinen et al. 2020
	S. Huang et al. 2023
	A. Nestor Shachar et al. 2023 (RC100)
	F. Rizzo et al. 2023 (ALPAKA)
	Z. Liu et al. 2024
	Z. Liu et al. 2025
Warm ([C II])	H. Umehata et al. 2025
Ionised (Hα, [O III], [O II], C III])	D. P. Stark et al. 2008†
	B. Epinat et al. 2009 (MASSIV)
	T. A. Jones et al. 2010†
	A. Gnerucci et al. 2011 (AMAZE-LSD)
	R. C. Livermore et al. 2015†
	E. M. Di Teodoro et al. 2016
	N. Leethochawalit et al. 2016†
	C. A. Mason et al. 2017 (KLASS)†
	O. J. Turner et al. 2017 (KDS)
	M. Girard et al. 2018 (KLENS)†
	V. Patrício et al. 2018†
	J. Hirtenstein et al. 2019†
	S. H. Price et al. 2020 (MOSDEF)
	L. Hogan et al. 2021
	A. Nestor Shachar et al. 2023 (RC100)
	A. Puglisi et al. 2023 (KURVS)
	J. E. Birkin et al. 2024 (KAOSS)
	I. Barišić et al. 2025 (MSA-3D)
	S. Rhoades et al. 2025*,†
	W. Wang et al. 2025

Table 3.5 (cont'd)

Gas phase (Tracer(s))	Reference
	$z \geqslant 4$
Cold (CO)	K.-i. Tadaki et al. 2018
Warm ([C II])	F. Rizzo et al. 2020[†,††]
	S. Fujimoto et al. 2021[†]
	G. C. Jones et al. 2021
	M. Neeleman et al. 2021
	F. Rizzo et al. 2021[†]
	T. Tsukui & S. Iguchi 2021
	M. Neeleman et al. 2023
	E. Parlanti et al. 2023
	A. C. Posses et al. 2023
	F. Roman-Oliveira et al. 2023a
	L. E. Rowland et al. 2024
	A. Venkateshwaran et al. 2024
	A. Amvrosiadis et al. 2025[†]
	Q. Fei et al. 2025
Ionised (Hα, [O III])	E. Parlanti et al. 2023
	A. de Graaff et al. 2024 (JADES)
	A. L. Danhaive et al. 2025 ('gold' only)

Note. — Sources listed in Table 3.6 are not duplicated here.

[*] Velocity dispersion only.

[**] Local analogues.

[†] Lensed.

[††] The object is potentially a system undergoing a minor merger with mass ratios of $\sim 1:6$ separated by ~ 4 kpc (J. Cathey et al., 2024). Still, the low dispersion of the system $\sim 32\,{\rm km\,s^{-1}}$ suggests the interaction has not significantly perturbed the dynamics. With an updated stellar mass of $\log(M_\star/{\rm M}_\odot) \approx 10.39$ and a $\log[{\rm SFR}/({\rm M}_\odot\,{\rm yr}^{-1})] \approx 2.13$, the galaxy would be shifted closer to the main sequence, with a revised $\Delta{\rm MS} = 0.23$ at $z = 4.2$.

Table 3.6. Literature sample with multi-phase gas kinematics measurement.

Object	z	Tracer	Reference
A521*,†	1.0	CO(4-3)	M. Girard et al. 2019
		[O II]	M. Girard et al. 2019
ALESS073.1	4.8	[C II]	F. Lelli et al. 2021
		Hα	E. Parlanti et al. 2024b
BX610	2.2	CO(4-3)	R. Genzel et al. 2023
		Hα	A. Nestor Shachar et al. 2023
Cosmic Snake*,†	1.0	CO(4-3)	M. Girard et al. 2019
		[O II]	M. Girard et al. 2019
EGS4-24985	1.4	CO(4-3)	H. Übler et al. 2018
		Hα	H. Übler et al. 2018
GN20	4.1	CO(2-1)	J. A. Hodge et al. 2012
		Hα	H. Übler et al. 2024b
J0235	6.1	[C II]	E. Parlanti et al. 2023
		[O III]	E. Parlanti et al. 2023
J0901†	2.3	CO(4-3)	D. Liu et al. 2023
		Hα	D. Liu et al. 2023
J1211	6.0	[C II]	E. Parlanti et al. 2023
		[O III]	E. Parlanti et al. 2023
J2310	6.0	CO(9-8)	Y. Shao et al. 2022
		[C II]	Y. Shao et al. 2022
MACS0717_Az9†	4.3	CO(4-3)	A. Mizener et al. 2024
		[C II]	A. Pope et al. 2023
PJ0116-24†	1.4	CO(3-2)	D. Liu et al. 2024
		Hα	D. Liu et al. 2024

Note. — See also R. Genzel et al. (2013) and S. Fujimoto et al. (2025) for qualitative comparisons between kinematics in different gas phases.

*Velocity dispersion only.

$\dagger$Lensed.

3.14 Appendix E – Model velocity profiles

Fig. 3.28 shows the intrinsic σ_0, circular velocity profiles of the DM and the baryonic components. The DM fraction profile inferred from the circular velocities $f_{\rm DM}(<R) = V^2_{\rm circ,DM}(R)/V^2_{\rm circ,tot}(R)$ is shown as the secondary y-axis.

3.15 Appendix F – Comparison to K18 model with total SFR

In Sect. 3.6.4, we compare the σ_0–$\Sigma_{\rm SFR}$ with the M. R. Krumholz et al. (2018) analytic models. Here, we also compare the CRISTAL values with the models in σ_0–SFR space. Integrating Eq. (3.4) with radius, the total SFR is related to σ_g by (Eq. (60) in M. R. Krumholz et al. (2018)):

$$\begin{aligned}\mathrm{SFR} =& \sqrt{\frac{2}{1+\beta}}\frac{\phi_a f_{\rm SF}}{\pi G Q} f_{\rm g,Q} v^2_{\phi,\rm out}\sigma_g \\ &\cdot \max\left[\sqrt{\frac{2(1+\beta)}{2 f_{g,P}\phi_{\rm mp}}}\frac{8\epsilon_{\rm ff} f_{g,Q}}{Q}, \frac{t_{\rm orb,out}}{t_{\rm sf,max}}\right],\end{aligned} \tag{3.11}$$

while for 'feedback-only' (fixed Q) model (Eq. (62) in M. R. Krumholz et al. 2018):

$$\mathrm{SFR} = \frac{4\eta\sqrt{\phi_{\rm mp}\phi^3_{\rm nt}}\phi_Q\phi_a}{GQ^2\langle p_*/m*\rangle}\frac{f^2_{g,Q}}{f_{g,P}} v^2_{\phi,\rm out}\sigma^2_g. \tag{3.12}$$

The definitions of the symbols and values adopted are described in Sect. 3.6.2 and Table 3.7. Here the rotation velocity v_ϕ that is related to the radial gradient of the potential ψ, is set to be $v_\phi = \sqrt{r\frac{\partial\psi}{\partial r}} \in [100, 350]\,\mathrm{km\,s^{-1}}$, in increments of $50\,\mathrm{km\,s^{-1}}$.

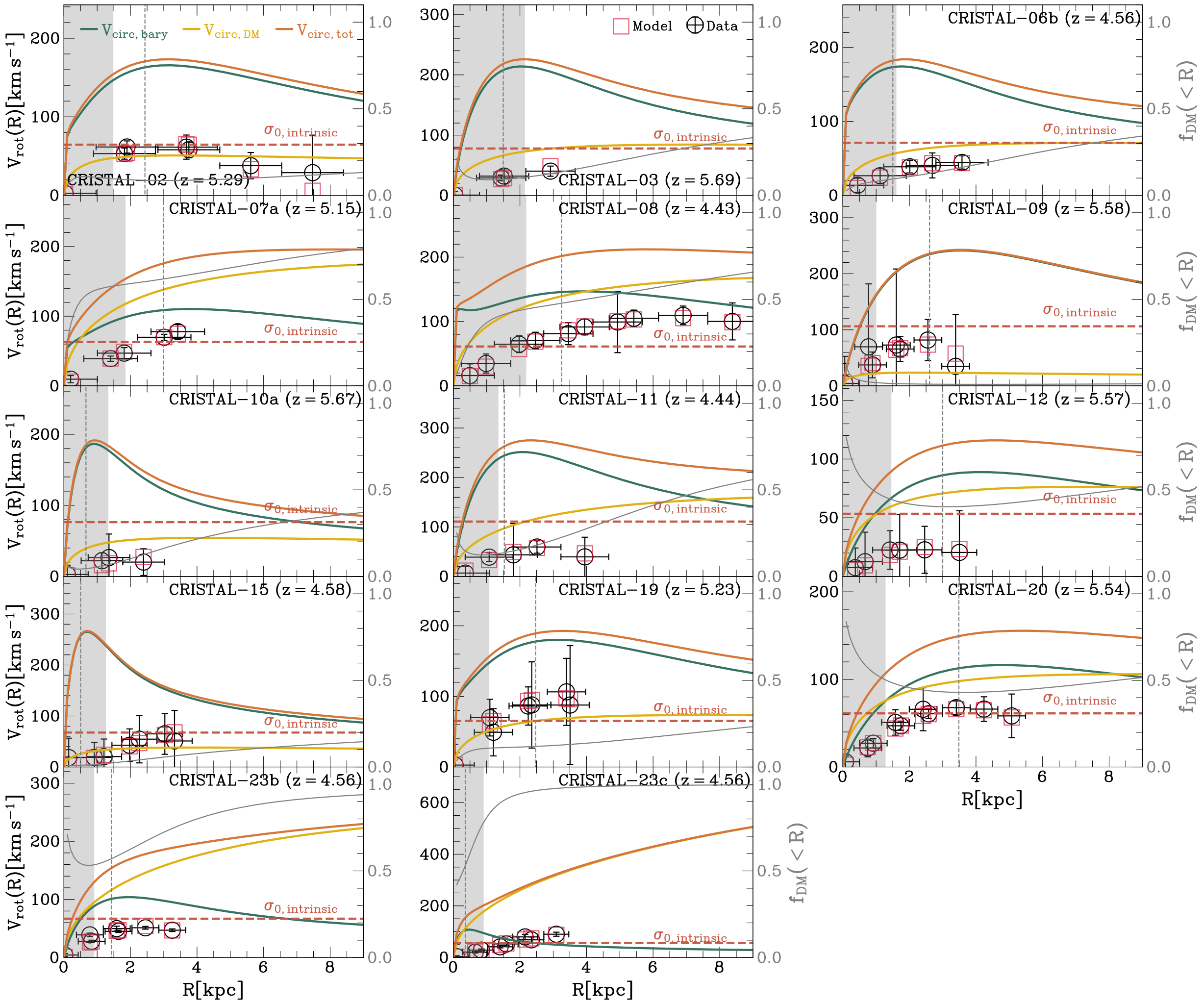

Figure 3.28 Intrinsic baryonic $V_{\rm circ,bary}$, DM, $V_{\rm circ,DM}$, and total circular velocity $V_{\rm circ,tot}$ profiles of the CRISTAL disk sample with asymmetric drift correction. The grey circles mark the folded 1D observed velocity profiles, and the red squares show the observed profiles extracted from the `DysmalPy`-modelled cubes. The red dashed line indicates the intrinsic constant velocity dispersion $\sigma_{0,\rm intrinsic}$. The DM fraction $f_{\rm DM}(<R) = V^2_{\rm circ,DM}(R)/V^2_{\rm circ,tot}(R)$ is shown in solid grey curves. The grey dashed vertical line marks the disk's effective radius.

Table 3.7. Fiducial values adopted for Equations 3.4, 3.5 and 3.6.

Symbol	Value	Unit
η	1.5	...
$t_{\rm max}$	2.0	Gyr
$Q_{\rm min}$	1.0	...
$\epsilon_{\rm ff}$	0.015	...
$\phi_{\rm mp}$	1.4	...
$\langle \frac{p_*}{m_*} \rangle$	$3000^{\dagger}$	$\rm km\,s^{-1}$
ϕ_Q	2.0	...

Note. — The definitions of each symbol can be found in Table 1 in M. R. Krumholz et al. (2018).

†The momentum injection rate used is based on simulations (e.g. C. C. Hayward & P. F. Hopkins, 2017; M. R. Krumholz et al., 2018, and references therein) and assumes that supernova remnants undergo an energy-conserving (Sedov-Taylor) phase (L. I. Sedov, 1946, 1959; G. Taylor, 1950), where energy is converted into momentum. However, this value can vary by up to a factor of 4, which could sustain a higher velocity dispersion of the critical value $\sim 20\,\rm km\,s^{-1}$. To match the properties of CRISTAL disks using star-formation feedback alone, a factor of 10 larger than this adopted value would be required.

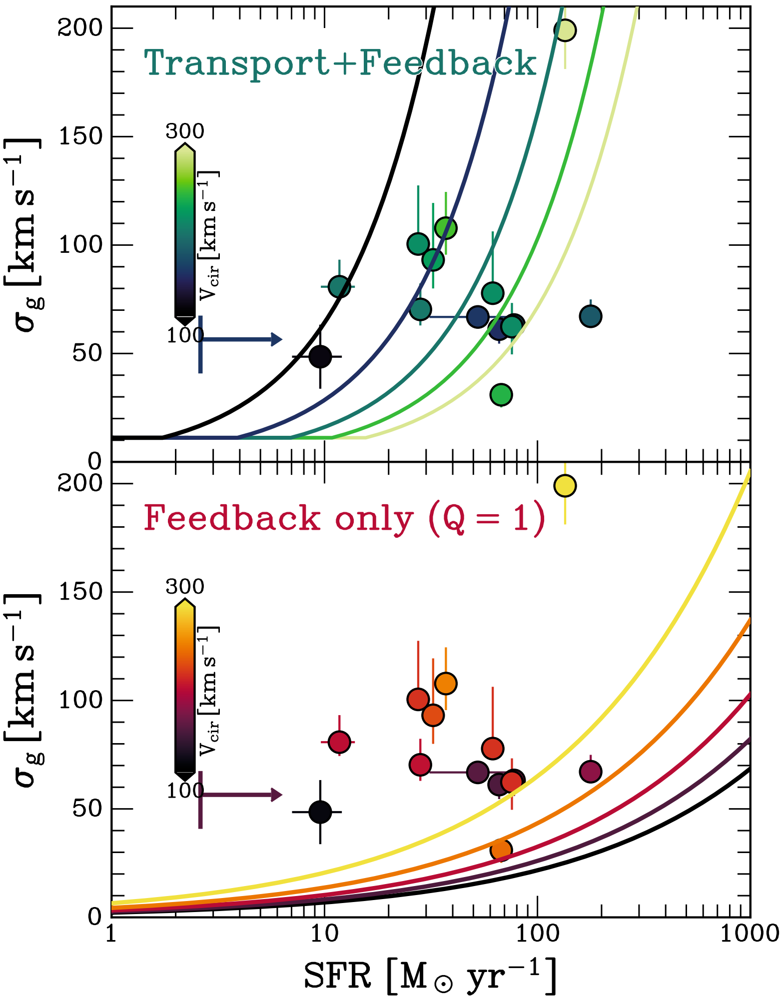

Figure 3.29 Same as Figure 3.11 but for σ_0 vs total star formation rate (SFR). The solid lines are analytical models from M. R. Krumholz et al. (2018) based on Equations 3.11 and 3.12.

Chapter 4

The ALPINE-CRISTAL-JWST Survey: Gas-phase abundance gradients of main sequence star-forming galaxies and their kinematics at $4 < z < 6$

> This Chapter is based on the submitted manuscript The ALPINE-CRISTAL-JWST Survey: Gas-phase abundance gradients of main sequence star-forming galaxies and their kinematics at $4 < z < 6$ by Lee et al. (2025c). Submitted to A&A.

ABSTRACT – We present gas-phase radial metallicity profiles for 20 main-sequence galaxies at $4 < z < 6$, primarily based on JWST NIRSpec IFU observations obtained as part of the ALPINE-CRISTAL-JWST programme. Our study aims to connect the metallicity gradients of these galaxies with their kinematic properties from [C II] 158μm ALMA observations. We map the radial profiles of oxygen abundance using the strong-line method leveraging the rich set of rest-frame optical emission lines. Linear fits to the annular-binned radial profiles show that, on average, the metallicity gradients are slightly positive with a median of $+0.039 \pm 0.010\,\mathrm{dex\,kpc}^{-1}$. There are no substantial systematic offsets in gradients when using different line diagnostics. However, only three galaxies show a gradient $> 0.05\,\mathrm{dex\,kpc}^{-1}$ at 1σ, and none have a significant negative gradient. We investigate the correlation between the metallicity gradients and the intrinsic gas velocity dispersion σ_0, as well as the ratio $V_{\mathrm{rot}}/\sigma_0$ of the disks. Combining our sample with mass-matched literature samples at $3 \lesssim z \lesssim 7$, we find a negative shallow correlation between $V_{\mathrm{rot}}/\sigma_0$ and the metallicity gradients, but no strong relationships with σ_0. As $V_{\mathrm{rot}}/\sigma_0$ increases towards later cosmic times, the observed negative trend with $V_{\mathrm{rot}}/\sigma_0$ is consistent with the overall cosmic evolution of metallicity gradients from high to low redshifts. This suggests that disk maturity plays a crucial role in shaping the radial metallicity gradients. We do not find the metallicity gradients of disk galaxies significantly different from non-disk galaxies, which could be attributed to the frequent accretion events that took place in these gas-rich

systems. Additionally, we find no strong dependence of metallicity gradients on stellar mass and only a marginal positive dependence on specific star-formation rate. Our study extends the efforts to connect the internal kinematics of galaxies with their gas-phase chemical enrichment at kpc scales from cosmic noon to $z > 4$.

4.1 Introduction

The distribution of heavy elements (metals) at high redshifts ($z \gtrsim 1$) places important constraints on the effects of gas flows in the early phase of disk growth. The radial gradient of oxygen abundance (metallicity gradient henceforth), or of other α elements, in the gas phase is commonly used as a sensitive probe of baryonic assembly, and the complex gas flows driven by both galactic feedback and tidal interactions that can transport the stellar nucleosynthesis yields from where they are produced. In the local Universe, observations from various large surveys indicate a typical negative gas-phase metallicity gradient of oxygen ranging from ~ -0.05 to $0\,\mathrm{dex\,kpc}^{-1}$ (e.g. D. Zaritsky et al., 1994; S. F. Sánchez et al., 2014; I. T. Ho et al., 2015; K. Grasha et al., 2022), indicating a chemically richer central region compared to the outskirts. Similarly for the Milky Way, typical radial metallicity gradients inferred from different tracers range from -0.06 to $-0.01\,\mathrm{dex\,kpc}^{-1}$ (R. Maiolino & F. Mannucci, 2019, and references therein). The observed negative metallicity gradient in the local Universe could arise from an inside-out growth scenario, where the inner disk forms stars first from the high density of gas and has more time to enrich the interstellar medium (ISM) than the outer regions (e.g. F. Matteucci & P. Francois, 1989).

Metallicity measurements of galaxies at cosmic noon ($z \sim 1-3$), obtained with sensitive Integral Field Units (IFUs) mounted on 8–10 m class ground-based telescopes, have revealed a wide range of metallicity gradients, with both negative, positive, and flat gradients observed (G. Cresci et al., 2010; T. T. Yuan et al., 2011; J. Queyrel et al., 2012; A. M. Swinbank et al., 2012b; T. Jones et al., 2013; J. P. Stott et al., 2014; P. Troncoso et al., 2014; N. Leethochawalit et al., 2016; E. Wuyts et al., 2016; X. Wang et al., 2017, 2022; D. Carton et al., 2018; N. M. Förster Schreiber et al., 2018; M. Curti et al., 2020b). Some studies suggest that more massive galaxies tend to have steeper metallicity gradients, while galaxies with higher specific star formation rates (sSFRs) tend to have flatter gradients (e.g. S. Gillman et al., 2021; Y. Cheng et al., 2024). The majority of $z \lesssim 3$ results are consistent with flat within errors or only moderately negative.

In the case of the Milky Way (MW), its metallicity gradient (of oxygen) has evolved from $\sim -0.01\,\mathrm{dex\,kpc}^{-1}$ at $z = 1$ to the current steepness of $\sim -0.04\,\mathrm{dex\,kpc}^{-1}$ based on e.g. planetary nebulae that probe longer look-back times and chemical evolution models (C. Chiappini et al., 2001; L. Stanghellini et al., 2014; M. Mollá et al., 2019). Therefore, based on observations, one expects metallicity gradients to become increasingly negative with cosmic time, eventually matching the steeper gradients seen in nearby disks. This evolutionary trend is reproduced in only a subset of simulations (e.g. MaGICC, B. K. Gibson et al., 2013). Most simulations, however, predict the opposite behaviour, namely that gradients start steeper at high redshift and subsequently flatten (P. Taylor & C. Kobayashi, 2017; A. Acharyya et al., 2025; A. M. Garcia et al., 2025), while others find very little evolution between $z \lesssim 3$ and the present epoch (X. Ma et al., 2017; Z. S. Hemler et al., 2021; P. B. Tissera et al., 2022; X. Sun et al., 2025). The difference in behaviour is largely because of the influence of feedback, where models or simulations with strong feedback lead to flatter gradients at higher redshifts when feedback and outflows were more important.

The advent of the *James Webb* Space Telescope (JWST) has enabled access to multiple rest-frame strong optical lines at $z > 4$. Recent JWST-based metallicity measurements suggest flat to positive gradients for a large fraction of galaxies at $z > 6$, albeit based on a heterogeneous sample (S. Arribas et al., 2024; G. Venturi et al., 2024; I. Barišić et al., 2025; Z. Li et al., 2025a; M. Ju et al., 2025, see also J. E. Birkin et al. 2023). However, there have been no systematic studies of metallicity gradients at $4 < z < 6$ to date.

Several internal secular processes can contribute to the flattening or even inversion of the gas-phase metallicity gradients in disk galaxies, or even prevent the formation of gradients altogether. Radial flows of gas and migration of young massive stars, for instance, can dilute the central regions and flatten the metallicity gradients (E. Spitoni & F. Matteucci, 2011; A. Mott et al., 2013; E. Spitoni et al., 2015). Additionally, strong feedback in the form of galactic outflows can redistribute metals produced by the central starburst region towards the external regions of galactic disks, potentially inverting the gradient to become positive if the outflows have a strong metal-loading (P. B. Tissera et al., 2022). The presence of a bar may also play a role in flattening the abundance gradient, likely due to the non-circular motions induced in the gas (e.g. D. Alloin et al., 1981; D. Zaritsky et al., 1994) with its impact correlating with bar strength (P. Martin & J.-R. Roy, 1994, but see L. Sánchez-Menguiano et al. 2018 and M. E. Wisz et al. 2025 for a contrasting view).

Positive gradients could also result from external stochastic processes such as galaxy interactions (D. S. N. Rupke et al., 2010a; P. Taylor & C. Kobayashi, 2017) or the dilution of metallicity in the central regions by cold flows of pristine gas from the intergalactic medium (A. Dekel et al., 2009b). The complex interplay between these various mechanisms could contribute to the observed diversity of metallicity gradients in galaxies (P. Sharda et al., 2021a).

Nevertheless, simulation work on metallicity gradients have largely been focussed at $z \lesssim 3$, with only a handful of studies covering earlier cosmic epochs (e.g. A. M. Garcia et al., 2025; D. Ibrahim & C. Kobayashi, 2025). Most simulations predict strong negative metallicity gradients at early cosmic times, likely due to their similar treatments of relatively smooth stellar feedback allowing for sustained inside-out growth and weak subgrid metal diffusion (Z. S. Hemler et al., 2021; P. B. Tissera et al., 2022; X. Sun et al., 2025, see discussion in A. M. Garcia et al. 2025).

From a dynamical perspective, kinematics and metals distribution are tightly connected. At low-redshift and up to $z \sim 1-3$, an emerging trend suggests that more turbulent galaxies, characterised by their low rotational support relative to velocity dispersion, tend to have flatter metallicity gradients (e.g. J. Queyrel et al., 2012; T. Jones et al., 2013; N. Leethochawalit et al., 2016; C. Lyu et al., 2025), a tendency also seen in simulations (X. Ma et al., 2017; Z. S. Hemler et al., 2021) and reproduced well with analytical models with efficient metal mixing (e.g. P. Sharda et al., 2021b). In general, the flat gradient can be attributed to the unstable internal dynamics of turbulent disks, making them more susceptible to disturbances caused by strong feedback-driven gas flows, in addition to mixing from advection and accretion. As a result, large-scale metal redistribution over several kiloparsecs (kpcs) within the galaxy can occur, leading to the flat to positive gradients observed.

At cosmic noon and up to $z \sim 4$, there is also growing evidence suggesting the prevalence of non-circular motion and radial gas flows in gas-rich disk galaxies, characterised by velocities of the order of few tens of $\mathrm{km\,s^{-1}}$, which could efficiently transport gas inwards (e.g. S. H. Price et al., 2021; R. Genzel et al., 2023; H. Übler et al., 2024b; T. Tsukui et al., 2024; S. Huang et al., 2025; S. Pastras et al., 2025). If these secular mixing processes occur on a timescale comparable to that of metal production by stars, the ISM could remain well mixed from the outset, and stayed such way until the disk settles into a dynamically cold and thin disk, at which point the classical inside-out formation scenario may dominate, leading to a negative metallicity gradient.

While measurements of metallicity gradients in galactic disks at $z > 4$ remain scarce due to rest-frame optical lines being shifted out of the atmospheric window, kinematics studies are benefitted from sub-mm interferometers such as ALMA and NOEMA, with the bright [C II] line emission as a commonly used tracer. The [C II] line is a primary radiative line coolant of the cold ISM, associated with photo-dissociation region (PDR) and H II regions (e.g. M. G. Wolfire et al., 2003; L. Vallini et al., 2015; P. C. Clark et al., 2019). The high spectral and spatial resolution of these facilities have allowed for high-resolution resolved kinematics at scales of $\sim 1\,\mathrm{kpc}$ (e.g. T. Tsukui & S. Iguchi, 2021; F. Rizzo et al., 2021; F. Roman-Oliveira et al., 2023a; L. E. Rowland et al., 2024; L. L. Lee et al., 2025b).

We here exploit the synergy between ALMA and JWST to investigate the connection between the kinematic nature and metallicity gradients of star-forming galaxies (SFG(s)) at $4 < z < 6$, a previously under-explored area. Our analysis combines ALMA-CRISTAL survey data (R. Herrera-Camus et al., 2025), which provides high-resolution kinematic information via the [C II] line emission, with JWST NIRSpec IFU data from primarily the ALPINE-CRISTAL-JWST survey (A. L. Faisst et al., 2025), which enables the measurement of chemical abundance gradients using strong rest-optical nebular lines that are commonly used at lower redshift.

Our sample consists of a homogeneously selected set of main-sequence MS SFG(s) representative of the galaxy population at $4 < z < 6$. Building on the kinematic analysis presented in L. L. Lee et al. (2025b), we aim to explore the relationship between internal dynamics and chemical abundance distribution in these galaxies, and investigate potential differences between disk and non-disk galaxies classified in L. L. Lee et al. (2025b). The differences between the kinematic classifications using the ALPINE and CRISTAL data are discussed in more detail by L. L. Lee et al. (2025b).

Separate work by A. L. Faisst et al. (2025) will present a more detailed analysis of the integrated metallicity and mass-metallicity relation. S. Fujimoto et al. (2025) will discuss the cosmic evolution of metallicity gradients, and in conjunction with F. Lopez et al. (in prep.), they will present the metallicity maps for the full ALPINE-CRISTAL-JWST sample. This work builds upon the analysis of S. Fujimoto et al. (2025) by incorporating a broader range of strong line diagnostics available from the data. Additionally, we investigate the impact of different diagnostics and beam smearing on the resulting metallicity gradients, thereby complementing the analysis of S. Fujimoto et al. (2025).

This work is structured as follows. In Sect. 4.2, we describe the sample selection and data reduction process. Sect. 4.3 presents the method of emission line fitting, followed by Sect. 4.4 that describes the methods used to infer metallicity and examines the systematic effects of different strong-line diagnostics on the inferred gradients. Sect. 4.5 explores the relationship between the measured metallicity gradients and their kinematic nature, as well as other physical properties of the samples. Sect. 4.6 investigates the impacts of beam smearing on the inferred metallicity gradients. Finally, Sect. 4.7 summarises the key findings.

Throughout, we adopt a flat ΛCDM cosmology with $H_0 = 70\,\mathrm{km\,s^{-1}\,Mpc^{-1}}$, and $\Omega_m = 0.3$. Solar metallicity is taken to be $12 + \log(\mathrm{O/H}) = 8.69$ (M. Asplund et al., 2009). Physical size is always reported in physical kiloparsecs (pkpc), but we use kpc henceforth for brevity.

Table 4.1. Physical properties of the 20 galaxies in the sample

CRISTAL ID	Full name	$z_{[\mathrm{CII}]}$	R.A. (°)	Decl. (°)	$\log\,(M_\star/\mathrm{M}_\odot)$[a] (dex)	$\log\,[\mathrm{SFR}/(\mathrm{M}_\odot\,\mathrm{yr}^{-1})]$[a] (dex)	Class.[b]
01	DC_842313	4.554	150.2271	2.5762	10.65	2.31	Non-Disk
02[†]	DC_848185, HZ6, LBG-1	5.294	150.0896	2.5864	10.30	2.25	Disk
03[†]	DC_536534, HZ1	5.689	149.9719	2.1182	10.40	1.79	Best-Disk[c]
04a	vc_5100822662	4.520	149.7413	2.0809	10.15	1.89	Non-Disk
05[†]	DC_683613, HZ3	5.541	150.0393	2.3372	10.16	1.83	Disk
06a	vc_5100541407	4.562	150.2538	1.8094	10.09	1.62	Disk
06b	. . .	4.562	150.2542	1.8097	9.19	1.07	Non-Disk
07a[†]	DC_873321, HZ8	5.154	150.0169	2.6266	10.00	1.89	Disk
07b	. . .	5.154	150.0166	2.6268	. . .	. . .	Non-Disk
09[†]	DC_519281	5.575	149.7537	2.0910	9.84	1.51	Disk[c]
10a-E[†]	DC_417567, HZ2	5.671	150.5172	1.9290	9.99	1.86	Disk
11	DC_630594	4.439	150.1358	2.2579	9.68	1.57	Best Disk[c]
13	vc_5100994794	4.579	150.1715	2.2873	9.65	1.51	Non-Disk
14	DC_709575	4.411	149.9461	2.3758	9.53	1.45	Non-Disk [d]
15	vc_5101244930	4.580	150.1986	2.3006	9.69	1.44	Best Disk
19	DC_494763	5.233	150.0213	2.0534	9.51	1.45	Best Disk[c]
20	DC_494057, HZ4	5.545	149.6188	2.0518	10.11	1.82	Best Disk[e]
22a	HZ10-E	5.653	150.2471	1.5554	10.35	2.13	Disk
25	vc_5101218326	4.573	150.3021	2.3146	10.90	2.75	Non-Disk
VC-7875	vc_5110377875	4.551	150.3848	2.4084	10.17	2.00	Disk[f]

[a] Derived from SED modellings in I. Mitsuhashi et al. (2024) and J. Li et al. (2024b). The typical uncertainty for $\log(M_\star)$ and log(SFR) are about 0.3 dex.

[b] Classified in L. L. Lee et al. (2025b).

[c] Classified as rotating disks also in D. Gomez-Espinoza et al. (in prep.) with the Hα data.

[d] Classified as compact in D. Gomez-Espinoza et al. (in prep.).

[†] Candidate Type-1 AGNs identified in W. Ren et al. (2025) based on the tentative detection of Hα broad component.

[e] See E. Parlanti et al. 2025 for a contrasting view.

[f] Classified as 'Rotator' in G. C. Jones et al. (2021) but with signatures of interaction with an extended halo or an extended outflow (S. Fujimoto et al., 2020), so it will fall closest to the 'Disk' classification in L. L. Lee et al. (2025b).

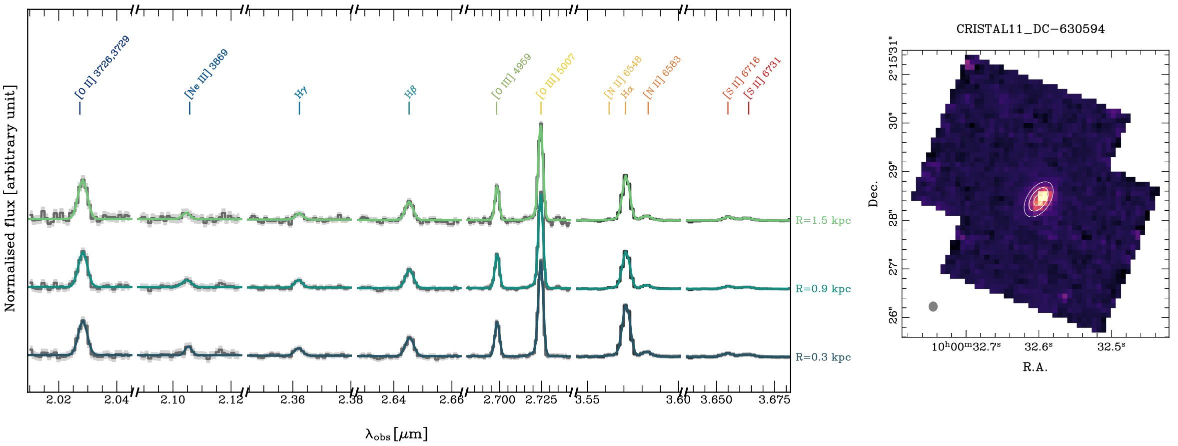

Figure 4.1 Example spectral fit of CRISTAL-11 ($z = 4.439$) for each annulus (*left*). The fitting procedure of the spectra is described in Sect. 4.3. The radius of the corresponding annulus is indicated in physical units on the right. The lines used for inferring metallicity in Sect. 4.4 are annotated at the top. The shape of the annuli are shown in the *right* panel, overlaid on the line flux map of Hα. The PSF after PSF homogenisation is shown at the bottom left.

4.2 Samples

In this study, we investigate the abundance distribution of the sample presented in L. L. Lee et al. (2025b), which examines the kinematic properties of 32 galaxies at $4 < z < 6$ using [C II] emission, as part of the ALMA-CRISTAL survey (R. Herrera-Camus et al., 2025) and samples supplemented from the ALMA archive. The NIRSpec/IFU data used for metallicity measurements are drawn from the ALPINE-CRISTAL-JWST survey (PID: 3045, PI: A. Faisst), a GO programme (PID: 4265, PI: J. Gonzalez Lopez) and the Galaxy Assembly with NIRSpec Integral Field Spectroscopy (GA-NIFS) Guaranteed Time Observations (GTO) programme (PID: 1217, PI: N. Luetzgendorf). The NIRSpec data from ALPINE-CRISTAL-JWST survey additionally covers vc_5110377875 (VC-7875 henceforth), for which the kinematics results are presented in S. Fujimoto et al. (2020) and G. C. Jones et al. (2021). The key properties of our sample is listed in Table 3.1.

For a detailed description of the samples, we refer the reader to the survey papers: R. Herrera-Camus et al. (2025) for the original ALMA-CRISTAL sample and A. L. Faisst et al. (2025) for the NIRSpec/IFU data and data reduction (S. Fujimoto et al., 2025).

In brief, ALMA-CRISTAL (R. Herrera-Camus et al., 2025) is a high-resolution follow-up of a subset of galaxies from the ALMA-ALPINE survey (M. Béthermin et al., 2020; O. Le Fèvre et al., 2020; A. L. Faisst et al., 2020b), with stellar masses $\log(M_\star/\mathrm{M}_\odot) \geqslant 9.5$ and sSFRs within a factor of 3 of the main sequence, with higher angular resolution, resolving the galaxies at $\sim$ 1kpc scale.[1] Both programmes carried out ALMA observations in Band 7, targeting [C II] 158μm and the dust continuum emission of MS SFG(s) at $4 < z < 6$. The ALPINE-CRISTAL-JWST survey is a NIRSpec IFU follow-up of 18 galaxies from the two ALMA large programmes.

The NIRSpec/IFU data cover a wavelength range of 1.66 to 5.10 μm (rest-frame 0.28–0.85 μm at $z = 5$) at a medium spectral resolution of $R \sim 1000$ ($\approx 125\,\mathrm{km\,s^{-1}}$ at 3 μm) with two gratings: G235M and G395M.

Since the ALPINE-CRISTAL-JWST sample does not include all galaxies in the kinematics sample presented in L. L. Lee et al. (2025b), we supplement our analysis by incorporating NIRSpec/IFU data for CRISTAL-01, 20, and 22a from two separate programmes. Specifically, we utilise data from a GO programme (PID: 4265, PI: J. Gonzalez Lopez, M. Solimano et al. 2025) for CRISTAL-01, and from the GA-NIFS survey for CRISTAL-20 and 22a. The GO programme employed a nine-point (‘SMALL’) dither pattern, while the GA-NIFS GTO programme used an eight-point (‘MEDIUM’) dither pattern. Both datasets were obtained at high spectral resolution using the G395H/F290LP configuration, which provides a spectral resolution of $R \sim 2700$. For CRISTAL-20 and 22a, we adopt the published metallicity maps presented in E. Parlanti et al. (2025) and G. C. Jones et al. (2025), respectively, which have a pixel scale of $0\farcs05\,\mathrm{pix}^{-1}$.

The important rest-frame optical emission lines for inferring metallicity, listed in order of increasing wavelength, are: [O II] $\lambda\lambda$3726,29, [Ne III] λ3869, Hβ, [O III] λ4959,5007, [N II] $\lambda\lambda$6548,6583, Hα, and [S II] $\lambda\lambda$6716,6731. Higher Balmer transition lines up to Hϵ are also detected in some cases (A. L. Faisst et al., 2025; S. Fujimoto et al., 2025). The auroral line [O III] λ4363 is also detected in five galaxies, and for these cases, the non-T_e-based metallicities are in good agreement with the T_e-based metallicities, albeit with larger uncertainties (A. L. Faisst et al., 2025).

Six objects in our sample were classified as candidate Type-1 AGNs by W. Ren et al. (2025) (see Table 4.1) due to the tentative presence of broad Hα emission. We retain them because their [N II]/Hα ratios are low ($f_{\mathrm{[NII]}}/f_{\mathrm{H}\alpha} \lesssim 0.1$), and they lie very close to the star-forming sequence in the BPT diagrams. These properties suggest that any AGN contribution to their nebular emission is weak, so contamination from AGN-driven shocks or excess ionising radiation is expected to be minor. However, CRISTAL-24 (DEIMOS_COSMOS_873756) has a very high [N II]/Hα (W. Ren et al., 2025) hinting at strong AGN activity or the presence of shocks (e.g. M. A. Dopita & R. S. Sutherland, 1995). We therefore excluded this galaxy from our analysis. The stacking of [C II] data indicates that the sample as a whole

---

[1] The ALMA data of VC-7875 and CRISTAL-24 (DEIMOS_COSMOS_873756) also come from two other ALMA observations (ALMA project 2019.1.00226.S, 2022.1.01118.S, PIs: E. Ibar, M. Béthermin).

exhibits weak outflow signatures (J. E. Birkin et al., 2025), and for the majority of the sample, outflows are expected to have a negligible impact on the line fluxes. CRISTAL-17 (DEIMOS_COSMOS_742174) is also not included in this work since it is too faint in the ALMA data for kinematic classification and modelling in L. L. Lee et al. (2025b). The metallicity gradients of CRISTAL-17 and 24 are investigated in S. Fujimoto et al. (2025). The final sample size of our study is 20.

4.3 Emission line measurements

To avoid introducing artificial metallicity gradients caused by variations in angular resolution as a function of wavelength, we homogenise the point spread function (PSF) of all channels to the size of the PSF at the wavelength of the reddest line used in our metallicity diagnostics (see Sect. 4.4). This line is chosen as either [S II] $\lambda6731$ or [N II] $\lambda6583$, depending on whether [S II] is detected with sufficient S/N. Since no stars are detected in our data cubes, we characterise the PSF using a data cube from another GO program (PID: 2957, PIs: H. Übler and R. Maiolino). In each channel, we fit a 2D Gaussian to the star to determine the orientation and size of the PSF both across and along the slicer. We observe that the PSF is more elongated in the direction along the IFU slicer, consistent with F. D'Eugenio et al. (2024). The minor and major axes of the PSF range from $[0.16, 0.18]''$ and $[0.19, 0.20]''$, respectively, equivalent to 1–1.3 kpc at $z = 5$.

After subtraction of the background from the data cube, and PSF homogenisation with the PSF models constructed above, by convolving each image with a kernel whose σ equals the quadrature difference between its native PSF and the chosen target PSF, we sum spectra from spaxels located within concentric elliptical annuli. The annuli had a with equal to one PSF HWHM (half-width at half-maximum, taken as the geometric mean of the along- and across-slicer directions), with typical width of $\lesssim 0\farcs2$, ≈ 0.6 kpc at $z = 5$. The number of rings is adjusted based on the outermost radius set by the S/N of the integrated line maps of [O III] $\lambda5007$ or Hα. However, when calculating line flux ratios, we consider the S/N of the individual lines involved in the extracted spectra, the outermost radii for each line diagnostic therefore vary. At this stage we do not apply any pixel-by-pixel rejection. The spectra are extracted using all pixels in an annulus, and the selection relies solely on the azimuthally integrated S/N. Rejection of pixels that have low fluxes to give robust line ratios is introduced later, in Sect. 4.5.3, where we investigate azimuthal variations across radii. The apparent centre, axial ratio and position angle of the galaxy are derived from the emission line maps of the brightest line, either [O III] $\lambda5007$ or Hα, by fitting a 2D

Gaussian profile. The error spectrum is calculated as the root-mean square (RMS) error using a moving window of 160 channels, with emission lines and any spurious noise spikes masked out.

We correct for dust reddening by comparing the observed Balmer line ratios to the theoretical values on an annulus-to-annulus basis. We assume the theoretical Hα/Hβ ratio equal to 2.86 as expected for case-B recombination (i.e., ionising photons are absorbed as soon as they are emitted) and an electron temperature of $T_e \sim 10^4$ K (D. E. Osterbrock & G. J. Ferland, 2006, Table 4.2). We then assume the nebular extinction that follows the D. Calzetti et al. (2000) curve. For CRISTAL-06a and 25, the Hβ emission is too weak in the individual annuli, we then apply the correction using a global A_V which is inferred from the spectrum integrated over a larger aperture with size covering the entire galaxy. CRISTAL-06b has no Hβ detection even in the integrated spectrum, so we adopt only diagnostics that are close in wavelength for inferring metallicity. For some galaxies, higher transition Balmer lines Hγ and Hδ are also detected at lower S/N.[2] They tend to give more uncertain A_V than that inferred from Hα/Hβ. We therefore adopt the A_V from Hα/Hβ only. We do not correct for Galactic extinction explicitly, since for our sources, the foreground Galactic $A_V \lesssim 0.4\,\mathrm{mag}$ (E. F. Schlafly & D. P. Finkbeiner, 2011), and becomes negligible at IR wavelengths following E. L. Fitzpatrick & D. Massa (2007) extinction curve.

To extract the flux for each emission line that will be used in Sect. 4.4, we use `CapFit` (M. Cappellari, 2023) to fit a single Gaussian profile to each detected line. We included an underlying first-order polynomial to model the baseline. If present in the spectra, we tie the line ratios of [O III] and [N II] doublets to the theoretical values of 2.98 and 3.071 (P. J. Storey & C. J. Zeippen, 2000), respectively. All emission lines within the same annulus are fixed to the same redshift, but their line centroids are allowed to vary within two channels ($0.002\,\mu$m or ≈ 160–$300\,\mathrm{km\,s^{-1}}$ at the wavelengths of interest) from the theoretical wavelength position. This margin accommodates bulk gas motions that can induce velocity shifts of at most $\sim 150\,\mathrm{km\,s^{-1}}$, as observed for [C II] (see Table 2 of L. L. Lee et al. 2025b), as well as the wavelength-dependent line spread function (LSF) across the cube.

Their (observed) line widths are tied to the same value but can vary within five channels as a whole. For five galaxies that are classified as candidate Type-1 AGNs in W. Ren et al. (2025) (see Table 4.1), we additionally include a broad Gaussian component to model the emission lines, which otherwise would result in residuals around the narrow component. However, except for the stronger lines such as [O III] λ5007, Hα, and in some cases Hβ, the broad component flux converges to zero for other lines, suggesting the S/N for these fainter

---

[2] Hϵ is detected in some cases; however, due to its blending with [Ne III] λ3967, we refrain from using it to infer A_V.

lines is insufficient to recover the broad component. In cases where the broad component is non-zero, it contributes a relatively small fraction of the total line flux, ranging from a few to $< 20\%$. For our subsequent analysis, we only consider the flux from the narrow component. We find that the gradients are consistent with those obtained when using a single-component fit, only the normalisation differs. This agreement is expected, given that the broad component contributes only a minor fraction of the total line flux. An example best-fit is shown in Fig. 4.1.

4.4 Strong line metallicity indicators and metallicity gradients

In this section, we leverage the rich set of lines observed, giving access to multiple strong line diagnostics. As discussed below, different diagnostics have different strengths and combining them would give a tightened constraint on the metallicity. Building on the work of S. Fujimoto et al. (2025), who presented metallicity gradients inferred from two diagnostics, we expand our analysis to include a broader range of strong line diagnostics available from the data. We assess the impact of different diagnostics on the resulting metallicity gradients, complementing the analysis of S. Fujimoto et al. (2025).

We derive the gas-phase metallicity by jointly analysing the measured emission line ratios using the empirical calibrations summarised in Table 4.2. The diagnostic line ratios often involve collisionally-excited lines from either singly and/or doubly ionised oxygen (O^+ and O^{2+}), or singly ionised nitrogen and sulphur (N^+ and S^+), each measured relative to hydrogen recombination lines (Hα and Hβ in our case), except for O32 or Ne3O2. The strengths and limitations of each line diagnostic are summarised in Table 1 of R. Maiolino & F. Mannucci (2019) (see also L. J. Kewley et al., 2019). In brief, some diagnostics—such as R3—are double-valued with respect to metallicity and thus require auxiliary diagnostics such as O32 and N2 to resolve this degeneracy. Because nitrogen is not an α-element and, at the metallicities relevant to our sample, is produced mainly as a secondary element, nitrogen-line indices probe the oxygen abundance only indirectly through the N/O–O/H correlation. This makes them more sensitive to variations in chemical evolution history than oxygen-based indices. On the other hand, indices such as N2 increase monotonically with O/H, so they do not suffer from the degeneracy that affects R3 and similar oxygen-line diagnostics. Therefore, since some diagnostics are more sensitive to the ionisation parameter, reddening corrections, and nitrogen enrichment than others, we can better marginalise over different systematic effects by combining the various diagnostics. We are aware, however,

Table 4.2. Line diagnostics and the calibrations used.

Indicators	Emission line ratio	Z Range[a]
N2[†]	[N II] λ6583/Hα	[7.8,8.6]
R3[†]	[O III] λ5007/Hβ	[7.3,8.6]
Ne3O2[†]	[Ne III] λ3869/[O II] $\lambda\lambda$3726, 29	[7.4,8.6]
O32	[O III] λ5007/[O II] $\lambda\lambda$3726, 29	[7.3,8.6]
O2	[O II] $\lambda\lambda$3726, 29/Hβ	[7.3,8.6]
S2	[S II] $\lambda\lambda$6716, 33/Hα	[7.9,8.6]

Note. — The calibrations are based on R. L. Sanders et al. (2025).

[a] The metallicity range where each diagnostic can be reliably applied.

[†] Relatively unaffected by dust reddening.

that the uncertainty estimates from such a Bayesian approach may not be statistically meaningful, since the line ratios are not independent of each other. As discussed later in this section and Appendix 4.9, to estimate uncertainties in an alternative way, we compute the metallicity gradients independently using each diagnostic and calculate the standard deviation of these gradients.

We utilise the empirical relations from R. L. Sanders et al. (2025) that are calibrated based on a sample of $\sim$ 140 SFG(s) at $z \sim$ 3–10 drawn from the AURORA survey (PID: 1914, PIs: A. Shapley and R. Sanders, A. E. Shapley et al. 2025) and the literature, covering the widest range in metallicity where multiple auroral lines are available (e.g. [O III] λ4363). It leverages the latter to infer metallicities via the direct electron-temperature (T_e) method, in which elemental abundances are inferred from the exponential dependence of line emissivity on T_e measured through highly temperature-sensitive auroral lines. The metallicity range where each diagnostic can be reliably applied is listed in Table 4.2.

In an absolute sense, different calibrations can introduce systematics of up to 0.7 dex (L. J. Kewley & S. L. Ellison, 2008) in absolute metallicity measurements, due to variations between empirical and theoretical methods, sample selections, and line tracers. However, these uncertainties are less problematic when measuring metallicity gradients, because gradients rely on relative (differential) abundances rather than absolute values, and the relative systematics are typically within ~ 0.15 dex. A more recent study by Z. Li et al. (2025b) (their Fig. 16) found < 0.1 dex scatter around equality when using different strong-line calibrations (e.g. R. Maiolino et al., 2008; M. Curti et al., 2020a; K. Nakajima et al., 2022; R. L. Sanders et al., 2024), which is within their measurement uncertainty; there are no obvious systematic offsets between different calibrations. We also investigate the systematics associated with using different line tracers from the R. L. Sanders et al. (2025) calibration to infer metallicity gradients later in this Section.

The specific line ratios used for each system in each annuli depend on the detection of the involved lines at S/N $\gtrsim 2.5$. When lines such as [O III] and Hβ are covered by both gratings (G235M and G395M), we select the grating that also includes the other relevant lines. For example, for R3, we use G395M for [O III] and Hβ for its higher S/N, if possible, but for O32, we switch to G235M to evaluate the line ratio involving [O III] and [O II], as both lines fall within this grating. This is to avoid potential differences in the absolute calibration of data from different gratings. The fluxes of the same line are consistent with each other in both gratings, but with larger uncertainty in G235M as expected.

We determine the metallicities in each radial bin using two methods. The first approach employs Bayesian inference with the `emcee` package (D. Foreman-Mackey et al., 2013) to sample the posterior probability distribution of $12 + \log(\mathrm{O/H})$, i.e. to find the metallicity that best satisfies all calibrations at once. We name this method Method I, and provide more description in Appendix 4.8. The inferred radial profile of these metallicities is then used to derive a gradient (denoted as 'Method I' in Table 4.3). This method is similarly applied in the spaxel-to-spaxel fitting in Sect. 4.5.3 to investigate azimuthal variations in metallicity.

For CRISTAL-20 and CRISTAL-22a, we utilised the metallicity maps presented in the works of E. Parlanti et al. (2025) and G. C. Jones et al. (2025), respectively. The metallicities were inferred from N2, R3, and O3N2 ($\equiv$ [O III] λ5007/Hβ)/([N II] λ6583/Hα) diagnostics, employing the calibrations from M. Curti et al. (2020a, 2024). Within the metallicity ranges spanned by the two objects ($\log(Z) \in [8.32, 8.38]$ for CRISTAL-20 and $\log(Z) \in [8.44, 8.47]$ for CRISTAL-22a), the slopes of the diagnostics used are negligibly different from those of R. L. Sanders et al. (2025). However, the absolute metallicity values may differ by up to 0.3 dex higher (see Fig. 15 of R. L. Sanders et al., 2025).

To quantify the systematic differences between the gradients inferred from different line diagnostics, and to provide an alternative estimate of the uncertainties associated with the metallicity gradients, we also derive metallicities from individual line diagnostics by directly inverting the empirical calibration curves for the measured line ratios. We name this method Method II. The gradient for each diagnostic is fitted individually only when

Table 4.3. Metallicity gradients inferred for the CRISTAL samples using multiple strong lines.

ID	Class.[a]	Method I[b] (dex kpc^{-1})	Method II[c] (dex kpc^{-1})
01a	Non-Disk	$0.107^{+0.054}_{-0.055}$	$0.107^{+0.028}_{-0.028}$
02	Disk	$0.031^{+0.016}_{-0.017}$	$0.029^{+0.015}_{-0.015}$
03	Best Disk	$0.065^{+0.030}_{-0.031}$	$0.080^{+0.039}_{-0.039}$
04a	Non-Disk	$0.031^{+0.020}_{-0.020}$	$0.041^{+0.058}_{-0.058}$
05a	Disk	$0.055^{+0.058}_{-0.057}$	$0.049^{+0.051}_{-0.051}$
06a	Non-Disk	$-0.054^{+0.083}_{-0.081}$	$-0.026^{+0.054}_{-0.054}$
06b	Disk	$-0.035^{+0.285}_{-0.292}$	$-0.004^{+0.032}_{-0.032}$
07a	Disk	$0.099^{+0.025}_{-0.026}$	$0.125^{+0.027}_{-0.027}$
07b	Non-Disk	$0.166^{+0.091}_{-0.090}$	$0.079^{+0.088}_{-0.088}$
09	Disk	$0.101^{+0.115}_{-0.114}$	$0.101^{+0.099}_{-0.099}$
10a-E	Disk	$0.017^{+0.026}_{-0.027}$	$0.020^{+0.018}_{-0.018}$
11	Best Disk	$0.025^{+0.042}_{-0.040}$	$0.025^{+0.046}_{-0.046}$
13	Non-Disk	$0.069^{+0.037}_{-0.038}$	$0.029^{+0.033}_{-0.033}$
14	Non-Disk	$0.036^{+0.067}_{-0.064}$	$0.013^{+0.025}_{-0.025}$
15	Best Disk	$0.057^{+0.044}_{-0.044}$	$0.033^{+0.061}_{-0.061}$
19	Best Disk	$0.038^{+0.036}_{-0.036}$	$0.024^{+0.045}_{-0.045}$
20	Best Disk	$-0.029^{+0.053}_{-0.056}$[d]	...
22a	Disk	$-0.019^{+0.042}_{-0.043}$[d]	...
25	Non-Disk	$0.051^{+0.099}_{-0.100}$	$0.044^{+0.029}_{-0.029}$
VC-7875	Disk	$0.040^{+0.024}_{-0.023}$	$0.039^{+0.029}_{-0.029}$

[a] Same as Table 4.1

[b] Best-fit metallicity gradients derived from the Bayesian fitting that combines the different diagnostics listed in Table 4.2.

[c] Median of the best-fit metallicity gradients derived from each individual diagnostic. The individual values of the gradients are listed in Table 4.5.

[d] Inferred from the metallicity maps in E. Parlanti et al. (2025) and G. C. Jones et al. (2025).

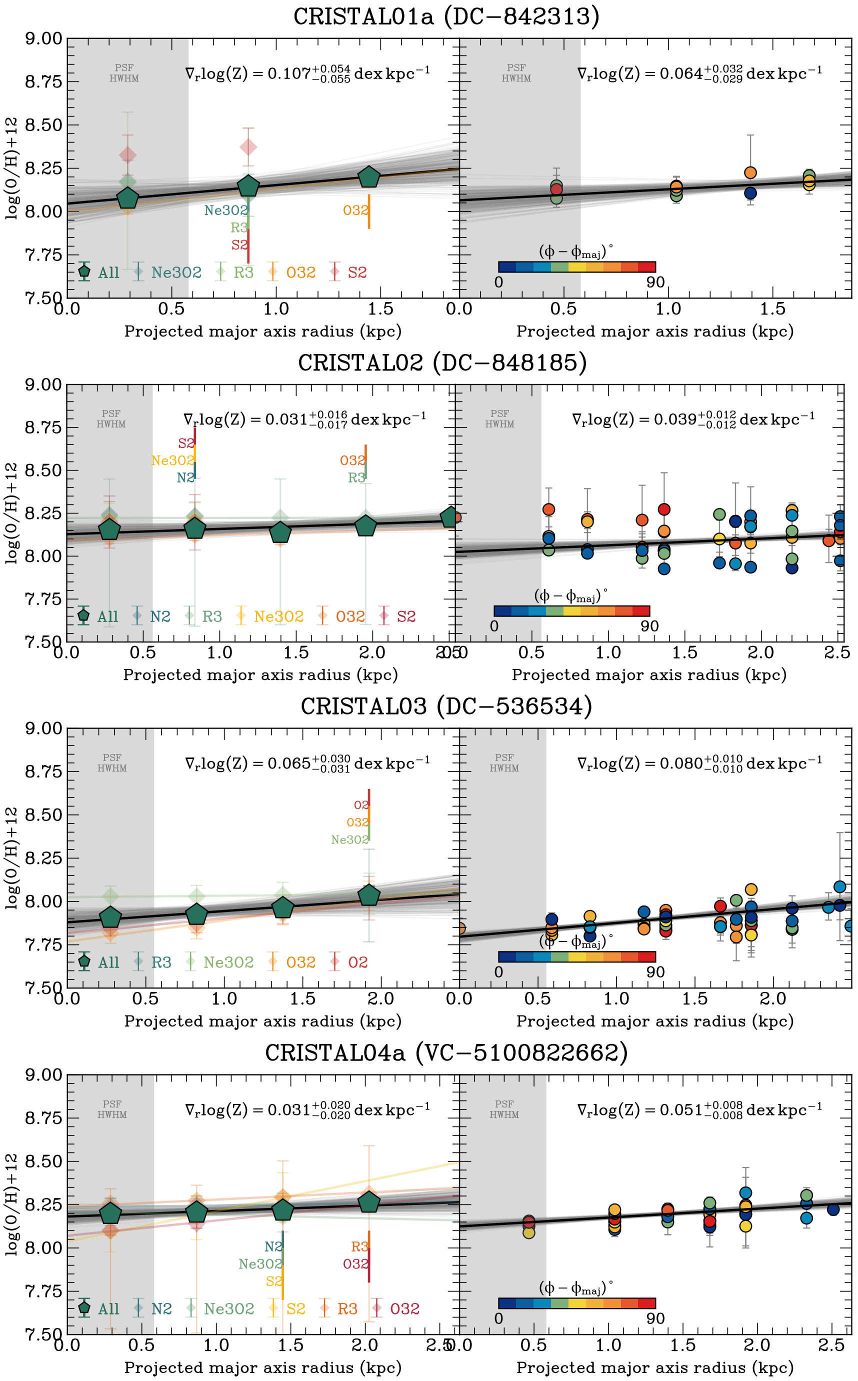

Figure 4.2 Radial profiles of metallicities and their best-fit linear models (black lines). For each galaxy, the left panel shows the azimuthally-averaged profiles, where dark green pentagons with black outlines represent the metallicities derived by combining the listed line diagnostics using a Bayesian approach (Method I). The translucent grey lines are 300 random draws from the posterior distribution of the model parameters. The outermost radius at which each diagnostic is used is annotated at the corresponding location on the profile. The fainter coloured diamonds represent the metallicities obtained from individual diagnostics via Method II, while the lines in the corresponding colours show the best-fit models for each diagnostic. Similarly, the right panel shows the pixel-based metallicity profile with each data point coloured coded by its (absolute) acute azimuthal angle difference from the major axis. Line diagnostics of which only two annuli are available are shown (coloured diamonds) but not fitted.

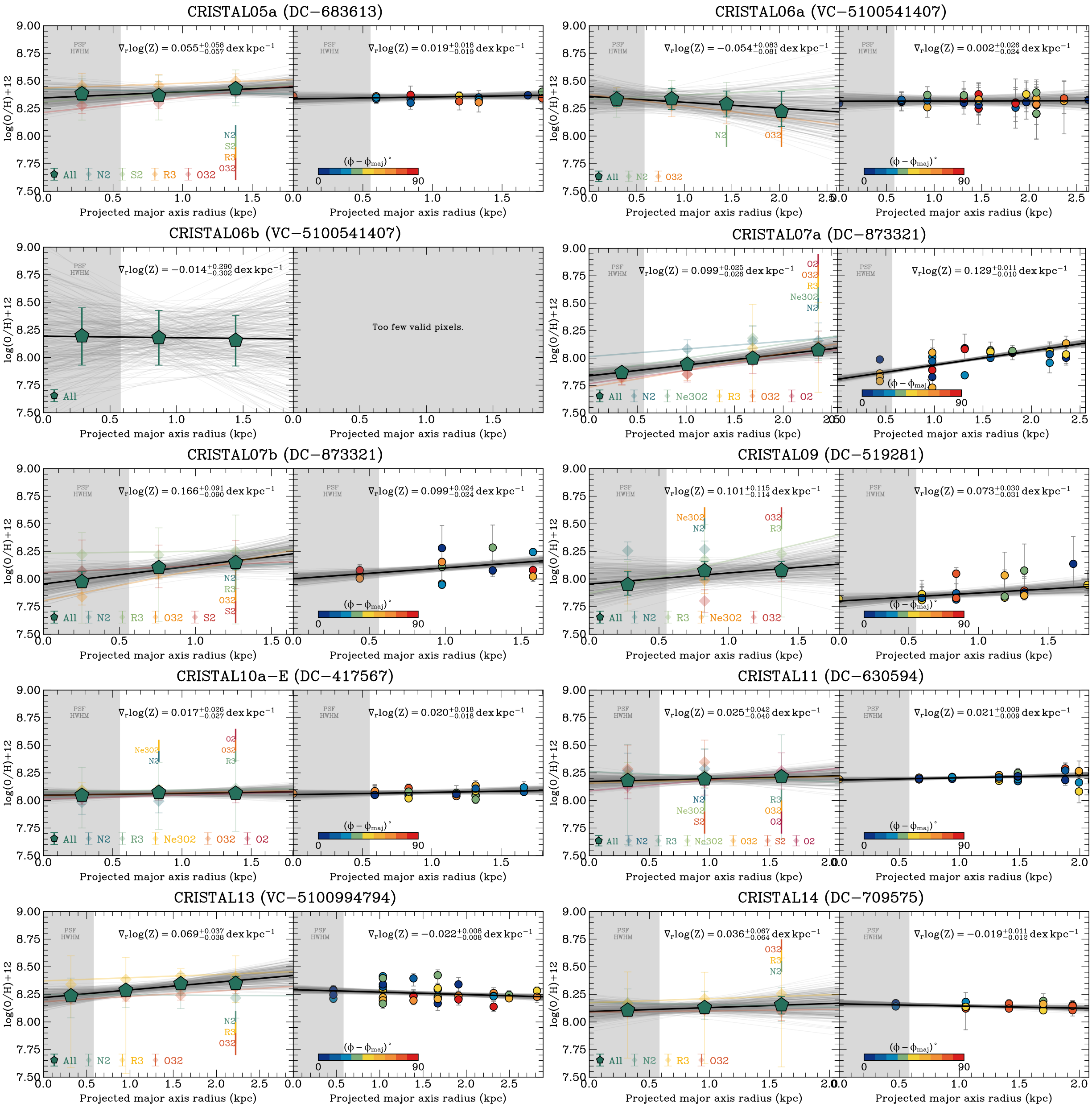

Figure 4.3 (Continued.)

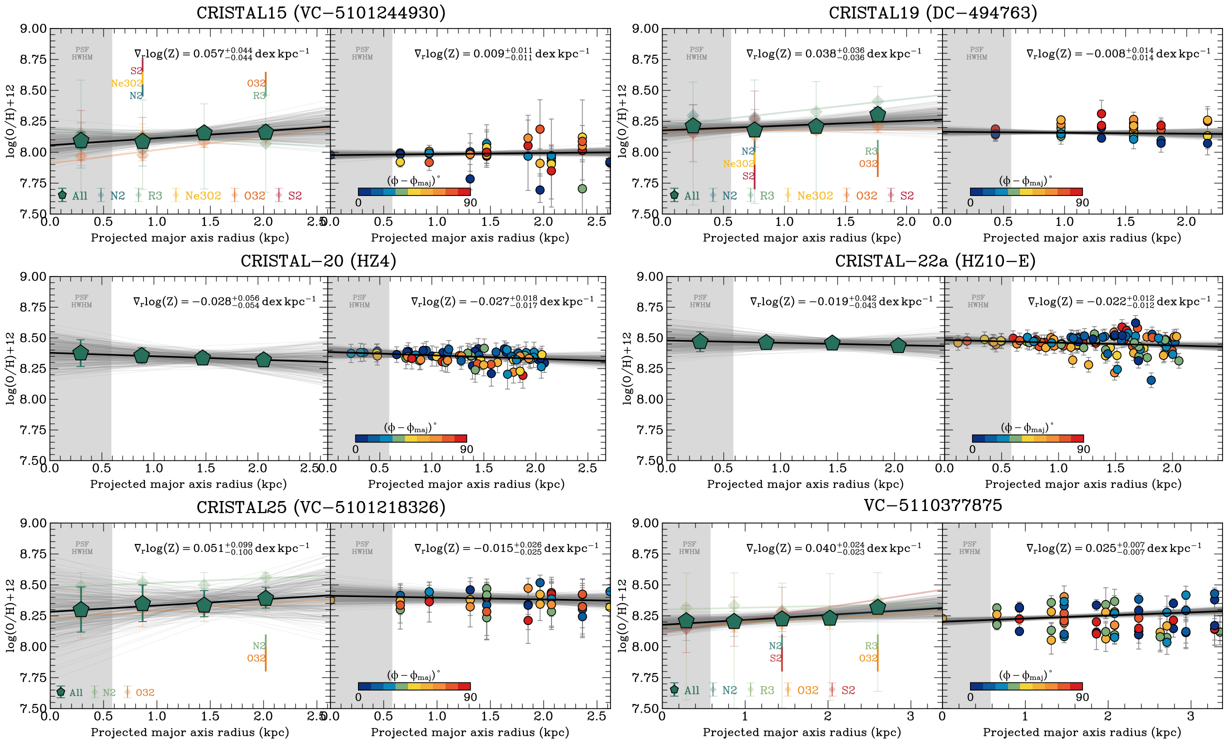

Figure 4.4 (Continued.)

there are more than two annuli available, and the median of these gradients is reported in Table 4.3.

Following other $z \gtrsim 1$ studies (e.g. J. P. Stott et al., 2014; E. Wuyts et al., 2016; D. Carton et al., 2018), we parametrise the radial metallicity profile using a linear function,

$$\log_{10} Z(r) = \nabla_r \log_{10}(Z) \cdot r + Z_0, \tag{4.1}$$

where $\log_{10} Z = 12 + \log(\mathrm{O/H})$, $\nabla_r \log(Z)$ is defined as the metallicity gradient and Z_0 is the central metallicity. For both Methods, we fit the radial profiles with `emcee`, assuming flat priors for both $\nabla_r \log(Z)$ and Z_0. The chains are initialised with the best-fitting solutions obtained from `mpfit` and then evolved with 64 walkers for 2000 steps, discarding the first 500 steps as burn-in.

The left panels of each galaxy in Fig. 4.2 plot the resulting best-fit metallicities profiles from Methods I and II. The values are summarised in Table 4.3. The typical value of measurement uncertainties is on average $\sim 0.06\,\mathrm{dex\,kpc}^{-1}$. We find that in general $\nabla_r \log(Z)$ and Z_0 obtained from Method II for individual diagnostics agree well with those from Method I, except in some cases where N2 (from Method II) prefers a flatter gradient. The

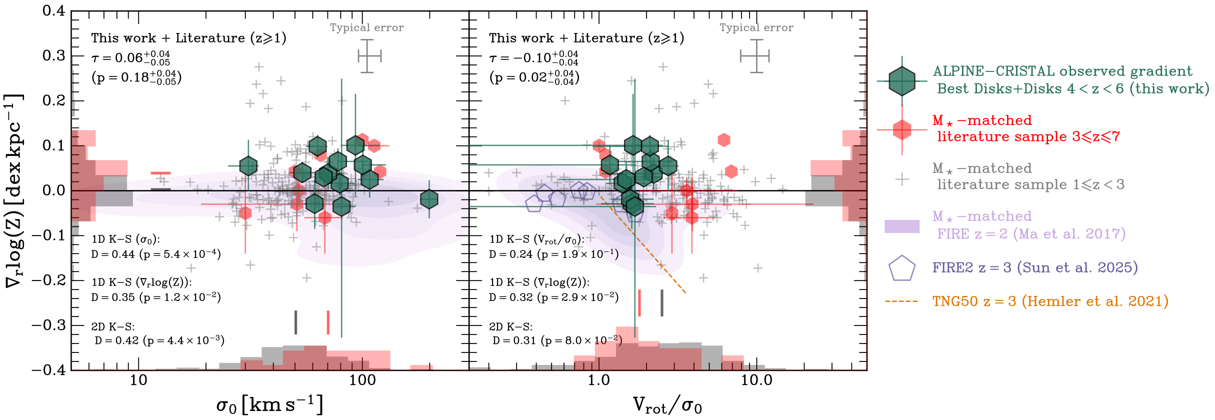

Figure 4.5 Distributions of metallicity gradients, $\nabla_r \log(Z)$, as a function of the velocity dispersion, σ_0 (*left*), and the ratio of rotational velocity to velocity dispersion, V_{rot}/σ_0 (*right*), for the CRISTAL disk galaxies (green hexagons). We also show $M_\star$-matched literature samples at $3 \lesssim z \lesssim 7$ as red hexagons, and $z < 3$ as grey crosses. The references for these literature samples are listed in Table 4.8. The Kendall's τ correlation coefficients and the p-values are annotated in the top left in each panel. Histograms of the distributions of the $3 \lesssim z \lesssim 7$ and $z < 3$ samples are shown along the x- and y-axes in red and grey, respectively. The combined CRISTAL and literature sample exhibits a shallow negative correlation between $\nabla_r \log(Z)$ and V_{rot}/σ_0, as indicated by the Kendall's τ value. In contrast, the Kendall's correlation test reveals no significant correlation with σ_0, which could be due to the inherently shallow trend and the large scatter. However, the overall distribution of the two populations at $z < 3$ (grey histogram) and $z \geqslant 3$ (red histogram), a clearer distinction emerges between the $z < 3$ and $z \geqslant 3$ populations. Specifically, the $z \geqslant 3$ population tends to have higher σ_0 values and more positive metallicity gradients, whereas the $z < 3$ population has lower σ_0 values and, on average, lower metallicity gradients. This distinction is supported by the significant 2D K-S test statistics, which gives a nearly 3-σ significance level (annotated at the bottom left of each panel). The predicted trends from cosmological simulations are shown, including FIRE at $z = 2$ from X. Ma et al. 2017 (purple contour), FIRE2 at $z = 3$ from X. Sun et al. 2025 (*right*, open purple pentagons), and TNG50 at $z = 3$ from Z. S. Hemler et al. 2021 (*right*, orange dashed line). While the simulations capture the slight positive and negative relationships between $\nabla_r \log(Z)$ and σ_0 and V_{rot}/σ_0, respectively, the normalisation and steepness of these relationships differ from the observations.

gradients inferred from Method I and II, in terms of median for the latter, agree within 1σ as shown in Fig. 4.13. We discuss further the difference between the two Methods in Appendix 4.9. Henceforth, we adopt the values from Method I as our fiducial values.

The mean metallicities of our radial profiles agree within 0.3 dex with A. L. Faisst et al. (2025), which uses R. L. Sanders et al. (2024) calibrations. When comparing our metallicity gradients with those inferred by S. Fujimoto et al. (2025), who used the R3 and O32 diagnostics based on the same calibrations from R. L. Sanders et al. (2025), we find good agreement if we restrict our analysis to the same two diagnostics. Minor differences between our results can be attributed to the choice of apertures in multiple-component systems, e.g. CRISTAL-01a. The choices are made because of the different science goals: our study focuses on the component whose kinematics can be reliably classified and studied, whereas S. Fujimoto et al. (2025) emphasise the full system.

Across the sample, the median $\nabla_r \log(Z) = +0.039 \pm 0.010\,\mathrm{dex\,kpc}^{-1}$ (standard deviation $= 0.053$). All galaxies except CRISTAL-06a, 06b, 20 and 22a have positive metallicity gradients. However, there are no galaxies with $\nabla_r \log(Z) > +0.05\,\mathrm{dex\,kpc}^{-1}$ at 3σ level, and only three galaxies at 1σ. If we consider strictly flat metallicity gradient, i.e. $\nabla_r \log(Z) = 0\,\mathrm{dex\,kpc}^{-1}$, there are 11 galaxies with $\nabla_r \log(Z) > 0\,\mathrm{dex\,kpc}^{-1}$, but only at 1σ level. For CRISTAL-06a, 06b, 20 and 22a, none of them have gradients significantly steeper than $-0.05\,\mathrm{dex\,kpc}^{-1}$ (typical values of the MW and local spirals) and they are consistent with $0\,\mathrm{dex\,kpc}^{-1}$ at 1σ level.

For the galaxies that exhibit mild positive gradients, the gradients could be produced by (at least) two non-exclusive mechanisms: (1) the accretion of metal-poor filaments that stream gas penetrating the galaxy halo and deliver pristine gas directly to the inner kiloparsec (A. Dekel et al., 2009b; D. Ceverino et al., 2016), (2) galactic outflows with high mass loading factors could preferentially remove metals from the central regions, and a fraction of this enriched gas could cool and be re-accreted at the outer regions of the galaxy, the so-called galactic fountain (B. K. Gibson et al., 2013; X. Ma et al., 2017), although direct evidence for metal-rich fountains at $z > 4$ is still lacking. These processes could lead to an increase in the outer metallicity, resulting in positive metallicity gradients .

The flatness of our observed metallicity gradients could be potentially an observational effect of angular resolution (T. T. Yuan et al., 2011; S. Wuyts et al., 2016). We will explore whether beam smearing could contribute to the shallow gradients observed in most of our sample in Sect. 4.6.

Notably, the three galaxies with the steepest gradients are CRISTAL-01a, 07a and 07b, which are known to have an immediate neighbour within $\sim 10\,\mathrm{kpc}$. CRISTAL-01a resides in a dense region with multiple companions and a massive neighbour, SMG J1000+0234

(E. F. Jiménez-Andrade et al., 2023; M. Solimano et al., 2024, 2025; M. Rubet et al., 2025). The observed kinematic features suggest that this system may be in the later stages of a merger, and the misaligned velocity gradient hints at gas inflow triggered by the merger (L. L. Lee et al., 2025b). CRISTAL-07a and 07b is an interacting pair, with CRISTAL-07a retaining a lot of its disk rotation signatures.

The interacting nature of CRISTAL-01a, 07a, and 07b may contribute to their observed positive metallicity gradients as found at lower redshifts (e.g. L. J. Kewley et al., 2010; D. S. N. Rupke et al., 2010b; J. Queyrel et al., 2012; D. Carton et al., 2018; X. Wang et al., 2022), and also reported in one case at $z \sim 8$ by G. Venturi et al. (2024). However, not all interacting pair systems in our sample exhibit positive gradients; for example, CRISTAL-06a and 06b have slight negative gradients instead. The uncertain stage of merger for these systems complicates a direct association between interaction and metallicity gradients.

4.5 Gas-phase abundance gradients and their potential drivers

In this section, we will discuss the values of $\nabla_r \log(Z)$ for different sub-populations in our sample.

4.5.1 Metallicity gradients in disks

Studies of star-forming disks at cosmic noon have found that galaxies with higher gas velocity dispersions σ_0 tend to have flatter and in some cases even positive radial metallicity gradients (J. Queyrel et al., 2012; T. Jones et al., 2013; S. Gillman et al., 2021; N. Leethochawalit et al., 2016; X. Wang et al., 2022). Consistent with this trend, the metallicity gradients exhibit a mild anti-correlation with the ratio $V_{\mathrm{rot}}/\sigma_0$, where V_{rot} is the rotation velocity.[3] Both trends between metallicity gradients and σ_0 and $V_{\mathrm{rot}}/\sigma_0$ observed in the literature are illustrated in Fig. 4.5.

We investigate the relationships between metallicity gradients, $\nabla_r \log(Z)$, and the gas-phase velocity dispersion, σ_0, as well as $V_{\mathrm{rot}}/\sigma_0$, from [C II] for the 13 disk galaxies (S. Fujimoto et al., 2020; L. L. Lee et al., 2025b) and samples compiled from the literature at $z \gtrsim 1$ (see Appendix 4.10) in Fig. 4.5.

We find a shallow yet statistically significant ($p < 0.05$) negative correlation between

---

[3] As discussed in Sect. 6.1 in L. L. Lee et al. (2025b), the definition and methodology used to derived V_{rot} and σ_0 varies across literature.

$\nabla_r \log(Z)$ and $V_{\rm rot}/\sigma_0$ among the CRISTAL disks and literature values, with a Kendall's τ correlation coefficient of -0.10. Observations of MS SFG(s) from $z \lesssim 8$ to $z = 1$ suggest that $V_{\rm rot}/\sigma_0$ increases with cosmic time (Fig. 9 in L. L. Lee et al., 2025b), a trend that is also seen in simulations (e.g. A. Pillepich et al., 2019; X. Sun et al., 2025). Therefore, the correlation between $\nabla_r \log(Z)$ and $V_{\rm rot}/\sigma_0$ likely reflects the cosmic evolution of $\nabla_r \log(Z)$ with redshift, where $\nabla_r \log(Z)$ becomes more negative towards lower redshift, as discussed in S. Fujimoto et al. (2025) in the context of our sample and M. Curti et al. (2020b); G. Venturi et al. (2024) for a general discussion.

Since $V_{\rm rot}/\sigma_0$ is an indicator of disk maturity in terms of rotational support, the coherent picture of metallicity gradients decreasing with both $V_{\rm rot}/\sigma_0$ and cosmic time implies that disk maturity plays a dominant role in driving the negative metallicity gradient, among also other evolving variables with redshift. This is consistent with simulations, such as those presented in X. Ma et al. (2017); M. A. Bellardini et al. (2021) and X. Sun et al. (2025), which show that disks become increasingly rotationally supported over time and consequently, suppress radial mixing of metals, leading to a gradual steepening of the radial metallicity gradients over time.

In contrast, no discernible correlation is observed between $\nabla_r \log(Z)$ and σ_0, as indicated by a Kendall's τ of 0.06 and a p-value $= 0.18$, which rules out any strong trends. The lack of trend between $\nabla_r \log(Z)$ and σ_0 could be attributed to the inherently shallow trend as predicted by FIRE simulation (for $z = 2$, X. Ma et al., 2017), and the large scatter preclude any trends. Nevertheless, the overall distribution of the two populations at $z < 3$ and $z \geqslant 3$, a clearer distinction emerges between the $z < 3$ and $z \geqslant 3$ populations. Observationally, σ_0 exhibits a decreasing trend with decreasing redshift (Fig. 9 in L. L. Lee et al., 2025b). Consequently, the distinction between the $z < 3$ and $z \geqslant 3$ populations could be, in part, reflecting the trend between σ_0 and the metallicity gradient. This distinction is supported by the two-dimensional Kolmogorov-Smirnov (K-S) D-statistics (J. A. Peacock, 1983; G. Fasano & A. Franceschini, 1987; W. H. Press et al., 2007) test statistics, which gives a nearly 3-σ significance level. For reference, the D-statistics from the 1D K-S test of the galaxies in our sample for each variable are also provided in Fig. 4.5.

The σ_0 and $V_{\rm rot}/\sigma_0$ values could be used to gauge the local stability of a gaseous disk through the Toomre Q parameter, in which $Q \propto (\sigma_0/V_{\rm rot}) f_{\rm gas}^{-1}$ (e.g. R. Genzel et al., 2011).[4] The lower the Q, the more unstable the disk against local collapse. CRISTAL galaxies have high gas fractions, $f_{\rm gas} \approx 0.5$ on average, and a median $Q \sim 0.6$ (L. L. Lee et al., 2025b),

---

[4] An approximation neglecting the contribution from the stellar and other gaseous components, a multi-component or effective Q would give a slightly different numerical value but the same qualitative behaviour (B. Wang & J. Silk, 1994; A. B. Romeo & N. Falstad, 2013).

close to the critical value for a marginally stable thick disc (e.g. M. Behrendt et al., 2015). In such low-Q conditions, the disk is expected to fragment into giant, star-forming clumps that could contain $\sim 7\%$ of the total stellar mass (N. M. Förster Schreiber & S. Wuyts, 2020, and references therein). The gravitational torques exerted by these clumps, together with global non-axisymmetric modes, drive radial gas inflow that can efficiently flatten the metallicity gradient (e.g. F. Bournaud et al., 2007, 2011; N. J. Goldbaum et al., 2016). Simulations suggest, however, that only the most massive and densest long-lived clumps are likely to survive the inward migration across the disk (A. Dekel et al., 2022; D. Ceverino et al., 2023). Observations have yet to provide clear evidence for such clump migration (A. Claeyssens et al., 2025; B. S. Kalita et al., 2025).

Morphologically, many CRISTAL galaxies exhibit pronounced clumpy structure in rest-frame optical JWST/NIRCam images (L. L. Lee et al., 2025b, see also R. Herrera-Camus et al., in prep.), whereas their stellar-mass distributions, inferred from resolved SED modelling (J. Li et al., 2024b; N. E. P. Lines et al., 2025) and ALMA [C II] data (R. Ikeda et al., 2025; L. L. Lee et al., 2025b), appear relatively smooth.

Most of the disks in our sample lack a massive bulge, as inferred from kinematic analysis (L. L. Lee et al., 2025b). The flat metallicity gradients observed in these disks lend additional support for the absence of a strong and mature bulge component at $4 < z < 6$.

The empirical trends between metallicity gradients and σ_0 and $V_{\rm rot}/\sigma$ are broadly reproduced by cosmological simulations from FIRE and TNG50 (X. Ma et al., 2017; Z. S. Hemler et al., 2021) for $z \gtrsim 2$ (see also the analytical model by P. Sharda et al. 2021b). They suggest that a galaxy requires a highly rotation-dominated cold disk to develop a steep negative metallicity gradient, whereas galaxies lacking ordered rotation tend to exhibit flat gradients. More recently in X. Sun et al. (2025), they also found galaxies with weak rotational support ($V_{\rm rot}/\sigma_0 \lesssim 1$) are more likely to develop positive metallicity gradients. In these simulations, the observed correlation with $V_{\rm rot}/\sigma_0$ is driven by the effective redistribution of metal-rich gas in dispersion-dominated galaxies through processes such as rapid gas infall, which flattens the metallicity gradients.

4.5.2 Metallicity gradients in disks versus non-disks

Figure 4.6 shows the distribution of $\nabla_r \log(Z)$ of disks and non-disks of our sample. We find no significant distinction between disks and non-disks as classified in L. L. Lee et al. (2025b), with median $\nabla_r \log(Z) = +0.038 \pm 0.013\,\mathrm{dex\,kpc}^{-1}$ and $+0.051 \pm 0.026\,\mathrm{dex\,kpc}^{-1}$, respectively, with a negligible difference of $< 1\sigma$ level, and a K-S test does not indicate the two populations are distinct with score of 0.32 ($p = 0.64$).

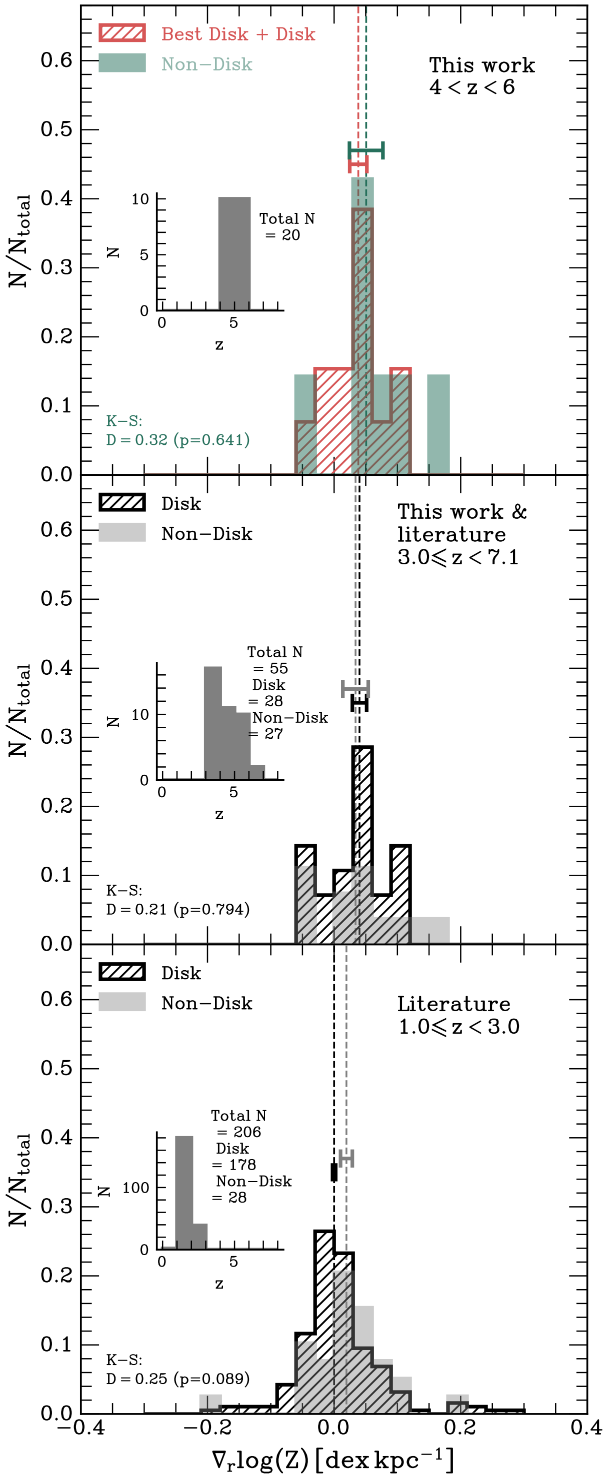

Figure 4.6 Metallicity gradients in disk and non-disk subsets of our sample (*top*) and compiled stellar mass-matched sample from literature at $3 < z \lesssim 8$ (*middle*) and $1 < z < 3$ (*bottom*). The median values of the distributions are indicated by the vertical dashed line of the corresponding colours, and similarly for the errors of the median (obtained by bootstrapping) which are represented by the horizontal error bars of the same colour. The literature references are listed in Table 4.8.

To compare with the literature samples listed in Table 4.8 (and see discussion in Appendix 4.10), we first select galaxies that fall within a comparable mass range to our sample. The resulting distribution of stellar masses is shown in Fig. 4.15. The stellar mass values are taken directly from the literature, which were derived from spectral energy distribution (SED) fitting using various tools and assuming different initial mass functions (IMFs). We then select the disks and non-disks based on either the classifications in the original works as ‘rotating’ or ‘non-rotating’ from kinematics, or based on morphology from imaging data, including those from *Hubble* Space Telescope (HST).

For the literature sample at $3 \leqslant z \lesssim 7$, we find no significant distinction between the disk and non-disk populations, with an insignificant difference in their median values (disk: $+0.040 \pm 0.011\,\mathrm{dex\,kpc}^{-1}$, non-disk: $+0.034 \pm 0.020\,\mathrm{dex\,kpc}^{-1}$). When combining our sample with the existing literature at $3 \leqslant z \lesssim 7$ (Fig. 4.6), increasing the number of objects from 35 to 55, the difference between the disk and non-disk populations remains negligible in terms of median difference, with high $p-$value $= 0.80$ from K-S test.

On the other hand, a more noticeable difference in metallicity gradients between disks and non-disks is observed at $1 \leqslant z < 3$ in our compiled sample of 206 galaxies shown in Fig. 4.6, with median values of $0.000 \pm 0.003\,\mathrm{dex\,kpc}^{-1}$ and $0.0195 \pm 0.009\,\mathrm{dex\,kpc}^{-1}$, respectively, although this difference in median values is only significant at 2σ level. This significance is comparable to that reported in the 21 disk and non-disk samples in SINS/zC-SINF at $z \sim 2$ by N. M. Förster Schreiber et al. (2018). Similarly, S. Gillman et al. (2021) found no difference in the metallicity gradients between morphologically irregular and disk galaxies in a sample of ≈ 650 SFG(s) at $z \sim 1$, albeit based on HST data available at the time.

The lack of a strong distinction between disks and non-disks in our sample may be attributed to the ambiguous nature of non-disks, as discussed in L. L. Lee et al. (2025b). Non-disks could be potential mergers or disks with strong non-circular motions that are not resolved with the current data quality. The merger stage for the former scenario is largely unknown, while the latter scenario would make non-disks less distinct from disks.

Furthermore, the overall high molecular gas fraction ($f_{\mathrm{gas}} = M_{\mathrm{gas}}/(M_{\mathrm{gas}} + M_{\star}) \gtrsim 50\%$) of the sample with little systematic difference between disks and non-disks (L. L. Lee et al., 2025b) imply rapid and efficient inward gas streaming from the pristine circum-galactic medium (CGM) and inter-galactic medium (IGM), as well as minor mergers, which feed the galaxy to maintain a large gas fraction (e.g. L. J. Tacconi et al., 2020). As discussed in Sect. 4.5.1, the gas-rich nature of these systems could induce efficient formation of clumps, and their migration and further gas inflow driven by tidal torques exerted on the gas could flatten metallicity gradients. Nevertheless, observational evidence remains unclear on whether the clumps can actually survive this migration (A. Claeyssens et al., 2025; B. S. Kalita et al., 2025).

Further supporting the above picture is the growing evidence for rapid radial gas inflow ($v_{\rm inflow} \approx 50\,{\rm km\,s^{-1}}$) in star-forming disks at $z \sim 2$ (R. Genzel et al., 2023; S. Huang et al., 2025; S. Pastras et al., 2025, C. Pulsoni et al., in prep.). This would imply material migrates over a flow (dynamical) time of < 100 Myr, much shorter than that of local disks. Because this inflow timescale is shorter than, or at best comparable to, the gas-consumption (star-formation) timescale ($\lesssim$ Gyr, L. J. Tacconi et al., 2020), relatively small in-situ metal enrichment can occur during a single episode of inward transport. Consequently, these galaxies are expected to develop relatively flat metallicity gradients, and with little azimuthal variations (A. C. Petit et al., 2015), which we will investigate further in Sect. 4.5.3.

Comparable gradient flattening could also take place in interacting and merging systems at all epochs, where tidal torques likewise drive efficient radial gas mixing (e.g. D. S. N. Rupke et al., 2010b; K. V. Croxall et al., 2015; X. Wang et al., 2019; G. Venturi et al., 2024). Hence, both high-redshift gas-rich disks and mergers may share a common, rapid, large-scale gas redistribution that suppresses steep abundance gradients.

The high gas fraction at $z \sim 5$ also sustain elevated star-formation rates compared to the local Universe. The ensuing strong stellar feedback launches outflows that could redistribute metals into the outer disk (B. K. Gibson et al., 2013; H. Übler et al., 2014; P. B. Tissera et al., 2022). Subsequent re-accretion of this material, together with turbulent mixing, is expected to further moderate radial variations in chemical composition, which could ultimately diminish the difference between disk and non-disk galaxies at $4 < z < 6$.

4.5.3 Azimuthal variations

As found in many $z \sim 1-3$ galaxies, metallicity distribution is often very irregular, with considerable local variations even on kpc scales (e.g. N. M. Förster Schreiber et al., 2006, 2018; S. Gillman et al., 2022), as well as in simulations (M. A. Bellardini et al., 2021). These irregularities may reflect the non-symmetric processes such as chaotic accretion, feedback, gravitational instabilities and transport processes during these early galaxy evolution phases. The presence of more metal-poor clumps or unresolved small companions will also introduce local variations in metallicities. Hence, averaging large azimuthal variations into the same radial bins could wash out such features and result in an apparently flat radial gradient.

To quantify the azimuthal variations in our sample, we apply the same procedure used for the annular-binned profile in Sect. 4.4, but on a spaxel-to-spaxel basis. We select only those pixels where the line ratios exceed the 2.5σ limit (see Sect. 8.3 of N. M. Förster

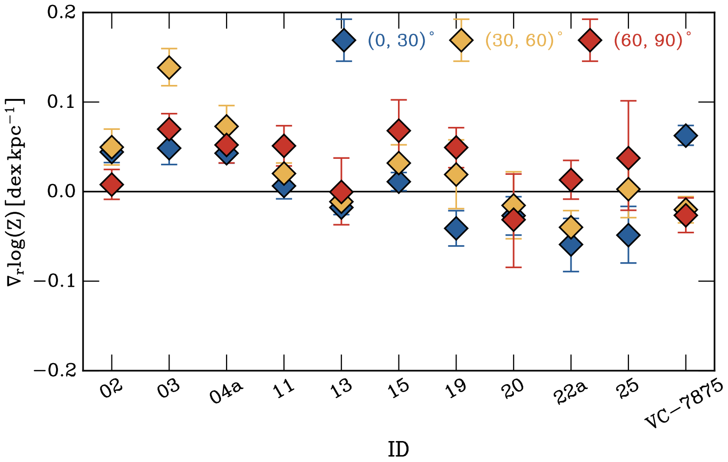

Figure 4.7 Metallicity gradients inferred in three azimuthal bins: $[0°, 30°)$ (blue), $[30°, 60°)$ (yellow), and $[60°, 90°)$ (red).

Schreiber et al. 2018), which implies the line flux of the fainter line (e.g. Hβ in R3) must also exceed 2.5σ. For this analysis, we focus on oxygen-based diagnostics (e.g. O32) if available, which typically have higher S/N and larger radial coverage. For CRISTAL-06a and 06b, only N2 is available. The Fig. 4.2 shows the per-pixel metallicities profile for our sample, the data points are colour-coded by their acute azimuthal angle difference relative to the position angle of the morphological major axis ($\Delta\phi = |\phi - \phi_{\rm maj}|$).

We then fit the metallicity gradients for pixels within an azimuthal bin of $\Delta\phi = 30°$, dividing the galaxies into three bins spanning $[0, 90]°$. Out of the 20 galaxies in our sample, 11 have sufficient pixels within an azimuthal bin for this measurement. Fig. 4.7 presents the distribution of metallicity gradients for the 11 galaxies in each azimuthal bin, and Table 4.6 summarises the values. The scatter among the azimuthal-binned values around their mean values is relatively low, averaging 0.02 dex kpc $^{-1}$, with a maximum scatter of 0.04 dex kpc $^{-1}$ observed for CRISTAL-03, 19, 25 and VC-7875, which is still smaller than the typical measurement uncertainties of the annular-binned gradients of $\sim$0.06 dex kpc $^{-1}$ from Method I in Sect. 4.4

Comparing the mean difference between the azimuthally-binned above and annular-binned metallicity gradients inferred from Method I, we find that none of the galaxies show a significant deviation from the annular-binned metallicity gradient, with no galaxies showing a mean difference exceeding 3σ. Only four galaxies (CRISTAL-03, 04a, 13, and VC-7875) show a difference at 1σ level, indicating there could be mild azimuthal variations these cases, given the uncertainties of this pixel-based method.

To assess the azimuthal variation in the whole sample, especially in cases where the

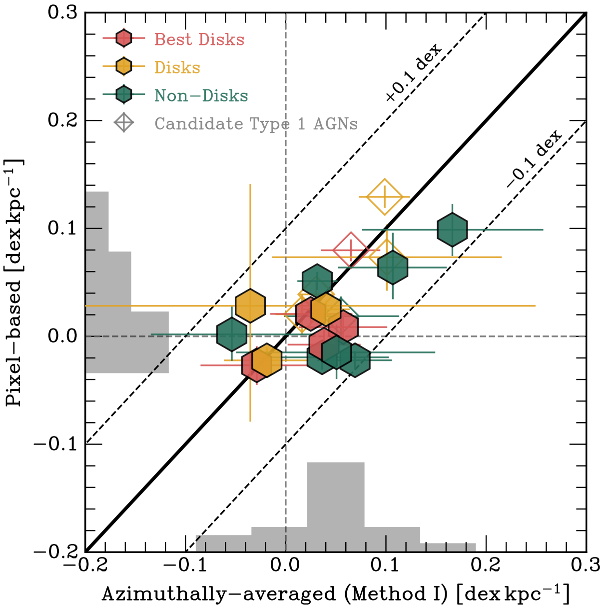

Figure 4.8 Comparison between the azimuthally-averaged (from Method I) and pixel-based metallicity gradients. The disks and non-disks classified in L. L. Lee et al. (2025b) are shown in pink/yellow and green, respectively. The candidate Type-1 AGNs identified in Ren et el. (2025) are marked with the diamond symbol.

azimuthal binning method above could not be applied, we fit the radial profile of these per-pixel metallicities in the full azimuthal range, following e.g. N. M. Förster Schreiber et al. (2018), using the same procedure as Method I in Sect. 4.4. The derived gradients are presented in Fig. 4.2 on the right of each panel. Fig. 4.8 compares the gradients from Method I and the pixel-based metallicity profiles derived here.

In all cases, the two profiles agree within 1σ, indicating that there are generally no strong azimuthal variations in the radial profiles. The pixel-based metallicity gradients are only slightly flatter than those derived from azimuthal averaging, with a mean $\nabla_r \log(Z)$ of $+0.027 \pm 0.007\,\mathrm{dex\,kpc}^{-1}$, compared to $+0.043 \pm 0.019\,\mathrm{dex\,kpc}^{-1}$, with a marginal difference of $\approx 1\sigma$. Such small discrepancy could be attributed to several factors, including the different radial coverage of the azimuthally-averaged and pixel-based metallicity gradients, and the inherently light-weighted nature of the azimuthally-averaged method.

Overall, we do not find strong azimuthal variations that are statistically significant above the measurement uncertainties. However, six galaxies, namely CRISTAL-03, 04a, 13, 19, 25, and VC-7875, exhibit slightly stronger azimuthal variations compared to the rest of the sample. CRISTAL-03 was identified by W. Ren et al. (2025) as candidate Type-1 AGN because their spectra exhibit broad Balmer components. In their BPT diagrams, however, it lies around the star-forming/composite locus, showing no significant excess of hard ionising photons. CRISTAL-04a is in an interacting system with CRISTAL-04b (L. L. Lee et al., 2025b), and similarly for VC-7875, which is a disturbed disk galaxy, as identified by S. Fujimoto et al. (2020), and further supported by JWST NIRCam imaging data that it is part of an interacting system. CRISTAL-13 may also be an interacting system, comprising two distinct components: one characterised by older, smooth stellar populations, and the other populated by young stellar clumps (Fig. 13 in R. Herrera-Camus et al., 2025, see also N. E. P. Lines et al. 2025). For CRISTAL-25, J. Li et al. (2024b) suggested the potential presence of a Type 1 AGN based on NIRCam broadband photometry, which hinted at an excess of flux from the broad component of [Mg II] $\lambda2798$ and Hβ+[O III] $\lambda5007$. However, our G235M data are unable to confirm this due to the low S/N of Hβ+[O III] (even [O III] $\lambda4959$ is barely detected), and [Mg II] being shifted out of the spectral coverage. For CRISTAL-19, a disk system, the origin of the mild azimuthal variation is unclear.

The overall lack of strong azimuthal variations is also found in some studies in the local Universe (K. Kreckel et al., 2020), which, despite having much better statistics based on over hundreds of H II regions, report RMS scatter of $\lesssim 0.05\,\mathrm{dex}$ after removing the large-scale gradient, suggesting a high level of chemical homogeneity over large spatial scales. T. G. Williams et al. (2022) also finds no clear systematic enrichment in the spiral arms, which is somewhat unexpected, given that the primary source of oxygen is Type II supernovae, which are typically more densely populated along the spiral arms.

The lack of azimuthal variations in disks could be explained if the turbulent mixing timescale is much shorter than the orbital time required for differential rotation to wind non-axisymmetric abundance patterns into tight spirals. The resulting shear-mixing could therefore erase most of the contrast, resulting in the weak azimuthal scatter observed at fixed galacto-centric radius (C.-C. Yang & M. Krumholz, 2012). Given that the disk galaxies in our sample have higher velocity dispersions, averaging $\sim 70\,\mathrm{km\,s^{-1}}$, than local disks, the turbulence-driven mixing is likely even more efficient, which could explain the absence of strong azimuthal variations.

Nevertheless, we are cautious that observational limitations may also explain why the majority of the galaxies do not exhibit a large azimuthal variation in metallicities. A single pixel in the NIRSpec IFU of size $0\farcs1$ corresponds to a physical scale of 0.5–0.7 kpc at redshifts $z = 4$ to 6. Because our observations employ only the standard 2-point dither pattern (with the exception of CRISTAL-01, 20 and 22a see S. Fujimoto et al., 2025; G. C. Jones et al., 2025; E. Parlanti et al., 2025), the data provide only modest sub-pixel sampling. It is further exacerbated by the limited angular resolution of a similar order, which altogether limits our view to the non-axisymmetric features that may bring about local metallicity variations, such as clumps (e.g. X. Wang et al., 2017; V. Estrada-Carpenter et al., 2025; V. Sok et al., 2025, E. Parlanti et al., in prep.) and spiral arms, which have been observed in some other local studies (F. P. A. Vogt et al., 2017; F. Bresolin et al., 2025) and simulations (E. Spitoni et al., 2019; M. E. Orr et al., 2023). Hence, it is difficult to confirm or rule out the presence of these features as drivers of metallicity variations (R. Genzel et al., 2011; S. F. Newman et al., 2012; S. Khoperskov et al., 2023) within the physical scales probed by our current data.

4.5.4 Mass and sSFR

A positive correlation between sSFR and radial metallicity gradients was identified by studies of SFG(s) at cosmic noon (e.g. J. P. Stott et al., 2014; E. Wuyts et al., 2016; M. Curti et al., 2020a). A negative correlation with $M_\star$ (e.g. E. Wuyts et al., 2016; X. Wang et al., 2020; Y. Cheng et al., 2024, but see also Z. Li et al. 2025b for $M_\star \lesssim 10^9 M_\odot$ at $z > 6$) has also been found. In general, these studies found that low-mass and high-sSFR galaxies tend to have flatter to even positive gradients, as shown in Fig. 4.9. This may be due to the higher mass loading of starburst-driven galactic winds at early times in those low-mass systems, which eject metal-enriched gas from galaxy centres and may deposit it at larger radii. In simulations, this is attributed to efficient feedback in such systems, which keeps them in the 'bursty' star formation mode (X. Ma et al., 2017).

We cannot confirm any significant trends between metallicity gradients and $M_\star$ or sSFR in our sample, with low Kendall's τ correlation coefficients ($\tau \lesssim 0.15$, $p \gg 0.05$). We do not observe any significant correlation with the surface density of star formation, $\Sigma_{\rm SFR}$ either. Even when combining our sample with literature samples compiled at $z > 3.0$ (Table 4.8), which extend to lower stellar masses ($\log(M_\star/M_\odot) < 9.0$) and higher sSFR values ($\log(\mathrm{sSFR/yr^{-1}}) \gtrsim -8$), the negative and positive trends with $M_\star$ and sSFR, respectively, are only marginally stronger. However, the statistical significance of these trends remains weak, as indicated by the low Kendall's τ values and high p-values annotated in Fig. 4.9.

Comparing our results with cosmological simulations, the lack of a trend between $\log(M_\star)$ and metallicity gradient is not entirely unexpected. At $z \leqslant 2.5$, both the FIRE (X. Ma et al., 2017) and FIRE2 (X. Sun et al., 2025) simulations found very shallow to no correlation with $\log(M_\star)$. Given the uncertainties present in our data and the literature, constraining a weak trend like this remains challenging. Although our results show a better match with the EAGLE simulation within the mass range of our sample, the relationship with $M_\star$ is not well reproduced for the literature-compiled sample at $z \geqslant 3$ across a broader

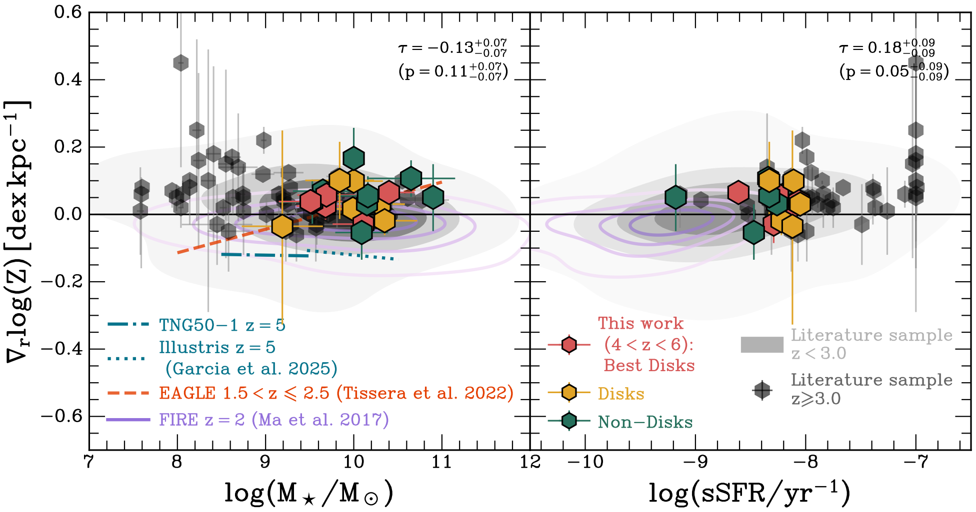

Figure 4.9 Observed metallicity gradients as a function of $M_\star$ (*left*) and specific star formation rate (sSFR, *right*). The literature samples at $z < 3.5$ and $z \geqslant 3.5$ are represented by black contours and black hexagons, respectively. The references for the literature sample are listed in Table 4.8. Predictions from the cosmological simulations TNG50-1 and Illustris (A. M. Garcia et al., 2025) are plotted as dot-dashed and dotted blue lines, respectively. Additionally, we show the trends from other simulations at $z \approx 2$, including EAGLE (P. B. Tissera et al., 2022) as an orange dashed line (*left* only) and FIRE (X. Ma et al., 2017) as purple contours. The values from FIRE2 (X. Sun et al., 2025) are within the FIRE contours, therefore not plotted. The Kendall's τ correlation coefficient and the p-value for the combined distribution of our sample and the literature sample are annotated in the top right corner of each panel.

mass range, particularly at the low-mass end. However, studies by P. B. Tissera et al. (2022) (EAGLE) and Z. S. Hemler et al. (2021) (TNG) do suggest that lower-mass galaxies exhibit greater fluctuations, and our current limited sample may be too small to capture the full scatter. A more recent study by A. M. Garcia et al. (2025) found that the TNG50-1 and Illustris simulations at $z = 5$ capture the flat dependence on $M_{\star}$, but predict an overall more negative gradients than our observed results for our mass range.

4.6 Effects of beam smearing

The observed shallow gradients in our sample could be partly caused by observational effects (T. T. Yuan et al., 2011; S. Wuyts et al., 2016; D. Carton et al., 2018; A. Acharyya et al., 2020). Convolution of the intrinsic line flux distribution with the PSF acts as a spatial blurring kernel that reduces local contrast and any kind of gradients would be suppressed and appear shallower, an effect known as beam smearing. Intuitively, the steeper the intrinsic gradient and the broader the PSF relative to the size of the galaxy, the stronger the flattening. To the extreme, for a flat gradient, beam smearing has no effect.

To quantify the beam-smearing effect and understand the impact on our measurements, we generate 1500 mock galaxies with a given intrinsic metallicity gradient ranging between $\nabla_r \log(Z) \in [-0.2, +0.2]\,\mathrm{dex\,kpc}^{-1}$. The mock data cubes are built out of exponential disk models using `DysmalPy`[5] (R. I. Davies et al., 2004a,b; G. Cresci et al., 2009; R. Davies et al., 2011; S. Wuyts et al., 2016; P. Lang et al., 2017; S. H. Price et al., 2021; L. L. Lee et al., 2025a) with parameters listed in Table 4.4. Since the purpose here is to test the effect of beam-smearing on metallicity gradient, we set the mass model to $\log(M_{\rm bary}/M_{\odot}) = 10.5$, where $M_{\rm bary}$ is the total baryonic mass, and $R_{\rm e,disk} = 2\,\mathrm{kpc}$ which are representative of the galaxies in our sample (R. Herrera-Camus et al., 2025). We do not vary these physical properties for the mock models, but vary only the ratio of the effective radius to that of the beam size, as well as the S/N ratio. The inclination is fixed at 20° because, as demonstrated by S. Wuyts et al. (2016), in practice, the ellipticity of the apertures is typically tailored to match the observed isophotes, and hence variations with respect to inclination is less relevant.

We add [O II], [Ne III], Hβ and [O III] line emissions assuming a linear radial gradient (Eq. 4.1), such that the line intensity of Hβ, [O II] and [Ne III] relative to [O III] are controlled via the R3, O32 and Ne3O2 relations listed in Table 4.2, assuming the spectra have already been de-reddened. The light profile follows that of an exponential disk (Sérsic

---

[5] `https://www.mpe.mpg.de/resources/IR/DYSMALPY`

Table 4.4. Parameters of mock data cubes at $z = 5$

Parameter	(Range of) Value
$\log(M_{\rm bary}/M_\odot)$	10.5
$R_{\rm e,disk}$ (kpc)	2
σ_0 (km s^{-1})	80
$\sigma_{\rm LSF}$ (km s^{-1})[a]	125
beam$_{\rm FWHM}$	0″.1–1″.0
$2 \times R_{\rm e,disk}/{\rm beam}_{\rm FWHM}$	0.6–6.4
S/N[b]	20–40
Pixel scale	0″.05
$\nabla_r \log(Z)$ (dex kpc^{-1})	$[-0.20, +0.20]$
Inclination	20°

[a] In σ.

[b] Average per-pixel S/N within an effective radius of the channel of the brightest line.

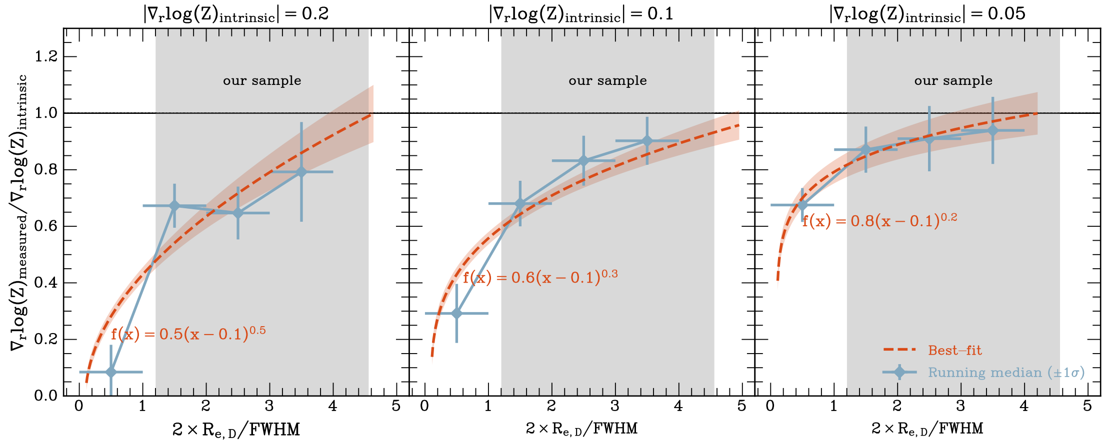

Figure 4.10 Ratio of the measured ($\nabla_r \log(Z)_{\rm measured}$) vs. intrinsic ($\nabla_r \log(Z)_{\rm intrinsic}$) metallicity gradient for a set of mock exponential disk models imprinted with a linear intrinsic gradient ranging from $\pm[0.05, 0.10, 0.20]$ dex kpc^{-1}(from right to left) as a function of $2 \times R_{\rm e,disk}/{\rm beam}_{\rm FWHM}$. The orange dashed line denotes the best-fit polynomials through the distribution, with the functional form annotated. The light blue curve shows the running median through the same distribution. The vertical grey band indicates the range of $2 \times R_{\rm e,disk}/{\rm beam}_{\rm FWHM}$ spanned by our data. We infer the correction factor by inverting the orange curves for different intrinsic gradients. The median $2 \times R_{\rm e,disk}/{\rm beam}_{\rm FWHM}$ of our sample is 2.5.

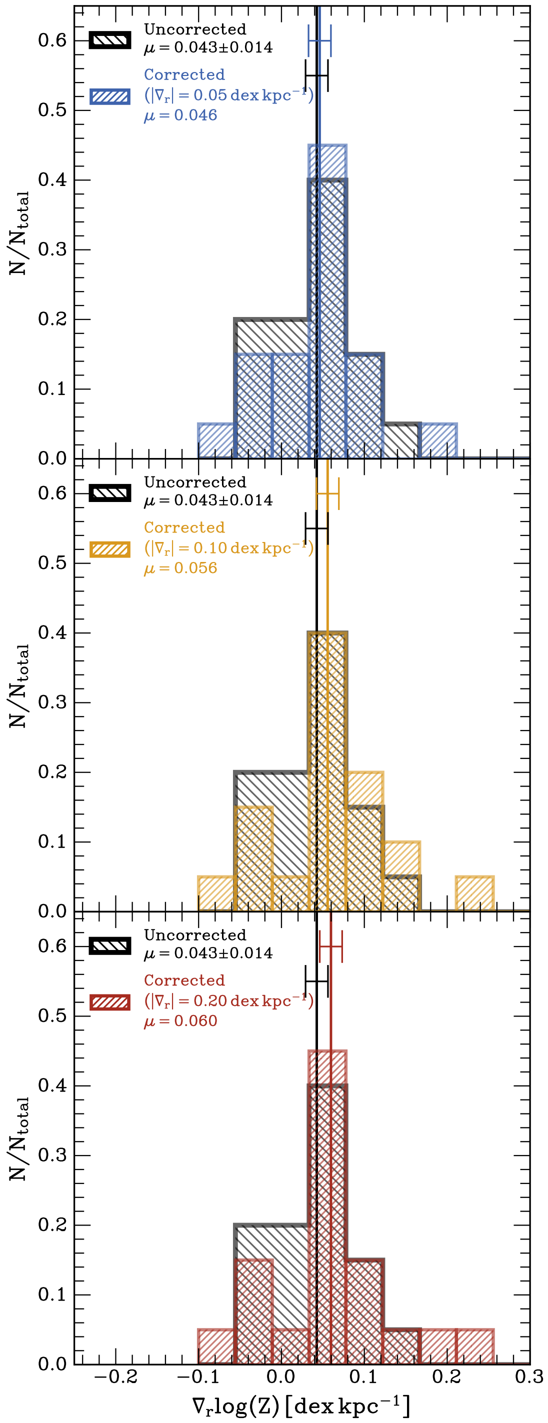

Figure 4.11 Distributions of the observed metallicity gradients, as well as the corrected gradients obtained by applying correction factors derived from correction curves that assume different intrinsic metallicity gradients presented in Fig. 4.10. The error of the mean of the gradients is indicated by the horizontal error bar. Note that the error of the mean will not change after beam-smearing correction is applied.

index = 1). The central metallicity Z_0 is chosen such that over the extent of the profile, $\log_{10} Z(r)$ falls within the valid range of R3, O32 and Ne3O2 as listed in Table 4.2.

The cubes are convolved with a PSF of varying sizes, such that the galaxy extent in diameter ($2 \times R_{\mathrm{e,disk}}$) is covered by 0.6 to 6.4 beams in FWHM ($\mathrm{beam}_{\mathrm{FWHM}}$). The intrinsic effective radii of our galaxies range from $0\farcs11$ to $0\farcs40$, measured from `imfit` modelling of the F444W photometry (L. L. Lee et al., 2025b).[6] We assume that the line emission follows the stellar light traced by the F444W continuum. Therefore, for our data, $2 \times R_{\mathrm{e,disk}}/\mathrm{beam}_{\mathrm{FWHM}} \sim 2.5$ (median), with a range of ~ 1.2–4.5.

The cubes are also convolved with a LSF kernel of size (in σ) $125\,\mathrm{km\,s^{-1}}$ ($1.28 \times 10^{-3}\,\mu$m), corresponding approximately to the spectral resolution of the $R \sim 1000$ NIRSpec IFU at the observed wavelength of [O III] ($\sim 3\,\mu$m). The channel width is fixed at $106\,\mathrm{km\,s^{-1}}$. The pixel scale is set to $0\farcs05\,\mathrm{pix}^{-1}$ (compared to $0\farcs1\,\mathrm{pix}^{-1}$ in the NIRSpec data) to sample the smaller PSF in some of the mock cubes. This finer pixel scale is chosen to avoid the undesirable situation where the pixel size is larger than the smallest beam FWHM. Since the axis ratios of the actual PSF $\gtrsim 0.9$, the PSF shape of the mock cubes is set to be circular. To simulate a range of S/N covered by our data and slightly beyond to recover trends, we add Gaussian noise to the data cubes, resulting in average per-pixel S/N values of 20 to 100 within the effective radius of the brightest channel of the [O III] λ5007 emission line. Such definition of S/N means that the [Ne III] λ3869 line may be undetected in some of the mock cubes, particularly those with high metallicity. In such cases, we exclude the use of the Ne3O2 diagnostic to recover the metallicity, as in our treatment of the actual data.

We then repeat the spectral line fitting and derive the azimuthally-averaged metallicity gradients of the mock data cubes following the same procedure in Sect. 4.3 and Sect. 4.4, respectively. The resulting distributions of the recovered versus the intrinsic metallicity gradients as a function of $2 \times R_{\mathrm{e,disk}}/\mathrm{beam}_{\mathrm{FWHM}}$ is shown in Fig. 4.10.

As expected, we find a positive correlation between the number of beams covering a galaxy and the accuracy of the recovered intrinsic metallicity gradient. Additionally, there is a secondary dependence on the intrinsic metallicity gradient, as evidenced by the shallower correlation when the intrinsic gradient is $0.05\,\mathrm{dex\,kpc}^{-1}$ in absolute value, compared to $0.2\,\mathrm{dex\,kpc}^{-1}$. This suggests that a shallower intrinsic gradient is less affected by beam smearing, consistent with the findings of E. Wuyts et al. (2016). We do not observe a substantial difference in the correlation between the sign (negative vs. positive) of the gradients for a fixed magnitude. Furthermore, we find no strong dependence on S/N, which

---

[6] For CRISTAL-10a-E, in which F444W is unavailable, we measure the effective radius from the Hα line map.

only affects the uncertainties and scatter, which is also reported by E. Wuyts et al. (2016) and S. Gillman et al. (2021).

To quantify the correlation between the measured and intrinsic metallicity gradients, we fit a polynomial to the relationship between $\nabla_r \log(Z)_{\rm measured}/\nabla_r \log(Z)_{\rm intrinsic}$ and $2 \times R_{\rm e,disk}/{\rm beam}_{\rm FWHM}$. The resulting fit is a reasonably good match to the running medians of the distribution, as shown in Fig. 4.10.

We can then invert the best-fit polynomials to derive a 'correction factor' based on the $2 \times R_{\rm e,disk}/{\rm beam}_{\rm FWHM}$ ratio of an individual galaxy. Since the correction factor also depends on the unknown intrinsic metallicity gradient, we report the corrected gradients in Table 4.7 for the range of $|\nabla_r \log(Z)_{\rm intrinsic}| = [0.05, 0.2]$ that we have examined. For our data, the correction factors as we defined, $\nabla_r \log(Z)_{\rm measured}/\nabla_r \log(Z)_{\rm intrinsic}$, for $|\nabla_r \log(Z)_{\rm intrinsic}| = [0.05, 0.10, 0.20]$ range across $[0.8, 1.0]$, $[0.6, 1.0]$ and $[0.5, 1.0]$, respectively. It is an interesting ancillary finding that, regardless of the intrinsic steepness of the gradients, the correction factors all asymptotically approach unity when the ratio of $2 \times R_{\rm e,disk}/{\rm beam}_{\rm FWHM}$ reaches ~ 5. In other words, one should aim for an angular resolution of this order to determine the intrinsic gradient that is not compromised too much by beam smearing.

After applying these correction factors, we find that the corrected metallicities remain largely consistent with a flat gradient, as found previously in Sect. 4.4, with a maximum correction of up to 20% (mean $\sim$10%) correction needed. For the 16/20 galaxies that exhibit positive metallicity gradients, applying the correction factors derived from an intrinsic gradient of $|\nabla_r \log(Z)_{\rm intrinsic}| = 0.05\,{\rm dex\,kpc}^{-1}$, we find that none of the galaxies have a metallicity gradient of $\nabla_r \log(Z) > +0.05\,{\rm dex\,kpc}^{-1}$ at 3σ level, and only three galaxies (CRISTAL-01a, 07a, and 07b) have gradients at 1σ, consistent with the uncorrected results presented in Sect. 4.4. Even when applying the most extreme correction, assuming an intrinsic gradient of $|\nabla_r \log(Z)_{\rm intrinsic}| = 0.2$, none of the galaxies have a metallicity gradient of $\nabla_r \log(Z) > +0.2\,{\rm dex\,kpc}^{-1}$. For the 4/20 galaxies that exhibit negative metallicity gradients, their gradients remain consistent with a strictly flat metallicity gradient ($\nabla_r \log(Z) = 0\,{\rm dex\,kpc}^{-1}$) within their 1σ uncertainty, regardless of the assumed intrinsic gradient. Fig. 4.11 presents the distributions of the corrected metallicity gradients, along with their mean values and the error of the mean, assuming different intrinsic gradients.

The investigation presented here demonstrates that, regardless of sign, the intrinsic metallicity gradients are unlikely to be extreme. This finding suggests that the intrinsic metallicity gradients of these galaxies are likely to be flat, rather than being solely an artefact of observational effects such as beam smearing.

Nevertheless, we note that our first-order beam-smearing correction has several caveats.

First, we assume a smooth linear gradient when imprinting the mock data cubes, but observations of nearby galaxies have shown that their metallicity gradients may not be strictly linear. Instead, many local disks exhibit a double-linear slope within $\sim 2R_\mathrm{e}$ (from P. Martin & J.-R. Roy 1995 to more recent IFU studies L. Sánchez-Menguiano et al. 2018; B. Easeman et al. 2022; A. F. S. Cardoso et al. 2025), but evidence at higher redshifts is still lacking. Furthermore, high-z disks are often characterised by actively star-forming clumps, which could introduce local metallicity irregularities (e.g. X. Wang et al., 2017; V. Estrada-Carpenter et al., 2025; V. Sok et al., 2025), and light-weighting effects distinct from those for our assumed exponential disk profiles, in addition to other mechanisms that would give rise to local variations as discussed in Sect. 4.5.3, that a smooth gradient as a function of galactic radius only cannot capture.

4.7 Summary

In this work, we analysed the gas-phase oxygen abundance (metallicity) gradients of 20 MS SFG(s) at $4 < z < 6$ using JWST/NIRSpec IFU at $\sim 1\,\mathrm{kpc}$ resolution. We measured the metallicity at each radial position using the strong-line method with T_e-based metallicity calibration (R. L. Sanders et al., 2025), leveraging the multiple optical emission lines available, from [O II] $\lambda\lambda 3726, 29$ to [S II] $\lambda\lambda 6716, 33$. We find the metallicity gradients across the sample are consistent with a flat gradient, with only three galaxies showing a gradient $> 0.05\,\mathrm{dex\,kpc}^{-1}$ at only 1σ level (Sect. 4.4). We do not find a significant systematic offset in the metallicity gradients inferred from different line diagnostics and the Bayesian approach could tighten the overall constraint on the metallicity (Sect. 4.4). We then examined the correlations between the metallicity gradient, kinematic properties, and other physical properties. We find the following:

1. By combining our disk sample with literature data, our study effectively increases the number of available samples at $3 \leqslant z \lesssim 8$ by 50% within the comparable mass range. The combined data set reveals a shallow yet statistically significant negative relationship between metallicity gradients and V_rot/σ_0, but not with σ_0 This trend is consistent with the reported cosmic evolution of metallicity gradients, which become progressively more negative from early to recent epochs (S. Fujimoto et al., 2025, and references therein). Fundamentally, our results suggest that the dynamical maturity of a galaxy disk, as indicated by V_rot/σ, plays a crucial role in shaping the radial metallicity gradients (Sect. 4.5.1).

2. There is no strong distinction between disks and non-disks; this could be due to the frequent accretion events and efficient gas transport at $z \sim 5$ as implied from their high gas fraction (Sect. 4.5.2).

3. The majority of our galaxies do not exhibit significant azimuthal variations, which may be attributed to the efficient azimuthal mixing in turbulent disks. However, we also acknowledge the potential observational limitations in resolving the physical scales of structures, such as clumps and spirals, that could potentially drive local metallicity variations (Sect. 4.5.3).

4. There is no statistically significant correlation with $M_\star$, and only a marginal positive trend with sSFR, even when combining with literature samples at $z > 3$ of wider range in $M_\star$ and sSFR (Sect. 4.5.4).

5. Applying a beam-smearing correction to our sample, using correction factors derived from a large suite of mock galaxies that mimic the observational sample, indicates that beam smearing can account for a maximum of 20% flattening, and typically only 10%. Given the uncertainties, we rule out very steep metallicity gradients in the sample, regardless of sign (Sect. 4.6).

Overall, the lack of a strong correlation between the metallicity gradients and the kinematic nature and global physical properties, especially the former, may be due to the limited dynamic range of the sample and the substantial scatter in the empirical data. Consequently, this only allows the identification of the steepest trends, while shallower trends, such as those presented here, will require much larger statistics to constrain more robustly. Our study, together with the two other works by A. L. Faisst et al. (2025) and S. Fujimoto et al. (2025), nevertheless provides a homogeneously selected set of MS SFG(s) sample available at $4 < z < 6$ that allows for comparison with gas kinematics properties.

Ideally, future studies should aim at even higher spatial resolution to examine the local metallicity variations on smaller physical scales than resolvable by JWST $\lesssim$ kpc. Gravitational lensing can alleviate some observational limitations, yet strong lensing events are intrinsically rare, especially for sources at $z > 4$, so assembling a statistically significant sample to study at population-level remains challenging. The next-generation IFU, HARMONI, to be equipped on the Extremely Large Telescope (ELT), will offer a significant improvement in capabilities for study at $4 < z < 6$. With a linear spatial resolution ~ 6 times better and at least five-fold higher spectral resolution, HARMONI will enable the study of local metallicity variations at physical scales of < 100 pc, although this will be restricted to rest-frame UV lines blueward of [Ne III] $\lambda3869$ and [O II] $\lambda\lambda3726,29$ at $z \sim 5$ due to atmospheric transmission, which will require additional empirical calibrations for metallicity inference.

ACKNOWLEDGEMENTS

We acknowledge Michele Perna and Francesco D'Eugenio for their work in developing reduction scripts for NIRSpec IFU data. N.M.F.S., J.C. and G.T. acknowledge financial support from the European Research Council (ERC) Advanced Grant under the European Union's (EU's) Horizon Europe research and innovation programme (grant agreement AdG GALPHYS, No. 101055023). H.Ü. acknowledges funding by the EU (ERC APEX, 101164796). Views and opinions expressed are, however, those of the author(s) only and do not necessarily reflect those of the EU or the ERC. Neither the EU nor the granting authority can be held responsible for them. R.H-C. thanks the Max Planck Society for support under the Partner Group project 'The Baryon Cycle in Galaxies' between the Max Planck for Extraterrestrial Physics and the Universidad de Concepción. T.N. acknowledges support from the Deutsche Forschungsgemeinschaft (DFG, German Research Foundation) under Germany's Excellence Strategy – EXC - 2094 - 390783311 from the DFG Cluster of Excellence 'ORIGINS'. M.A. is supported by FONDECYT grant number 1252054, and gratefully acknowledges support from ANID Basal Project FB210003. M.A. and J.M. gratefully acknowledges support from ANID MILENIO NCN2024_112. E.d.C. acknowledges support from the Australian Research Council (project DP240100589). M.B. acknowledges support from the ANID BASAL project FB210003. This work was supported by the French government through the France 2030 investment plan managed by the National Research Agency (ANR), as part of the Initiative of Excellence of Université Côte d'Azur under reference number ANR-15-IDEX-01. R.L.D. is supported by the Australian Research Council through the Discovery Early Career Researcher Award (DECRA) Fellowship DE240100136 funded by the Australian Government. D.R. gratefully acknowledges support from the Collaborative Research Center 1601 (SFB 1601 subprojects C1, C2, C3, and C6) funded by the Deutsche Forschungsgemeinschaft (DFG) – 500700252. M.R. acknowledges support from project PID2023-150178NB-I00 financed by MCIU/AEI/10.13039/501100011033, and by FEDER, UE. D.B.S. gratefully acknowledges support from NSF Grant 2407752. W.W. also acknowledges support associated with program JWST-GO-03950. These observations are associated with programs JWST-GO-03045 and JWST-GO-04265. Support for program JWST-GO-03045 was provided by NASA through a grant from the Space Telescope Science Institute, which is operated by the Association of Universities for Research in Astronomy, Inc., under NASA contract NAS 5-03127. This work is based in part on observations made with the NASA/ESA/CSA James Webb Space Telescope. The data were obtained from the Mikulski Archive for Space Telescopes (MAST) at the Space Telescope Science Institute, which is operated by the Association of Universities for Research in Astronomy, Inc., under NASA contract NAS 5-03127.

SOFTWARE

This work made use of the following Python packages: `Astropy` (Astropy Collaboration et al., 2022), `corner` (D. Foreman-Mackey, 2016), `DysmalPy` (R. I. Davies et al., 2004a,b; G. Cresci et al., 2009; R. Davies et al., 2011; S. Wuyts et al., 2016; P. Lang et al., 2017; S. H. Price et al., 2021; L. L. Lee et al., 2025a), `emcee` (D. Foreman-Mackey et al., 2013), `Matplotlib` (J. D. Hunter, 2007), `Numpy` (C. R. Harris et al., 2020), `pymccorrelation` (P. A. Curran, 2014; G. C. Privon et al., 2020), and `Scipy` (P. Virtanen et al., 2020).

4.8 Appendix A – Inferring metallicity with Bayesian method

In Sect. 4.4, we describe how we derive metallicity using the various diagnostics in Table 4.2 using a Bayesian approach (our Method I). The χ^2 value is computed from the residuals between the observed line ratios and the values predicted by the calibration relations at a given metallicity, and we use the `emcee` ensemble sampler to map the posterior distribution. The metallicity that minimises χ^2 (equivalently, maximises the likelihood for flat priors) is taken as our best-fitting value. Fig. 4.12 shows an example (CRISTAL-19) of the resulting χ^2-$12 + \log(\mathrm{O/H})$ curves, plotted for each diagnostic individually and in combination. The figure demonstrates the advantage of combining multiple diagnostics, which provides greater constraining power than any single diagnostic on its own.

4.9 Appendix B – Metallicity gradients inferred from each diagnostic

As discussed in Sect. 4.4, the line diagnostics we used are not all independent, which would underestimate the uncertainties of the best-fit gradients using the Bayesian approach (Method I). To better estimate the uncertainties and to examine the systematics associated with different line tracers, we alternatively infer the metallicities by simply inverting the

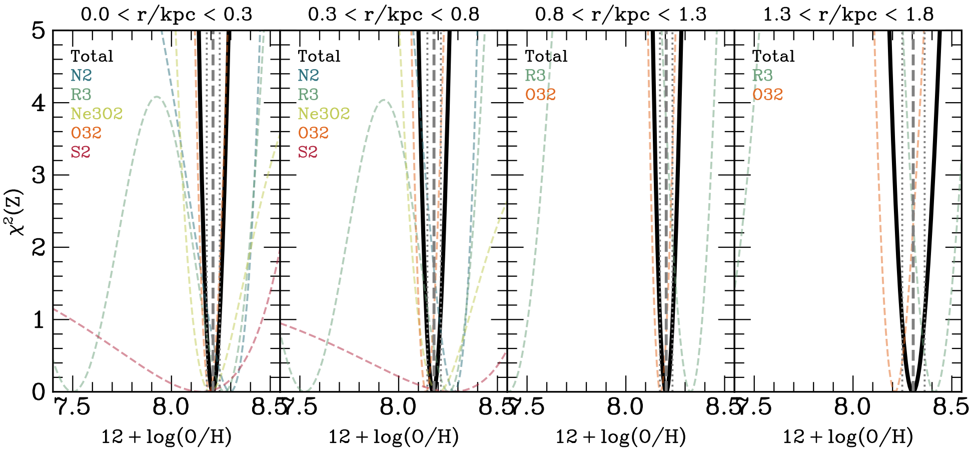

Figure 4.12 Example of the χ^2 landscape as a function of metallicity for CRISTAL-19 for each radial bin. The χ^2 values for each diagnostic are shown as coloured dashed lines, while the total χ^2 from the combined measurements is represented by a black thick curve. The 1σ confidence interval is indicated by two vertical dotted lines, and the best-fitting value is marked with a thick vertical grey dashed line.

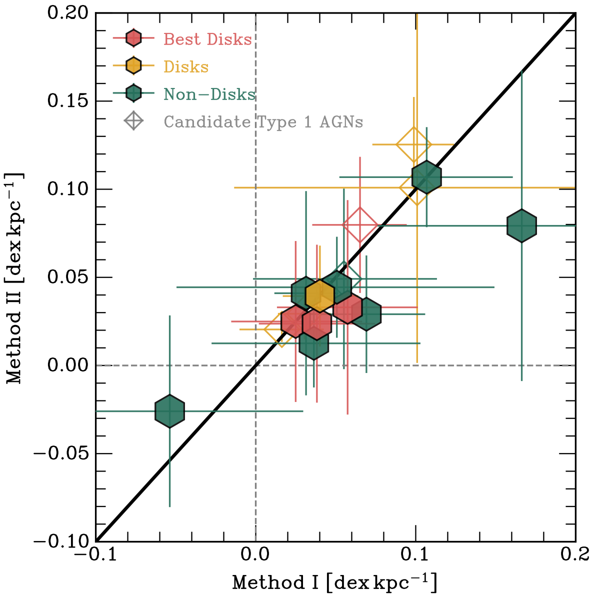

Figure 4.13 Comparison between the metallicity gradients inferred from the Bayesian method (Method I) and the median from Method II. The disks and non-disks classified in L. L. Lee et al. (2025b) are shown in pink/yellow and green, respectively. The candidate Type-1 AGNs identified in W. Ren et al. (2025) are marked with the empty diamond symbol. CRISTAL-06b is not shown because only one diagnostic N2 is used for Method I.

Table 4.5. Metallicity gradients inferred from individual diagnostics.

ID	R3 (dex kpc^{-1})	O32 (dex kpc^{-1})	N2 (dex kpc^{-1})	Ne3O2 (dex kpc^{-1})	S2 (dex kpc^{-1})	O2 (dex kpc^{-1})
01a	...	$0.133^{+0.052}_{-0.052}$	...	...	...	...
02	$0.000^{+0.290}_{-0.282}$	$0.028^{+0.027}_{-0.026}$	...	...	...	...
03	...	$0.123^{+0.057}_{-0.058}$	...	$0.005^{+0.068}_{-0.065}$	...	$0.089^{+0.061}_{-0.060}$
04a	$0.041^{+0.276}_{-0.261}$	$0.088^{+0.024}_{-0.024}$	$0.011^{+0.069}_{-0.068}$	$-0.020^{+0.107}_{-0.100}$	$0.174^{+0.149}_{-0.156}$	...
05a	$0.043^{+0.115}_{-0.116}$	$0.135^{+0.069}_{-0.073}$	$-0.027^{+0.114}_{-0.114}$	...	$0.090^{+0.233}_{-0.234}$	...
06a	...	$-0.104^{+0.081}_{-0.082}$	$0.040^{+0.167}_{-0.166}$	...	...	...
06b	...	...	$-0.035^{+0.285}_{-0.292}$	...	...	...
07a	...	$0.155^{+0.035}_{-0.037}$	$0.070^{+0.127}_{-0.125}$	$0.130^{+0.107}_{-0.113}$	...	$0.122^{+0.070}_{-0.069}$
07b	$0.019^{+0.512}_{-0.512}$	$0.279^{+0.105}_{-0.105}$	$0.048^{+0.155}_{-0.152}$	...	$0.060^{+0.299}_{-0.312}$	...
09	$0.297^{+0.406}_{-0.439}$	...	...	...	...	...
10a-E	$0.013^{+0.372}_{-0.370}$	$0.024^{+0.033}_{-0.032}$	...	...	...	$0.033^{+0.076}_{-0.075}$
11	$-0.046^{+0.462}_{-0.445}$	$0.030^{+0.046}_{-0.046}$	...	...	...	$0.099^{+0.150}_{-0.148}$
13	$0.029^{+0.230}_{-0.224}$	$0.048^{+0.036}_{-0.037}$	$-0.004^{+0.129}_{-0.127}$	...	...	...
14	$0.036^{+0.429}_{-0.426}$	$0.013^{+0.062}_{-0.062}$	$-0.020^{+0.153}_{-0.151}$	...	...	...
15	$-0.056^{+0.317}_{-0.304}$	$0.109^{+0.050}_{-0.052}$	...	...	...	...
19	$0.110^{+0.263}_{-0.263}$	$0.009^{+0.037}_{-0.037}$	...	...	...	...
25	...	$0.059^{+0.092}_{-0.093}$	$0.038^{+0.081}_{-0.081}$	...	...	...
VC-7875	$0.015^{+0.238}_{-0.232}$	$0.039^{+0.030}_{-0.031}$	$0.057^{+0.113}_{-0.125}$	...	$0.103^{+0.245}_{-0.221}$	...

Note. — The outermost radius at which each diagnostic line is measured for each galaxy is annotated in Fig. 4.2. We only fit a gradient when there are more than two data points available for the diagnostic. Fig. 4.14 shows a comparison between these gradients with that inferred from Method I.

calibration relations to find the solution given a line ratio, which we refer to as Method II in Sect. 4.4.

Table 4.5 lists the metallicity gradients derived with Method II for each emission-line diagnostic. Figure 4.14 compares these values with the gradients obtained using Method I. Overall, the two methods agree within 1σ uncertainties. The figure also demonstrates that gradients inferred from a single diagnostic carry relatively large uncertainties, whereas the Bayesian method adopted in Method I provides tighter constraints.

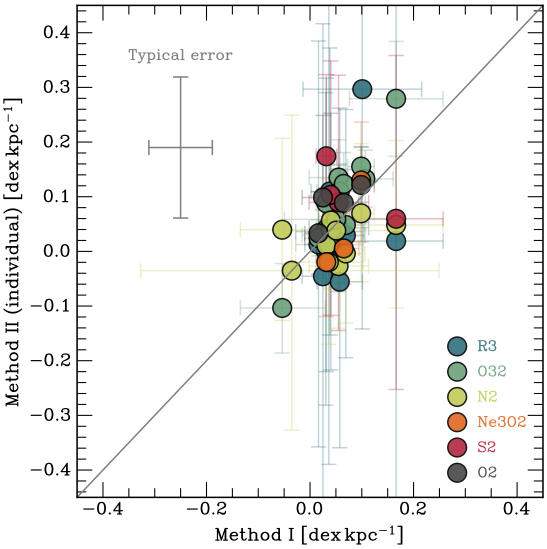

Figure 4.14 Comparison of the metallicity gradients derived from Method I and individual line diagnostics (Method II). The values are listed in Table 4.5. The grey diagonal line is the line of equality. The typical uncertainty is shown at the upper left. The uncertainties associated with individual line diagnostics are large, but combining multiple line diagnostics with the Bayesian approach in Method I can tightens the overall constraints.

4.10 Appendix C – Literature sample

Table 4.8 lists the references from which we compiled the metallicity gradient measurements, as well as kinematics results where available. In most cases, the kinematics results are not presented in the same work as the metallicity gradient measurements. The data were obtained using a variety of instruments, ranging from ground-based to space-based, and from grism (e.g. HST WFC3, JWST NIRCam WFSS) to IFU spectrographs (e.g. SINFONI, OSIRIS, and JWST NIRSpec IFU), with widely varying spatial and spectral resolutions. Furthermore, the metallicities were inferred using different strong-line diagnostics and calibrations, resulting in a heterogeneous dataset. Although the sample is heterogeneous, which is less than ideal, applying a stellar mass cut to select a subsample within the mass range of our sample results in a significantly reduced sample size: only 206 at cosmic noon and 35 galaxies beyond (see Fig. 4.6). Therefore, to maximise the statistics, we have chosen to retain the literature sample as is. However, future work on a more unified sample selection would be highly valuable.

Fig. 4.15 presents the stellar mass distribution of the final mass-matched sample at $z < 3$ and $z \geqslant 3$. The stellar mass distribution of the $z < 3$ sample is generally well-matched with our sample. However, the $z \geqslant 3$ sample skews towards $\log(M_\star/M_\odot) \lesssim 9.4$, which is

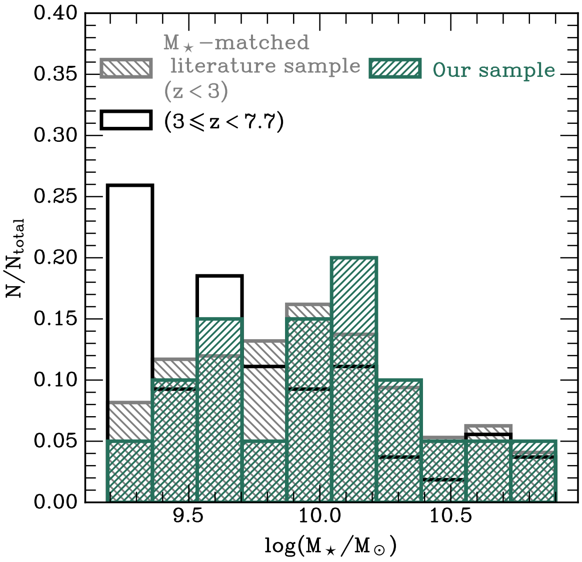

Figure 4.15 Distributions of stellar mass $M_\star$ for literature samples within the mass range of our sample ($z \geqslant 3$ in black, $z < 3$ in hatched grey). The $M_\star$ distribution of our sample is overlaid in hatched green. The peak at $\log(M_\star/M_\odot) \lesssim 9.4$ for the $z \geqslant 3$ sample is primarily contributed by the sources at $z > 6$.

contributed mostly from $z > 6$ galaxies in this redshift range. These high-redshift galaxies are predominantly low-mass sources in the literature.

To maximise statistical coverage in our kinematics measurement, we do not unify the gas phase from which the measurement is taken. As discussed in L. L. Lee et al. (2025b), it remains unclear whether differences exist in σ_0 and $V_{\rm rot}/\sigma_0$ at $z \gtrsim 1$ as traced by different gas phases, due to the heterogeneity of existing samples and measurements. Furthermore, there has been so far little consensus on this issue among studies that have employed multiple tracers for the same object due to limited statistics. Future work would benefit from comparing kinematics from multiple tracers for a consistent set of objects. For ALPINE-CRISTAL-JWST, D. Gomez-Espinoza et al. (in prep.) will present the kinematics of our sample as traced by ionised gas.

4.11 Appendix D – Azimuthally-binned metallicity gradients

To examine the azimuthal variation at a fixed radius, as discussed in Sect. 4.5.3, we binned the pixels within every azimuthal angle range of $\Delta\phi = 30°$, where the azimuthal angle is defined as the acute angle difference from the morphological major axis. The resulting

Table 4.6. Metallicity gradients of 11 galaxies in three azimuthal bins.

ID	$[0°, 30°)$[a] ($\mathrm{dex\,kpc^{-1}}$)	$[30°, 60°)$[a] ($\mathrm{dex\,kpc^{-1}}$)	$[60°, 90°)$[a] ($\mathrm{dex\,kpc^{-1}}$)
02	$0.044^{+0.011}_{-0.012}$	$0.050^{+0.020}_{-0.020}$	$0.008^{+0.017}_{-0.016}$
03	$0.048^{+0.018}_{-0.018}$	$0.138^{+0.021}_{-0.020}$	$0.070^{+0.017}_{-0.018}$
04a	$0.043^{+0.010}_{-0.011}$	$0.073^{+0.023}_{-0.020}$	$0.052^{+0.023}_{-0.020}$
11	$0.006^{+0.015}_{-0.014}$	$0.020^{+0.012}_{-0.012}$	$0.051^{+0.022}_{-0.022}$
13	$-0.018^{+0.008}_{-0.008}$	$-0.011^{+0.011}_{-0.011}$	$-0.000^{+0.038}_{-0.037}$
15	$0.011^{+0.010}_{-0.010}$	$0.032^{+0.020}_{-0.019}$	$0.068^{+0.034}_{-0.035}$
19	$-0.041^{+0.020}_{-0.020}$	$0.019^{+0.039}_{-0.038}$	$0.049^{+0.022}_{-0.023}$
20	$-0.027^{+0.021}_{-0.022}$	$-0.015^{+0.038}_{-0.037}$	$-0.031^{+0.051}_{-0.053}$
22a	$-0.059^{+0.029}_{-0.030}$	$-0.040^{+0.019}_{-0.018}$	$0.013^{+0.022}_{-0.021}$
25	$-0.049^{+0.032}_{-0.031}$	$0.003^{+0.033}_{-0.032}$	$0.037^{+0.064}_{-0.058}$
VC-7875	$0.062^{+0.011}_{-0.011}$	$-0.020^{+0.015}_{-0.015}$	$-0.027^{+0.019}_{-0.019}$

[a] The acute azimuthal angle difference from the major axis.

metallicity gradients for 11 galaxies for each azimuthal bin are summarised in Table 4.6.

4.12 Appendix E – Beam smearing-corrected metallicity gradients

Table 4.7 lists the metallicity gradients that are corrected for beam smearing, based on the correction curves derived in Sect. 4.6. Since the correction factors for a given angular resolution relative to galaxy size depend on the absolute intrinsic unknown gradients, we report the corrected values for a range of assumed intrinsic gradients that we have examined, i.e. $|\nabla_r \log(Z)| = [0.05, 0.10, 0.20]$.

Table 4.7. Metallicity gradients corrected for beam smearing.

ID	$\nabla_r \log(Z)$ $(\lvert\nabla_r \log(Z)\rvert = 0.20)$ (dex kpc^{-1})	$\nabla_r \log(Z)$ $(\lvert\nabla_r \log(Z)\rvert = 0.10)$ (dex kpc^{-1})	$\nabla_r \log(Z)$ $(\lvert\nabla_r \log(Z)\rvert = 0.05)$ (dex kpc^{-1})
01a	0.115	0.120	0.108
02	0.038	0.037	0.032
03	0.094	0.087	0.072
04a	0.049	0.044	0.035
05a	0.071	0.069	0.058
06a	−0.072	−0.068	−0.058
06b	−0.053	−0.049	−0.039
07a	0.135	0.128	0.107
07b	0.234	0.219	0.181
09	0.189	0.159	0.120
10a-E	0.023	0.021	0.018
11	0.040	0.035	0.028
13	0.077	0.079	0.070
14	0.053	0.049	0.040
15	0.062	0.064	0.058
19	0.063	0.055	0.044
20	−0.035	−0.035	−0.030
22a	−0.033	−0.028	−0.022
25	0.105	0.085	0.062
VC-7875	0.043	0.043	0.041

Note. — Similar to Table 4.3, but with beam-correction factors applied based on the correction curves in Fig. 4.11 derived in Sect. 4.6, for different assumed intrinsic metallicity gradients $\lvert\nabla_r \log(Z)\rvert = [0.20, 0.10, 0.05]$ (from left to right).

Table 4.8. Literature sample of metallicity gradients and kinematics

z	Reference (Survey)	Kinematics Reference
$0.1 < z < 3.5$	D. P. Stark et al. (2008)[*]	D. P. Stark et al. (2008)
	J. Queyrel et al. (2012) (MASSIV)	B. Epinat et al. (2012)
	A. M. Swinbank et al. (2012a) (SHiZELS)	A. M. Swinbank et al. (2012a)
	T. Jones et al. (2013)[*]	T. Jones et al. (2013)
	J. P. Stott et al. (2014) (KMOS-HiZELS)[b]	J. P. Stott et al. (2014)
	P. Troncoso et al. (2014) (AMAZE-LSD) (see also G. Cresci et al., 2010)	A. Gnerucci et al. (2011)
	T. Jones et al. (2015) (GLASS-HST)[*]	. . .
	N. Leethochawalit et al. (2016)[a,*]	N. Leethochawalit et al. (2016)
	E. Wuyts et al. (2016) (KMOS$^{\mathrm{3D}}$)	H. Übler et al. (2019)
	J. Molina et al. (2017) (SHiZELS)	J. Molina et al. (2017)
	X. Wang et al. (2017) (GLASS-HST)[*] (see also T. T. Yuan et al., 2011)	E. M. Di Teodoro et al. (2018); J. Hirtenstein et al. (2019); M. Girard et al. (2020)
	D. Carton et al. (2018) (MUSE-WIDE)	P. Sharda et al. (2021b)
	N. M. Förster Schreiber et al. (2018) (SINS/zC-SINF)	N. M. Förster Schreiber et al. (2018)
	M. Girard et al. (2018)[*]	M. Girard et al. (2018)
	V. Patrício et al. (2019)[*]	. . .
	C. E. Sharon et al. (2019)[*]	D. Liu et al. (2023)
	X. Wang et al. (2019) (GLASS-HST)	. . .
	M. Curti et al. (2020b) (KLEVER)[*]	. . .
	X. Wang et al. (2020)[*]	J. Hirtenstein et al. (2019); M. Girard et al. (2020)
	S. Gillman et al. (2021) (KROSS-KGES)	C. M. Harrison et al. (2017); H. L. Johnson et al. (2018); A. L. Tiley et al. (2021)
	R. C. Simons et al. (2021) (CLEAR)	. . .
	S. Gillman et al. (2022) (KURVS)	A. Puglisi et al. (2023)
	X. Wang et al. (2022) (GLASS-JWST)[*]	. . .

Table 4.8 (cont'd)

z	Reference (Survey)	Kinematics Reference
	Z. Li et al. (2022) (MAMMOTH-Grism)	...
	I. Barišić et al. (2025) (MSA-3D)	I. Barišić et al. (2025)
	M. Ju et al. (2025) (MSA-3D)	M. Ju et al. (2025)
$z > 3.5$	P. Troncoso et al. (2014) (AMAZE-LSD)	P. Troncoso et al. (2014)
	S. Arribas et al. (2024) (GA-NIFS)	S. Arribas et al. (2024)
	L. Vallini et al. (2024)	E. Parlanti et al. (2023); A. C. Posses et al. (2023)
	G. Venturi et al. (2024) (JWST GO #1893)[c]	...
	Z. Li et al. (2025b)	...

[a] No stellar mass published for individual objects, we take the approximate median $\log(M_\star/M_\odot) = 9.3$ for the entire sample.

[b] Included the KMOS-HiZELS-SV1 sample from D. Sobral et al. (2013), and we adopt the kinematics results presented therein.

[c] S. Carniani et al. (2021)

[*] Gravitationally lensed.

Chapter 5

Summary and Outlook

This thesis presents a study of the kinematic and chemical properties of star-forming galaxies (SFGs) in the first 1–2 billion years of the Universe's history, featuring extensive modelling tests and data obtained from state-of-the-art facilities both on the ground and in space. The thesis first rests on the foundational aspects of kinematic modelling within the framework of high-redshift observations, drawing on existing knowledge of galaxy properties as revealed by studies at redshifts $z \sim 1$–3. It then explores galaxy evolution at $4 < z < 6$ through the first systematic study of typical SFG(s), utilising state-of-the-art observations of [C II] 158 μm kinematics on kiloparsec scales with the ALMA. Finally, the thesis concludes with the first exploration of metal distribution at these epochs in connection with kinematics.

5.1 Chapter 2 summary

This chapter details the work undertaken to quantify the effects of different methodologies on modelling the kinematics of data cubes from typical high-redshift galaxies, where both angular resolution and S/N ratios are modest. The investigation was realised through a large set of mock galaxies.

The findings indicate that parametric modelling remains the more robust approach for recovering first-order intrinsic kinematics from data cubes with conditions typical of most observations and physically motivated assumptions on mass distribution. In contrast, the high sensitivity of non-parametric tools to S/N, together with their strong tendency to underestimate velocity dispersion when the S/N falls short, warrants careful interpretation of observational data modelled with such methods. This is particularly important when attempting to pinpoint the epoch of disk settling, the drivers of velocity dispersion, and the evolution of disk velocity dispersion with redshift.

The behaviour of different modelling approaches may account for some of the scatter observed in the literature, but not all of it. The residual scatter could be attributed to physical reasons beyond the scope of Chap. 2, but could include the SFR, offset from the main sequence, and sizes.

To mitigate the model dependence and S/N sensitivity of inferred kinematic properties, observations should strive for deeper data and give precedence to a larger sample size to mitigate the model dependence of inferred kinematic properties better. Different modelling approaches converge to consistent results at sufficiently high S/N. Although the results may seem intuitive, this study is the first of its kind to quantify these effects with large statistical significance.

5.2 Chapter 3 summary

As important as the methodologies is the selection of samples. This chapter presents a systematic study of a sizeable sample of typical massive SFG(s) at $4 < z < 6$, utilising the [C II] 158μm line as a kinematic tracer.

Half of the sample is disk-like (morpho)kinematically, which is a lower fraction than that observed at cosmic noon, but still a high proportion given the frequent galaxy-galaxy interactions at $4 < z < 6$. After accounting for observational effects, kinematic modelling of the disk galaxies reveals that they are turbulence-supported, characterised by elevated velocity dispersions. The measured velocity dispersions agree well with the predicted evolution based on Toomre theory and the extrapolated evolutionary trends of galaxies at cosmic noon and lower redshifts, in particular of their gas content.

A tentative correlation is observed between gas content and velocity dispersion. Comparison with analytical models suggests that the high velocity dispersions are likely sustained by gravitational instability, with a subdominant contribution from stellar feedback.

The overall galactic-scale DM fractions are low, but show a large scatter. There is a tentative trend of DM fractions decreases with higher baryon mass surface density, which is in broad agreement with the trend based on studies of cosmic noon galaxies, suggesting similar feedback processes and dynamical heating as well as efficient inward gas transport may be at play to lower the DM content in the inner regions.

5.3 Chapter 4 summary

This chapter investigates the gas-phase metallicity gradients and kinematic nature of the galaxies studied in Chap. 3, supplemented by additional but smaller samples from the literature at the same epoch. The analysis reveals that the metallicity gradients are consistent with a flat gradient, with only a few galaxies exhibiting marginally positive gradients, suggesting efficient metal mixing in these systems. There is however no substantial distinction between disk and non-disk galaxies, which may be attributed to the frequent accretion events and efficient gas transport at $z \sim 5$. Combining with literature data, a tentative trend exists for systems with high velocity dispersion and low $V_{\rm rot}/\sigma$ to exhibit flatter or even slightly positive gradients. The majority of the galaxies sample do not exhibit significant azimuthal variations in metallicity. It could be indicative of the short timescale for mixing processes such as inflow and turbulence. There is no statistically significant correlation between metallicity gradients and $M_\star$ or sSFR. Beam-smearing corrections suggest that angular resolution effects cannot solely explain the flatness of the gradients.

5.4 Outlook

The last two chapters of this thesis illustrate how cutting-edge instruments enable us to unravel the detailed kinematics and chemical abundance distributions of galaxies just 1–2 billion years after the Big Bang, a feat that astronomers in the early 1980s could only have dreamed of. This is an exciting time for studying these early galaxies, and the existing facilities will continue to deliver more exquisite data, in tandem with the ever-improving resolution and sub-grid recipes of cosmological simulations. At the same time, we have the capacity to be more ambitious and strive for more.

Higher angular resolution and deeper data will bring further improvements on many fronts. The constraint on DM fraction will benefit from larger radial coverage of RCs, extending to over three times the disk effective radius, allowing us to probe the region where DM begins to dominate over baryons. The outer regions are also where the effects of beam smearing are minimal if the RCs are about flat. Ultimately, better data will benefit all modelling approaches, whether parametric or non-parametric.

Another crucial piece in the picture is multi-phase (molecular to ionised gas) kinematics for the same set of samples, to chart the full baryon cycle (Fig. 1.7) for typical galaxies at $z > 4$. It will serve as an important input for sub-grid models implemented in cosmological simulations. This is becoming possible with greater synergies between ground-based interferometry, such as ALMA and NOEMA, and space-based IFUs.

In the near future, the next generation IFU instruments mounted on 30–40 m-diameter ground-based telescopes, such as HARMONI on the ELT and IRIS on the Thirty Meter Telescope will deliver diffraction-limited resolution that is over an order-of-magnitude improvement in spatial resolution and spectral resolution compared to current state-of-the-art instrumentation. These future facilities will open up studies on $\sim 100\,\mathrm{pc}$ scale or better across all redshifts. For kinematics, the [O II] $\lambda\lambda 3726, 29$, an ionised gas tracer, is still within reach in the K-band out to $z \sim 5$ from the ground.

Excitingly, next-generation instruments will push spatially resolved stellar-kinematic studies of massive galaxies out to $z > 2$, expanding the current redshift limit at $z \sim 1$ (C. M. S. Straatman et al., 2022; H. Übler et al., 2024c, see also M. Slob et al. 2025 for a slit-based study), bringing them on a par with gas-kinematic studies at the same epoch. As discussed in the Introduction and in Chap. 3, a pressure-support correction is required when gas is used as a kinematic tracer in high-dispersion systems. Equation 1.21 is one way to correct it if one does not know the vertical density profile better. JWST photometry could provide some constraints but would be mostly restricted to edge-on galaxies (T. Tsukui et al., 2025). We could in principle improve the current situation if spatially resolved stellar circular-velocity measurements are available. Because the stellar velocity dispersion is driven purely by the gravitational potential, one can recover V_{circ} by applying stellar-dynamical methods such as Jeans Anisotropic Models (JAM, M. Cappellari, 2008) or orbit-based Schwarzschild models (M. Schwarzschild, 1979). With an independent stellar estimate of V_{circ}, one can determine what fraction of the observed gas velocity dispersion must be attributed to turbulent motions so that the pressure-support correction reproduces the stellar-based V_{circ}. This approach could decompose the gas dispersion into its gravitational and turbulent components. Altogether, we will be better informed about the best way to improve pressure-support correction for gas kinematics at higher redshifts.

Chap. 3 resorts to dust continuum observations to infer molecular gas mass, which in itself is a quantity dependent on metallicity and dust temperature. A more direct measurement of molecular gas from low-J CO lines would be ideal, but this is currently lacking for typical SFG(s) at $z \sim 5$, as such measurements are mostly restricted to luminous quasar host galaxies and SMGs. Detecting CO lines at $z \sim 5$ is deemed borderline impossible due to the bright CMB at $\sim 16\,\mathrm{K}$, which suppresses the brightness contrast of the CO line by a factor of several. Furthermore, the low metallicity of these galaxies implies a lower CO/H_2 ratio, making the CO line even fainter, which is exacerbated by cosmic surface brightness dimming. The Band 1 receiver of ALMA (Fig. 1.13) and the next-generation Very Large Array (ngVLA) offers a potential solution to these challenges (C. M. Casey et al., 2015; C. L. Carilli & Y. Shao, 2018), which could routinely detect and resolve $z > 4$ sources

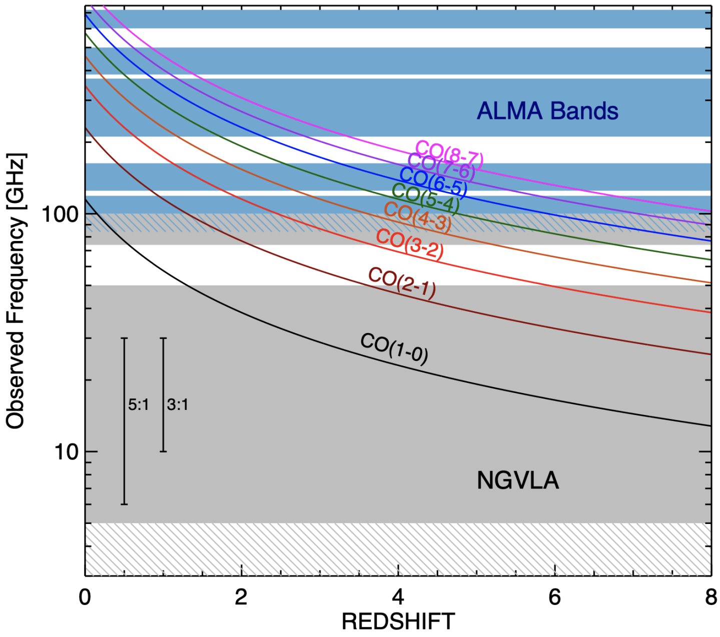

Figure 5.1 Observed frequencies of various transitions of CO at $0 < z < 8$. With the low frequency coverage of ngVLA, the CO(1-0) line would be well within reach for $4 < z < 6$. [Figure adopted from C. M. Casey et al. 2015]

in the CO(1-0) line (but need $T_{\rm gas} > 20\,{\rm K}$) in few tens hour of exposure time (Fig. 5.1).

In the analysis in Chap. 3, the contribution of the neutral hydrogen H I is neglected, because it is expected to be minor relative to molecular gas within the central few scale lengths of early disks, due to the high ISM pressure in $z \gtrsim 1$ SFG(s) with high surface-density. However, direct confirmation with the H I 21 cm emission line of such expectation at $z > 4$ is beyond our technological grip; direct detection of H I in galaxies has been limited to $z \lesssim 0.6$ (I. Heywood et al., 2024; H. Xi et al., 2024), with $z \sim 1$ only achievable through stacking (A. Chowdhury et al., 2020). In the coming years, the Square Kilometre Array (SKA) will extend the redshift frontier for massive SFG(s) more routinely to $z \sim 1$, and through stacking, to $z \gtrsim 4$ galaxies as well.

One aspect that remains almost unexplored in this thesis is the influence of the environment on the kinematics of $z \gtrsim 4$ star-forming galaxies. Addressing it requires a spectroscopic sample that is wide enough to sample the full range of overdensities and nearly complete in redshift so that local-density estimates are reliable. Achieving such completeness was nearly impossible in the HST era: by $z \approx 5$ the strongest rest-frame optical emission lines have redshifted beyond its reddest wavelength coverage through the WFC3/IR grism bandpass; HST slitless spectra were too shallow and heavily contaminated, and the small footprints of ground-based IFU or narrow-band surveys left the number-density and clustering measurements heavily affected by cosmic variance. The capability provided by JWST's Wide-Field Slitless Spectroscopy (WFSS) will make the observational requirement more reachable in the near future. For instance, the COSMOS-3D programme (K. Kakiichi et al., 2024) will deliver contiguous NIRCam-WFSS coverage $0.33\,\mathrm{deg}^2$, yielding >4 000 secure spectroscopic redshifts at $z > 5$. This is roughly an order-of-magnitude leap in our ability to characterise the environment in which these galaxies reside.

In short, this thesis has benefited from data obtained from state-of-the-art space- and ground-based facilities over the past five years. With the forthcoming 30–40 m observatories, which will expand our exploration power, in tandem with the increasingly powerful cosmological simulations bridging our physical understanding, the next decade will usher in a new golden age for unveiling the physics that governs galaxy formation and evolution in the infant Universe on parsec scales.

Bibliography

Abraham, R. G., Tanvir, N. R., Santiago, B. X., et al. 1996 MNRAS, 279, L47, doi: `10.1093/mnras/279.3.L47`

Acharyya, A., Krumholz, M. R., Federrath, C., et al. 2020 MNRAS, 495, 3819, doi: `10.1093/mnras/staa1100`

Acharyya, A., Peeples, M. S., Tumlinson, J., et al. 2025 ApJ, 979, 129, doi: `10.3847/1538-4357/ad9dd8`

Adamo, A., Atek, H., Bagley, M. B., et al. 2025 Nature Astronomy, 9, 1134, doi: `10.1038/s41550-025-02624-5`

Albanese, D., Filosi, M., Visintainer, R., et al. 2012 Bioinformatics, 29, 407, doi: `10.1093/bioinformatics/bts707`

Alloin, D., Collin-Souffrin, S., Joly, M., & Vigroux, L. 1979 A&A, 78, 200

Alloin, D., Edmunds, M. G., Lindblad, P. O., & Pagel, B. E. J. 1981 A&A, 101, 377

Amvrosiadis, A., Lange, S., Nightingale, J. W., et al. 2025 MNRAS, 537, 1163, doi: `10.1093/mnras/staf048`

Arribas, S., Perna, M., Rodríguez Del Pino, B., et al. 2024 A&A, 688, A146, doi: `10.1051/0004-6361/202348824`

Asplund, M., Grevesse, N., Sauval, A. J., & Scott, P. 2009 ARA&A, 47, 481, doi: `10.1146/annurev.astro.46.060407.145222`

Astropy Collaboration, Robitaille, T. P., Tollerud, E. J., et al. 2013 A&A, 558, A33, doi: `10.1051/0004-6361/201322068`

Astropy Collaboration, Price-Whelan, A. M., Lim, P. L., et al. 2022 ApJ, 935, 167, doi: `10.3847/1538-4357/ac7c74`

Babcock, H. W. 1939 Lick Observatory Bulletin, 498, 41, doi: `10.5479/ADS/bib/1939LicOB.19.41B`

Bacchini, C. 2020, PhD thesis, University of Groningen, doi: `10.33612/diss.133157780`

Bacon, R., Adam, G., Baranne, A., et al. 1995 A&AS, 113, 347

Bacon, R., Brinchmann, J., Richard, J., et al. 2015 A&A, 575, A75, doi: `10.1051/0004-6361/201425419`

Barišić, I., Jones, T., Mortensen, K., et al. 2025 ApJ, 983, 139, doi: `10.3847/1538-4357/ada617`

Baugh, C. M. 2006 Reports on Progress in Physics, 69, 3101, doi: `10.1088/0034-4885/69/12/R02`

Beckers, J. M. 1982 Optica Acta, 29, 361, doi: 10.1080/713820871

Begeman, K. G. 1989 A&A, 223, 47

Behrendt, M., Burkert, A., & Schartmann, M. 2015 MNRAS, 448, 1007, doi: 10.1093/mnras/stv027

Bekiaris, G., Glazebrook, K., Fluke, C. J., & Abraham, R. 2016 MNRAS, 455, 754, doi: 10.1093/mnras/stv2292

Bellardini, M. A., Wetzel, A., Loebman, S. R., et al. 2021 MNRAS, 505, 4586, doi: 10.1093/mnras/stab1606

Benson, A. J. 2010 Phys. Rep., 495, 33, doi: 10.1016/j.physrep.2010.06.001

Bernal, J. L., & Kovetz, E. D. 2022 A&A Rev., 30, 5, doi: 10.1007/s00159-022-00143-0

Bernard-Salas, J., Habart, E., Arab, H., et al. 2012 A&A, 538, A37, doi: 10.1051/0004-6361/201118083

Béthermin, M., Daddi, E., Magdis, G., et al. 2015 A&A, 573, A113, doi: 10.1051/0004-6361/201425031

Béthermin, M., Wu, H.-Y., Lagache, G., et al. 2017 A&A, 607, A89, doi: 10.1051/0004-6361/201730866

Béthermin, M., Fudamoto, Y., Ginolfi, M., et al. 2020 A&A, 643, A2, doi: 10.1051/0004-6361/202037649

Béthermin, M., Accard, C., Guillaume, C., et al. 2023 A&A, 680, L8, doi: 10.1051/0004-6361/202348115

Bewketu Belete, A., Andreani, P., Fernández-Ontiveros, J. A., et al. 2021 A&A, 654, A24, doi: 10.1051/0004-6361/202140492

Bigiel, F., Leroy, A. K., Walter, F., et al. 2011 ApJ, 730, L13, doi: 10.1088/2041-8205/730/2/L13

Binney, J., & Tremaine, S. 2008, Galactic Dynamics: Second Edition (Princeton University Press)

Birkin, J. E., Hutchison, T. A., Welch, B., et al. 2023 ApJ, 958, 64, doi: 10.3847/1538-4357/acf712

Birkin, J. E., Puglisi, A., Swinbank, A. M., et al. 2024 MNRAS, 531, 61, doi: 10.1093/mnras/stae1089

Birkin, J. E., Spilker, J. S., Herrera-Camus, R., et al. 2025 ApJ, 985, 243, doi: 10.3847/1538-4357/adced3

Bischetti, M., Feruglio, C., Piconcelli, E., et al. 2021 A&A, 645, A33, doi: 10.1051/0004-6361/202039057

Biswas, P., Kalinova, V., Roy, N., Patra, N. N., & Tyulneva, N. 2023 MNRAS, 524, 6213, doi: 10.1093/mnras/stad2285

Bland-Hawthorn, J., & Gerhard, O. 2016 ARA&A, 54, 529, doi: 10.1146/annurev-astro-081915-023441

Blumenthal, G. R., Faber, S. M., Flores, R., & Primack, J. R. 1986 ApJ, 301, 27, doi: 10.1086/163867

Bolatto, A. D., Wolfire, M., & Leroy, A. K. 2013 ARA&A, 51, 207, doi: 10.1146/annurev-astro-082812-140944

Boomsma, R., Oosterloo, T. A., Fraternali, F., van der Hulst, J. M., & Sancisi, R. 2008 A&A, 490, 555, doi: 10.1051/0004-6361:200810120

Bosma, A. 2023 arXiv e-prints, arXiv:2309.06390, doi: 10.48550/arXiv.2309.06390

Bouché, N., Carfantan, H., Schroetter, I., Michel-Dansac, L., & Contini, T. 2015 AJ, 150, 92, doi: 10.1088/0004-6256/150/3/92

Bouché, N., Cresci, G., Davies, R., et al. 2007 ApJ, 671, 303, doi: 10.1086/522221

Bouché, N., Dekel, A., Genzel, R., et al. 2010 ApJ, 718, 1001, doi: 10.1088/0004-637X/718/2/1001

Bouché, N. F., Genel, S., Pellissier, A., et al. 2021 A&A, 654, A49, doi: 10.1051/0004-6361/202040225

Bouché, N. F., Bera, S., Krajnović, D., et al. 2022 A&A, 658, A76, doi: 10.1051/0004-6361/202141762

Bournaud, F. 2016, in Astrophysics and Space Science Library, Vol. 418, Galactic Bulges, ed. E. Laurikainen, R. Peletier, & D. Gadotti, 355, doi: 10.1007/978-3-319-19378-6_13

Bournaud, F., Dekel, A., Teyssier, R., et al. 2011 ApJ, 741, L33, doi: 10.1088/2041-8205/741/2/L33

Bournaud, F., Elmegreen, B. G., & Elmegreen, D. M. 2007 ApJ, 670, 237, doi: 10.1086/522077

Bournaud, F., Elmegreen, B. G., & Martig, M. 2009 ApJ, 707, L1, doi: 10.1088/0004-637X/707/1/L1

Bouwens, R. J., Smit, R., Schouws, S., et al. 2022 ApJ, 931, 160, doi: 10.3847/1538-4357/ac5a4a

Bovy, J., & Rix, H.-W. 2013 ApJ, 779, 115, doi: 10.1088/0004-637X/779/2/115

Boylan-Kolchin, M., Ma, C.-P., & Quataert, E. 2008 MNRAS, 383, 93, doi: 10.1111/j.1365-2966.2007.12530.x

Bresolin, F., Fernández-Arenas, D., Rousseau-Nepton, L., et al. 2025 MNRAS, 539, 755, doi: 10.1093/mnras/staf510

Broadhurst, T. J., Ellis, R. S., & Glazebrook, K. 1992 Nature, 355, 55, doi: 10.1038/355055a0

Burkert, A., Genzel, R., Bouché, N., et al. 2010 ApJ, 725, 2324, doi: 10.1088/0004-637X/725/2/2324

Burkert, A., Förster Schreiber, N. M., Genzel, R., et al. 2016 ApJ, 826, 214, doi: 10.3847/0004-637X/826/2/214

Calzetti, D., Armus, L., Bohlin, R. C., et al. 2000 ApJ, 533, 682, doi: 10.1086/308692

Calzetti, D., Kinney, A. L., & Storchi-Bergmann, T. 1994 ApJ, 429, 582, doi: 10.1086/174346

Cao, Y., Wong, T., Bolatto, A. D., et al. 2023 ApJS, 268, 3, doi: 10.3847/1538-4365/acd840

Cappellari, M. 2008 MNRAS, 390, 71, doi: 10.1111/j.1365-2966.2008.13754.x

Cappellari, M. 2023 MNRAS, 526, 3273, doi: 10.1093/mnras/stad2597

Cardelli, J. A., Clayton, G. C., & Mathis, J. S. 1989 ApJ, 345, 245, doi: 10.1086/167900

Cardoso, A. F. S., Cavichia, O., Mollá, M., & Sánchez-Menguiano, L. 2025 ApJ, 980, 45, doi: 10.3847/1538-4357/ad9eab

Carignan, C., Chemin, L., Huchtmeier, W. K., & Lockman, F. J. 2006 ApJ, 641, L109, doi: 10.1086/503869

Carilli, C. L., & Shao, Y. 2018, in Astronomical Society of the Pacific Conference Series, Vol. 517, Science with a Next Generation Very Large Array, ed. E. Murphy, 535, doi: 10.48550/arXiv.1810.05053

Carniani, S., Arribas, S., Bunker, A., et al. 2021, Galaxy assembly at z > 6: unraveling the origin of the spatial offset between the UV and FIR emission,, JWST Proposal. Cycle 1, ID. #1893

Carton, D., Brinchmann, J., Contini, T., et al. 2018 MNRAS, 478, 4293, doi: 10.1093/mnras/sty1343

CASA Team, Bean, B., Bhatnagar, S., et al. 2022 PASP, 134, 114501, doi: 10.1088/1538-3873/ac9642

Casey, C. M., Hodge, J. A., Lacy, M., et al. 2015 arXiv e-prints, arXiv:1510.06411, doi: 10.48550/arXiv.1510.06411

Cathey, J., Gonzalez, A. H., Lower, S., et al. 2024 ApJ, 967, 11, doi: 10.3847/1538-4357/ad33c9

Ceverino, D., Dekel, A., Mandelker, N., et al. 2012 MNRAS, 420, 3490, doi: 10.1111/j.1365-2966.2011.20296.x

Ceverino, D., Mandelker, N., Snyder, G. F., et al. 2023 MNRAS, 522, 3912, doi: 10.1093/mnras/stad1255

Ceverino, D., Sánchez Almeida, J., Muñoz Tuñón, C., et al. 2016 MNRAS, 457, 2605, doi: 10.1093/mnras/stw064

Cheng, Y., Giavalisco, M., Simons, R. C., et al. 2024 ApJ, 964, 94, doi: 10.3847/1538-4357/ad234a

Chiappini, C., Matteucci, F., & Romano, D. 2001 ApJ, 554, 1044, doi: 10.1086/321427

Chisholm, J., Tremonti, C., & Leitherer, C. 2018 MNRAS, 481, 1690, doi: 10.1093/mnras/sty2380

Chowdhury, A., Kanekar, N., Chengalur, J. N., Sethi, S., & Dwarakanath, K. S. 2020 Nature, 586, 369, doi: 10.1038/s41586-020-2794-7

Christy, J. W., Wellnitz, D. D., & Currie, D. G. 1981 Lowell Observatory Bulletin, 9, 28

Ciotti, L., & Bertin, G. 1999 A&A, 352, 447, doi: 10.48550/arXiv.astro-ph/9911078

Claeyssens, A., Adamo, A., Messa, M., et al. 2025 MNRAS, 537, 2535, doi: 10.1093/mnras/staf058

Clark, P. C., Glover, S. C. O., Ragan, S. E., & Duarte-Cabral, A. 2019 MNRAS, 486, 4622, doi: 10.1093/mnras/stz1119

Coe, D., Umetsu, K., Zitrin, A., et al. 2012 ApJ, 757, 22, doi: 10.1088/0004-637X/757/1/22

Cole, J. W., Papovich, C., Finkelstein, S. L., et al. 2025 ApJ, 979, 193, doi: 10.3847/1538-4357/ad9a6a

Colley, W. N., Rhoads, J. E., Ostriker, J. P., & Spergel, D. N. 1996 ApJ, 473, L63, doi: 10.1086/310394

Condon, J. J., Cotton, W. D., Greisen, E. W., et al. 1998 AJ, 115, 1693, doi: 10.1086/300337

Contini, T., Epinat, B., Bouché, N., et al. 2016 A&A, 591, A49, doi: 10.1051/0004-6361/201527866

Cormier, D., Abel, N. P., Hony, S., et al. 2019 A&A, 626, A23, doi: 10.1051/0004-6361/201834457

Costantin, L., Gillman, S., Boogaard, L. A., et al. 2025 A&A, in press, doi: 10.1051/0004-6361/202451330

Courteau, S. 1997 AJ, 114, 2402, doi: 10.1086/118656

Courteau, S., & Dutton, A. A. 2015 ApJ, 801, L20, doi: 10.1088/2041-8205/801/2/L20

Cowie, L. L., Hu, E. M., & Songaila, A. 1995 AJ, 110, 1576, doi: 10.1086/117631

Crawford, M. K., Genzel, R., Townes, C. H., & Watson, D. M. 1985 ApJ, 291, 755, doi: 10.1086/163113

Cresci, G., Mannucci, F., Maiolino, R., et al. 2010 Nature, 467, 811, doi: 10.1038/nature09451

Cresci, G., Hicks, E. K. S., Genzel, R., et al. 2009 ApJ, 697, 115, doi: 10.1088/0004-637X/697/1/115

Croxall, K. V., Pogge, R. W., Berg, D. A., Skillman, E. D., & Moustakas, J. 2015 ApJ, 808, 42, doi: 10.1088/0004-637X/808/1/42

Cuddeford, P. 1993 MNRAS, 262, 1076, doi: 10.1093/mnras/262.4.1076

Curran, P. A. 2014 arXiv e-prints, arXiv:1411.3816, doi: 10.48550/arXiv.1411.3816

Curti, M., Mannucci, F., Cresci, G., & Maiolino, R. 2020a MNRAS, 491, 944, doi: 10.1093/mnras/stz2910

Curti, M., Maiolino, R., Cirasuolo, M., et al. 2020b MNRAS, 492, 821, doi: 10.1093/mnras/stz3379

Curti, M., Maiolino, R., Curtis-Lake, E., et al. 2024 A&A, 684, A75, doi: 10.1051/0004-6361/202346698

Dalcanton, J. J., & Stilp, A. M. 2010 ApJ, 721, 547, doi: 10.1088/0004-637X/721/1/547

Danhaive, A. L., Tacchella, S., Übler, H., et al. 2025 MNRAS, 543, 3249, doi: 10.1093/mnras/staf1540

Davies, R., & Kasper, M. 2012 ARA&A, 50, 305, doi: 10.1146/annurev-astro-081811-125447

Davies, R., Förster Schreiber, N. M., Cresci, G., et al. 2011 ApJ, 741, 69, doi: 10.1088/0004-637X/741/2/69

Davies, R. I., Maciejewski, W., Hicks, E. K. S., et al. 2009 ApJ, 702, 114, doi: 10.1088/0004-637X/702/1/114

Davies, R. I., Tacconi, L. J., & Genzel, R. 2004a ApJ, 602, 148, doi: 10.1086/380995

Davies, R. I., Tacconi, L. J., & Genzel, R. 2004b ApJ, 613, 781, doi: 10.1086/423315

Davies, R. I., Maciejewski, W., Hicks, E. K. S., et al. 2014 ApJ, 792, 101, doi: 10.1088/0004-637X/792/2/101

Davies, R. L., Fisher, D. B., Herrera-Camus, R., et al. 2025 submitted

Davis, T. A., Bureau, M., Onishi, K., et al. 2017 MNRAS, 468, 4675, doi: 10.1093/mnras/stw3217

Davis, T. A., Alatalo, K., Bureau, M., et al. 2013 MNRAS, 429, 534, doi: 10.1093/mnras/sts353

de Blok, W. J. G., Healy, J., Maccagni, F. M., et al. 2024 A&A, 688, A109, doi: 10.1051/0004-6361/202348297

de Graaff, A., Rix, H.-W., Carniani, S., et al. 2024 A&A, 684, A87, doi: 10.1051/0004-6361/202347755

de la Vega, A., Mobasher, B., Manesh, F., et al. 2025 arXiv e-prints, arXiv:2508.14972, doi: 10.48550/arXiv.2508.14972

de Vaucouleurs, G. 1948 Annales d'Astrophysique, 11, 247

Deg, N., Spekkens, K., Westmeier, T., et al. 2022 PASA, 39, e059, doi: 10.1017/pasa.2022.43

Dekel, A., & Burkert, A. 2014 MNRAS, 438, 1870, doi: 10.1093/mnras/stt2331

Dekel, A., Ginzburg, O., Jiang, F., et al. 2020 MNRAS, 493, 4126, doi: 10.1093/mnras/staa470

Dekel, A., Mandelker, N., Bournaud, F., et al. 2022 MNRAS, 511, 316, doi: 10.1093/mnras/stab3810

Dekel, A., Sari, R., & Ceverino, D. 2009a ApJ, 703, 785, doi: 10.1088/0004-637X/703/1/785

Dekel, A., Birnboim, Y., Engel, G., et al. 2009b Nature, 457, 451, doi: 10.1038/nature07648

Delgado-Serrano, R., Hammer, F., Yang, Y. B., et al. 2010 A&A, 509, A78, doi: 10.1051/0004-6361/200912704

Dessauges-Zavadsky, M., Ginolfi, M., Pozzi, F., et al. 2020 A&A, 643, A5, doi: 10.1051/0004-6361/202038231

D'Eugenio, F., Pérez-González, P. G., Maiolino, R., et al. 2024 Nature Astronomy, 8, 1443, doi: 10.1038/s41550-024-02345-1

Devereaux, T., Cassata, P., Ibar, E., et al. 2024 A&A, 686, A156, doi: 10.1051/0004-6361/202348511

Di Teodoro, E. M., & Fraternali, F. 2015 MNRAS, 451, 3021, doi: 10.1093/mnras/stv1213

Di Teodoro, E. M., Fraternali, F., & Miller, S. H. 2016 A&A, 594, A77, doi: 10.1051/0004-6361/201628315

Di Teodoro, E. M., Grillo, C., Fraternali, F., et al. 2018 MNRAS, 476, 804, doi: `10.1093/mnras/sty175`

Donahue, M., & Voit, G. M. 2022 Phys. Rep., 973, 1, doi: `10.1016/j.physrep.2022.04.005`

Dopita, M. A., & Sutherland, R. S. 1995 ApJ, 455, 468, doi: `10.1086/176596`

Draine, B. T. 2003 ARA&A, 41, 241, doi: `10.1146/annurev.astro.41.011802.094840`

Draine, B. T. 2011, Physics of the Interstellar and Intergalactic Medium (Princeton University Press)

Duan, Q., Conselice, C. J., Li, Q., et al. 2025 MNRAS, staf638, doi: `10.1093/mnras/staf638`

Duncan, K., Conselice, C. J., Mundy, C., et al. 2019 ApJ, 876, 110, doi: `10.3847/1538-4357/ab148a`

Dutton, A. A., & Macciò, A. V. 2014 MNRAS, 441, 3359, doi: `10.1093/mnras/stu742`

Easeman, B., Schady, P., Wuyts, S., & Yates, R. M. 2022 MNRAS, 511, 371, doi: `10.1093/mnras/stac017`

Eisenhauer, F., Tecza, M., Thatte, N., et al. 2003 The Messenger, 113, 17

Ejdetjärn, T., Agertz, O., Östlin, G., Renaud, F., & Romeo, A. B. 2022 MNRAS, 514, 480, doi: `10.1093/mnras/stac1414`

El-Zant, A., Shlosman, I., & Hoffman, Y. 2001 ApJ, 560, 636, doi: `10.1086/322516`

Elmegreen, B. G., & Elmegreen, D. M. 2006 ApJ, 650, 644, doi: `10.1086/507578`

Elmegreen, B. G., Elmegreen, D. M., Fernandez, M. X., & Lemonias, J. J. 2009 ApJ, 692, 12, doi: `10.1088/0004-637X/692/1/12`

Elmegreen, B. G., Elmegreen, D. M., Vollbach, D. R., Foster, E. R., & Ferguson, T. E. 2005 ApJ, 634, 101, doi: `10.1086/496952`

Elmegreen, B. G., Martinez, Z., & Hunter, D. A. 2022 ApJ, 928, 143, doi: `10.3847/1538-4357/ac559c`

Elmegreen, D. M., Elmegreen, B. G., & Hirst, A. C. 2004 ApJ, 604, L21, doi: `10.1086/383312`

Elmegreen, D. M., Elmegreen, B. G., Rubin, D. S., & Schaffer, M. A. 2005 ApJ, 631, 85, doi: `10.1086/432502`

Epinat, B., Amram, P., & Marcelin, M. 2008 MNRAS, 390, 466, doi: `10.1111/j.1365-2966.2008.13796.x`

Epinat, B., Contini, T., Le Fèvre, O., et al. 2009 A&A, 504, 789, doi: `10.1051/0004-6361/200911995`

Epinat, B., Tasca, L., Amram, P., et al. 2012 A&A, 539, A92, doi: `10.1051/0004-6361/201117711`

Erwin, P. 2015 ApJ, 799, 226, doi: `10.1088/0004-637X/799/2/226`

Espejo Salcedo, J. M., Pastras, S., Vácha, J., et al. 2025 A&A, 700, A42, doi: `10.1051/0004-6361/202554725`

Estrada-Carpenter, V., Sawicki, M., Abraham, R., et al. 2025 ApJ, 991, 188, doi: 10.3847/1538-4357/adfb64

Faisst, A. L., Fudamoto, Y., Oesch, P. A., et al. 2020a MNRAS, 498, 4192, doi: 10.1093/mnras/staa2545

Faisst, A. L., Fudamoto, Y., Oesch, P. A., et al. 2020b MNRAS, 498, 4192, doi: 10.1093/mnras/staa2545

Faisst, A. L., Fujimoto, F., Tsujita, A., et al. 2025 ApJ, submitted

Faisst, A. L., Schaerer, D., Lemaux, B. C., et al. 2020c ApJS, 247, 61, doi: 10.3847/1538-4365/ab7ccd

Fall, S. M., & Efstathiou, G. 1980 MNRAS, 193, 189, doi: 10.1093/mnras/193.2.189

Fan, L., Knudsen, K. K., Han, Y., & Tan, Q.-h. 2019 ApJ, 887, 74, doi: 10.3847/1538-4357/ab5059

Fasano, G., & Franceschini, A. 1987 MNRAS, 225, 155, doi: 10.1093/mnras/225.1.155

Fei, Q., Silverman, J. D., Fujimoto, S., et al. 2025 ApJ, 980, 84, doi: 10.3847/1538-4357/ada145

Ferreira, L., Conselice, C. J., Sazonova, E., et al. 2023 ApJ, 955, 94, doi: 10.3847/1538-4357/acec76

Fitzpatrick, E. L., & Massa, D. 2007 ApJ, 663, 320, doi: 10.1086/518158

Foreman-Mackey, D. 2016 The Journal of Open Source Software, 1, 24, doi: 10.21105/joss.00024

Foreman-Mackey, D., Hogg, D. W., Lang, D., & Goodman, J. 2013 PASP, 125, 306, doi: 10.1086/670067

Förster Schreiber, N. M., & Wuyts, S. 2020 ARA&A, 58, 661, doi: 10.1146/annurev-astro-032620-021910

Förster Schreiber, N. M., Genzel, R., Lehnert, M. D., et al. 2006 ApJ, 645, 1062, doi: 10.1086/504403

Förster Schreiber, N. M., Genzel, R., Bouché, N., et al. 2009 ApJ, 706, 1364, doi: 10.1088/0004-637X/706/2/1364

Förster Schreiber, N. M., Shapley, A. E., Genzel, R., et al. 2011 ApJ, 739, 45, doi: 10.1088/0004-637X/739/1/45

Förster Schreiber, N. M., Renzini, A., Mancini, C., et al. 2018 ApJS, 238, 21, doi: 10.3847/1538-4365/aadd49

Fraternali, F., Karim, A., Magnelli, B., et al. 2021 A&A, 647, A194, doi: 10.1051/0004-6361/202039807

Freeman, K. C. 1970 ApJ, 160, 811, doi: 10.1086/150474

Freundlich, J., Dekel, A., Jiang, F., et al. 2020 MNRAS, 491, 4523, doi: 10.1093/mnras/stz3306

Freundlich, J., Combes, F., Tacconi, L. J., et al. 2019 A&A, 622, A105, doi: 10.1051/0004-6361/201732223

Fujimoto, S., Silverman, J. D., Bethermin, M., et al. 2020 ApJ, 900, 1, doi: 10.3847/1538-4357/ab94b3

Fujimoto, S., Oguri, M., Brammer, G., et al. 2021 ApJ, 911, 99, doi: 10.3847/1538-4357/abd7ec

Fujimoto, S., Ouchi, M., Kohno, K., et al. 2025 Nature Astronomy, doi: 10.1038/s41550-025-02592-w

Fukugita, M., & Peebles, P. J. E. 2004 ApJ, 616, 643, doi: 10.1086/425155

Garcia, A. M., Torrey, P., Bhagwat, A., et al. 2025 ApJ, 989, 147, doi: 10.3847/1538-4357/adea51

Gatto, A., Walch, S., Low, M. M. M., et al. 2015 MNRAS, 449, 1057, doi: 10.1093/mnras/stv324

Genzel, R. 1991, Molecular Clouds in Regions of Massive Star Formation (Dordrecht: Springer Netherlands), 123–170, doi: 10.1007/978-94-009-0695-2_5

Genzel, R., Tacconi, L. J., Eisenhauer, F., et al. 2006 Nature, 442, 786, doi: 10.1038/nature05052

Genzel, R., Burkert, A., Bouché, N., et al. 2008 ApJ, 687, 59, doi: 10.1086/591840

Genzel, R., Newman, S., Jones, T., et al. 2011 ApJ, 733, 101, doi: 10.1088/0004-637X/733/2/101

Genzel, R., Tacconi, L. J., Combes, F., et al. 2012 ApJ, 746, 69, doi: 10.1088/0004-637X/746/1/69

Genzel, R., Tacconi, L. J., Kurk, J., et al. 2013 ApJ, 773, 68, doi: 10.1088/0004-637X/773/1/68

Genzel, R., Förster Schreiber, N. M., Lang, P., et al. 2014a ApJ, 785, 75, doi: 10.1088/0004-637X/785/1/75

Genzel, R., Förster Schreiber, N. M., Rosario, D., et al. 2014b ApJ, 796, 7, doi: 10.1088/0004-637X/796/1/7

Genzel, R., Tacconi, L. J., Lutz, D., et al. 2015 ApJ, 800, 20, doi: 10.1088/0004-637X/800/1/20

Genzel, R., Förster Schreiber, N. M., Übler, H., et al. 2017 Nature, 543, 397, doi: 10.1038/nature21685

Genzel, R., Price, S. H., Übler, H., et al. 2020 ApJ, 902, 98, doi: 10.3847/1538-4357/abb0ea

Genzel, R., Jolly, J. B., Liu, D., et al. 2023 ApJ, 957, 48, doi: 10.3847/1538-4357/acef1a

Gibson, B. K., Pilkington, K., Brook, C. B., Stinson, G. S., & Bailin, J. 2013 A&A, 554, A47, doi: 10.1051/0004-6361/201321239

Gillman, S., Tiley, A. L., Swinbank, A. M., et al. 2021 MNRAS, 500, 4229, doi: 10.1093/mnras/staa3400

Gillman, S., Puglisi, A., Dudzevičiūtė, U., et al. 2022 MNRAS, 512, 3480, doi: 10.1093/mnras/stac580

Gilmore, G., Wilkinson, M. I., Wyse, R. F. G., et al. 2007 ApJ, 663, 948, doi: 10.1086/518025

Ginzburg, O., Dekel, A., Mandelker, N., & Krumholz, M. R. 2022 MNRAS, 513, 6177, doi: 10.1093/mnras/stac1324

Girard, M., Dessauges-Zavadsky, M., Combes, F., et al. 2019 A&A, 631, A91, doi: 10.1051/0004-6361/201935896

Girard, M., Dessauges-Zavadsky, M., Schaerer, D., et al. 2018 A&A, 613, A72, doi: 10.1051/0004-6361/201731988

Girard, M., Mason, C. A., Fontana, A., et al. 2020 MNRAS, 497, 173, doi: 10.1093/mnras/staa1907

Girard, M., Fisher, D. B., Bolatto, A. D., et al. 2021 ApJ, 909, 12, doi: 10.3847/1538-4357/abd5b9

Glazebrook, K. 2013 PASA, 30, e056, doi: 10.1017/pasa.2013.34

Gnerucci, A., Marconi, A., Capetti, A., Axon, D. J., & Robinson, A. 2010 A&A, 511, A19, doi: 10.1051/0004-6361/200912530

Gnerucci, A., Marconi, A., Cresci, G., et al. 2011 A&A, 528, A88, doi: 10.1051/0004-6361/201015465

Goldbaum, N. J., Krumholz, M. R., & Forbes, J. C. 2016 ApJ, 827, 28, doi: 10.3847/0004-637X/827/1/28

Goldreich, P., & Lynden-Bell, D. 1965 MNRAS, 130, 125, doi: 10.1093/mnras/130.2.125

Goldsmith, P. F., Langer, W. D., Pineda, J. L., & Velusamy, T. 2012 ApJS, 203, 13, doi: 10.1088/0067-0049/203/1/13

Grasha, K., Chen, Q. H., Battisti, A. J., et al. 2022 ApJ, 929, 118, doi: 10.3847/1538-4357/ac5ab2

Guo, Y., Ferguson, H. C., Bell, E. F., et al. 2015 ApJ, 800, 39, doi: 10.1088/0004-637X/800/1/39

Guo, Y., Rafelski, M., Bell, E. F., et al. 2018 ApJ, 853, 108, doi: 10.3847/1538-4357/aaa018

Harikane, Y., Ouchi, M., Shibuya, T., et al. 2018 ApJ, 859, 84, doi: 10.3847/1538-4357/aabd80

Harris, C. R., Millman, K. J., van der Walt, S. J., et al. 2020 Nature, 585, 357, doi: 10.1038/s41586-020-2649-2

Harrison, C. M., Johnson, H. L., Swinbank, A. M., et al. 2017 MNRAS, 467, 1965, doi: 10.1093/mnras/stx217

Hayward, C. C., & Hopkins, P. F. 2017 MNRAS, 465, 1682, doi: 10.1093/mnras/stw2888

Hayward, C. C., Sparre, M., Chapman, S. C., et al. 2021 MNRAS, 502, 2922, doi: 10.1093/mnras/stab246

Hemler, Z. S., Torrey, P., Qi, J., et al. 2021 MNRAS, 506, 3024, doi: 10.1093/mnras/stab1803

Hernquist, L. 1990 ApJ, 356, 359, doi: 10.1086/168845

Herrera-Camus, R., Förster Schreiber, N. M., Price, S. H., et al. 2022 A&A, 665, L8, doi: 10.1051/0004-6361/202142562

Herrera-Camus, R., González-López, J., Förster Schreiber, N., et al. 2025 A&A, 699, A80, doi: 10.1051/0004-6361/202553896

Heywood, I., Ponomareva, A. A., Maddox, N., et al. 2024 MNRAS, 534, 76, doi: 10.1093/mnras/stae2081

Hirtenstein, J., Jones, T., Wang, X., et al. 2019 ApJ, 880, 54, doi: 10.3847/1538-4357/ab113e

Ho, I. T., Kudritzki, R.-P., Kewley, L. J., et al. 2015 MNRAS, 448, 2030, doi: 10.1093/mnras/stv067

Hodge, J. A., Carilli, C. L., Walter, F., et al. 2012 ApJ, 760, 11, doi: 10.1088/0004-637X/760/1/11

Hogan, L., Rigopoulou, D., Magdis, G. E., et al. 2021 MNRAS, 503, 5329, doi: 10.1093/mnras/stab527

Hogan, L., Rigopoulou, D., García-Burillo, S., et al. 2022 MNRAS, 512, 2371, doi: 10.1093/mnras/stac520

Hollenbach, D. J., & Tielens, A. G. G. M. 1999 Reviews of Modern Physics, 71, 173, doi: 10.1103/RevModPhys.71.173

Huang, S., Kawabe, R., Umehata, H., et al. 2025 Nature, 641, 861, doi: 10.1038/s41586-025-08914-2

Huang, S., Kawabe, R., Kohno, K., et al. 2023 ApJ, 958, L26, doi: 10.3847/2041-8213/acff63

Hubble, E. P. 1926 ApJ, 64, 321, doi: 10.1086/143018

Huertas-Company, M., Iyer, K. G., Angeloudi, E., et al. 2024 A&A, 685, A48, doi: 10.1051/0004-6361/202346800

Huertas-Company, M., Shuntov, M., Dong, Y., et al. 2025 A&A, 704, A94, doi: 10.1051/0004-6361/202553782

Hung, C.-L., Hayward, C. C., Yuan, T., et al. 2019 MNRAS, 482, 5125, doi: 10.1093/mnras/sty2970

Hunter, J. D. 2007 Computing in Science and Engineering, 9, 90, doi: 10.1109/MCSE.2007.55

Ibrahim, D., & Kobayashi, C. 2025 MNRAS, 544, 815, doi: 10.1093/mnras/staf1727

Ikeda, R., Tadaki, K.-i., Mitsuhashi, I., et al. 2025 A&A, 693, A237, doi: 10.1051/0004-6361/202451811

Immeli, A., Samland, M., Gerhard, O., & Westera, P. 2004a A&A, 413, 547, doi: 10.1051/0004-6361:20034282

Immeli, A., Samland, M., Westera, P., & Gerhard, O. 2004b ApJ, 611, 20, doi: 10.1086/422179

Iorio, G., Fraternali, F., Nipoti, C., et al. 2017 MNRAS, 466, 4159, doi: 10.1093/mnras/stw3285

Jacobs, C., Glazebrook, K., Calabrò, A., et al. 2023 ApJ, 948, L13, doi: 10.3847/2041-8213/accd6d

Jiménez, E., Lagos, C. d. P., Ludlow, A. D., & Wisnioski, E. 2023 MNRAS, 524, 4346, doi: 10.1093/mnras/stad2119

Jiménez-Andrade, E. F., Cantalupo, S., Magnelli, B., et al. 2023 MNRAS, 521, 2326, doi: 10.1093/mnras/stad594

Jog, C. J., & Solomon, P. M. 1984 ApJ, 276, 114, doi: 10.1086/161597

Johnson, H. L., Harrison, C. M., Swinbank, A. M., et al. 2018 MNRAS, 474, 5076, doi: 10.1093/mnras/stx3016

Jones, G. C., Béthermin, M., Fudamoto, Y., et al. 2020 MNRAS, 491, L18, doi: 10.1093/mnrasl/slz154

Jones, G. C., Vergani, D., Romano, M., et al. 2021 MNRAS, 507, 3540, doi: 10.1093/mnras/stab2226

Jones, G. C., Bunker, A. J., Telikova, K., et al. 2025 MNRAS, 540, 3311, doi: 10.1093/mnras/staf899

Jones, T., Ellis, R. S., Richard, J., & Jullo, E. 2013 ApJ, 765, 48, doi: 10.1088/0004-637X/765/1/48

Jones, T., Wang, X., Schmidt, K. B., et al. 2015 AJ, 149, 107, doi: 10.1088/0004-6256/149/3/107

Jones, T. A., Swinbank, A. M., Ellis, R. S., Richard, J., & Stark, D. P. 2010 MNRAS, 404, 1247, doi: 10.1111/j.1365-2966.2010.16378.x

Jorsater, S., & van Moorsel, G. A. 1995 AJ, 110, 2037, doi: 10.1086/117668

Józsa, G. I. G., Kenn, F., Klein, U., & Oosterloo, T. A. 2007 A&A, 468, 731, doi: 10.1051/0004-6361:20066164

Ju, M., Wang, X., Jones, T., et al. 2025 ApJ, 978, L39, doi: 10.3847/2041-8213/ada150

Kaasinen, M., Scoville, N., Walter, F., et al. 2019 ApJ, 880, 15, doi: 10.3847/1538-4357/ab253b

Kaasinen, M., Walter, F., Novak, M., et al. 2020 ApJ, 899, 37, doi: 10.3847/1538-4357/aba438

Kakiichi, K., Egami, E., Fan, X., et al. 2024, COSMOS-3D: A Legacy Spectroscopic/Imaging Survey of the Early Universe,, JWST Proposal. Cycle 3, ID. #5893

Kalita, B. S., Silverman, J. D., Daddi, E., et al. 2025 MNRAS, 537, 402, doi: 10.1093/mnras/staf031

Kamphuis, P., Józsa, G. I. G., Oh, S. . H., et al. 2015 MNRAS, 452, 3139, doi: 10.1093/mnras/stv1480

Kartaltepe, J. S., Rose, C., Vanderhoof, B. N., et al. 2023 ApJ, 946, L15, doi: 10.3847/2041-8213/acad01

Kassin, S. A., Weiner, B. J., Faber, S. M., et al. 2012 ApJ, 758, 106, doi: 10.1088/0004-637X/758/2/106

Kennicutt, R. C., & Evans, N. J. 2012 ARA&A, 50, 531, doi: 10.1146/annurev-astro-081811-125610

Kennicutt, Jr., R. C. 1984 ApJ, 287, 116, doi: 10.1086/162669

Kennicutt, Jr., R. C. 1989 ApJ, 344, 685, doi: 10.1086/167834

Kewley, L. J., & Ellison, S. L. 2008 ApJ, 681, 1183, doi: 10.1086/587500

Kewley, L. J., Nicholls, D. C., & Sutherland, R. S. 2019 ARA&A, 57, 511, doi: 10.1146/annurev-astro-081817-051832

Kewley, L. J., Rupke, D., Zahid, H. J., Geller, M. J., & Barton, E. J. 2010 ApJ, 721, L48, doi: 10.1088/2041-8205/721/1/L48

Khoperskov, S., Sivkova, E., Saburova, A., et al. 2023 A&A, 671, A56, doi: 10.1051/0004-6361/202142581

Kim, C.-G., & Ostriker, E. C. 2018 ApJ, 853, 173, doi: 10.3847/1538-4357/aaa5ff

Klypin, A. A., Trujillo-Gomez, S., & Primack, J. 2011 ApJ, 740, 102, doi: 10.1088/0004-637X/740/2/102

Kohandel, M., Pallottini, A., Ferrara, A., et al. 2024 A&A, 685, A72, doi: 10.1051/0004-6361/202348209

Koposov, S., Speagle, J., Barbary, K., et al. 2023, joshspeagle/dynesty,, v2.1.3 Zenodo, doi: 10.5281/zenodo.8408702

Koprowski, M. P., Wijesekera, J. V., Dunlop, J. S., et al. 2024 A&A, 691, A164, doi: 10.1051/0004-6361/202449948

Krajnović, D., Cappellari, M., de Zeeuw, P. T., & Copin, Y. 2006 MNRAS, 366, 787, doi: 10.1111/j.1365-2966.2005.09902.x

Kreckel, K., Ho, I. T., Blanc, G. A., et al. 2020 MNRAS, 499, 193, doi: 10.1093/mnras/staa2743

Kretschmer, M., Dekel, A., Freundlich, J., et al. 2021 MNRAS, 503, 5238, doi: 10.1093/mnras/stab833

Krumholz, M. R., Burkhart, B., Forbes, J. C., & Crocker, R. M. 2018 MNRAS, 477, 2716, doi: 10.1093/mnras/sty852

Lambert, T. S., Posses, A., Aravena, M., et al. 2023 MNRAS, 518, 3183, doi: 10.1093/mnras/stac3016

Lang, P., Wuyts, S., Somerville, R. S., et al. 2014 ApJ, 788, 11, doi: 10.1088/0004-637X/788/1/11

Lang, P., Förster Schreiber, N. M., Genzel, R., et al. 2017 ApJ, 840, 92, doi: 10.3847/1538-4357/aa6d82

Larkin, J., Barczys, M., Krabbe, A., et al. 2006, in Society of Photo-Optical Instrumentation Engineers (SPIE) Conference Series, Vol. 6269, Ground-based and Airborne Instrumentation for Astronomy, ed. I. S. McLean & M. Iye, 62691A, doi: 10.1117/12.672061

Law, D. R., Steidel, C. C., Erb, D. K., et al. 2009 ApJ, 697, 2057, doi: 10.1088/0004-637X/697/2/2057

Le Fèvre, O., Abraham, R., Lilly, S. J., et al. 2000 MNRAS, 311, 565, doi: 10.1046/j.1365-8711.2000.03083.x

Le Fèvre, O., Béthermin, M., Faisst, A., et al. 2020 A&A, 643, A1, doi: 10.1051/0004-6361/201936965

Lee, B., Giavalisco, M., Williams, C. C., et al. 2013 ApJ, 774, 47, doi: 10.1088/0004-637X/774/1/47

Lee, J. H., Park, C., Hwang, H. S., & Kwon, M. 2024 ApJ, 966, 113, doi: 10.3847/1538-4357/ad3448

Lee, L. L., Förster Schreiber, N. M., Price, S. H., et al. 2025a ApJ, 978, 14, doi: 10.3847/1538-4357/ad90b5

Lee, L. L., Förster Schreiber, N. M., Herrera-Camus, R., et al. 2025b A&A, 701, A260, doi: 10.1051/0004-6361/202555362

Leethochawalit, N., Jones, T. A., Ellis, R. S., et al. 2016 ApJ, 820, 84, doi: 10.3847/0004-637X/820/2/84

Lelli, F., De Breuck, C., Falkendal, T., et al. 2018 MNRAS, 479, 5440, doi: 10.1093/mnras/sty1795

Lelli, F., Di Teodoro, E. M., Fraternali, F., et al. 2021 Science, 371, 713, doi: 10.1126/science.abc1893

Lelli, F., Zhang, Z.-Y., Bisbas, T. G., et al. 2023 A&A, 672, A106, doi: 10.1051/0004-6361/202245105

Lemaux, B. C., Le Fèvre, O., Cucciati, O., et al. 2018 A&A, 615, A77, doi: 10.1051/0004-6361/201730870

Leroy, A. K., Bolatto, A., Gordon, K., et al. 2011 ApJ, 737, 12, doi: 10.1088/0004-637X/737/1/12

Li, J., Da Cunha, E., González-López, J., et al. 2024a ApJ, 976, 70, doi: 10.3847/1538-4357/ad7fee

Li, J., Da Cunha, E., González-López, J., et al. 2024b ApJ, 976, 70, doi: 10.3847/1538-4357/ad7fee

Li, Z., Wang, X., Cai, Z., et al. 2022 ApJ, 929, L8, doi: 10.3847/2041-8213/ac626f

Li, Z., Kakiichi, K., Christensen, L., et al. 2025a A&A, 703, A106, doi: 10.1051/0004-6361/202555372

Li, Z., Cai, Z., Wang, X., et al. 2025b ApJS, 280, 62, doi: 10.3847/1538-4365/adfa70

Lilly, S. J., Carollo, C. M., Pipino, A., Renzini, A., & Peng, Y. 2013 ApJ, 772, 119, doi: 10.1088/0004-637X/772/2/119

Lin, M.-Y., Davies, R. I., Burtscher, L., et al. 2016 MNRAS, 458, 1375, doi: 10.1093/mnras/stw401

Lines, N. E. P., Bowler, R. A. A., Adams, N. J., et al. 2025 MNRAS, staf627, doi: 10.1093/mnras/staf627

Liu, D., Schinnerer, E., Groves, B., et al. 2019 ApJ, 887, 235, doi: 10.3847/1538-4357/ab578d

Liu, D., Förster Schreiber, N. M., Genzel, R., et al. 2023 ApJ, 942, 98, doi: 10.3847/1538-4357/aca46b

Liu, D., Förster Schreiber, N. M., Harrington, K. C., et al. 2024 Nature Astronomy, doi: 10.1038/s41550-024-02296-7

Liu, Z., Silverman, J. D., Daddi, E., et al. 2024 ApJ, 968, 15, doi: 10.3847/1538-4357/ad4096

Liu, Z., Kodama, T., Morishita, T., et al. 2025 ApJ, 980, 69, doi: 10.3847/1538-4357/ada937

Livermore, R. C., Jones, T. A., Richard, J., et al. 2015 MNRAS, 450, 1812, doi: 10.1093/mnras/stv686

Lodders, K., Palme, H., & Gail, H. P. 2009 Landolt Börnstein, 4B, 712, doi: `10.1007/978-3-540-88055-4_34`

Loiacono, F., Talia, M., Fraternali, F., et al. 2019 MNRAS, 489, 681, doi: `10.1093/mnras/stz2170`

Lovell, M. R., Pillepich, A., Genel, S., et al. 2018 MNRAS, 481, 1950, doi: `10.1093/mnras/sty2339`

Lynden-Bell, D., & Kalnajs, A. J. 1972 MNRAS, 157, 1, doi: `10.1093/mnras/157.1.1`

Lyu, C., Wang, E., Zhang, H., et al. 2025 ApJ, 981, L6, doi: `10.3847/2041-8213/adb4ed`

Ma, X., Hopkins, P. F., Wetzel, A. R., et al. 2017 MNRAS, 467, 2430, doi: `10.1093/mnras/stx273`

Madau, P., & Dickinson, M. 2014 ARA&A, 52, 415, doi: `10.1146/annurev-astro-081811-125615`

Maiolino, R., & Mannucci, F. 2019 A&A Rev., 27, 3, doi: `10.1007/s00159-018-0112-2`

Maiolino, R., Nagao, T., Grazian, A., et al. 2008 A&A, 488, 463, doi: `10.1051/0004-6361:200809678`

Mancera Piña, P. E., Fraternali, F., Adams, E. A. K., et al. 2019 ApJ, 883, L33, doi: `10.3847/2041-8213/ab40c7`

Mancera Piña, P. E., Fraternali, F., Oman, K. A., et al. 2020 MNRAS, 495, 3636, doi: `10.1093/mnras/staa1256`

Mancini, C., Förster Schreiber, N. M., Renzini, A., et al. 2011 ApJ, 743, 86, doi: `10.1088/0004-637X/743/1/86`

Mandelker, N., Dekel, A., Ceverino, D., et al. 2017 MNRAS, 464, 635, doi: `10.1093/mnras/stw2358`

Marinacci, F., Pakmor, R., & Springel, V. 2014 MNRAS, 437, 1750, doi: `10.1093/mnras/stt2003`

Markwardt, C. B. 2009, in Astronomical Society of the Pacific Conference Series, Vol. 411, Astronomical Data Analysis Software and Systems XVIII, ed. D. A. Bohlender, D. Durand, & P. Dowler, 251, doi: `10.48550/arXiv.0902.2850`

Martin, P., & Roy, J.-R. 1994 ApJ, 424, 599, doi: `10.1086/173917`

Martin, P., & Roy, J.-R. 1995 ApJ, 445, 161, doi: `10.1086/175682`

Martinsson, T. P. K., Verheijen, M. A. W., Westfall, K. B., et al. 2013a A&A, 557, A131, doi: `10.1051/0004-6361/201321390`

Martinsson, T. P. K., Verheijen, M. A. W., Westfall, K. B., et al. 2013b A&A, 557, A130, doi: `10.1051/0004-6361/201220515`

Mason, C. A., Treu, T., Fontana, A., et al. 2017 ApJ, 838, 14, doi: `10.3847/1538-4357/aa60c4`

Matteucci, F., & Francois, P. 1989 MNRAS, 239, 885, doi: `10.1093/mnras/239.3.885`

Mendel, J. T., Beifiori, A., Saglia, R. P., et al. 2020 ApJ, 899, 87, doi: `10.3847/1538-4357/ab9ffc`

Méndez-Delgado, J. E., Amayo, A., Arellano-Córdova, K. Z., et al. 2022 MNRAS, 510, 4436, doi: `10.1093/mnras/stab3782`

Miller, T. B., Suess, K. A., Setton, D. J., et al. 2025 ApJ, 988, 196, doi: `10.3847/1538-4357/ade438`

Mitsuhashi, I., Tadaki, K.-i., Ikeda, R., et al. 2024 A&A, 690, A197, doi: `10.1051/0004-6361/202348782`

Mizener, A., Pope, A., McKinney, J., et al. 2024 ApJ, 970, 30, doi: `10.3847/1538-4357/ad4965`

Mo, H., van den Bosch, F. C., & White, S. 2010, Galaxy Formation and Evolution (Cambridge University Press), doi: `10.1017/CBO9780511807244`

Mo, H. J., Mao, S., & White, S. D. M. 1998 MNRAS, 295, 319, doi: `10.1046/j.1365-8711.1998.01227.x`

Mogotsi, K. M., de Blok, W. J. G., Caldú-Primo, A., et al. 2016 AJ, 151, 15, doi: `10.3847/0004-6256/151/1/15`

Molina, J., Ibar, E., Smail, I., et al. 2019 MNRAS, 487, 4856, doi: `10.1093/mnras/stz1643`

Molina, J., Ibar, E., Swinbank, A. M., et al. 2017 MNRAS, 466, 892, doi: `10.1093/mnras/stw3120`

Mollá, M., Díaz, Á. I., Cavichia, O., et al. 2019 MNRAS, 482, 3071, doi: `10.1093/mnras/sty2877`

Moster, B. P., Naab, T., & White, S. D. M. 2018 MNRAS, 477, 1822, doi: `10.1093/mnras/sty655`

Mott, A., Spitoni, E., & Matteucci, F. 2013 MNRAS, 435, 2918, doi: `10.1093/mnras/stt1495`

Müller-Sánchez, F., Prieto, M. A., Mezcua, M., et al. 2013 ApJ, 763, L1, doi: `10.1088/2041-8205/763/1/L1`

Naab, T., Oser, L., Emsellem, E., et al. 2014 MNRAS, 444, 3357, doi: `10.1093/mnras/stt1919`

Nair, P. B., & Abraham, R. G. 2010 ApJS, 186, 427, doi: `10.1088/0067-0049/186/2/427`

Nakajima, K., Ouchi, M., Isobe, Y., et al. 2023 ApJS, 269, 33, doi: `10.3847/1538-4365/acd556`

Nakajima, K., Ouchi, M., Xu, Y., et al. 2022 ApJS, 262, 3, doi: `10.3847/1538-4365/ac7710`

Navarro, J. F., Frenk, C. S., & White, S. D. M. 1996 ApJ, 462, 563, doi: `10.1086/177173`

Neeleman, M., Prochaska, J. X., Kanekar, N., & Rafelski, M. 2020 Nature, 581, 269, doi: `10.1038/s41586-020-2276-y`

Neeleman, M., Walter, F., Decarli, R., et al. 2023 ApJ, 958, 132, doi: `10.3847/1538-4357/ad05d2`

Neeleman, M., Novak, M., Venemans, B. P., et al. 2021 ApJ, 911, 141, doi: `10.3847/1538-4357/abe70f`

Nelder, J. A., & Mead, R. 1965 The Computer Journal, 7, 308, doi: 10.1093/comjnl/7.4.308

Nestor Shachar, A., Price, S. H., Förster Schreiber, N. M., et al. 2023 ApJ, 944, 78, doi: 10.3847/1538-4357/aca9cf

Newman, A. B., Treu, T., Ellis, R. S., & Sand, D. J. 2013 ApJ, 765, 25, doi: 10.1088/0004-637X/765/1/25

Newman, S. F., Shapiro Griffin, K., Genzel, R., et al. 2012 ApJ, 752, 111, doi: 10.1088/0004-637X/752/2/111

Newman, S. F., Genzel, R., Förster Schreiber, N. M., et al. 2013 ApJ, 767, 104, doi: 10.1088/0004-637X/767/2/104

Noguchi, M. 1998 Nature, 392, 253, doi: 10.1038/32596

Noguchi, M. 1999 ApJ, 514, 77, doi: 10.1086/306932

Noordermeer, E. 2008 MNRAS, 385, 1359, doi: 10.1111/j.1365-2966.2008.12837.x

Oh, S.-H., Hunter, D. A., Brinks, E., et al. 2015 AJ, 149, 180, doi: 10.1088/0004-6256/149/6/180

O'Leary, J. A., Moster, B. P., & Krämer, E. 2021 MNRAS, 503, 5646, doi: 10.1093/mnras/stab889

Oppenheimer, B. D., & Davé, R. 2008 MNRAS, 387, 577, doi: 10.1111/j.1365-2966.2008.13280.x

Orr, M. E., Hayward, C. C., Medling, A. M., et al. 2020 MNRAS, 496, 1620, doi: 10.1093/mnras/staa1619

Orr, M. E., Burkhart, B., Wetzel, A., et al. 2023 MNRAS, 521, 3708, doi: 10.1093/mnras/stad676

Osterbrock, D. E., & Ferland, G. J. 2006, Astrophysics of gaseous nebulae and active galactic nuclei

Pandya, V., Zhang, H., Huertas-Company, M., et al. 2024 ApJ, 963, 54, doi: 10.3847/1538-4357/ad1a13

Parlanti, E., Carniani, S., Pallottini, A., et al. 2023 A&A, 673, A153, doi: 10.1051/0004-6361/202245603

Parlanti, E., Carniani, S., Übler, H., et al. 2024a A&A, 684, A24, doi: 10.1051/0004-6361/202347914

Parlanti, E., Carniani, S., Übler, H., et al. 2024b A&A, 684, A24, doi: 10.1051/0004-6361/202347914

Parlanti, E., Carniani, S., Venturi, G., et al. 2025 A&A, 695, A6, doi: 10.1051/0004-6361/202451692

Pastras, S., Genzel, R., Tacconi, L. J., et al. 2025 arXiv e-prints, arXiv:2505.07925, doi: 10.48550/arXiv.2505.07925

Patrício, V., Richard, J., Carton, D., et al. 2018 MNRAS, 477, 18, doi: 10.1093/mnras/sty555

Patrício, V., Richard, J., Carton, D., et al. 2019 MNRAS, 489, 224, doi: 10.1093/mnras/stz2114

Pavesi, R., Riechers, D. A., Faisst, A. L., Stacey, G. J., & Capak, P. L. 2019 ApJ, 882, 168, doi: `10.3847/1538-4357/ab3a46`

Peacock, J. A. 1983 MNRAS, 202, 615, doi: `10.1093/mnras/202.3.615`

Perna, M., Arribas, S., Colina, L., et al. 2022 A&A, 662, A94, doi: `10.1051/0004-6361/202142659`

Perna, M., Arribas, S., Ji, X., et al. 2025 A&A, 694, A170, doi: `10.1051/0004-6361/202453090`

Péroux, C., Bouché, N., Kulkarni, V. P., & York, D. G. 2013 MNRAS, 436, 2650, doi: `10.1093/mnras/stt1760`

Peschken, N., Łokas, E. L., & Athanassoula, E. 2020 MNRAS, 493, 1375, doi: `10.1093/mnras/staa299`

Petit, A. C., Krumholz, M. R., Goldbaum, N. J., & Forbes, J. C. 2015 MNRAS, 449, 2588, doi: `10.1093/mnras/stv493`

Pettini, M., & Pagel, B. E. J. 2004 MNRAS, 348, L59, doi: `10.1111/j.1365-2966.2004.07591.x`

Pillepich, A., Nelson, D., Springel, V., et al. 2019 MNRAS, 490, 3196, doi: `10.1093/mnras/stz2338`

Pilyugin, L. S., & Thuan, T. X. 2005 ApJ, 631, 231, doi: `10.1086/432408`

Planck Collaboration, Abergel, A., Ade, P. A. R., et al. 2011 A&A, 536, A21, doi: `10.1051/0004-6361/201116455`

Planck Collaboration, Aghanim, N., Akrami, Y., et al. 2020 A&A, 641, A6, doi: `10.1051/0004-6361/201833910`

Pope, A., McKinney, J., Kamieneski, P., et al. 2023 ApJ, 951, L46, doi: `10.3847/2041-8213/acdf5a`

Posses, A., Aravena, M., González-López, J., et al. 2025 A&A, in press, doi: `10.1051/0004-6361/202449843`

Posses, A. C., Aravena, M., González-López, J., et al. 2023 A&A, 669, A46, doi: `10.1051/0004-6361/202243399`

Press, W. H., Teukolsky, S. A., Vetterling, W. T., & Flannery, B. P. 2007, Numerical Recipes 3rd Edition: The Art of Scientific Computing, 3rd edn. (USA: Cambridge University Press)

Price, S. H., Kriek, M., Barro, G., et al. 2020 ApJ, 894, 91, doi: `10.3847/1538-4357/ab7990`

Price, S. H., Shimizu, T. T., Genzel, R., et al. 2021 ApJ, 922, 143, doi: `10.3847/1538-4357/ac22ad`

Price, S. H., Übler, H., Förster Schreiber, N. M., et al. 2022 A&A, 665, A159, doi: `10.1051/0004-6361/202244143`

Privon, G. C., Ricci, C., Aalto, S., et al. 2020 ApJ, 893, 149, doi: `10.3847/1538-4357/ab8015`

Puglisi, A., Dudzevičiūtė, U., Swinbank, M., et al. 2023 MNRAS, 524, 2814, doi: `10.1093/mnras/stad1966`

Puskás, D., Tacchella, S., Simmonds, C., et al. 2025 MNRAS, 540, 2146, doi: `10.1093/mnras/staf813`

Queyrel, J., Contini, T., Kissler-Patig, M., et al. 2012 A&A, 539, A93, doi: `10.1051/0004-6361/201117718`

Rafikov, R. R. 2001 MNRAS, 323, 445, doi: `10.1046/j.1365-8711.2001.04201.x`

Rathjen, T.-E., Naab, T., Walch, S., et al. 2023 MNRAS, 522, 1843, doi: `10.1093/mnras/stad1104`

Reddy, N. A., Shapley, A. E., Sanders, R. L., et al. 2025 arXiv e-prints, arXiv:2506.17396, doi: `10.48550/arXiv.2506.17396`

Rees, M. J., & Ostriker, J. P. 1977 MNRAS, 179, 541, doi: `10.1093/mnras/179.4.541`

Remus, R.-S., Dolag, K., Naab, T., et al. 2017 MNRAS, 464, 3742, doi: `10.1093/mnras/stw2594`

Ren, W., Silverman, J. D., Faisst, A. L., et al. 2025 MNRAS, 544, 211, doi: `10.1093/mnras/staf1709`

Reshef, D. N., Reshef, Y. A., Finucane, H. K., et al. 2011 Science, 334, 1518, doi: `10.1126/science.1205438`

Rhoades, S., Jones, T., Vasan G. C., K., et al. 2025 ApJ, 991, 86, doi: `10.3847/1538-4357/adfa22`

Riechers, D. A., Carilli, C. L., Capak, P. L., et al. 2014 ApJ, 796, 84, doi: `10.1088/0004-637X/796/2/84`

Rizzo, F., Kohandel, M., Pallottini, A., et al. 2022 A&A, 667, A5, doi: `10.1051/0004-6361/202243582`

Rizzo, F., Vegetti, S., Fraternali, F., Stacey, H. R., & Powell, D. 2021 MNRAS, 507, 3952, doi: `10.1093/mnras/stab2295`

Rizzo, F., Vegetti, S., Powell, D., et al. 2020 Nature, 584, 201, doi: `10.1038/s41586-020-2572-6`

Rizzo, F., Roman-Oliveira, F., Fraternali, F., et al. 2023 A&A, 679, A129, doi: `10.1051/0004-6361/202346444`

Roberts, M. S., & Whitehurst, R. N. 1975 ApJ, 201, 327, doi: `10.1086/153889`

Robertson, B., Bullock, J. S., Cox, T. J., et al. 2006 ApJ, 645, 986, doi: `10.1086/504412`

Robertson, B. E. 2022 ARA&A, 60, 121, doi: `10.1146/annurev-astro-120221-044656`

Rodighiero, G., Daddi, E., Baronchelli, I., et al. 2011 ApJ, 739, L40, doi: `10.1088/2041-8205/739/2/L40`

Rodriguez-Gomez, V., Genel, S., Vogelsberger, M., et al. 2015 MNRAS, 449, 49, doi: `10.1093/mnras/stv264`

Rogstad, D. H., Lockhart, I. A., & Wright, M. C. H. 1974 ApJ, 193, 309, doi: `10.1086/153164`

Roman-Oliveira, F., Fraternali, F., & Rizzo, F. 2023a MNRAS, 521, 1045, doi: `10.1093/mnras/stad530`

Roman-Oliveira, F., Fraternali, F., & Rizzo, F. 2023b MNRAS, 521, 1045, doi: `10.1093/mnras/stad530`

Romano, M., Cassata, P., Morselli, L., et al. 2021 A&A, 653, A111, doi: `10.1051/0004-6361/202141306`

Romeo, A. B. 1992 MNRAS, 256, 307, doi: `10.1093/mnras/256.2.307`

Romeo, A. B., & Falstad, N. 2013 MNRAS, 433, 1389, doi: `10.1093/mnras/stt809`

Roper, F. A., Oman, K. A., Frenk, C. S., et al. 2023 MNRAS, 521, 1316, doi: `10.1093/mnras/stad549`

Rowland, L. E., Hodge, J., Bouwens, R., et al. 2024 MNRAS, 535, 2068, doi: `10.1093/mnras/stae2217`

Rubet, M., Menéndez-Delmestre, K., Gonçalves, T. S., et al. 2025 ApJ, 991, 35, doi: `10.3847/1538-4357/adf18c`

Rubin, V. C., & Ford, Jr., W. K. 1970 ApJ, 159, 379, doi: `10.1086/150317`

Rupke, D. S. N., Kewley, L. J., & Barnes, J. E. 2010a ApJ, 710, L156, doi: `10.1088/2041-8205/710/2/L156`

Rupke, D. S. N., Kewley, L. J., & Chien, L. H. 2010b ApJ, 723, 1255, doi: `10.1088/0004-637X/723/2/1255`

Russell, R. W., Melnick, G., Gull, G. E., & Harwit, M. 1980 ApJ, 240, L99, doi: `10.1086/183332`

Sánchez, S. F., Rosales-Ortega, F. F., Iglesias-Páramo, J., et al. 2014 A&A, 563, A49, doi: `10.1051/0004-6361/201322343`

Sánchez-Menguiano, L., Sánchez, S. F., Pérez, I., et al. 2018 A&A, 609, A119, doi: `10.1051/0004-6361/201731486`

Sancisi, R. 2004, in IAU Symposium, Vol. 220, Dark Matter in Galaxies, ed. S. Ryder, D. Pisano, M. Walker, & K. Freeman, 233, doi: `10.1017/S0074180900183299`

Sanders, R. L., Shapley, A. E., Topping, M. W., Reddy, N. A., & Brammer, G. B. 2024 ApJ, 962, 24, doi: `10.3847/1538-4357/ad15fc`

Sanders, R. L., Shapley, A. E., Reddy, N. A., et al. 2020 MNRAS, 491, 1427, doi: `10.1093/mnras/stz3032`

Sanders, R. L., Shapley, A. E., Topping, M. W., et al. 2025 arXiv e-prints, arXiv:2508.10099. `https://arxiv.org/abs/2508.10099`

Sani, E., Davies, R. I., Sternberg, A., et al. 2012 MNRAS, 424, 1963, doi: `10.1111/j.1365-2966.2012.21333.x`

Sargent, M. T., Béthermin, M., Daddi, E., & Elbaz, D. 2012 ApJ, 747, L31, doi: `10.1088/2041-8205/747/2/L31`

Schaye, J., Crain, R. A., Bower, R. G., et al. 2015 MNRAS, 446, 521, doi: `10.1093/mnras/stu2058`

Schlafly, E. F., & Finkbeiner, D. P. 2011 ApJ, 737, 103, doi: `10.1088/0004-637X/737/2/103`

Schruba, A., Leroy, A. K., Walter, F., et al. 2011 AJ, 142, 37, doi: `10.1088/0004-6256/142/2/37`

Schwarzschild, M. 1979 ApJ, 232, 236, doi: `10.1086/157282`

Scoville, N., Sheth, K., Aussel, H., et al. 2016 ApJ, 820, 83, doi: `10.3847/0004-637X/820/2/83`

Scoville, N., Lee, N., Vanden Bout, P., et al. 2017 ApJ, 837, 150, doi: `10.3847/1538-4357/aa61a0`

Sedov, L. I. 1946 Journal of Applied Mathematics and Mechanics, 10, 241

Sedov, L. I. 1959, Similarity and Dimensional Methods in Mechanics

Sérsic, J. L. 1968, Atlas de Galaxias Australes

Shao, Y., Wang, R., Weiss, A., et al. 2022 A&A, 668, A121, doi: `10.1051/0004-6361/202244610`

Shapiro, K. L., Genzel, R., Förster Schreiber, N. M., et al. 2008 ApJ, 682, 231, doi: `10.1086/587133`

Shapley, A. E., Sanders, R. L., Topping, M. W., et al. 2025 ApJ, 980, 242, doi: `10.3847/1538-4357/adad68`

Sharda, P., Krumholz, M. R., Wisnioski, E., et al. 2021a MNRAS, 502, 5935, doi: `10.1093/mnras/stab252`

Sharda, P., Wisnioski, E., Krumholz, M. R., & Federrath, C. 2021b MNRAS, 506, 1295, doi: `10.1093/mnras/stab1836`

Sharda, P., da Cunha, E., Federrath, C., et al. 2019 MNRAS, 487, 4305, doi: `10.1093/mnras/stz1543`

Sharma, G., Salucci, P., Harrison, C. M., van de Ven, G., & Lapi, A. 2021 MNRAS, 503, 1753, doi: `10.1093/mnras/stab249`

Sharma, G., Salucci, P., & van de Ven, G. 2022 A&A, 659, A40, doi: `10.1051/0004-6361/202141822`

Sharma, G., van de Ven, G., Salucci, P., & Martorano, M. 2025 A&A, 699, A164, doi: `10.1051/0004-6361/202347922`

Sharon, C. E., Tagore, A. S., Baker, A. J., et al. 2019 ApJ, 879, 52, doi: `10.3847/1538-4357/ab22b9`

Sharples, R., Bender, R., Agudo Berbel, A., et al. 2013 The Messenger, 151, 21

Shetty, R., & Ostriker, E. C. 2012 ApJ, 754, 2, doi: `10.1088/0004-637X/754/1/2`

Shibuya, T., Ouchi, M., Kubo, M., & Harikane, Y. 2016 ApJ, 821, 72, doi: `10.3847/0004-637X/821/2/72`

Shibuya, T., Ito, Y., Asai, K., et al. 2025 PASJ, 77, 21, doi: `10.1093/pasj/psae096`

Shu, F. H. 1992, The physics of astrophysics. Volume II: Gas dynamics. (Mill Valley, Calif. : University Science Books)

Shull, J. M., Smith, B. D., & Danforth, C. W. 2012 ApJ, 759, 23, doi: `10.1088/0004-637X/759/1/23`

Sicking, F. J. 1997, PhD thesis, University of Groningen

Simons, R. C., Kassin, S. A., Weiner, B., et al. 2018, in American Astronomical Society Meeting Abstracts, Vol. 231, American Astronomical Society Meeting Abstracts #231, 309.02

Simons, R. C., Papovich, C., Momcheva, I., et al. 2021 ApJ, 923, 203, doi: 10.3847/1538-4357/ac28f4

Slipher, V. M. 1914 Lowell Observatory Bulletin, 2, 66

Slob, M., Kriek, M., de Graaff, A., et al. 2025 A&A, 702, A110, doi: 10.1051/0004-6361/202555812

Smit, R., Bouwens, R. J., Carniani, S., et al. 2018 Nature, 553, 178, doi: 10.1038/nature24631

Sobral, D., Swinbank, A. M., Stott, J. P., et al. 2013 ApJ, 779, 139, doi: 10.1088/0004-637X/779/2/139

Sofue, Y., & Rubin, V. 2001 ARA&A, 39, 137, doi: 10.1146/annurev.astro.39.1.137

Sok, V., Muzzin, A., Jablonka, P., et al. 2025 ApJ, 979, 14, doi: 10.3847/1538-4357/ad96bb

Solimano, M., González-López, J., Aravena, M., et al. 2024 A&A, 689, A145, doi: 10.1051/0004-6361/202449192

Solimano, M., González-López, J., Aravena, M., et al. 2025 A&A, 693, A70, doi: 10.1051/0004-6361/202451551

Sommovigo, L., Ferrara, A., Carniani, S., et al. 2022 MNRAS, 517, 5930, doi: 10.1093/mnras/stac2997

Sotillo-Ramos, D., Pillepich, A., Donnari, M., et al. 2022 MNRAS, 516, 5404, doi: 10.1093/mnras/stac2586

Speagle, J. S., Steinhardt, C. L., Capak, P. L., & Silverman, J. D. 2014 ApJS, 214, 15, doi: 10.1088/0067-0049/214/2/15

Spearman, C. 1904 The American Journal of Psychology, 15, 72. http://www.jstor.org/stable/1412159

Spitoni, E., Cescutti, G., Minchev, I., et al. 2019 A&A, 628, A38, doi: 10.1051/0004-6361/201834665

Spitoni, E., & Matteucci, F. 2011 A&A, 531, A72, doi: 10.1051/0004-6361/201015749

Spitoni, E., Romano, D., Matteucci, F., & Ciotti, L. 2015 ApJ, 802, 129, doi: 10.1088/0004-637X/802/2/129

Spitzer, Jr., L. 1942 ApJ, 95, 329, doi: 10.1086/144407

Springel, V., Frenk, C. S., & White, S. D. M. 2006 Nature, 440, 1137, doi: 10.1038/nature04805

Springel, V., & Hernquist, L. 2005 ApJ, 622, L9, doi: 10.1086/429486

Springel, V., White, S. D. M., Jenkins, A., et al. 2005 Nature, 435, 629, doi: 10.1038/nature03597

Springel, V., Pakmor, R., Pillepich, A., et al. 2018 MNRAS, 475, 676, doi: 10.1093/mnras/stx3304

Stacey, G. J., Geis, N., Genzel, R., et al. 1991 ApJ, 373, 423, doi: 10.1086/170062

Stach, S. M., Smail, I., Swinbank, A. M., et al. 2018 ApJ, 860, 161, doi: 10.3847/1538-4357/aac5e5

Stanghellini, L., Magrini, L., Casasola, V., & Villaver, E. 2014 A&A, 567, A88, doi: 10.1051/0004-6361/201423423

Stark, D. P., Swinbank, A. M., Ellis, R. S., et al. 2008 Nature, 455, 775, doi: 10.1038/nature07294

Stefanon, M., Yan, H., Mobasher, B., et al. 2017 ApJS, 229, 32, doi: 10.3847/1538-4365/aa66cb

Storey, P. J., & Zeippen, C. J. 2000 MNRAS, 312, 813, doi: 10.1046/j.1365-8711.2000.03184.x

Stott, J. P., Sobral, D., Swinbank, A. M., et al. 2014 MNRAS, 443, 2695, doi: 10.1093/mnras/stu1343

Straatman, C. M. S., van der Wel, A., van Houdt, J., et al. 2022 ApJ, 928, 126, doi: 10.3847/1538-4357/ac4e18

Su, Y.-C., Lin, L., Pan, H.-A., et al. 2022 ApJ, 934, 173, doi: 10.3847/1538-4357/ac77fd

Sun, X., Wang, X., Ma, X., et al. 2025 ApJ, 986, 179, doi: 10.3847/1538-4357/addab5

Swinbank, A. M., Smail, I., Sobral, D., et al. 2012a ApJ, 760, 130, doi: 10.1088/0004-637X/760/2/130

Swinbank, A. M., Sobral, D., Smail, I., et al. 2012b MNRAS, 426, 935, doi: 10.1111/j.1365-2966.2012.21774.x

Swinbank, A. M., Papadopoulos, P. P., Cox, P., et al. 2011 ApJ, 742, 11, doi: 10.1088/0004-637X/742/1/11

Tacconi, L. J., Genzel, R., & Sternberg, A. 2020 ARA&A, 58, 157, doi: 10.1146/annurev-astro-082812-141034

Tacconi, L. J., Genzel, R., Smail, I., et al. 2008 ApJ, 680, 246, doi: 10.1086/587168

Tacconi, L. J., Genzel, R., Neri, R., et al. 2010 Nature, 463, 781, doi: 10.1038/nature08773

Tacconi, L. J., Neri, R., Genzel, R., et al. 2013 ApJ, 768, 74, doi: 10.1088/0004-637X/768/1/74

Tacconi, L. J., Genzel, R., Saintonge, A., et al. 2018 ApJ, 853, 179, doi: 10.3847/1538-4357/aaa4b4

Tadaki, K.-i., Kodama, T., Nelson, E. J., et al. 2017 ApJ, 841, L25, doi: 10.3847/2041-8213/aa7338

Tadaki, K.-i., Iono, D., Yun, M. S., et al. 2018 Nature, 560, 613, doi: 10.1038/s41586-018-0443-1

Tadaki, K.-i., Iono, D., Yun, M. S., et al. 2020 ApJ, 889, 141, doi: 10.3847/1538-4357/ab64f4

Tamburro, D., Rix, H. W., Leroy, A. K., et al. 2009 AJ, 137, 4424, doi: 10.1088/0004-6256/137/5/4424

Tanaka, T. S., Silverman, J. D., Nakazato, Y., et al. 2024 PASJ, 76, 1323, doi: 10.1093/pasj/psae091

Taylor, G. 1950 Proceedings of the Royal Society of London Series A, 201, 159, doi: `10.1098/rspa.1950.0049`

Taylor, P., & Kobayashi, C. 2017 MNRAS, 471, 3856, doi: `10.1093/mnras/stx1860`

Telikova, K., González-López, J., Aravena, M., et al. 2025 A&A, 669, A5, doi: `10.1051/0004-6361/202452990`

Tiley, A. L., Swinbank, A. M., Harrison, C. M., et al. 2019 MNRAS, 485, 934, doi: `10.1093/mnras/stz428`

Tiley, A. L., Gillman, S., Cortese, L., et al. 2021 MNRAS, 506, 323, doi: `10.1093/mnras/stab1692`

Tissera, P. B., Rosas-Guevara, Y., Sillero, E., et al. 2022 MNRAS, 511, 1667, doi: `10.1093/mnras/stab3644`

Tohill, C., Bamford, S. P., Conselice, C. J., et al. 2024 ApJ, 962, 164, doi: `10.3847/1538-4357/ad17b8`

Toomre, A. 1964 ApJ, 139, 1217, doi: `10.1086/147861`

Troncoso, P., Maiolino, R., Sommariva, V., et al. 2014 A&A, 563, A58, doi: `10.1051/0004-6361/201322099`

Tsukui, T., & Iguchi, S. 2021 Science, 372, 1201, doi: `10.1126/science.abe9680`

Tsukui, T., Wisnioski, E., Bland-Hawthorn, J., & Freeman, K. 2025 MNRAS, 540, 3493, doi: `10.1093/mnras/staf604`

Tsukui, T., Wisnioski, E., Bland-Hawthorn, J., et al. 2024 MNRAS, 527, 8941, doi: `10.1093/mnras/stad3588`

Turner, O. J., Cirasuolo, M., Harrison, C. M., et al. 2017 MNRAS, 471, 1280, doi: `10.1093/mnras/stx1366`

Übler, H., Naab, T., Oser, L., et al. 2014 MNRAS, 443, 2092, doi: `10.1093/mnras/stu1275`

Übler, H., Genzel, R., Tacconi, L. J., et al. 2018 ApJ, 854, L24, doi: `10.3847/2041-8213/aaacfa`

Übler, H., Genzel, R., Wisnioski, E., et al. 2019 ApJ, 880, 48, doi: `10.3847/1538-4357/ab27cc`

Übler, H., Genel, S., Sternberg, A., et al. 2021 MNRAS, 500, 4597, doi: `10.1093/mnras/staa3464`

Übler, H., Förster Schreiber, N. M., van der Wel, A., et al. 2024a MNRAS, 527, 9206, doi: `10.1093/mnras/stad3826`

Übler, H., D'Eugenio, F., Perna, M., et al. 2024b MNRAS, 533, 4287, doi: `10.1093/mnras/stae1993`

Übler, H., Förster Schreiber, N. M., van der Wel, A., et al. 2024c MNRAS, 527, 9206, doi: `10.1093/mnras/stad3826`

Umehata, H., Steidel, C. C., Smail, I., et al. 2025 PASJ, 77, 432, doi: `10.1093/pasj/psaf010`

Vallini, L., Gallerani, S., Ferrara, A., Pallottini, A., & Yue, B. 2015 ApJ, 813, 36, doi: `10.1088/0004-637X/813/1/36`

Vallini, L., Witstok, J., Sommovigo, L., et al. 2024 MNRAS, 527, 10, doi: `10.1093/mnras/stad3150`

van Albada, T. S., Bahcall, J. N., Begeman, K., & Sancisi, R. 1985 ApJ, 295, 305, doi: `10.1086/163375`

van de Hulst, H. C., Raimond, E., & van Woerden, H. 1957 Bull. Astron. Inst. Netherlands, 14, 1

van den Bergh, S., Abraham, R. G., Ellis, R. S., et al. 1996 AJ, 112, 359, doi: `10.1086/118020`

van der Hulst, J. M., Terlouw, J. P., Begeman, K. G., Zwitser, W., & Roelfsema, P. R. 1992, in Astronomical Society of the Pacific Conference Series, Vol. 25, Astronomical Data Analysis Software and Systems I, ed. D. M. Worrall, C. Biemesderfer, & J. Barnes, 131

van der Kruit, P. C., & Allen, R. J. 1978 ARA&A, 16, 103, doi: `10.1146/annurev.aa.16.090178.000535`

van der Kruit, P. C., & Freeman, K. C. 2011 ARA&A, 49, 301, doi: `10.1146/annurev-astro-083109-153241`

van der Wel, A., Franx, M., van Dokkum, P. G., et al. 2014 ApJ, 788, 28, doi: `10.1088/0004-637X/788/1/28`

van Houdt, J., van der Wel, A., Bezanson, R., et al. 2021 ApJ, 923, 11, doi: `10.3847/1538-4357/ac1f29`

Varadaraj, R. G., Bowler, R. A. A., Jarvis, M. J., et al. 2024 MNRAS, 533, 3724, doi: `10.1093/mnras/stae2022`

Varidel, M., & Croom, S. 2023, Blobby3D: Bayesian inference for gas kinematics,, Astrophysics Source Code Library, record ascl:2303.005 `http://ascl.net/2303.005`

Varidel, M. R., Croom, S. M., Lewis, G. F., et al. 2019 MNRAS, 485, 4024, doi: `10.1093/mnras/stz670`

Venkateshwaran, A., Weiss, A., Sulzenauer, N., et al. 2024 ApJ, 977, 161, doi: `10.3847/1538-4357/ad7bb4`

Venturi, G., Carniani, S., Parlanti, E., et al. 2024 A&A, 691, A19, doi: `10.1051/0004-6361/202449855`

Villanueva, V., Herrera-Camus, R., González-López, J., et al. 2024 A&A, 691, A133, doi: `10.1051/0004-6361/202451490`

Virtanen, P., Gommers, R., Oliphant, T. E., et al. 2020 Nature Methods, 17, 261, doi: `10.1038/s41592-019-0686-2`

Vogelsberger, M., Genel, S., Springel, V., et al. 2014 MNRAS, 444, 1518, doi: `10.1093/mnras/stu1536`

Vogt, F. P. A., Pérez, E., Dopita, M. A., Verdes-Montenegro, L., & Borthakur, S. 2017 A&A, 601, A61, doi: `10.1051/0004-6361/201629853`

Wang, B., & Silk, J. 1994 ApJ, 427, 759, doi: `10.1086/174182`

Wang, W., Cantalupo, S., Pensabene, A., et al. 2025 Nature Astronomy, doi: `10.1038/s41550-025-02500-2`

Wang, X., Jones, T. A., Treu, T., et al. 2017 ApJ, 837, 89, doi: 10.3847/1538-4357/aa603c

Wang, X., Jones, T. A., Treu, T., et al. 2019 ApJ, 882, 94, doi: 10.3847/1538-4357/ab3861

Wang, X., Jones, T. A., Treu, T., et al. 2020 ApJ, 900, 183, doi: 10.3847/1538-4357/abacce

Wang, X., Jones, T., Vulcani, B., et al. 2022 ApJ, 938, L16, doi: 10.3847/2041-8213/ac959e

Weitzel, L., Krabbe, A., Kroker, H., et al. 1996 A&AS, 119, 531

Wellons, S., Faucher-Giguère, C.-A., Anglés-Alcázar, D., et al. 2020 MNRAS, 497, 4051, doi: 10.1093/mnras/staa2229

Wetzel, A., Hayward, C. C., Sanderson, R. E., et al. 2023 ApJS, 265, 44, doi: 10.3847/1538-4365/acb99a

Whitaker, K. E., van Dokkum, P. G., Brammer, G., & Franx, M. 2012 ApJ, 754, L29, doi: 10.1088/2041-8205/754/2/L29

Whiting, M. T. 2012 MNRAS, 421, 3242, doi: 10.1111/j.1365-2966.2012.20548.x

Whittet, D. C. B. 1992, Dust in the galactic environment

Williams, T. G., Kreckel, K., Belfiore, F., et al. 2022 MNRAS, 509, 1303, doi: 10.1093/mnras/stab3082

Wilson, C. D., Warren, B. E., Irwin, J., et al. 2011 MNRAS, 410, 1409, doi: 10.1111/j.1365-2966.2010.17646.x

Wisnioski, E., Mendel, J. T., Leaman, R., et al. 2025 MNRAS, doi: 10.1093/mnras/staf1606

Wisnioski, E., Förster Schreiber, N. M., Wuyts, S., et al. 2015 ApJ, 799, 209, doi: 10.1088/0004-637X/799/2/209

Wisnioski, E., Förster Schreiber, N. M., Fossati, M., et al. 2019 ApJ, 886, 124, doi: 10.3847/1538-4357/ab4db8

Wisz, M. E., Masters, K. L., Daniel, K. J., Stark, D. V., & Belfiore, F. 2025 ApJ, 983, 57, doi: 10.3847/1538-4357/adbb6f

Wolfire, M. G., McKee, C. F., Hollenbach, D., & Tielens, A. G. G. M. 2003 ApJ, 587, 278, doi: 10.1086/368016

Wolfire, M. G., Vallini, L., & Chevance, M. 2022 ARA&A, 60, 247, doi: 10.1146/annurev-astro-052920-010254

Wuyts, E., Wisnioski, E., Fossati, M., et al. 2016 ApJ, 827, 74, doi: 10.3847/0004-637X/827/1/74

Wuyts, S., Förster Schreiber, N. M., van der Wel, A., et al. 2011 ApJ, 742, 96, doi: 10.1088/0004-637X/742/2/96

Wuyts, S., Förster Schreiber, N. M., Genzel, R., et al. 2012 ApJ, 753, 114, doi: 10.1088/0004-637X/753/2/114

Wuyts, S., Förster Schreiber, N. M., Nelson, E. J., et al. 2013 ApJ, 779, 135, doi: 10.1088/0004-637X/779/2/135

Wuyts, S., Förster Schreiber, N. M., Wisnioski, E., et al. 2016 ApJ, 831, 149, doi: 10.3847/0004-637X/831/2/149

Wyithe, J. S. B., Turner, E. L., & Spergel, D. N. 2001 ApJ, 555, 504, doi: 10.1086/321437

Xi, H., Peng, B., Staveley-Smith, L., et al. 2024 ApJS, 274, 18, doi: `10.3847/1538-4365/ad67d5`

Xu, D., & Yu, S.-Y. 2024 A&A, 682, L17, doi: `10.1051/0004-6361/202449252`

Yang, C.-C., & Krumholz, M. 2012 ApJ, 758, 48, doi: `10.1088/0004-637X/758/1/48`

Yuan, T. T., Kewley, L. J., Swinbank, A. M., Richard, J., & Livermore, R. C. 2011 ApJ, 732, L14, doi: `10.1088/2041-8205/732/1/L14`

Zabl, J., Bouché, N. F., Schroetter, I., et al. 2019 MNRAS, 485, 1961, doi: `10.1093/mnras/stz392`

Zabl, J., Bouché, N. F., Schroetter, I., et al. 2020 MNRAS, 492, 4576, doi: `10.1093/mnras/stz3607`

Zabl, J., Bouché, N. F., Wisotzki, L., et al. 2021 MNRAS, 507, 4294, doi: `10.1093/mnras/stab2165`

Zanella, A., Daddi, E., Magdis, G., et al. 2018 MNRAS, 481, 1976, doi: `10.1093/mnras/sty2394`

Zaritsky, D., Kennicutt, Jr., R. C., & Huchra, J. P. 1994 ApJ, 420, 87, doi: `10.1086/173544`

Zhao, H. 1996 MNRAS, 278, 488, doi: `10.1093/mnras/278.2.488`

Zolotov, A., Dekel, A., Mandelker, N., et al. 2015 MNRAS, 450, 2327, doi: `10.1093/mnras/stv740`

Zwicky, F. 1933 Helvetica Physica Acta, 6, 110

Danksagung

Many thanks go to my supervisor, Natascha Förster Schreiber, whose advice, encouragement, and unwavering support have guided me throughout my PhD, both professionally and personally. Without her immensely valuable and motivational feedback on every draft of the publications, this thesis would never have been completed. My sincere thanks to Reinhard Genzel and Linda Tacconi for giving me the invaluable opportunity to pursue my PhD within such a vibrant, resource-rich research group, and for their steadfast support and trust, especially during challenging times.

I am most grateful for my mentors, Daizhong Liu and Sedona Price, for the time we shared at MPE. They have been exceptional mentors and friends, always willing to lend a listening ear and offer advice. Though we have parted to different continents, they continued to be encouraging and supportive far beyond what I could have hoped, and never stopped being a constant source of inspiration and motivation, shining the way forward.

There are also many people to whom I am grateful. Thank you to Rodrigo Herrera-Camus and the entire CRISTAL collaboration for their confidence and support during my first experience working in a large collaboration. I feel fortunate to have had the opportunity to work with such a valuable dataset and to collaborate with so many great minds. Thank you, Rodrigo, for your incredible hospitality during my visit to Concepción.

My heartfelt thanks also extend to other members of the MPE IR group, past and present. In particular, I thank Minju Lee, whose engaging conversations always left me feeling encouraged and motivated. I also appreciate the warm hospitality she showed me during my visit to Copenhagen. I am thankful to Hannah Übler for her support during the initial phase of my PhD, and now for her assistance with the German translation of the abstract. Other colleagues, particularly Daryl, Jianhang, Amit, Giulia, and Yixian, have been wonderful companions over the past few years. I appreciate the camaraderie that formed along the way.

The administrative staff in the group, particularly Adriane Richter, Susanne Dengler, Benjamin Herfert, and Sandra Redl, have made navigating the complex bureaucratic landscape immeasurably easier. Thank you all.

My officemate, Stavros Pastras, deserves special thanks for sharing his office space, offering words of encouragement, and engaging in stimulating discussions (though sometimes too intense) on various topics. His patience and listening (tolerating) to my lament from time to time have been a great source of support.

I am deeply thankful to my master supervisors, Jeremy Lim and Tom Broadhurst, for their generosity in offering me the opportunity to embark on research as an undergraduate, and for their guidance throughout my research at HKU, which laid the bedrock for my PhD journey.

To Mr. Lam and Mr. Yin, my high school physics and chemistry teachers: thank you for lighting the spark that instilled in me the courage to pursue my curiosity in physics and astronomy, even when it seemed like an impossible dream for a 15-year-old.

Thank you also to Tommy Lau, Xueying Zheng and David Kaltenbrunner, for their company in this foreign land from time to time when off work. I would also like to thank my neighbours, the late Hermann Winstermann and his wife Gabriele, for their hospitality when I first moved in and for the warmth and support they continued to offer me thereafter.

And to the old friends, Yin Tung Ng and Man Wai Se, for the friendship since those blissful, clueless teenage days.

Above all, Michael, for everything in the bygone days, the present and the days to come.